Contribution to the Control of Doubly-Fed Induction Generators in Wind Power Plants with Particular Consideration of Asymmetrical Grid Conditions

DISSERTATION

zur Erlangung des akademischen Grades Doktoringenieur (Dr.-Ing.)

der

Fakultät für Elektrotechnik und Informationstechnik
der Technischen Universität Ilmenau

vorgelegt von

Dipl.-Ing. Marlies Richter

Gutachter

Univ.-Prof. Dr.-Ing. habil. Jürgen Petzoldt, TU Ilmenau
Univ.-Prof. Dr.-Ing. Wilfried Hofmann, TU Dresden
Dr.-Ing. Daniel Navarro, Ennera Energy and Mobility, S.L.

Tag der Einreichung 20.12.2011
Tag der wissenschaftlichen Aussprache 21.06.2012

urn:nbn:de:gbv:ilm1-2012000372

Theses

- The rotor-side and grid-side inverter currents of a doubly-fed induction generator can be controlled using different current control strategies.
- Field-oriented control is the most common means of controlling the inverter currents of a doubly-fed induction generator but does not allow for a systematic manipulation of negative-sequence currents during asymmetrical grid voltage dips.
- Contrarily to field-oriented control, which uses proportional-integral controllers in a rotating coordinate system, it is possible to control the inverter currents in a static coordinate system using frequency-selective controllers (FSC).
- The control of positive-sequence and negative-sequence rotor current components enables torque oscillations during asymmetrical grid faults with limited dip-depth to be reduced.
- The control of positive-sequence and negative-sequence grid-side inverter current components enables DC-link voltage oscillations during asymmetrical grid faults with limited dip-depth to be reduced. For this purpose a feed-forward algorithm using rotor voltages and rotor currents is essential.
- The control of positive-sequence and negative-sequence current components can be realised in two different coordinate systems which rotate in opposite directions, using proportional-integral controllers (PNC); or in a static coordinate system, using frequency-selective controllers (FSC(PN)).
- The improvements achieved by means of alternative control strategies (FSC, PNC, FSC(PN)) are subject to the constraints of the hardware – such as current and voltage limits, time delays in the control strategies deployed and the nonlinear behaviour of the doubly-fed induction generator.
- The proposed control strategies can be applied to such systems as solar converters or the active front-end of wind power plants which employ full-scale converters.

Abstract

In the study presented here, four different control strategies for the control of the inverter currents of a doubly-fed induction generator (DFIG) system are analysed and evaluated by means of simulation using Matlab/Simulink®. Special attention is paid to the behaviour of the generator during asymmetrical grid voltage dips. Different control schemes are employed to reduce torque and DC-link voltage oscillations and the resulting additional loads on the system during such dips.

The *field-oriented control* (FOC) scheme is the one usually deployed for the control of DFIGs in wind power plants and is used as the reference system within this study. The inverter currents (of the rotor-side inverter and the grid-side inverter) are regulated by proportional-integral controllers (PI) in a rotating coordinate system in which they are represented by dq-components. These components are direct quantities. A *positive-negative-sequence current control* (PNC) strategy is used to control the positive-sequence currents and the negative-sequence currents separately in two contra-rotating coordinate systems using PI-controllers. In contrast to the first two control strategies, *frequency-selective current controllers* (FSC) serve to regulate the currents in a static coordinate system. In this case the currents are represented by $\alpha\beta$-components which are alternating quantities. Combining the FSC and PNC strategies will produce *frequency-selective positive-negative-sequence current controllers* (FSC(PN)). These control the currents in a static coordinate system. The currents are represented by alternating $\alpha\beta$-components as in frequency-selective control but separate reference values for the negative-sequence currents are provided as in positive-negative-sequence control.

Theoretical reasoning suggests and simulations prove that the three proposed alternative control strategies can improve the behaviour of DFIG-systems during slight asymmetries in the grid voltage. During severe dips the effect is limited by several constraints, namely by the inverter rating (limited inverter voltages and currents), by time delays introduced by the component calculation for PNC and FSC(PN) and by the nonlinear behaviour of the DFIG-system (saturation of mutual inductance). Nevertheless, the proposed novel control strategies could be applied beneficially to other systems, such as photovoltaic inverters or full-scale inverters for wind power plants.

Zusammenfassung

Die vorgelegte Arbeit stellt vier Verfahren für die Regelung der Umrichterströme einer doppeltgespeisten Asynchronmaschine (DGASM) vor. Diese werden mit Hilfe von Simulationen mit Matlab/Simulink®analysiert. Besondere Beachtung wird dabei dem Verhalten des Generators während unsymmetrischer Spannungseinbrüche im elektrischen Netz geschenkt. Die vorgestellten Regelungsverfahren haben zum Ziel, Drehmoment- und Zwischenkreisspannungsschwingungen während solcher Fehlerfälle zu reduzieren und damit die zusätzlichen Belastungen des Systems zu verringern.

Die *feldorientierte Regelung* (FOR) wird häufig zur Regelung von DGASMs in Windkraftanlagen eingesetzt und dient in dieser Arbeit als Vergleichsbasis. Die Umrichterströme von maschinen- und netzseitigem Wechselrichter werden mittels Proportional-Integral-Reglern (PI) in einem rotierenden Koordinatensystem geregelt, in welchem sie Gleichgrößen darstellen, die in dq-Komponenten angegeben werden. Die getrennte Regelung von Mit- und Gegensystemströmen in zwei entgegengesetzt rotierenden Koordinatensystemen wird im Rahmen der vorgelegten Arbeit als *PN-Regelung* (PNR) bezeichnet. Auch für diese Regelung werden PI-Regler verwendet. Im Gegensatz zur feldorientierten und zur PN-Regelung arbeitet die *frequenzselektive Regelung* (FSR) in einem ruhenden Koordinatensystem. In diesem werden die Umrichterströme als Wechselgrößen in $\alpha\beta$-Komponenten geregelt. Die Kombination von frequenzselektiver und PN-Regelung ergibt die in dieser Arbeit als *FS(PN)-Regelung* bezeichnete Struktur, in der die Ströme ebenfalls in einem ruhenden Koordinatensystem als Wechselgrößen geregelt werden, wobei gezielt Sollwerte auch für die Gegensystemkomponenten vorgegeben werden.

Sowohl theoretische Überlegungen als auch die durchgeführten Simulationen zeigen, dass die drei vorgeschlagenen alternativen Regelungsverfahren das Verhalten der DGASM während leichter Unsymmetrien verbessern können. Die möglichen Verbesserungen sind allerdings sowohl durch die vorhandene Hardware (Auslegung der Umrichter: maximal zulässige Ströme und Spannungen), durch die Regelungsverfahren selber (zeitliche Verzögerungen durch die Berechnung der Mit- und Gegensystemkomponenten bei PN- und FS(PN)-Regelung) als auch durch Nichtlinearitäten des Systems (Sättigung der Hauptinduktivität der DGASM) begrenzt. Eine Anwendung der vorgestellten neuen Regelungsverfahren auf andere Probleme wie z.B. Photovoltaikwechselrichter oder Umrichter für Windkraftanlagen mit Vollumrichter erscheint dennoch vielversprechend.

Vorwort

Die vorliegende Dissertation entstand im Rahmen meines Promotionsstudiums am Fachgebiet Leistungselektronik und Steuerungstechnik in der elektrischen Energietechnik der Technischen Universität Ilmenau. Ein Teil der Arbeit wurde dabei im Rahmen eines Kooperationsprojektes mit dem spanischen Windkraftanlagenhersteller Gamesa Eólica, S.A. erstellt.

Meinem Doktorvater Prof. Dr.-Ing. habil. Jürgen Petzoldt möchte ich für die Möglichkeit zur Durchführung dieser Arbeit, für die Unterstützung während der Erstellung und für die Begutachtung der Arbeit danken.

Auch Prof. Dr.-Ing. Wilfried Hofmann und Dr.-Ing. Daniel Navarro danke ich herzlich für die Übernahme der Begutachtung.

Herrn Prof. Dr.-Ing. habil. em. W. Gens und Dr.-Ing. Uwe Rädel danke ich für das Interesse an meiner Arbeit und für ihre konstruktiven Hinweise zur Verbesserung des Manuskriptes. Ebenso danke ich den Mitarbeitern des Fachgebietes für den fachlichen Austausch und die moralische Unterstützung.

Die Arbeit wurde durch ein Stipendium der Stiftung der Deutschen Wirtschaft finanziell ermöglicht. Für das in mich gesetzte Vertrauen, die Geduld sowie die Möglichkeit zur parallelen Umsetzung außeruniversitärer Projekte möchte ich mich bei der Stiftung und ihren Mitarbeitern herzlich bedanken. Für die Finanzierung der letzten Arbeitsmonate danke ich dem Gleichstellungsbüro der TU Ilmenau.

Ein herzlicher Dank geht auch an alle Korrekturleser: Wiebke Müller, Lena te Boekhorst, Ines Richter, Matthias Hoder und Dr. Andreas Bley.

Muchas gracias a los collegas de Gamesa Eólica, S.A. – en particular Dr.-Ing. Daniel Navarro y Itziar Martinez, Marta Soto y Gerardo Medrano – por la cooperación y las discusiónes técnicas.

Last but not least, thanks to Susan Kubitz for proof reading the manuscript.

Contents

1 Introduction

1.1 Reasons for study, structure

In recent years, the number of wind energy plants installed has grown rapidly not only in Germany but all over the world. The total installed capacity in Germany was more than 27.000 MW in June 2011 (cf. [8]) and 197.000 MW worldwide in 2010 (cf. [14, p. 11]). As the feeding of wind-generated electricity to the grid has increased, the requirements of the network operators on the wind power plants have grown. These include fault-ride-through (FRT) capability and support of the grid voltage. To transform wind power into electrical power, the generators commonly used are firstly, synchronous generators, secondly asynchronous generators with a squirrel-cage rotor and, thirdly, doubly-fed induction generators (cf. [4, p. 159]). The third type will be analysed here. Four different control strategies for the converter currents are simulated and compared. The aim is to evaluate the behaviour of the system during asymmetrical grid conditions and its performance with regard to the grid connection requirements.

Chapter 1 introduces the technical system to be analysed. The grid code requirements for wind turbines are also outlined, as well as the loads on the system that originate from asymmetrical voltages in the electrical grid. In addition, Chapter 1 contains a review of the literature on existing control schemes for DFIG-systems affected by grid faults. All results presented in this study are based on simulations using Matlab/Simulink®. Chapter 2 presents the model of the DFIG's electrical system developed for the study and some of the results from the validation of this model. The main part of the study is to be found in Chapters 3, 4 and 5, in which four control strategies are described and analysed:

- field-oriented control (FOC, Chapter 3) which is generally used to control a doubly-fed induction generator and which serves as basis of comparison within this study,
- control of positive-sequence and negative-sequence currents in two coordinate systems (PNC, Chapter 4) and
- frequency-selective control (FSC, Chapter 5), also called "sine control" or "resonant control" in the literature, which is based on the "inner model principle"[1].
- In Section 5.8 the two types of frequency-selective and positive-negative-sequence control are combined into the FSC(PN)-control scheme.

[1] "Inneres-Modell Prinzip" described in [27].

In Chapter 6 the four control strategies analysed are compared and subjected to systematisation. Chapter 7 completes the dissertation, providing a summary and an indication of questions remaining.

1.2 Doubly-fed induction generator system

The electrical system of Doubly-Fed Induction Generators (DFIG) is analysed within this study and depicted in Fig. 1.1. The main parts of the system are

- the generator (DFIG),
- the main transformer, connecting the system to the grid,
- the back-to-back converter (consisting of the rotor-side inverter[2], the DC-link capacitor (C_{DC}) and the grid-side inverter) and
- a transformer connecting the grid-side inverter to the stator (GSC transformer).

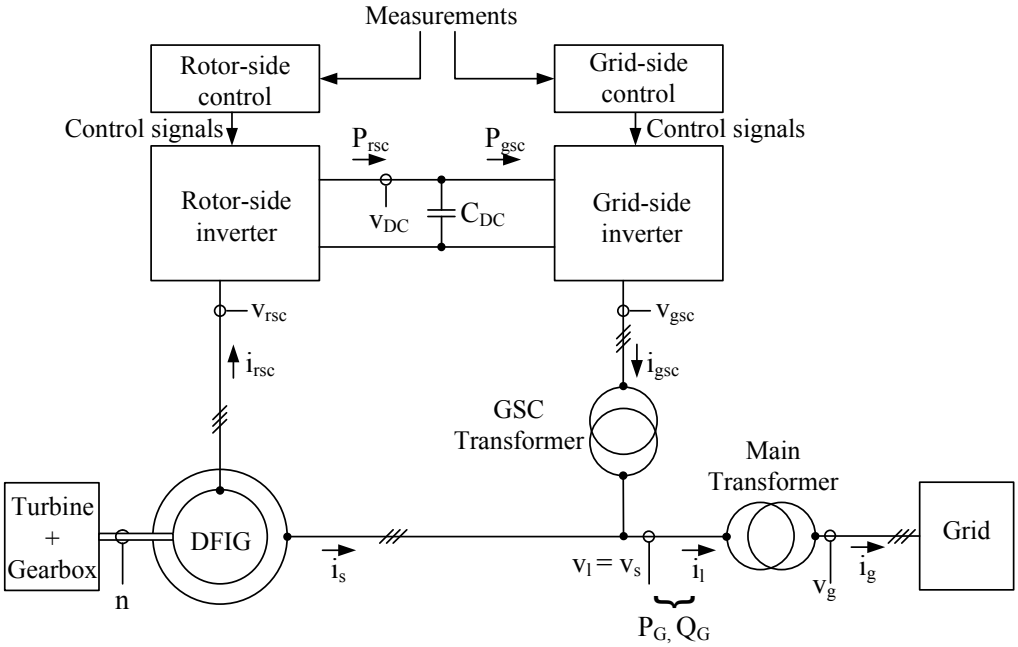

Figure 1.1: Electrical system of a DFIG

In this study, only this electrical system is considered. No analysis is given of the conversion of the wind energy into the rotational energy of the turbine and generator or of the superior turbine control. An overview of the principles of wind energy conversion and of different types of wind power plants is to be found at several points in the literature, among them [17]. Wind energy

[2]The rotor inductor, connecting the DFIG rotor and the rotor-side inverter, is always added to the rotor resistance and rotor leakage inductance. For the sake of simplicity it has been omitted from this illustration.

conversion systems, power electronic devices deployed for wind power applications and wind farm topologies are described in general in [3] and in [19]. The main parameters of the system simulated within this study are given in Appendix D in Table D.1.

There are two main parts to the control of the electrical system. The first part is the rotor-side control, consisting of the rotor current controllers and active and reactive power controllers[3]. Its structure is demonstrated in Fig. 1.2[4].

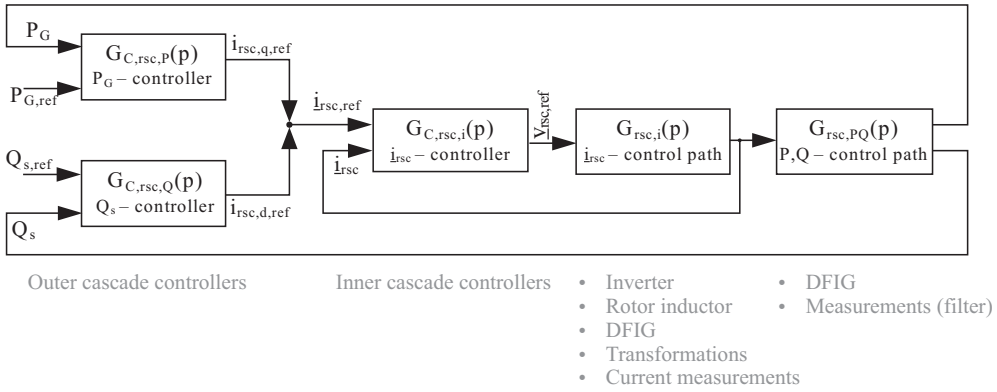

Figure 1.2: Rotor-side inverter control structure

The second part is the grid-side control, consisting of grid-side inverter current controllers and DC-link voltage control. Fig. 1.3 shows the structure of this part of the control system.

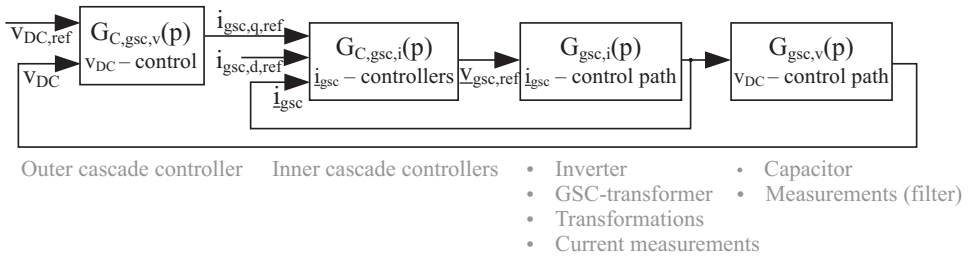

Figure 1.3: Grid-side inverter control structure

[3] Note: it is possible to control electrical torque and reactive stator current rather than active and reactive power.

[4] Within this study the output of the current controllers is denominated $v_{rsc,ref}$ and $v_{gsc,ref}$, although the subscript ref is usually used for reference values of a controller. $v_{rsc,ref}$ and $v_{gsc,ref}$ are not reference values for a controller, nor are they identical to the terminal voltages: they are the reference values for the calculation of control pulses (PWM or SVM) for the voltage source inverter (VSI). The terminal voltages will be delayed by the pulse period and in some cases limited by the DC-link voltage.

1.3 Demands and strains on a doubly-fed induction generator system affected by grid faults

The classification of different types of faults that can occur in electrical distribution networks can follow various criteria[5]:

- transverse faults (short circuits between two or three phases and/or earth faults) as opposed to longitudinal faults (e.g. disconnection of one or more phases),
- symmetrical or asymmetrical faults,
- faults with a certain origin[6],
- faults defined according to the distance between fault and generator,
- faults defined by their duration – short-term or long-term faults,
- faults which occur in isolation or which cause consecutive faults.

Within this study special attention is paid to asymmetrical faults with a duration of several 100 ms.

There are two main issues to consider in respect of a doubly-fed induction generator affected by grid faults. On the one hand, voltage dips or asymmetries will cause additional strains on the electrical and mechanical parts of the system. On the other hand, because of the increased number of wind turbines connected to the grid, the operators have, in recent years, raised the standards which wind turbines or wind farms connected to the grid have to meet.

Additional strains on DFIG-systems during grid faults The types of strain arising during grid faults depend on the type of fault. Any fault in the mains will mean that the three-phase voltages contain not only a positive-sequence component (x_p) but also a transient direct component (x_{DC}) and, during asymmetrical faults, also a negative-sequence component (x_n). Symmetrical – three-phase – faults cause less stresses for the system than asymmetrical ones. All types of fault cause the following types of stress.

- During fault start and fault clearance, current and torque peaks occur. The torque peaks may excite oscillations with eigenfrequency of the rotating part of the system.
- Stator and rotor power contain transient oscillating elements.

[5] Information about classification of faults and calculation of short circuit currents can be found at several points in the literature, among them [16, Chapter 15] and [42, Chapter 5].

[6] Causes for faults in the electrical grid may be overloads, insulation breakdown, generator tripping, interturn faults of generator windings, etc.

- Rotor currents and voltages contain not only slip frequency but also (transient) oscillations with electrical rotor frequency ($f_{DC} = p_p \cdot n$).
- The amplitudes of the induced rotor voltages and currents are higher than under normal conditions because of the higher frequency $f_{DC} = p_p \cdot n$.
- High active rotor currents cause the DC-link voltage to rise.
- Feeding of power to the grid by the grid-side inverter is reduced because the terminal voltages are reduced.
- To keep the DC-link voltage between prescriptive limits, the brake chopper will be activated. The power the brake chopper has to dissipate is a critical stress and determines the depth of voltage dip that can be supported. The mechanical power provided by the turbine is fed in part to the grid over the stator and some power can also be fed to the grid by the grid-side inverter. The rest has to be dissipated by the brake chopper. If this dissipation is not complete, the turbine speed will rise. In the simulations for the present study, no crowbar was applied.
- Transient torque oscillations with grid frequency are a further stress.

During asymmetrical faults additional strains arise:

- The asymmetrical stator currents cause unbalanced heating of the stator windings.
- The rotor currents and voltages contain oscillations with $f_n = (2-s) \cdot f_{grid}$ which do not decay (not a transient phenomenon).
- The amplitude of the induced rotor voltage components with $f_n = (2-s) \cdot f_{grid}$ and therefore of the corresponding rotor current components is higher than under normal conditions because of the higher frequency.
- The stator and rotor power contain continuous oscillating parts with an oscillation frequency of double the grid frequency.
- During asymmetrical faults the torque oscillates continuously at double the grid frequency.

A comprehensive analysis of the rotor voltages during grid faults can be found in [24] and in [25] and was also conducted within this study. The results are given in Section 4.4.1.

Grid code demands The connection of wind turbines to the electrical grid is regulated by the grid code of the respective transmission system operator. A variety of different grid codes exists, which contain varied requirements for different grid voltage levels and make allowance for the different grid characteristics (e.g. for a "weak" transmission system the connection requirements will be more demanding than for a strongly interconnected grid). An extensive analysis

and comparison of European and North American grid codes can be found in [20] and another comprehensive comparison of the wind farm connection requirements in Europe, USA, Canada and New Zealand is given in [44]. In Germany, the connection of wind power plants to the medium voltage and high voltage grid is regulated by law [2]. In general, the main elements of the grid codes are:

- Low voltage ride through – LVRT – or fault ride through – FRT – capability: the ability to stay connected during voltage dips[7] is defined by the voltage limiting curves, and it is prescribed that short circuit current and/or reactive power has to be fed to the grid during voltage dips.
- Disconnection and reconnection specifications define the ability of the plants to recognise islanded operation. They also define ramp rates of power restoration after fault clearance.
- Reactive power control and voltage support: the power factor has to remain within prescriptive limits, which vary with the current grid voltage and/or the active power fed to the grid.
- Active power control capabilities for participation in frequency control: some grid codes stipulate a reduction of active power output during over-frequency and/or an increase of active power output during under-frequency. The latter requirement implies that the plant must not feed the maximum possible power to the grid during nominal frequency operation, which will reduce the amount of energy generated and therefore also the operating efficiency.
- Operation range for voltage and frequency: the ability of the power plants to operate under conditions which deviate from the nominal voltage and frequency values is prescribed.

The example given in Fig. 1.4 shows the voltage limiting curve and the voltage support requirements of the German operator E.ON Netz GmbH for high voltage grids. For the voltage areas ①, ② and ③ indicated in Fig. 1.4 a), the following behaviour of the wind power plant is prescribed: ①: Symmetrical dips must not cause instability or a disconnection of the plant. ②: The plant should ride through the dip without disconnection. Very brief disconnection is allowed under certain conditions and only with agreement of the grid operator. ③: Brief disconnection of the plant is allowed. During voltage dips below 90% of the nominal voltage, the power plant has to support the grid voltage by feeding reactive power to the grid according to Fig. 1.4 b).

[7] Different terms (voltage dip, voltage sag, undervoltage) are used in the literature to describe and differentiate deviations from the nominal voltages (see also [20]). In this study the term "voltage dip" is used.

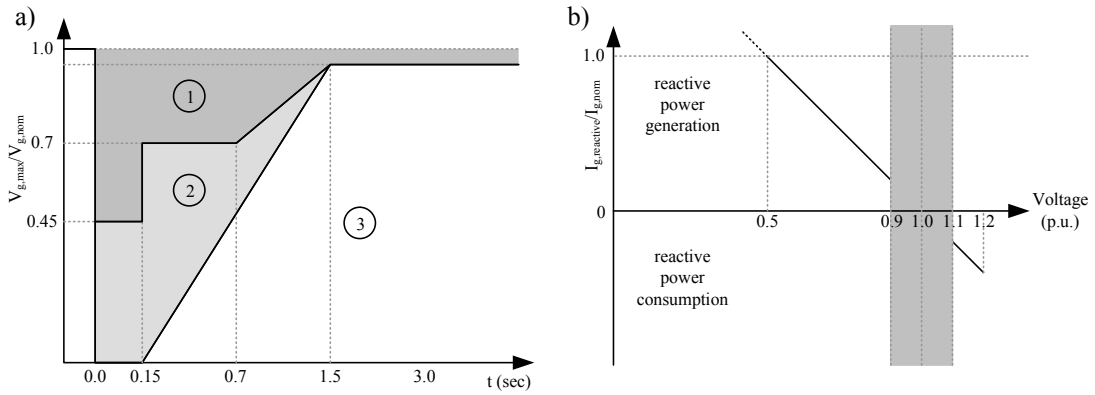

Figure 1.4: E.ON Grid Code (cf. [9]): a) voltage limiting curve, b) voltage support requirements

1.4 State of the art

1.4.1 Grid code compliance of wind power plants which use doubly-fed induction generators

Various possibilities are discussed in the literature and/or are employed in practice to protect the wind power plants from over-currents and over-voltages during grid faults and to fulfil the grid codes as described in [44, p. 324 et seqq.]. These are:

- Brake chopper – During voltage dips the DC-link voltage rises. To prevent damage to the DC-link capacitor and reduce its charge, a chopper resistance is used.
- Crowbar – During dip start and dip clearance high transient over-voltages and over-currents arise on the rotor terminals. A crowbar can be activated to short circuit the rotor terminals during severe voltage dips. While the crowbar is active, the generator acts like a squirrel-cage generator, consuming reactive power from the grid and this involves loss of generator controllability. Therefore, fast reconnection of the rotor-side converter is necessary as mentioned in [45] and described in [37].
- Converter oversizing – To avoid the necessity of a crowbar it is possible to oversize the converters allowing for high short-term over-currents in the rotor-side converter.
- DC-link oversizing – The DC-link capacitor can accumulate a part of the energy surplus provided by the turbine that cannot be fed to the grid during voltage dips because of the reduced terminal voltages. Oversizing the DC-link capacitor may therefore reduce the acceleration of the turbine and the time the brake chopper is active during dips.
- A stator switch may be employed to disconnect the stator for a short time during the initial transient of a voltage dip. Within this disconnection time the mutual inductance will be

demagnetised. The grid-side converter will stay connected and can feed reactive current to the grid.

- Stator current feedback – In [22] and in [23] changing the rotor current control during voltage dips is suggested: instead of using the output of the superior power controllers, the stator currents are set as reference values for the rotor currents. The strategy is evaluated in [45] and compared to the classical crowbar concept. As the author notes, its applicability is limited by the DC-link voltage to less severe voltage dips.
- Pitch-control – The DFIG-system is a variable-speed system. Rapid control of the pitch angle will enable less mechanical power to be obtained from the wind during grid faults so that the increase of DC-link voltage and turbine speed is limited and brake chopper action is kept short.
- STATCOM – It is possible to apply a STATCOM in parallel to the wind turbine or the wind farm to supply additional reactive power during grid faults. Different control strategies for the STATCOM are outlined and evaluated in [41]. The considerations are similar to those in Section 4.3.3. In the literature, this possibility is suggested for wind power plants using squirrel cage induction generators, as they consume reactive power during regular operation. Alternatively, in [44, p. 329] there is the suggestion of using switched capacitor banks to compensate the reactive power consumption of large wind farms.
- Active and reactive power control – As a matter of principle, DFIG systems will enable the control of active and reactive power and therefore will meet the requirements of grid codes regarding frequency and voltage support during normal operating conditions if these are taken into account in the control strategy design.

1.4.2 Current control strategies for doubly-fed induction generators

The most common way of controlling a doubly-fed induction generator is *field-oriented control (FOC)*, a scheme described widely in the literature, e.g. in [34] and in [36]. Chapter 3 gives the derivation of its function. FOC is the basis of comparison for the different control schemes proposed within this study. The inner cascade current controllers of the rotor-side control are designed as proportional-integral (PI) controllers in a coordinate system rotating synchronously to the linked stator flux. This allows independent control of electrical torque and flux. The grid-side inverter currents can be controlled in the same coordinate system or in one that is coupled to the grid voltage vector.

Some authors propose the addition of two current controllers for the negative-sequence currents to the field-oriented control scheme. This approach is described in [1] and in [39] and in this study is called *positive-negative-sequence control (PN-control or PNC)*. The additional current

controllers can be used to control the negative-sequence current components which arise during asymmetries in the grid, improving the behaviour of the system during such faults. This control scheme is described in detail in Chapter 4, is evaluated on the basis of simulation with Matlab/Simulink®and is compared to the field-oriented control scheme.

The third control strategy analysed in the present study (in Chapter 5) is *frequency-selective control (FSC)*. This control scheme is suggested in [12] for a three-phase converter and in [15] for the control of a hybrid filter. It is based on the inner model principle described in [27].

Besides these three control strategies, the four following schemes are also described in the literature.

A modification of field-oriented control, *PI-R control*, is proposed in [18]. It adds to the PI current controllers a frequency-selective component (named "resonant" controller, PI-R, by the authors), to control the negative-sequence components in the rotating (positive-sequence) field-oriented coordinate system.

[26] contains a proposal to control the rotor currents directly in the rotor coordinate system using frequency-selective controllers without an integrating element (PR-controller).This control scheme is called *VOC-RRF* in the article (Voltage Oriented Control in a Rotating Reference Frame). In this case, as the resonant frequency of the current controllers varies across a wide range because it is identical to the slip frequency ($\approx -0.3 \ldots 0.3 \cdot f_{grid}$), it has to be adapted continuously. During synchronous operation the PR-controller reduces to a PI-controller as the resonant frequency becomes 0. The superior active and reactive power control is realised by a feed-forward algorithm supplemented by auxiliary PI-controllers.

All five control strategies mentioned above are based on the assumption of a linear system and apply linear controllers. They are summarised and compared in Section 6.2. Some authors, however, propose nonlinear control schemes for the control of DFIG systems. Two possibilities are "passivity-based control" and "hysteresis current controllers".

Passivity-based control of the DFIG is suggested and analysed in [31]. An outline of the principle of this form of control can be found in [35] (amongst others). The control structure suggested contains several feed-forward algorithms and a variable proportional gain. The reference values are calculated on the basis of a nonlinear model of the generator and using the measured load torque, which may be a drawback for the implementation of this control scheme.

Another approach, *hysteresis control* of the converter currents, is suggested in [30]. In the control scheme there proposed, the active and reactive stator power are regulated by two rotor-side outer control loop PI-controllers. The inner loop current controllers are implemented as vector-based hysteresis controllers. An analogous strategy is used for the grid-side control of the back-to-back converter. Here, one outer loop controller is used to control the DC-link voltage and another to

control the grid-side inverter reactive power. Equidistant hysteresis bands are used to overcome one main problem of hysteresis control, the varying switching frequency.

2 Modelling and simulation of the electrical system of the doubly-fed induction generator

The four control schemes which are described in the following chapters (3 – 5) are tested by means of simulation using Matlab/Simulink®. The model developed for the simulations is described in this chapter. As it is important to recall the simplifications and assumptions on which the model is based when evaluating the results, these simplifications are described in Section 2.1. Section 2.2 gives the results of validation of the model. The simulation and measurements for the validation were carried out in a cooperative project which determined the detailed specifications and hardware used.

2.1 Matlab/Simulink®model: description and simplifications

The main elements of the system that have to be simulated are shown in Fig. 1.1. The mathematical models are described in detail in Appendix B. The assumptions and simplifications upon which they are based are as follows.

The *DFIG* is assumed to rotate with fixed speed; no model of the mechanical part of the system, namely the turbine, the gear box and the shaft, is employed. This simplification is used because the mechanical time constant of the power train is large in comparison with the time constants of the electrical system. The mechanical speed can, therefore, be assumed to be constant during short simulation periods. The DFIG is simulated in a static coordinate system using $\alpha\beta$-components. The linked stator and rotor fluxes are taken to be state variables. The mathematical model corresponds to the T-equivalent circuit shown in Fig. B.4 and is described in Appendix B.2.2. The resistance of the rotor and of the stator, also any leakage inductance, are all assumed to be constant, whereas saturation effects are taken into account for the mutual inductance (see Appendix B.2.3). The saturation is modelled using a look-up-table and the results are compared to measurement and simulation results of the aforementioned cooperation project. The resulting model is a time-invariant nonlinear model.

The *main transformer* connecting the DFIG to the grid is a ΔY-connected transformer. It is simulated using $\alpha\beta 0$-components and the equivalent circuits which are given in Appendix B.3 in Figs. B.9 and B.10. As no saturation effects are taken into account, the resulting model is a linear time-invariant (LTI) model.

The autotransformer used as *GSC-transformer* is modelled by a simple LTI model, one PT1-element for the α-component and one PT1-element for the β-component, both consisting of the leakage inductance and the ohmic resistance of the windings. The main inductance, core losses and possible asymmetries of the transformer are disregarded.

The mathematical model of the *DC-link* capacitor is given in Appendix B.4. As can be seen from Eq. B.83, the model is time-invariant and nonlinear.

A simple average model is used for the *grid-side and rotor-side inverters*. They are represented by ideal three-phase voltage sources. As no switches are simulated, the resulting model takes into account neither switching and conducting losses nor any phenomena related to switching operations. This simplification is used because the switching frequency (5 kHz for the rotor-side inverter and 10 kHz for the grid-side inverter) is high compared to the time constants of the electrical system and the controllers.

To connect the aforementioned elements in the model, additional coupling elements are essential. These are described in Appendix B.5.

For the control of a DFIG system it is necessary to detect the angle of the grid voltage. Usually, this is realised by a phase-locked-loop (PLL). For the simulations on which the present study is based, a frequency-locked-loop (FLL) is implemented in the models. It is described in detail in Appendix B.6 and in the literature (cf. [40]).

2.2 Validation of the model

From the cooperation project mentioned, simulation (with PSCAD®) and measurement data was available for steady state, step responses and transient behaviour of the system ([33]). For validation purposes, the model developed is supplemented by a detailed model of the control scheme employed in practice[1]. Furthermore, the model of the main transformer is replaced by a model of the particular dip-generation-unit that had been used for the measurements. There are three parts to the validation:

1. the comparison of several steady-state working points (steady-state validation) with
   - generator speeds from $n = 0.73 \cdot n_{s=0}$ to $n = 1.2 \cdot n_{s=0}$,
   - generator active power from $P_G = 0$ to $P_G = P_{G,nom}$ and
   - generator reactive power from $Q_G = 0$ to $Q_G = 0.33 \cdot [P_{nom}]$kVAr,
2. the comparison of the step responses of the current d-components, of the active power and of the DC-link voltage (dynamic validation) and

[1] This control model is not used in the following chapters (3 – 7).

3. the comparison of currents, voltages and power during voltage dips (dip validation).

By way of example, some of the dynamic validation results are given in Appendix E.2. The simulations show good conformity to measurement and simulation results from PSCAD®. Differences from the measurement results are mainly caused by the simplicity of the converter model: the measurement results contain switching frequency components that are, of course, absent from the simulation results. There are further noteworthy differences to be seen in the grid-side inverter currents; these are probably caused by the simplicity of the autotransformer model. Nevertheless, as the simulation results are satisfactory, it is feasible to use the model as developed for the evaluation of the control schemes described in the following chapters.

3 Field-oriented control of doubly-fed induction generators

It is usually by field-oriented control (FOC) that DFIGs in wind turbines are controlled. The method is described widely in the literature, including [34], [36] and [39], and its aim is to control the active and reactive power of the generator independently. This is equivalent to controlling magnetising current and torque independently and will be possible if the rotor currents are transferred from the ("natural") rotor-oriented to a flux- or field-oriented coordinate system. The term "field-oriented control" commonly is used only for the rotor-side control of the DFIG. In this chapter it is also used for the grid-side control as both control parts – rotor-side and grid-side converter control – are implemented in the same coordinate system.

3.1 Field-oriented control – rotor-side control

The structure of the rotor-side field-oriented control of a DFIG is given in Fig. 3.1. To enable the current and power controllers to be designed, it is necessary to analyse the control paths for current and power.

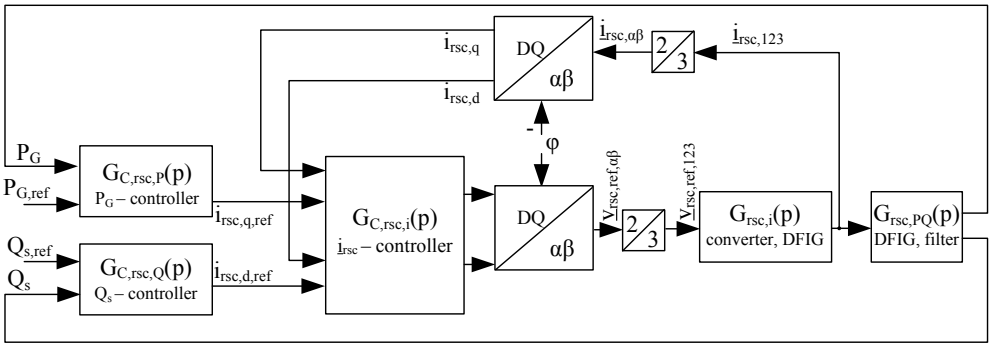

Figure 3.1: Rotor-side control structure

3.1.1 Flux model

The creation of a flux-oriented control scheme requires calculation of the linked stator flux vector using an observer structure. There are examples of different flux models in [10] and in [34]. For

the simulations on which this study is based, a simple flux model has been used. The ohmic resistance of the stator in Eq. B.30 is neglected and the linked stator flux is calculated from

$$\vec{\Psi}_s^s = \int_0^t \vec{v}_s^s \, d\theta \tag{3.1}$$

Then, the angle of the linked stator flux in stator-oriented coordinate system φ_μ^s can be calculated approximately from the stator voltages:

$$\varphi_\mu^s = \angle \left\{ \int_0^t \left(\vec{v}_s^s - R_s \cdot \vec{i}_s^s \right) d\theta \right\} \approx \angle \{\vec{v}_s^s\} - 90^\circ = \varphi_{grid} - 90^\circ \tag{3.2}$$

$$\varphi_\mu^r \approx \varphi_{grid} - 90^\circ - \gamma \tag{3.3}$$

These angles are used in the next section to convert the stator- and rotor quantities to the stator-flux-oriented coordinate system (Fig. 3.2).

3.1.2 Rotor current controllers

The rotor current controllers are inner cascade controllers. The rotor voltages act as actuating variables and the rotor currents as control variables. To design the current controllers, it is necessary to analyse the transfer function of the control path $G_{rsc,i}(p) = i_{rsc}(p)/v_{rsc,ref}(p)$. This transfer function can be deduced from the DFIG-equations given in Appendix B.2.2. The deduction – using space vector representation of currents and voltages – is given in this section and can also be found in [34, p. 15 et seqq.] and in [39, p. 51 et seqq.].[1]

Three different coordinate systems (CS) – the rotor-, stator- and the stator-flux-oriented coordinate systems – are necessary to describe the DFIG. A visualisation of these coordinate systems is given in Fig. 3.2 and how they correlate is summarised in Table 3.1.

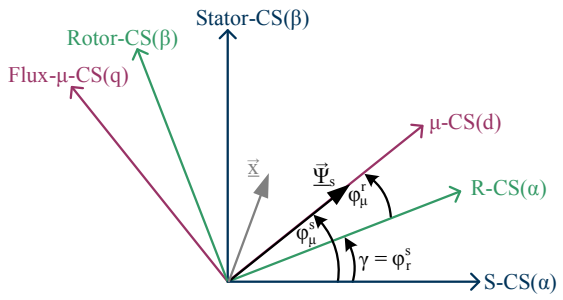

Figure 3.2: Coordinate systems for DFIG-description

$$\vec{x}^m = \vec{x}^n \cdot e^{j\varphi_n^m} \tag{3.4}$$

Table 3.1: Transformation between CSs

	S-CS	R-CS	μ-CS
S-CS	0	$\varphi_s^r = -\gamma$	φ_s^μ
R-CS	$\varphi_r^s = \gamma$	0	φ_r^μ
μ-CS	φ_μ^s	φ_μ^r	0

[1] In the design of the rotor current controller, all (stator) quantities of the DFIG used are quantities related to the rotor. The superscript $x^{(r)}$ indicates this relation. The subscript *rsc* is used for the rotor currents and voltages in the following equations.

The voltage equations B.30 and B.31 are now transferred to the stator-oriented coordinate system:

$$\vec{v}_s^{s,(r)} = R_s^{(r)} \cdot \vec{i}_s^{s,(r)} + \dot{\vec{\Psi}}_s^{s,(r)} \tag{3.5}$$

$$\vec{v}_{rsc}^{s} = R_r \cdot \vec{i}_{rsc}^{s} + \frac{d}{dt}\left(\vec{\Psi}_r^s \cdot e^{-j\gamma}\right) = R_r \cdot \vec{i}_{rsc}^{s} + \dot{\vec{\Psi}}_r^s - j \cdot \dot{\gamma} \cdot \vec{\Psi}_r^s \tag{3.6}$$

$\dot{\gamma}$ is the rotational speed of the generator, γ the angle between stator and rotor axis and thus the angle between stator-oriented and rotor-oriented coordinate system.

The linked stator- and rotor fluxes can be described by Eqs. 3.7 and 3.8:

$$\vec{\Psi}_s^{s,(r)} = L_s^{(r)} \cdot \vec{i}_s^{s,(r)} + L_m^{(r)} \cdot \vec{i}_{rsc}^{s} \tag{3.7}$$

$$\vec{\Psi}_r^{s} = L_r \cdot \vec{i}_{rsc}^{s} + L_m^{(r)} \cdot \vec{i}_s^{s,(r)} \tag{3.8}$$

with $L_s^{(r)} = L_{s\sigma}^{(r)} + L_m^{(r)}$ and $L_r = L_{r\sigma} + L_m^{(r)}$.

The purpose of the rearrangement is to establish the rotor currents in the stator-flux-oriented coordinate system as a function of the rotor voltages. For this, the stator current $\vec{i}_s^{s,(r)}$ must be eliminated.

$$\vec{i}_s^{s,(r)} = \frac{\vec{\Psi}_s^{s,(r)}}{L_s^{(r)}} - \frac{L_m^{(r)}}{L_s^{(r)}} \cdot \vec{i}_{rsc}^{s} \tag{3.9}$$

Substituting Eq. 3.9 into the Eqs. 3.8 and 3.5 yields:

$$\vec{\Psi}_r^{s} = L_\sigma \cdot \vec{i}_{rsc}^{s} + \frac{L_m^{(r)}}{L_s^{(r)}} \cdot \vec{\Psi}_s^{s,(r)} \tag{3.10}$$

$$\vec{v}_s^{s,(r)} = \frac{R_s^{(r)}}{L_s^{(r)}} \cdot \vec{\Psi}_s^{s,(r)} - R_s^{(r)} \cdot \frac{L_m^{(r)}}{L_s^{(r)}} \cdot \vec{i}_{rsc}^{s} + \dot{\vec{\Psi}}_s^{s,(r)} \tag{3.11}$$

with the equivalent leakage inductance $L_\sigma = L_r - {L_m^{(r)}}^2 / L_s^{(r)}$. Then, if one inserts Eq. 3.10 into Eq. 3.6, the rotor voltage $\vec{v}_{rsc}^{s}$ will be obtained:

$$\vec{v}_{rsc}^{s} = R_r \cdot \vec{i}_{rsc}^{s} + L_\sigma \cdot \dot{\vec{i}}_{rsc}^{s} - j \cdot \dot{\gamma} \cdot L_\sigma \cdot \vec{i}_{rsc}^{s} + \frac{L_m^{(r)}}{L_s^{(r)}} \cdot \dot{\vec{\Psi}}_s^{s,(r)} - j \cdot \dot{\gamma} \cdot \frac{L_m^{(r)}}{L_s^{(r)}} \cdot \vec{\Psi}_s^{s,(r)} \tag{3.12}$$

Because the linked stator flux needs to be eliminated, an equivalent magnetising current is introduced:

$$\vec{i}_\mu^{s} = \frac{1}{L_m^{(r)}} \cdot \vec{\Psi}_s^{s,(r)} \tag{3.13}$$

The derivative of this magnetising current can be calculated from Eq. 3.11:

$$\dot{\vec{i}}_{\mu}^{s} = \frac{1}{L_m^{(r)}} \cdot \vec{v}_s^{s,(r)} + \frac{R_s^{(r)}}{L_s^{(r)}} \cdot \vec{i}_{rsc}^{s} - \frac{R_s^{(r)}}{L_s^{(r)}} \cdot \vec{i}_{\mu}^{s} \tag{3.14}$$

If one inserts Eq. 3.13 and Eq. 3.14 into the voltage equation 3.12, the rotor voltage will be obtained independently of any flux:

$$\vec{v}_{rsc}^{s} = \frac{L_m^{(r)}}{L_s^{(r)}} \cdot \vec{v}_s^{s,(r)} + \bar{R} \cdot \vec{i}_{rsc}^{s} - j \cdot \dot{\gamma} \cdot L_\sigma \cdot \vec{i}_{rsc}^{s} - \frac{{L_m^{(r)}}^2}{L_s^{(r)}} \cdot \left(j \cdot \dot{\gamma} + \frac{R_s^{(r)}}{L_s^{(r)}} \right) \cdot \vec{i}_{\mu}^{s} + L_\sigma \cdot \dot{\vec{i}}_{rsc}^{s} \tag{3.15}$$

with $\bar{R} = R_r + R_s^{(r)} \cdot \left(\frac{L_m^{(r)}}{L_s^{(r)}} \right)^2$.
The currents and voltages of Eqs. 3.14 and 3.15 are alternating quantities. To get the direct quantities which it is possible to control using proportional-integral controllers, the two equations are transferred to the stator-flux-oriented coordinate system:

$$\dot{\vec{i}}_{\mu}^{\mu} = \frac{1}{L_m^{(r)}} \cdot \vec{v}_s^{\mu,(r)} + \frac{R_s^{(r)}}{L_s^{(r)}} \cdot \vec{i}_{rsc}^{\mu} - \frac{R_s^{(r)}}{L_s^{(r)}} \cdot \vec{i}_{\mu}^{\mu} - j \cdot \dot{\varphi}_{\mu}^{s} \cdot \vec{i}_{\mu}^{\mu} \tag{3.16}$$

$$\vec{v}_{rsc}^{\mu} = \frac{L_m^{(r)}}{L_s^{(r)}} \cdot \vec{v}_s^{\mu,(r)} + \bar{R} \cdot \vec{i}_{rsc}^{\mu} - j \cdot \dot{\gamma} \cdot L_\sigma \cdot \vec{i}_{rsc}^{\mu} - \frac{{L_m^{(r)}}^2}{L_s^{(r)}} \cdot \left(j \cdot \dot{\gamma} + \frac{R_s^{(r)}}{L_s^{(r)}} \right) \cdot \vec{i}_{\mu}^{\mu} + L_\sigma \cdot \dot{\vec{i}}_{rsc}^{\mu} + j \cdot \dot{\varphi}_{\mu}^{s} \cdot L_\sigma \cdot \vec{i}_{rsc}^{\mu} \tag{3.17}$$

φ_{μ}^{s} is the angle of the linked stator flux in the stator-oriented coordinate system, and thus the angle between stator-oriented and stator-flux-oriented coordinate system. In the stationary state, $\dot{\varphi}_{\mu}^{s}$ is identical to the angular frequency of the grid voltages.

From Eq. 3.17 one obtains $\dot{\vec{i}}_{rsc}^{\mu}$:

$$\dot{\vec{i}}_{rsc}^{\mu} = \frac{1}{L_\sigma} \cdot \left[\vec{v}_{rsc}^{\mu} - \frac{L_m^{(r)}}{L_s^{(r)}} \cdot \vec{v}_s^{\mu,(r)} - \bar{R} \cdot \vec{i}_{rsc}^{\mu} + j \cdot \dot{\gamma} \cdot L_\sigma \cdot \vec{i}_{rsc}^{\mu} + \cdots \right.$$
$$\left. \cdots \frac{{L_m^{(r)}}^2}{L_s^{(r)}} \cdot \left(j \cdot \dot{\gamma} + \frac{R_s^{(r)}}{L_s^{(r)}} \right) \cdot \vec{i}_{\mu}^{\mu} - j \cdot \dot{\varphi}_{\mu}^{s} \cdot L_\sigma \cdot \vec{i}_{rsc}^{\mu} \right] \tag{3.18}$$

Dividing Eq. 3.16 and Eq. 3.18 into d-components and q-components results in:

$$\dot{i}_{\mu,d}^{\mu} = \frac{1}{L_m^{(r)}} \cdot v_{s,d}^{\mu,(r)} + \frac{R_s^{(r)}}{L_s^{(r)}} \cdot i_{rsc,d}^{\mu} - \frac{R_s^{(r)}}{L_s^{(r)}} \cdot i_{\mu,d}^{\mu} \tag{3.19}$$

$$i_{\mu,q}^{\mu} = 0 \tag{3.20}$$

and:

$$\dot{i}^{\mu}_{rsc,d} = \frac{1}{L_\sigma} \cdot \left[v^{\mu}_{rsc,d} - \frac{L_m^{(r)}}{L_s^{(r)}} \cdot v^{\mu,(r)}_{s,d} - \bar{R} \cdot i^{\mu}_{rsc,d} - \left(\dot{\gamma} - \dot{\varphi}^{s}_{\mu}\right) \cdot L_\sigma \cdot i^{\mu}_{rsc,q} + \left(\frac{L_m^{(r)}}{L_s^{(r)}}\right)^2 \cdot R_s^{(r)} \cdot i^{\mu}_{\mu,d} \right] \tag{3.21}$$

$$\dot{i}^{\mu}_{rsc,q} = \frac{1}{L_\sigma} \cdot \left[v^{\mu}_{rsc,q} - \frac{L_m^{(r)}}{L_s^{(r)}} \cdot v^{\mu,(r)}_{s,q} - \bar{R} \cdot i^{\mu}_{rsc,q} + \left(\dot{\gamma} - \dot{\varphi}^{s}_{\mu}\right) \cdot L_\sigma \cdot i^{\mu}_{rsc,d} + \frac{{L_m^{(r)}}^2}{L_s^{(r)}} \cdot \dot{\gamma} \cdot i^{\mu}_{\mu,d} \right] \tag{3.22}$$

The transfer functions $G_{rsc,i,dq}(p) = i_{rsc,dq}(p) / v_{rsc,dq}(p)$ are obtained by applying the Laplace transformation to Eqs. 3.21 and 3.22 and setting all input variables except $v_{rsc,dq}$ to zero[2].

$$G_{rsc,i,dq}(p) = \frac{i_{rsc,dq}(p)}{v_{rsc,dq}(p)} = \frac{1}{\bar{R} + p \cdot L_\sigma} \tag{3.23}$$

The rotor voltages in Laplace domain are:

$$v_{rsc,d}(p) = (\bar{R} + p \cdot L_\sigma) \cdot i_{rsc,d}(p) + \left(\dot{\gamma} - \dot{\varphi}^{s}_{\mu}\right) \cdot L_\sigma \cdot i_{rsc,q}(p) + \frac{L_m}{L_s} \cdot v_{s,d}(p) - \frac{L_m^2}{L_s^2} \cdot R_s \cdot i_{\mu,d}(p) \tag{3.24}$$

$$v_{rsc,q}(p) = (\bar{R} + p \cdot L_\sigma) \cdot i_{rsc,q}(p) - \left(\dot{\gamma} - \dot{\varphi}^{s}_{\mu}\right) \cdot L_\sigma \cdot i_{rsc,d}(p) + \frac{L_m}{L_s} \cdot v_{s,q}(p) - \frac{L_m^2}{L_s} \cdot \dot{\gamma} \cdot i_{\mu,d}(p) \tag{3.25}$$

For present purposes the following simplifications have been made:

- $\frac{L_m^2}{L_s^2} \cdot R_s \cdot i_{\mu,d}(p)$ is small compared to the other components and is neglected,
- $\dot{\varphi}^{s}_{\mu} = \omega_{grid}$ during steady-state conditions,
- $v_{s,d}(p) \approx 0$ neglecting the voltage drop over R_s,
- $v_{s,q}(p) \approx w_G \cdot v_{l,nom}$ neglecting the voltage drop over R_s,
- $(\bar{R} + p \cdot L_\sigma) \cdot i_{rsc}(p)$ is replaced by the output of the controller $y_{C,rsc,i}(p)$, where
- $y_{C,rsc,i}(p) = G_{C,rsc,i}(p) \cdot (i_{rsc,ref}(p) - i_{rsc}(p))$.

Using these simplifications the following dependencies have to be taken into account by the controller:

$$v_{rsc,d}(p) = y_{C,rsc,i,d}(p) + \left(\dot{\gamma} - \omega_{grid}\right) \cdot L_\sigma \cdot i_{rsc,q}(p) \tag{3.26}$$

$$v_{rsc,q}(p) = y_{C,rsc,i,q}(p) - \left(\dot{\gamma} - \omega_{grid}\right) \cdot L_\sigma \cdot i_{rsc,d}(p) + \frac{L_m}{L_s} \cdot w_G \cdot v_{l,nom} - \frac{L_m^2}{L_s} \cdot \dot{\gamma} \cdot i_{\mu,d}(p) \tag{3.27}$$

[2]From now on in this chapter, the superscripts indicating the coordinate system and the rotor relation are omitted.

D-component and q-component are coupled by the term $\left(\dot{\gamma} - \omega_{grid}\right) \cdot L_\sigma \cdot i_{rsc,dq}(p)$. To control the two components independently, a decoupling algorithm is necessary. Furthermore, it is possible to compensate the two remaining summands $L_m \cdot w_G \cdot v_{l,nom}/L_s - L_m^2 \cdot \dot{\gamma} \cdot i_{\mu,d}(p)/L_s$ of Eq. 3.27 by a feed-forward algorithm. These two summands can be reduced to $L_m \cdot w_G \cdot s \cdot v_{l,nom}/L_s$ in the steady state ($s = 1 - \dot{\gamma}/\omega_{grid}$ =slip, $\omega_{grid} \cdot L_m \cdot i_{\mu,d} = w_G \cdot v_{l,nom}$).

The control structure shown in Fig. 3.3 considers all the simplifying and decoupling techniques mentioned so far in this section.

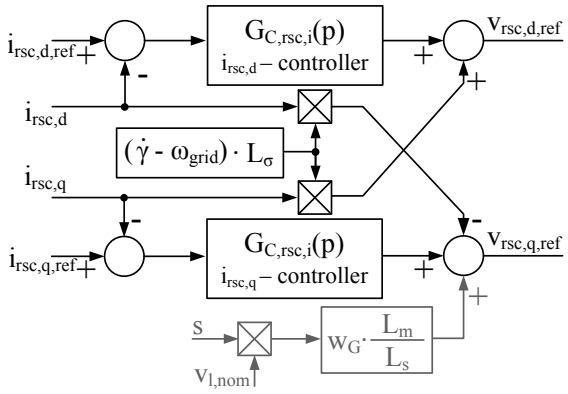

Figure 3.3: Rotor current control structure with decoupling and optional feed-forward

To define the parameters of the current controllers, all parts of the control path have to be considered. These parts are:

$$\frac{i_{rsc}(p)}{v_{rsc}(p)} = \frac{1}{\bar{R} + p \cdot L_\sigma} \qquad \text{DFIG + rotor inductor,} \tag{3.28}$$

$$\frac{v_{rsc}(p)}{v_{rsc,ref}(p)} = \frac{1}{1 + p \cdot T_{rsc,p}} \qquad \text{inverter (approximated) and} \tag{3.29}$$

$$\frac{i_{rsc,dq}(p)}{i_{rsc,123}(p)} \cdot \frac{v_{rsc,ref,123}(p)}{v_{rsc,ref,dq}(p)} = k_{nm} = 1 \qquad \text{modal transformations.} \tag{3.30}$$

The proportional gain of one modal transformation depends on which pair of components is considered (n = d or q, m = 1,2,3). The respective value can be gathered from the transformation matrix of Eq. A.25. The transformation is cancelled out by the back transformation, thus the coefficient k_{nm} is always one.

The complete transfer function of the control path is:

$$G_{rsc,i}(p) = \frac{i_{rsc}(p)}{v_{rsc,ref}(p)} = \frac{1}{\bar{R} + p \cdot L_\sigma} \cdot \frac{1}{1 + p \cdot T_{rsc,p}} \tag{3.31}$$

The controller used is the proportional-integral type and the parameters are defined using the amplitude optimum method described in [29, p. 440 et seqq.]. The controller is designed to

compensate the major time constant $T_\sigma = L_\sigma/\bar{R}$. The time constant of $v_{rsc}(p)/v_{rsc,ref}(p)$ is about ten times smaller than the time constant of $i_{rsc}(p)/v_{rsc}(p)$. The control parameters are, therefore:

$$G_{C,rsc,i}(p) = K_{IR} \cdot \left(1 + \frac{1}{p \cdot T_{IR}}\right) \tag{3.32}$$

$$T_{IR} = T_\sigma = \frac{L_\sigma}{\bar{R}} \tag{3.33}$$

$$K_{IR} = \frac{\bar{R} \cdot T_\sigma}{2 \cdot T_{rsc,p}} \tag{3.34}$$

The values of the control parameters are given in Table D.2.

If these definitions have been applied, the open loop transfer function of the inner control loop will reduce to:

$$\begin{aligned} G_{0,rsc,i}(p) &= G_{C,rsc,i}(p) \cdot \frac{1}{\bar{R} + p \cdot L_\sigma} \cdot \frac{1}{1 + p \cdot T_{rsc,p}} \\ &= \frac{1}{2 \cdot p \cdot T_{rsc,p} \cdot (1 + p \cdot T_{rsc,p})} \end{aligned} \tag{3.35}$$

3.1.3 Power controllers

The elements which constitute the control path of the superior power controllers are:

- the closed current control loop $\frac{G_{0,rsc,i}(p)}{1+G_{0,rsc,i}(p)}$,
- the correlation between machine power and rotor current $\frac{P_G(p)}{i_{rsc,q}(p)}$ and $\frac{Q_s(p)}{i_{rsc,d}(p)}$ and
- filtering of the calculated generator power $\frac{1}{1+p \cdot T_{f,PQ}}$.

The transfer function $P_G(p)/i_{rsc,q}(p)$ can be deduced from Eq. B.16[3]. If the machine rotational speed is assumed to be constant, the active power fed to or generated by the DFIG will be proportional to the electrical torque. The linked stator flux during such steady-state conditions can be written as $L_m \cdot \vec{i}_\mu$ and the stator current $\vec{i}_s$ can be replaced by $\left(\vec{\Psi}_s - L_m \cdot \vec{i}_{rsc}\right)/L_s$. It follows that the active power generated is proportional to the rotor current $i^\mu_{rsc,q}$:

$$\frac{P_G(p)}{i_{rsc,q}(p)} = -\frac{3}{2} \cdot p_p \cdot n \cdot \frac{L_m^2}{L_s} \cdot i_{\mu,d} \tag{3.36}$$

The transfer function $Q_s(p)/i_{rsc,d}(p)$ can be deduced from:

$$Q_s = \frac{3}{2} \cdot \mathrm{Im}\left\{\vec{v}_s \cdot \vec{i}_s^*\right\} \tag{3.37}$$

[3]The deduction is also to be found in detail in [39, p. 5 and p. 53].

$\vec{v}_s$ can be replaced by:

$$\vec{v}_s = 0 + j \cdot v_{l,nom} = j \cdot \omega_{grid} \cdot L_m \cdot i_{\mu,d} \tag{3.38}$$

and $\vec{i}_s^*$ is replaced by:

$$\vec{i}_s^* = \frac{1}{L_s} \cdot \left(\vec{\Psi}_s^* - L_m \cdot \vec{i}_{rsc}^* \right) = \frac{L_m}{L_s} \cdot \left(i_{\mu,d} - i_{rsc,d} + j \cdot i_{rsc,q} \right) \tag{3.39}$$

Inserting Eqs. 3.38 and 3.39 into Eq. 3.37 yields:

$$\frac{Q_s(p)}{i_{rsc,d}(p)} = -\frac{3}{2} \cdot \omega_{grid} \cdot \frac{L_m^2}{L_s} \cdot i_{\mu,d} \tag{3.40}$$

This means that, during steady-state conditions, the stator reactive power is proportional to the rotor current $i_{rsc,d}^{\mu}$. As is clear from Eqs. 3.36 and 3.40 the two outer cascade control loops are not coupled[4]. Therefore, no decoupling algorithm is necessary. The structure of the control loops is depicted in Fig. 3.4. Here, too, the type of controller used to control the machine

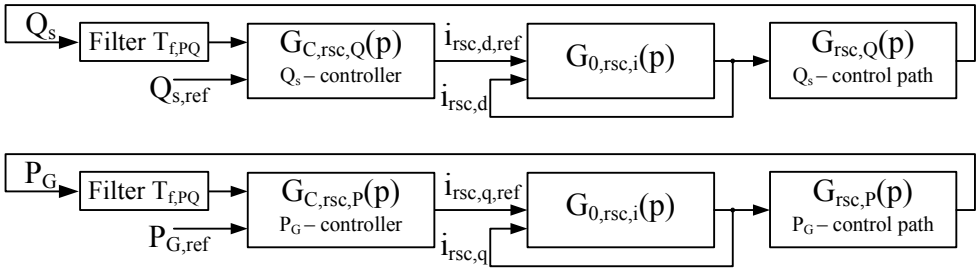

Figure 3.4: Power control loops

active power and the stator reactive power is proportional-integral. The structure of the control path, especially the filtering of the power values, makes it impossible to apply a standard rating procedure, such as amplitude or symmetrical optimum. Instead, the control parameters $K_{P,Q}$ and $T_{P,Q}$ of the control transfer function

$$G_{C,rsc,PQ}(p) = K_{P,Q} \cdot \left(1 + \frac{1}{p \cdot T_{P,Q}} \right) \tag{3.41}$$

were set by trial-and-error in the simulations on which this study is based. The values thus selected are given in Table D.2.

[4] If the inner control loops are assumed to be decoupled efficiently by the decoupling algorithms detailed in 3.1.2.

3.2 Field-oriented control – grid-side control

Like the rotor-side control, the grid-side control scheme contains a cascaded structure comprising two current controllers and a superior controller for the DC-link voltage. The grid-side current controllers work in the same coordinate system as the rotor current controllers, which precedes the line voltage with a phase shift of 90°. The DC-link voltage controller produces the reference value for the q-component of the converter current. The reference value of the d-component of the current is set to zero. This means that no reactive power is fed to the grid by the grid-side converter. The control structure is shown in Fig. 3.5.

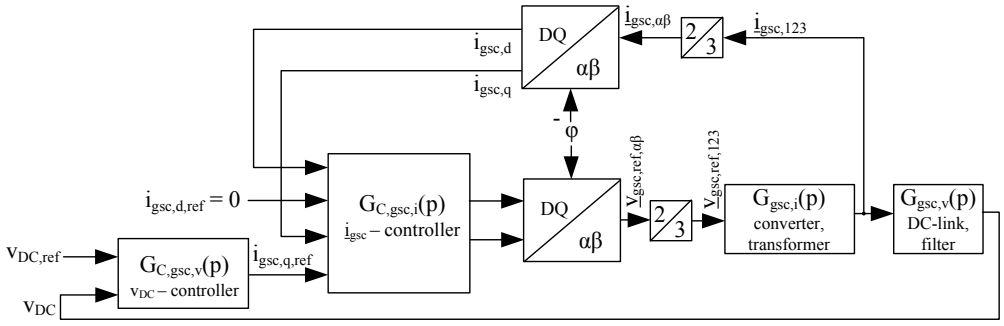

Figure 3.5: Grid-side control structure

3.2.1 Grid-side converter current controllers

The control path of the inner control loop $G_{gsc,i}(p)$ contains the converter, the GSC-transformer and the modal transformations between dq-components and three-phase quantities. If one considers only the winding losses and the leakage inductances, the transformer can be described by Eqs. 3.42 – 3.45 where the space vector is used in the stationary coordinate system. The equivalent circuit is shown in Fig. 3.6.

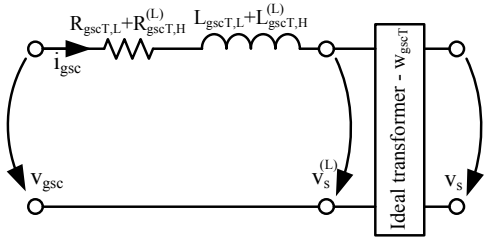

Figure 3.6: Simplified equivalent circuit of the GSC-Transformer

$$\vec{v}^{s}_{gsc} = \vec{v}^{s,(L)}_{s} + R_{gscT} \cdot \vec{i}^{s}_{L} + L_{gscT\sigma} \cdot \dot{\vec{i}}^{s}_{gsc} \tag{3.42}$$

$$R_{gscT} = R_{gscT,L} + R^{(L)}_{gscT,H} \tag{3.43}$$

$$L_{gscT\sigma} = L_{gscT,L} + L^{(L)}_{gscT,H} \tag{3.44}$$

$$\vec{v}^{s,(L)}_{s} = w_{gscT} \cdot \vec{v}^{s}_{s} \tag{3.45}$$

$$R^{(L)}_{gscT,H} = w^{2}_{gscT} \cdot R_{gscT,H} \tag{3.46}$$

$$L^{(L)}_{gscT,H} = w^{2}_{gscT} \cdot L_{gscT,H} \tag{3.47}$$

Eq. 3.42 can be transferred from the stationary coordinate system to stator-flux-oriented coordinate system. This yields:

$$\begin{aligned}\vec{v}_{gsc}^{\mu} &= \vec{v}_{s}^{\mu,(L)} + R_{gscT} \cdot \vec{i}_{gsc}^{\mu} + L_{gscT\sigma} \cdot j \cdot \dot{\varphi}_{\mu}^{s} \cdot \vec{i}_{gsc}^{\mu} + L_{gscT\sigma} \cdot \dot{\vec{i}}_{gsc}^{\mu} \\ &= \vec{v}_{s}^{\mu,(L)} + R_{gscT} \cdot \vec{i}_{gsc}^{\mu} + L_{gscT\sigma} \cdot j \cdot \omega_{grid} \cdot \vec{i}_{gsc}^{\mu} + L_{gscT\sigma} \cdot \dot{\vec{i}}_{gsc}^{\mu}\end{aligned} \tag{3.48}$$

Splitting Eq. 3.48 into d- and q-component reveals the coupling between the components:

$$v_{gsc,d}^{\mu} = v_{s,d}^{\mu,(L)} + R_{gscT} \cdot i_{gsc,d}^{\mu} - L_{gscT\sigma} \cdot \omega_{grid} \cdot i_{gsc,q}^{\mu} + L_{gscT} \cdot \dot{i}_{gsc,d}^{\mu} \tag{3.49}$$

$$v_{gsc,q}^{\mu} = v_{s,q}^{\mu,(L)} + R_{gscT} \cdot i_{gsc,q}^{\mu} + L_{gscT\sigma} \cdot \omega_{grid} \cdot i_{gsc,d}^{\mu} + L_{gscT} \cdot \dot{i}_{gsc,q}^{\mu} \tag{3.50}$$

In the field-oriented coordinate system used here, the following simplifications are possible:

$$v_{s,d}^{\mu,(L)} = 0 \tag{3.51}$$

$$v_{s,q}^{\mu,(L)} = w_{gscT} \cdot v_{l,nom} \tag{3.52}$$

The coupling between the two current components can be compensated by a decoupling algorithm and the summand $v_{s,q}^{\mu,(L)} = w_{gscT} \cdot v_{l,nom}$ can be compensated by a feed-forward algorithm. Fig. 3.7 shows the resulting control structure.

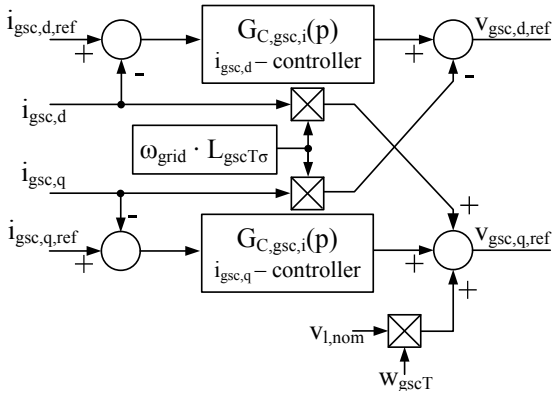

Figure 3.7: Current control structure of the GSC-control

The transfer function $i_{gsc}(p)/v_{gsc}(p)$ is obtained by applying Laplace transformation to Eqs. 3.49 and 3.50 and setting all input variables except v_{gsc} to zero.[5]

$$\frac{i_{gsc}(p)}{v_{gsc}(p)} = \frac{1}{R_{gscT} + p \cdot L_{gscT\sigma}} \qquad \text{represents the GSC-Transformer.} \tag{3.53}$$

$$\frac{v_{gsc}(p)}{v_{gsc,ref}(p)} = \frac{1}{1 + p \cdot T_{gsc,p}} \qquad \text{approximates the grid-side inverter.} \tag{3.54}$$

[5] In the following, the superscript of the variables μ, symbolising the stator-flux-oriented coordinate system that is used, is omitted for the sake of clarity.

$$\frac{i_{gsc,dq}(p)}{i_{gsc,123}(p)} \cdot \frac{v_{gsc,ref,123}(p)}{v_{gsc,ref,dq}(p)} = k_{nm} = 1 \text{ represents the modal transformations.} \tag{3.55}$$

$$G_{gsc,i}(p) = \frac{i_{gsc}(p)}{v_{gsc}(p)} \cdot \frac{v_{gsc}(p)}{v_{gsc,ref}(p)} \tag{3.56}$$

Like the rotor current controllers, the controllers for the grid-side inverter currents are designed using the amplitude optimum method[6] described in [29, p. 440 et seqq.]. The time constant of the GSC-Transformer $T_{gscT} = L_{gscT\sigma}/R_{gscT}$ is about 500 times bigger than the pulse period of the converter. This major time constant is compensated by the controller:

$$G_{C,gsc,i}(p) = K_{IG} \cdot \left(1 + \frac{1}{p \cdot T_{IG}}\right) \tag{3.57}$$

$$T_{IG} = \frac{L_{gscT\sigma}}{R_{gscT}} \tag{3.58}$$

$$K_{IG} = \frac{R_{gscT} \cdot T_{IG}}{2 \cdot T_{gsc,p}} \tag{3.59}$$

Table D.2 gives the values of the control parameters. With these definitions the open loop transfer function of the inner control loop reduces to:

$$\begin{aligned} G_{0,gsc,i}(p) &= G_{C,gsc,i}(p) \cdot \frac{1}{R_{gscT} + p \cdot L_{gscT\sigma}} \cdot \frac{1}{1 + p \cdot T_{gsc,p}} \\ &= \frac{1}{2 \cdot p \cdot T_{gsc,p} \cdot (1 + p \cdot T_{gsc,p})} \end{aligned} \tag{3.60}$$

3.2.2 DC-link voltage controller

As the reference value of the DC-link voltage is constant under normal operating conditions, high-speed reference action is not necessary. The power fed to or supplied from the rotor-side converter to the DC-link will act as disturbance input and will vary. The DC-link voltage controller is, therefore, designed using the symmetrical optimum method described in [29, p. 452 et seqq.]. The symmetrical optimum method is preferable if the intention is to minimise the disturbance reaction in the control loop. The DC-link voltage depends on the grid-side inverter

[6] The amplitude optimum method is to be favoured if good reference action of the control loop is desired in combination with absence of disturbance variables.

current as described by Eq. 3.62.

$$i_{gsc,DC,q} = \frac{P_{gsc}}{v_{DC}} = \frac{3}{2} \cdot \frac{w_{gscT} \cdot v_{l,nom}}{v_{DC}} \cdot i_{gsc,q} \tag{3.61}$$

$$\begin{aligned} v_{DC} &= \frac{1}{C_{DC}} \cdot \int_0^t \left(i_{gsc,DC,q} + i_{rsc,DC,q}\right) d\theta \\ &= \frac{1}{C_{DC}} \cdot \int_0^t \left(\frac{3}{2} \cdot \frac{w_{gscT} \cdot v_{l,nom}}{v_{DC}} \cdot i_{gsc,q} + i_{rsc,DC,q}\right) d\theta \end{aligned} \tag{3.62}$$

To get the transfer function $v_{DC}(p)/i_{gsc,q}(p)$, one must linearise Eq. 3.62 ($v_{DC} \approx v_{DC,nom}$) and subject it to Laplace transformation. The control loop of the DC-link voltage control now contains the controller and the following elements:

- DC-link capacitor

$$\frac{v_{DC}(p)}{i_{gsc,q}(p)} = \frac{1}{p \cdot C_{DC}} \cdot \frac{3 \cdot w_{gscT} \cdot v_{l,nom}}{2 \cdot v_{DC,nom}} \tag{3.63}$$

- filtering of v_{DC}

$$\frac{v_{DC,f}(p)}{v_{DC}(p)} = \frac{1}{1 + p \cdot T_{f,v}} \tag{3.64}$$

- closed inner control loop

$$\begin{aligned} \frac{i_{gsc,q}(p)}{i_{gsc,q,ref}(p)} &= \frac{1}{1 + 2 \cdot p \cdot T_{gsc,p} \cdot (1 + p \cdot T_{gsc,p})} \\ &\approx \frac{1}{1 + 2 \cdot p \cdot T_{gsc,p}} \qquad \text{(simplified)} \end{aligned} \tag{3.65}$$

The structure of the control loop is shown in Fig. 3.8[7].

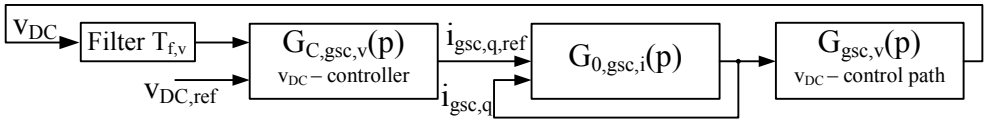

Figure 3.8: DC-link voltage control loop

[7] For the dimensioning of the control parameters the filter is seen as a part of the control path. The result is that not the DC-link voltage itself, but its filtered value will behave optimal; as is intended in the symmetrical optimum method.

The two low-pass elements of the control path can be summarised in one low-pass element (approximately). This yields the following transfer function for the open loop:

$$G_{0,gsc,v}(p) = G_{C,gsc,v}(p) \cdot \frac{1}{1 + p \cdot (2 \cdot T_{gsc,p} + T_{f,v})} \cdot \frac{3 \cdot w_{gscT} \cdot v_{l,nom}}{p \cdot C_{DC} \cdot 2 \cdot v_{DC,nom}} \tag{3.66}$$

The parameters of the controller are calculated according to [29, p. 452 et seqq.]:

$$G_{C,gsc,v}(p) = K_{VDC} \cdot \left(1 + \frac{1}{p \cdot T_{VDC}}\right) \tag{3.67}$$

$$T_{VDC} = a^2 \cdot (2 \cdot T_{gsc,p} + T_{f,v}) \qquad \text{with } a > 1 \tag{3.68}$$

$$K_{VDC} = \frac{C_{DC} \cdot 2 \cdot v_{DC,nom}}{a \cdot (2 \cdot T_{gsc,p} + T_{f,v}) \cdot 3 \cdot w_{gscT} \cdot v_{l,nom}} \tag{3.69}$$

The values of the control parameters for $a = 2$ are given in Table D.2.

3.3 Field-oriented control – simulation results

Simulation results of the field-oriented control scheme described in this chapter are given in Fig. 3.9 with the following specifications.

- Use of related quantities (scale bases are given in Table E.1),
- $n = 1.08 \cdot n_{s=0}$,
- $t = 1\,\text{s} \ldots 2\,\text{s}$ – 2-phase dip on the grid-side (HV) of the main transformer to 95% remaining voltage,
- $t = 3\,\text{s}$ – step from $v_{DC,ref} = v_{DC,nom}$ to $v_{DC,ref} = 1.025 \cdot v_{DC,nom}$,
- $t = 4\,\text{s}$ – step from $P_{G,ref} = P_{G,nom}$ to $P_{G,ref} = 0.75 \cdot P_{G,nom}$,
- $t = 5\,\text{s}$ – step from $Q_{G,ref} = 0\,\text{kVAr}$ to $Q_{G,ref} = 0.0625 \cdot [P_{G,nom}]\text{kVAr}$.

In the following two chapters, these simulation results will be the base of comparison for PN-control and frequency-selective control.

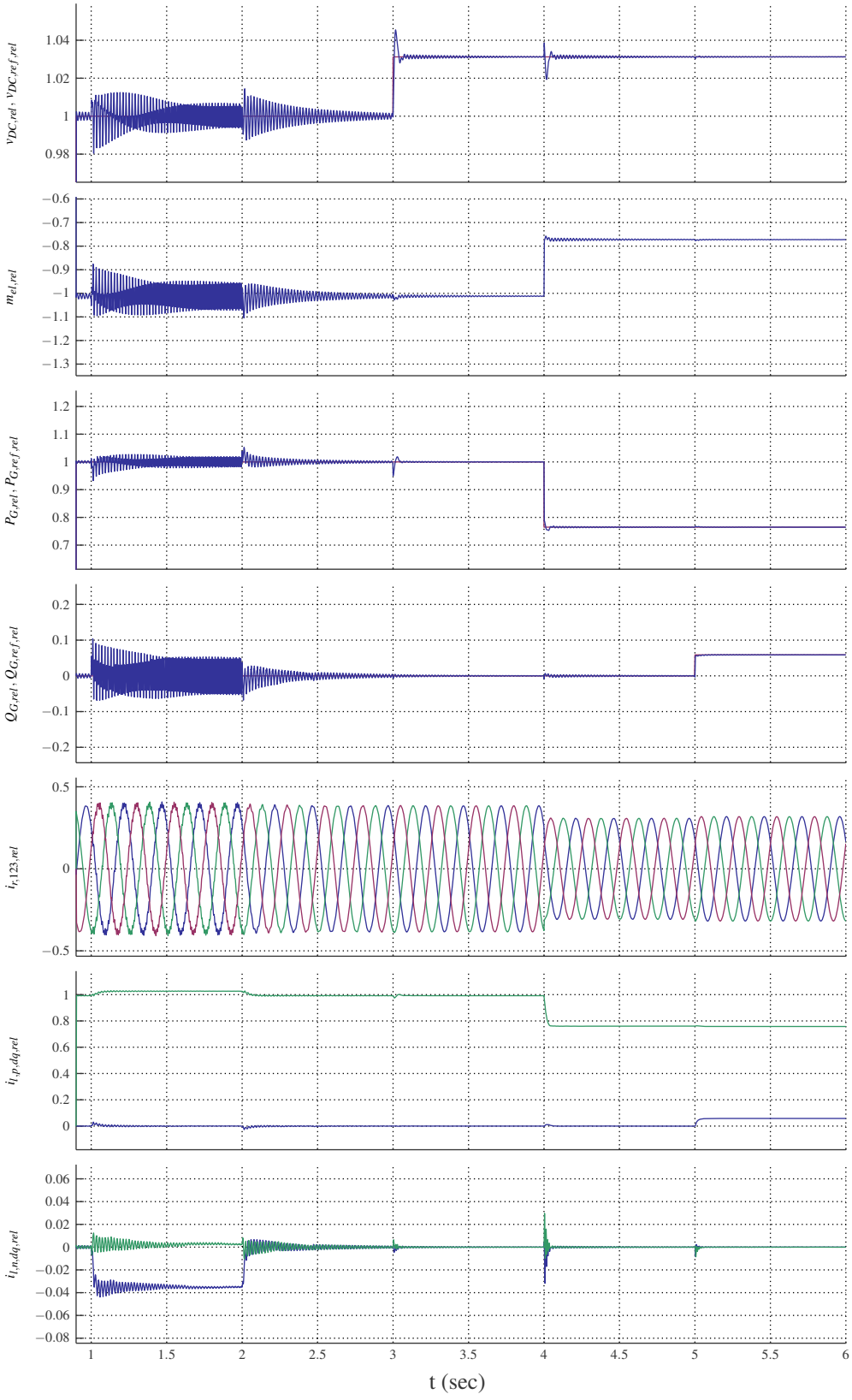

Figure 3.9: Field-oriented control results

4 Positive-negative-sequence control of doubly-fed induction generators

The field-oriented control described in Chapter 3 is based on the assumption that the grid voltages (and all other electrical quantities) are balanced. If asymmetries exist, the negative-sequence current components will neither be controlled separately nor filtered from the measurement values. In the field-oriented coordinate system used for the description, the negative-sequence current components appear as alternating components oscillating at twice the grid frequency and are superimposed on the positive-sequence direct quantities. The bandwidth of the PI-controllers does not cover the double grid frequency, therefore, these controllers are unable to control these current components (cf. [44, p. 327]).

To reduce the influence of the negative-sequence components on the system (this influence is described in Section 1.3), one possibility is to control the negative-sequence current components separately. For this, the term used from now on in this thesis is positive-negative-sequence control (PN-control or PNC). Descriptions of such a control scheme can be found in [1] for the control of a DFIG and in [43] for the control of a PWM converter. The PN-control scheme is based on the field-oriented control but contains the following additional elements:

- calculation of positive-sequence and negative-sequence components,
- two current controllers for negative-sequence grid-side inverter current components,
- two current controllers for negative-sequence rotor-side inverter current components and
- calculation of the reference values for the additional current controllers.

These control elements are described in the rest of this chapter.

4.1 Identification of symmetrical components

4.1.1 Symmetrical component theory and flux model

The principle of symmetrical component theory is summarised in Appendix A.3. For the PN-control scheme, only the first two components, the p-component and the n-component, are used,

the zero-sequence is disregarded. With $\underline{a} = e^{-j\cdot 2\pi/3}$, the transformation equations reduce to:

$$\begin{pmatrix} \underline{x}_p \\ \underline{x}_n \end{pmatrix} = \frac{1}{3} \cdot \begin{pmatrix} 1 & \underline{a} & \underline{a}^2 \\ 1 & \underline{a}^2 & \underline{a} \end{pmatrix} \cdot \begin{pmatrix} \underline{x}_1 \\ \underline{x}_2 \\ \underline{x}_3 \end{pmatrix} \tag{4.1}$$

$$\begin{pmatrix} \underline{x}_1 \\ \underline{x}_2 \\ \underline{x}_3 \end{pmatrix} = \begin{pmatrix} 1 & 1 \\ \underline{a}^2 & \underline{a} \\ \underline{a} & \underline{a}^2 \end{pmatrix} \cdot \begin{pmatrix} \underline{x}_p \\ \underline{x}_n \end{pmatrix} \tag{4.2}$$

The positive-sequence component corresponds to a space vector which is rotating with grid frequency in the stator-oriented coordinate system. The negative-sequence component can be represented by a space vector rotating in the opposite direction.

The PN-control scheme contains two control parts, working in different coordinate systems: in the positive-sequence (p-) and in the negative-sequence (n-) coordinate system. The positive-sequence coordinate system is (almost) identical to the stator-flux-oriented coordinate system described in Section 3.1.1. The negative-sequence coordinate system rotates in the opposite direction and is coupled to the negative-sequence linked stator flux. To define the two coordinate systems, it is necessary to calculate positive-sequence and negative-sequence components of the linked stator flux using an observer structure. Two options for this calculation are considered in this study:

1. applying the simple flux model of Section 3.1.1 to the modal components of the stator voltage:

$$\varphi^s_{\mu,p} \approx \angle\left\{\vec{v}^s_{s,p}\right\} - 90^\circ = \varphi_{grid,p} - 90^\circ \tag{4.3}$$

$$\varphi^s_{\mu,n} \approx \angle\left\{\vec{v}^s_{s,n}\right\} - 90^\circ = \varphi_{grid,n} - 90^\circ \tag{4.4}$$

2. assuming the angle of the negative-sequence voltages to be the opposite of the angle of the positive-sequence voltages:

$$\varphi^s_{\mu,p} \approx \quad \angle\left\{\vec{v}^s_{s,p}\right\} - 90^\circ \tag{4.5}$$

$$\varphi^s_{\mu,n} \approx -\angle\left\{\vec{v}^s_{s,p}\right\} - 90^\circ \tag{4.6}$$

The mathematical difference between the results of the two ways of calculating the negative-sequence flux angle will be a constant during steady state. Simulations and theoretical deductions[1] show that the control results (the currents in static coordinate system, active and reactive power

[1] For example, the calculation of reference values for the negative-sequence rotor current components is transferred from one coordinate system to another coordinate system in Appendix C.1. The calculation shows that the reference value calculation result is independent of the selected coordinate system.

and the DC-link voltage) do not differ during steady state. Some slight differences can be seen during transients. Fig. 4.1 shows the different coordinate systems. Table 4.1 summarises the transformation angles based on the calculation of positive-sequence and negative-sequence voltage angle (Eqs. 4.3 – 4.4).

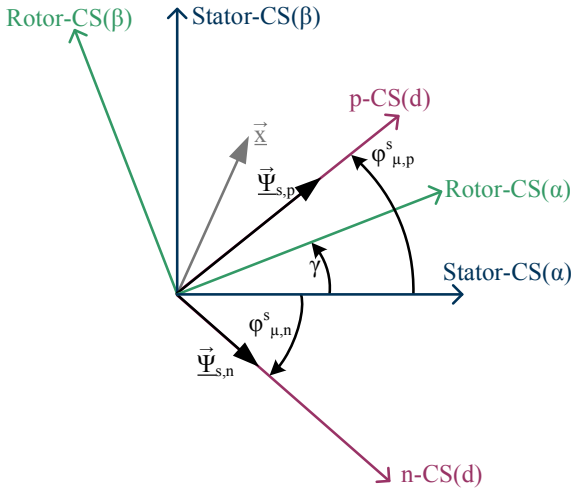

Figure 4.1: Coordinate systems for PN-control

Table 4.1: Transformation between CSs: $\vec{x}^m = \vec{x}^n \cdot e^{j\varphi_n^m}$

	S-CS: φ^s	R-CS: φ^r	p-CS: $\varphi^{\mu,p}$	n-CS: $\varphi^{\mu,n}$
φ_s	$= 0$	$= -\gamma$	$\approx -\varphi_{grid,p} + 90°$	$\approx -\varphi_{grid,n} + 90°$
φ_r	$= \gamma$	$= 0$	$\approx -\varphi_{grid,p} + 90° + \gamma$	$\approx -\varphi_{grid,n} + 90° + \gamma$
$\varphi_{\mu,p}$	$\approx \varphi_{grid,p} - 90°$	$\approx \varphi_{grid,p} - 90° - \gamma$	$= 0$	$\approx -\varphi_{grid,p} + \varphi_{grid,n}$
$\varphi_{\mu,n}$	$\approx \varphi_{grid,n} - 90°$	$\approx \varphi_{grid,n} - 90° - \gamma$	$\approx \varphi_{grid,p} - \varphi_{grid,n}$	$= 0$

4.1.2 Vector rotation and low-pass element filtering

The simplest way to compute the positive-sequence and negative-sequence components of an asymmetrical three-phase signal is described by the following steps.

1. The three-phase quantities to be analysed are represented by a space vector (Appendix A.4).
2. The space vector is transferred to two different coordinate systems (one rotating with grid frequency and one contra-rotating, p-CS and n-CS).
3. A low-pass filter is applied to the space vector in n-CS to eliminate the emerging double-grid frequency oscillations on the negative-sequence signals.
4. The positive-sequence components are not filtered to avoid introducing an additional delay to the positive-sequence control loop.

This approach corresponds to the following equations.

$$\vec{x}_p = \frac{2}{3} \cdot \left(x_1 + \underline{a} \cdot x_2 + \underline{a}^2 \cdot x_3\right) \cdot e^{-j \cdot \gamma_p} \qquad \text{or} \qquad \frac{\vec{x}_{p,dq}}{\vec{x}_{\alpha\beta}} = e^{-j \cdot \gamma_p} \tag{4.7}$$

$$\vec{x}_n = \frac{2}{3} \cdot \left(x_1 + \underline{a} \cdot x_2 + \underline{a}^2 \cdot x_3\right) \cdot e^{-j \cdot \gamma_n} \cdot \frac{1}{1 + p \cdot T_f} \qquad \text{or} \qquad \frac{\vec{x}_{n,dq}}{\vec{x}_{\alpha\beta}} = e^{-j \cdot \gamma_n} \cdot \frac{1}{1 + p \cdot T_f} \tag{4.8}$$

Fig. 4.2 shows the Simulink®structure of and the bode plot for the filter transfer function. Filter results for the test signal shown in Fig. 4.11 a) are to be found in Appendix E in Fig. E.5 for different filter time constants.

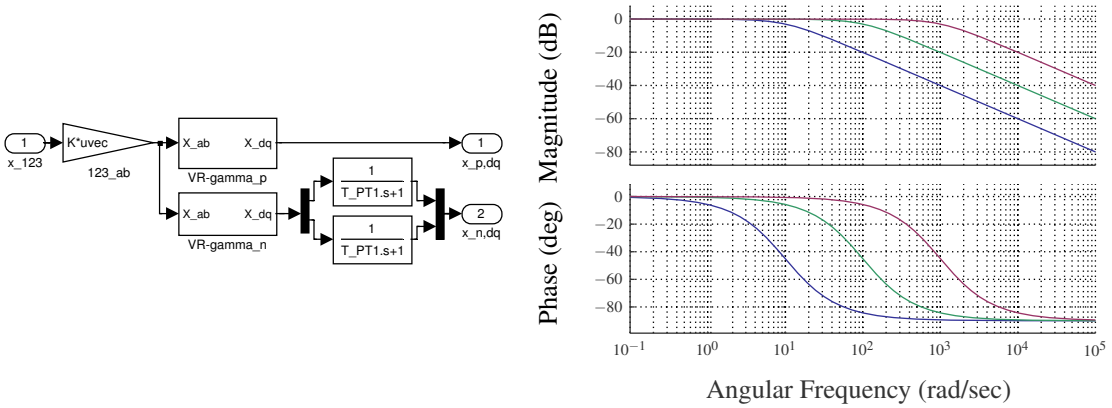

Figure 4.2: Component calculation with low-pass filter – filter structure and bode plot of the negative-sequence transfer function with $T_f = 100\,\text{ms}$, $10\,\text{ms}$ and $1\,\text{ms}$

4.1.3 Vector rotation and low-pass element filtering with signal feedback

To reduce the oscillations on the positive-sequence components, the filter structure of Section 4.1.2 is modified as shown in Fig. 4.3. The positive-sequence and negative-sequence components can be obtained using the algorithm described by the following steps.

1. Again, space vector representation is used to describe the quantities to be analysed.
2. The space vector is transferred to two different coordinate systems (p-CS and n-CS).
3. In these coordinate systems, the space vector is filtered using low-pass elements to eliminate the superposed oscillations.
4. The filtered space vectors are rotated back to the original (static) coordinate system.
5. In this coordinate system the the positive-sequence vector is subtracted from the original one to get the negative-sequence components and the negative-sequence vector is subtracted from the original vector to get the positive-sequence components.
6. The positive-sequence components are used directly without filtering, while the filtered negative-sequence components are used.

This filter procedure results in the following transfer functions for the positive-sequence and negative-sequence vectors:

$$\frac{\vec{x}_{p,dq}}{\vec{x}_{\alpha\beta}} = e^{-j\cdot\gamma_p} \cdot \frac{1+p\cdot T_f}{2+p\cdot T_f} \tag{4.9}$$

$$\frac{\vec{x}_{n,dq}}{\vec{x}_{\alpha\beta}} = e^{-j\cdot\gamma_n} \cdot \frac{1}{2+p\cdot T_f} \tag{4.10}$$

Fig. 4.4 shows the bode plots for the transfer functions for positive-sequence and negative-sequence components. Simulation results obtained with this filter algorithm are to be found in Appendix E in Fig. E.6 for the test signal of Fig. 4.11 a) for different filter time constants.

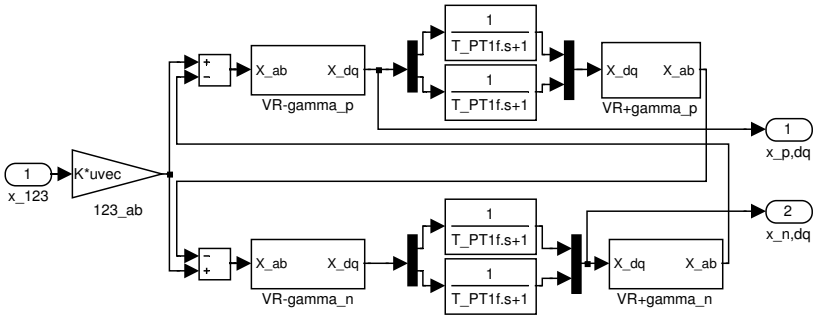

Figure 4.3: Component calculation with low-pass filter and signal feedback

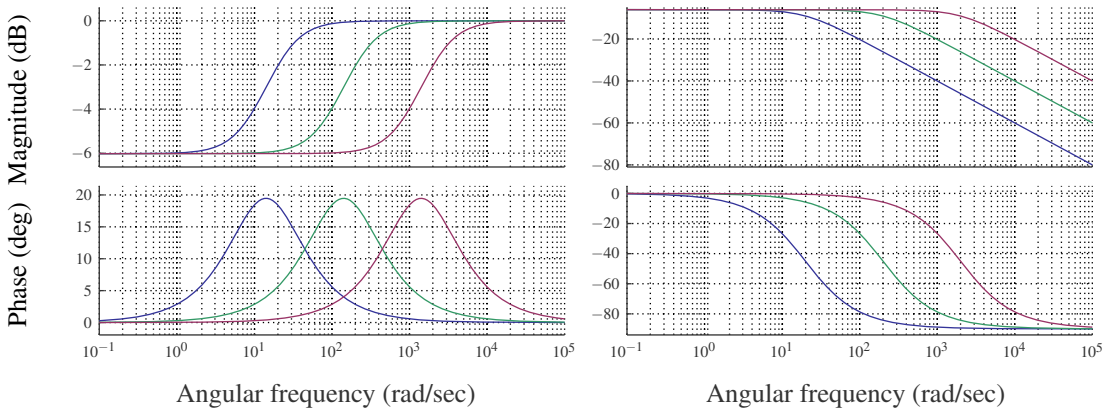

Figure 4.4: Bode plots of low-pass filter with signal feedback, with $T_f = 100\,\text{ms}$, $10\,\text{ms}$ and $1\,\text{ms}$ – left: positive-sequence components, right: negative-sequence components

4.1.4 Vector rotation and moving average elements

Similar to the structure with low-pass elements without signal feedback, moving average elements (MAV) can be used to separate the positive-sequence and negative-sequence components. This results in the approach described by the following steps.

1. Space vector representation is used.
2. The space vector is transferred to two different coordinate systems (p-CS and n-CS).

3. Moving average elements are applied on the space vector components in n-CS to eliminate the emerging double-grid frequency oscillations on the signals.
4. The positive-sequence components are not filtered, in order not to introduce an additional delay to the positive-sequence control loop.

This corresponds to the following equations:

$$\frac{\vec{x}_{p,dq}}{\vec{x}_{\alpha\beta}} = e^{-j\cdot\gamma_p} \tag{4.11}$$

$$\frac{\vec{x}_{n,dq}}{\vec{x}_{\alpha\beta}} = e^{-j\cdot\gamma_n} \cdot \frac{1}{p\cdot T_{MAV}} \cdot \left(1 - e^{p\cdot T_{MAV}}\right) \tag{4.12}$$

Fig. 4.5 shows the Simulink®structure of and the bode plot for the negative-sequence filter transfer function. The filter result for the test signal of Fig. 4.11 a) is given in Fig. 4.11 c).

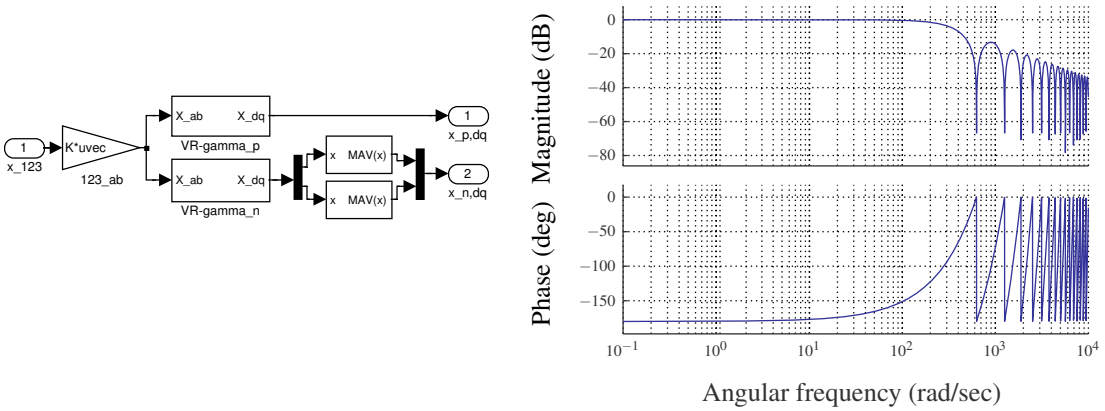

Figure 4.5: Component calculation with moving average elements – filter structure and bode plot of the negative-sequence transfer function with $T_{MAV} = 10\,\text{ms}$

4.1.5 Vector rotation and moving average elements with signal feedback

To reduce the oscillations on the positive-sequence components also without direct filtering, it is possible to subtract the MAV-filtered negative-sequence component before rotating the vector. The filter structure and the bode plot of the positive-sequence transfer function are depicted in Fig. 4.6. The bode plot for the negative-sequence component is identical to that in Fig. 4.5. The filter structure is shown by the following equations:

$$\frac{\vec{x}_{p,dq}}{\vec{x}_{\alpha\beta}} = e^{-j\cdot\gamma_p} \cdot \left(1 - \frac{1}{p\cdot T_{MAV}} \cdot \left(1 - e^{p\cdot T_{MAV}}\right)\right) \tag{4.13}$$

$$\frac{\vec{x}_{n,dq}}{\vec{x}_{\alpha\beta}} = e^{-j\cdot\gamma_n} \cdot \frac{1}{p\cdot T_{MAV}} \cdot \left(1 - e^{p\cdot T_{MAV}}\right) \tag{4.14}$$

The filter result for the test signal of Fig. 4.11 a) is to be found in Fig. 4.11 g).

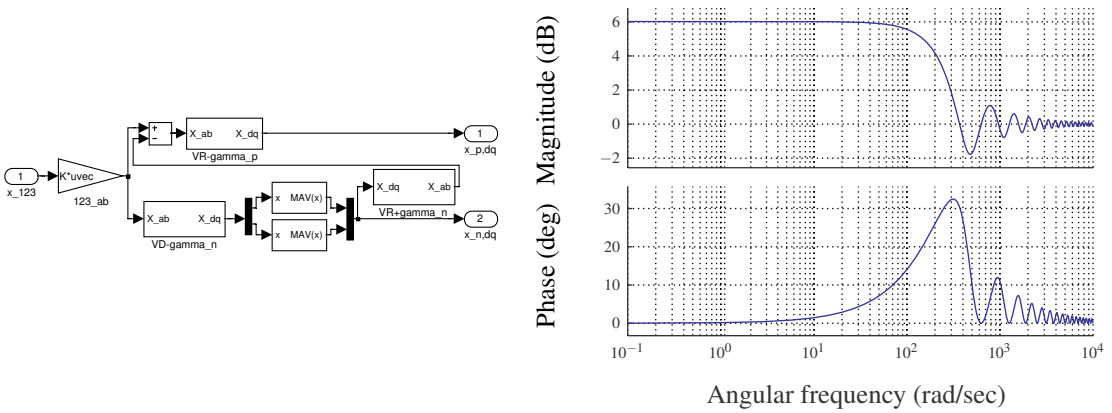

Figure 4.6: Component calculation with moving average elements – filter structure and bode plot of the positive-sequence transfer function with $T_{MAV} = 10\,\text{ms}$

4.1.6 Vector rotation and band rejection filter (notch-filter)

Instead of using low-pass filters or moving average elements, it is possible to eliminate the oscillations at double the grid frequency using a band rejection filter (a so called "notch-filter", cf. [43]). This algorithm comprises the following steps of calculation.

1. As with the aforementioned algorithms, space vector representation is applied.
2. The space vector is transferred to two different coordinate systems (p-CS and n-CS).
3. Notch filters are applied to the space vector components in the n-CS to eliminate the oscillations on the signals.
4. The positive-sequence components are not filtered.

This corresponds to the following equations (with $\omega_0 = 2 \cdot \omega_{grid}$):

$$\frac{\vec{x}_{p,dq}}{\vec{x}_{\alpha\beta}} = e^{-j\cdot\gamma_p} \tag{4.15}$$

$$\frac{\vec{x}_{n,dq}}{\vec{x}_{\alpha\beta}} = e^{-j\cdot\gamma_n} \cdot \frac{p^2+\omega_0^2}{p^2+Q_f\cdot\omega_0\cdot p+\omega_0^2} \tag{4.16}$$

Fig. 4.7 shows the Simulink®structure of and the bode plot for the negative-sequence filter transfer function. Fig. E.7 shows the filter result for the signal of Fig. 4.11 a) and different filter bandwidth values Q_f.

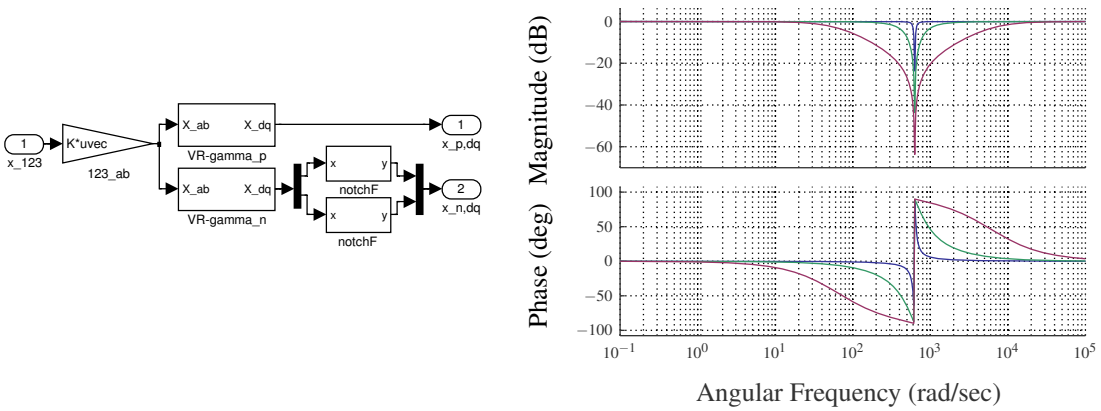

Figure 4.7: Component calculation with notch filter – filter structure and bode plot of the negative-sequence transfer function with $Q_f = 0.1$, 1 and 10

4.1.7 Fortescue transformation based on complex phasor representation

The filter procedures described above are all based on space vector representation and rotation of the space vector to different coordinate systems. Alternatively, the phasor representation (Appendix A.2) and Fortescue transformation (Appendix A.3) can be used to identify positive and negative-sequence components.

1. The phasors of the three-phase quantities are generated using a time delay of $T_{delay} = T_0/4$ ($T_0 =$ periodic time of the alternating quantities).
2. Positive-sequence and negative-sequence components are calculated from the three phasors according to Eq. A.8 given in Appendix A.3.
3. The positive-sequence and negative-sequence components are transferred to two rotating coordinate systems (p-CS and n-CS).

As phasor representation and Fortescue transformation are defined for steady-state conditions, the results during transients may not be useful. The applied equations are:

$$\underline{x}_1 = x_1(t) + j \cdot x_1\left(t - \frac{T_0}{4}\right) \tag{4.17}$$

$$\underline{x}_2 = x_2(t) + j \cdot x_2\left(t - \frac{T_0}{4}\right) \tag{4.18}$$

$$\underline{x}_3 = x_3(t) + j \cdot x_3\left(t - \frac{T_0}{4}\right) \tag{4.19}$$

$$\begin{pmatrix} \underline{x}_p \\ \underline{x}_n \end{pmatrix} = \frac{1}{3} \cdot \begin{pmatrix} 1 & \underline{a} & \underline{a}^2 \\ 1 & \underline{a}^2 & \underline{a} \end{pmatrix} \cdot \begin{pmatrix} \underline{x}_1 \\ \underline{x}_2 \\ \underline{x}_3 \end{pmatrix} \tag{4.20}$$

The structure of the Simulink®model is shown in Fig. 4.8. The filter result for the test signal of Fig. 4.11 a) is to be found in Fig. 4.11 e).

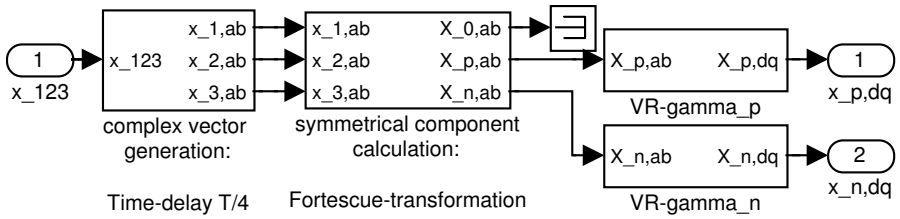

Figure 4.8: Component calculation with Fortescue transformation

4.1.8 Band-pass filter (DSOGI-QSG)

If the sequence of vector rotation and filtering of the approach described in Section 4.1.6 is changed, the following algorithm will be obtained.

1. Space vector representation is used to describe the quantities to be analysed.
2. α- and β-component of the space vector are filted by a band-pass filter – the results are the "direct components", subscript d, Eq. 4.21.
3. The band-pass filters also create signals with a 90°-phase shift – the "quadrature components", subscript q, Eq. 4.22.
4. From these four components the α- and the β-components of the positive-sequence and negative-sequence components are calculated by Eqs. 4.23 and 4.24.
5. The two resulting space vectors (p- and n-vector) are transferred to rotating coordinate systems (p-CS and n-CS) to get direct quantities (Eqs. 4.25 and 4.26).

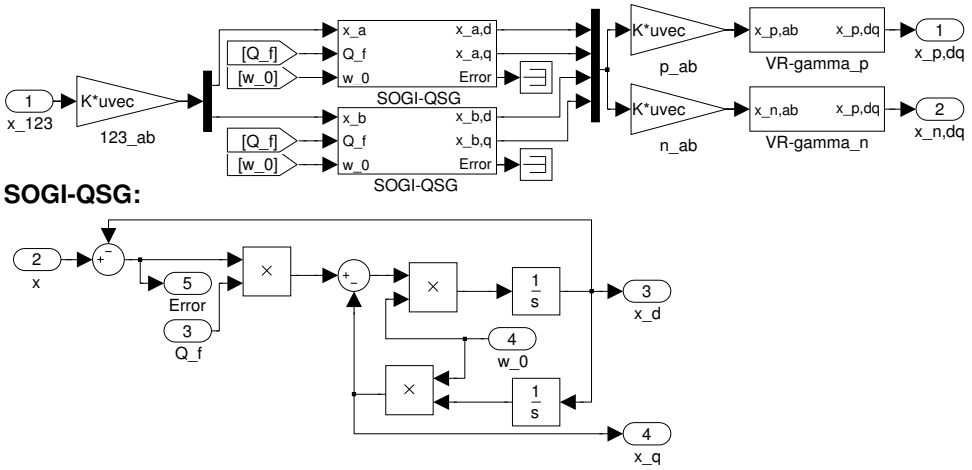

Figure 4.9: Component calculation with band-pass filter (DSOGI-QSG)

Filtering and the generation of the quadrature component are realised by one structure, the so-called "DSOGI-QSG" (Dual Second Order Generalised Integrator – Quadrature Signal Generation). The deduction and explanation of this procedure is given in [40], where it is used in combination with an FLL-algorithm (so called "DSOGI-FLL") to identify the positive-sequence and negative-sequence grid angle of the grid voltages. The filter procedure corresponds to the following equations:

$$\frac{x_{\alpha,d}}{x_\alpha} = \frac{x_{\beta,d}}{x_\beta} = \frac{Q_f \cdot \omega_0 \cdot p}{p^2 + Q_f \cdot \omega_0 \cdot p + \omega_0^2} \tag{4.21}$$

$$\frac{x_{\alpha,q}}{x_\alpha} = \frac{x_{\beta,q}}{x_\beta} = \frac{Q_f \cdot \omega_0^2}{p^2 + Q_f \cdot \omega_0 \cdot p + \omega_0^2} \tag{4.22}$$

$$\vec{x}_{p,\alpha\beta} = \frac{1}{2} \cdot \begin{pmatrix} 1 & 0 & 0 & -1 \\ 0 & 1 & 1 & 0 \end{pmatrix} \cdot \begin{pmatrix} x_{\alpha,d} \\ x_{\alpha,q} \\ x_{\beta,d} \\ x_{\beta,q} \end{pmatrix} \tag{4.23}$$

$$\vec{x}_{n,\alpha\beta} = \frac{1}{2} \cdot \begin{pmatrix} 1 & 0 & 0 & 1 \\ 0 & -1 & 1 & 0 \end{pmatrix} \cdot \begin{pmatrix} x_{\alpha,d} \\ x_{\alpha,q} \\ x_{\beta,d} \\ x_{\beta,q} \end{pmatrix} \tag{4.24}$$

$$\vec{x}_{p,dq} = e^{-j \cdot \gamma_p} \cdot \vec{x}_{p,\alpha\beta} \tag{4.25}$$

$$\vec{x}_{n,dq} = e^{-j \cdot \gamma_n} \cdot \vec{x}_{n,\alpha\beta} \tag{4.26}$$

Fig. 4.9 shows the respective Simulink®structure and Fig. 4.10 the bode plots of the two filter transfer functions deployed. Filter results for different filter bandwidth values Q_f and the test signal of Fig. 4.11 a) are given in Appendix E in Fig. E.8.

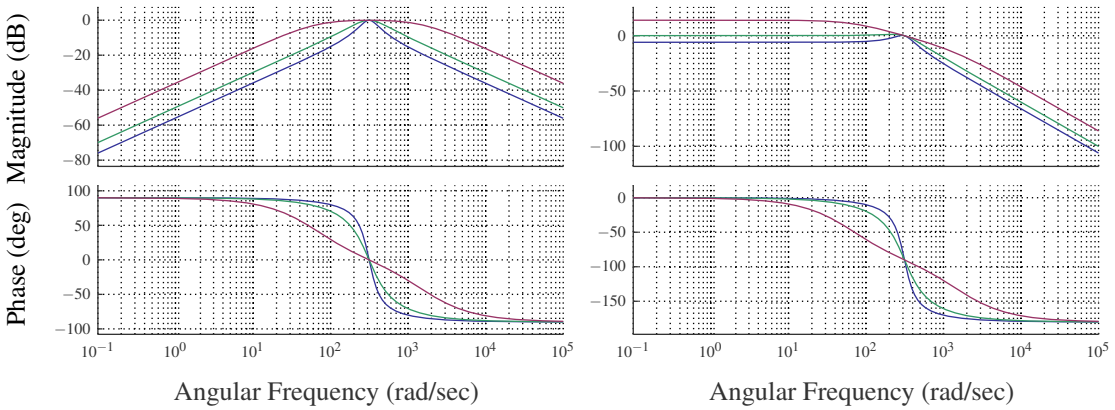

Figure 4.10: Bode plots of band-pass filters used in the DSOGI-structure with $Q_f = 5$, 1 and 0.5 – left: direct component, right: quadrature component

4.1.9 Comparison of the different filter options

The results of two simulation experiments are given in Figs. 4.11 and 4.12 to demonstrate the advantages and disadvantages of the different filter possibilities. The first simulation (Fig. 4.11) was performed using the following asymmetrical three-phase signals: the nominal amplitude of the test signals is 1. One of the three-phase test signals is reduced to 0.5 during a time period of 500 ms. The frequency of the test signal is set to the nominal grid frequency. For the second simulation not only the amplitude of one phase but also the grid frequency was reduced to 90%. The results of this simulation are given in Fig. 4.12. Table 4.2 summarises the filter transfer functions of the filter procedures described in Sections 4.1.2 – 4.1.6. The transfer functions described in Sections 4.1.7 and 4.1.8 cannot be represented by one equation. Table 4.3 summarises the characteristics of the different filter possibilities.

Table 4.2: Filter possibilities for PN-component calculation

Filter	Filter constant	$G_{filter,p} = \frac{\vec{x}_{p,dq}}{\vec{x}_{\alpha\beta}} = e^{-j\cdot\gamma_p}\cdot\ldots$	$G_{filter,n} = \frac{\vec{x}_{n,dq}}{\vec{x}_{\alpha\beta}} = e^{-j\cdot\gamma_n}\cdot\ldots$
PT1	$T_f = 100\,\text{ms}$	1	$\frac{1}{1+p\cdot T_f}$
PT1 & feedback	$T_f = 5\,\text{ms}$	$\frac{1+p\cdot T_f}{2+p\cdot T_f}$	$\frac{1}{2+p\cdot T_f}$
MAV	$T_{MAV} = 10\,\text{ms}$	1	$\frac{1}{p\cdot T_{MAV}}\cdot\left(1-e^{p\cdot T_{MAV}}\right)$
MAV & feedback	$T_{MAV} = 10\,\text{ms}$	$\left(1-\frac{1}{p\cdot T_{MAV}}\cdot\left(1-e^{p\cdot T_{MAV}}\right)\right)$	$\frac{1}{p\cdot T_{MAV}}\cdot\left(1-e^{p\cdot T_{MAV}}\right)$
Notch	$Q_f = 1.41$	1	$\frac{p^2+\omega_0^2}{p^2+Q_f\cdot\omega_0\cdot p+\omega_0^2}$
DSOGI-QSG	$Q_f = 1.41$		

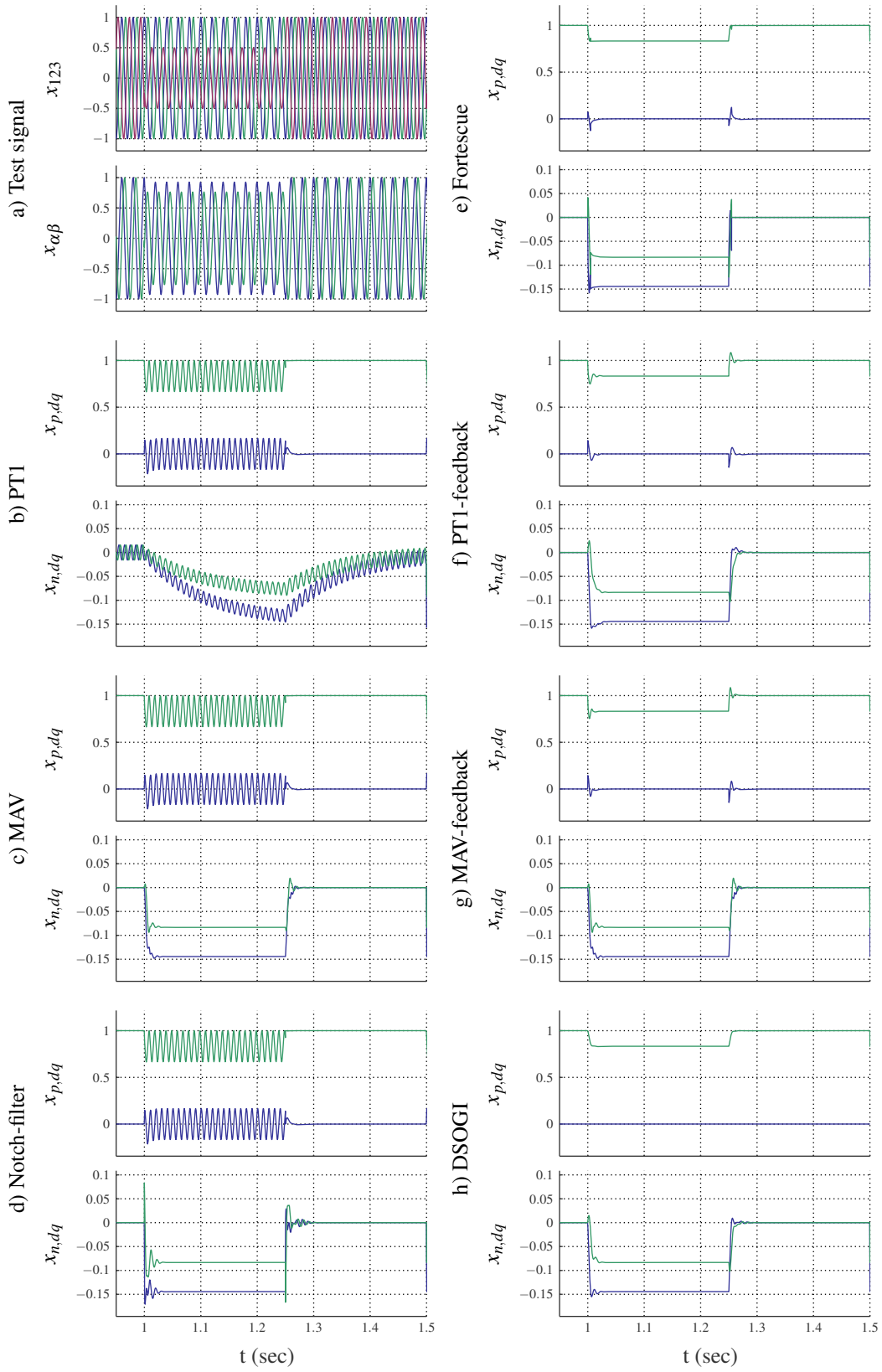

Figure 4.11: Comparison of component calculation possibilities: one phase dip to 50%

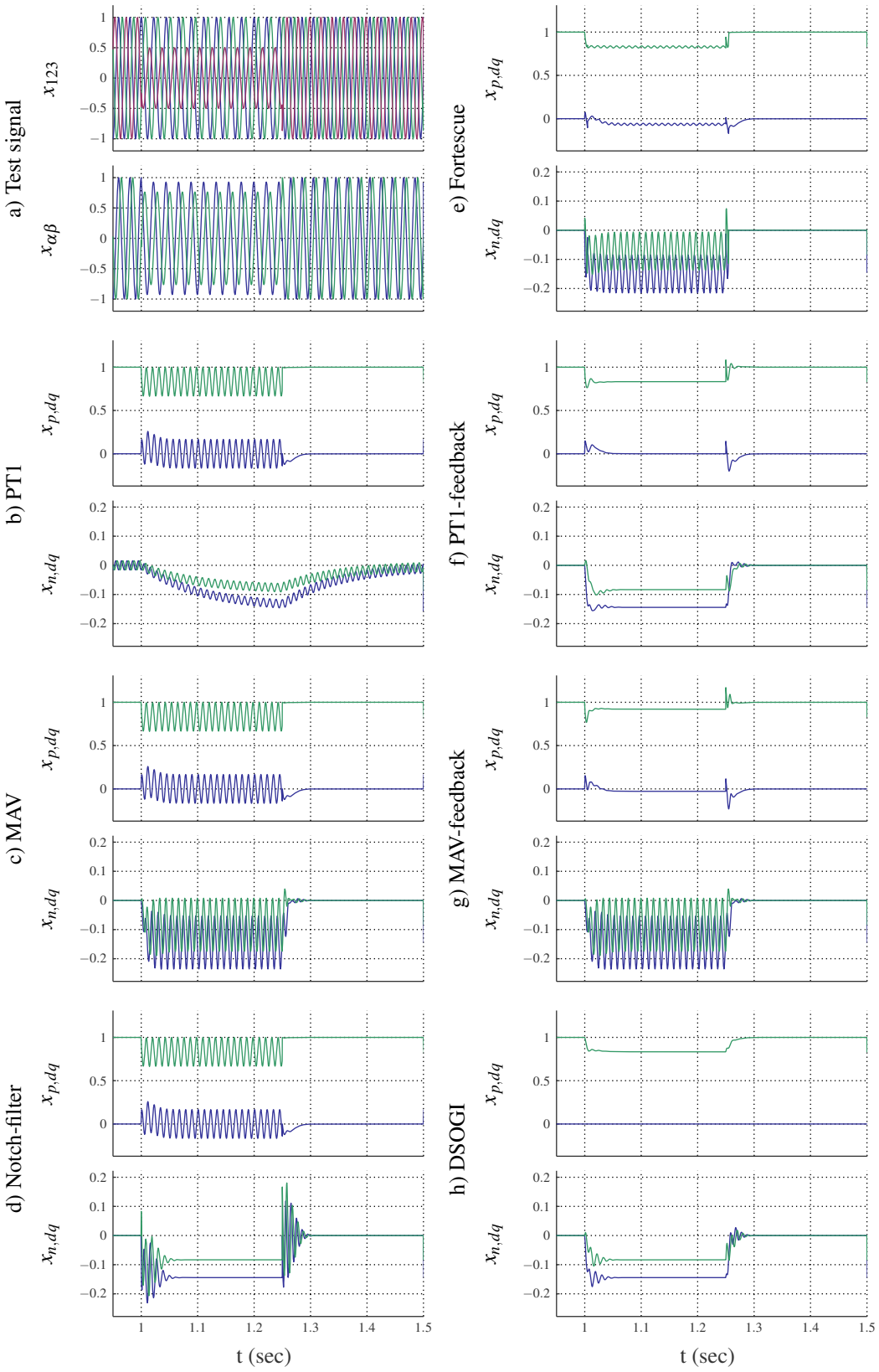

Figure 4.12: Comparison of component calculation possibilities: one phase dip to 50% and simultaneous frequency reduction of 10%

Table 4.3: Overview about different filter possibilities (+: good, −: unfavourable)

	Oscillation suppression in steady state – positive-sequence	Oscillation suppression in steady state – negative-sequence	Setting time	Robustness to frequency variations	Implementation
PT1-filter (without signal feedback)	-[a]	-	500 ms with $T_f = 100$ ms	+	1 Integrator/signal
PT1-filter (with signal feedback)	+	+	20 ms with $T_f = 5$ ms	+	1 Integrator/signal
MAV-filter (without signal feedback)	-[b]	+	20 ms with $T_{MAV} = 10$ ms	-	1 Integrator/signal, high storage demand
MAV-filter (with signal feedback)	+	+	20 ms with $T_{MAV} = 10$ ms	-	1 Integrator/signal, high storage demand
Notch-filter	-[c]	+	20 ms with $Q_f = 1$	+ (if ω_0 is adapted to double grid frequency)	3 Integrators/signal
Fortescue transformation	+[d]	+	10 ms	-	0 Integrators/signal, high storage demand
DSOGI-QSG	+	+	20 ms with $Q_f = 1.41$	+ (if ω_0 is adapted to double grid frequency)	2 Integrators/signal

[a] The oscillation on the positive-sequence components can be suppressed if the PT1-filters are applied also to the positive-sequence components.
[b] The oscillation on the positive-sequence components can be suppressed if the MAV-elements are applied also to the positive-sequence components.
[c] The oscillation on the positive-sequence components can be suppressed if the notch-filters are applied also to the positive-sequence components.
[d] If the positive-sequence is calculated directly from the three-phase signals – avoiding the time delay introduced by the phasor generation – the oscillations on the positive-sequence components will not be suppressed.

4.2 Rotor-side positive-negative-sequence control

The aim of application of the rotor-side PN-control is to reduce the oscillations of the inner torque of the machine during asymmetrical grid conditions. To control the positive-sequence and negative-sequence rotor currents separately, the control structure deduced in Section 3.1 is modified as follows.

- From the three-phase rotor currents the positive-sequence and negative-sequence components are calculated as described in Section 4.1.
- Two current controllers for the negative-sequence current components are added. These work in a coordinate system rotating in the opposite direction to the coordinate system of the positive-sequence current controllers.
- The two positive-sequence current controllers are decoupled by $L_\sigma \cdot \left(\omega_{grid} - \dot{\gamma}\right)$ as shown in Fig. 3.3 for the field-oriented rotor-side control.
- Analogously, the two negative-sequence current controllers are decoupled by $L_\sigma \cdot \left(-\omega_{grid} - \dot{\gamma}\right)$ using the "negative-sequence slip frequency".
- The reference values for the negative-sequence current components are either set to zero or are calculated as described in Section 4.2.3.
- The actuating variables of the four current controllers are transferred back to the rotor-oriented coordinate system. The negative-sequence and the positive-sequence components are summed up in this coordinate system.
- The superior power controllers are not changed.

The structure of the rotor-side PN-control scheme is depicted in Fig. 4.13.

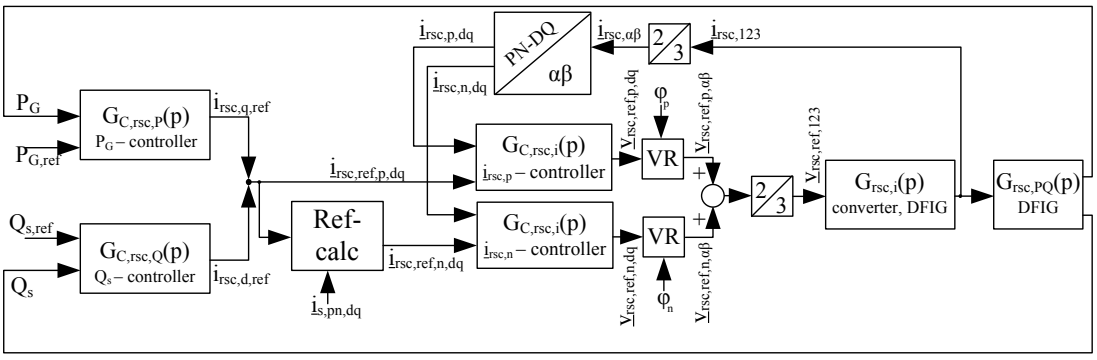

Figure 4.13: Rotor-side PN-control

Each of the two blocks "$G_{C,rsc,i}(p) - \underline{i}_{rsc,pn}$-controller" contains two current controllers (one for the d-component, one for the q-component) and a decoupling algorithm. The block "*Ref-calc*" represents the calculation of the four current reference values described in Section 4.2.3.

4.2.1 Current controller parameters

The transfer function of the rotor current control path is given in Eq. 3.31 for field-oriented control. The separation of positive-sequence and negative-sequence components adds another element to this transfer function, which depends on the chosen filter method and on the component (p- or n-component). The respective transfer functions are given in Sections 4.1.2 – 4.1.8 and in Table 4.2. Thus, the overall transfer functions are:

$$G_{rsc,i,p}(p) = \frac{i_{rsc}(p)}{v_{rsc,ref}(p)} = \frac{1}{\bar{R} + p \cdot L_\sigma} \cdot \frac{1}{1 + p \cdot T_{rsc,p}} \cdot G_{filter,p}(p) \tag{4.27}$$

$$G_{rsc,i,n}(p) = \frac{i_{rsc}(p)}{v_{rsc,ref}(p)} = \frac{1}{\bar{R} + p \cdot L_\sigma} \cdot \frac{1}{1 + p \cdot T_{rsc,p}} \cdot G_{filter,n}(p) \tag{4.28}$$

In some cases (positive-sequence component and PT1-filter, MAV-filter or notch-filter) the transfer function does not change, so the same control parameters as for the field-oriented control could be used. The simulations showed that also in these cases it is favourable to adapt the control parameters of the positive-sequence controllers. This may be caused by a coupling of positive-sequence and negative-sequence components (the action of the negative-sequence controllers affects the positive-sequence controllers – and vice versa – and so the dynamic behaviour of the overall system). In other cases (negative-sequence component and/or PT1-filter with feedback or MAV-filter with feedback) the control parameters have to be changed because the transfer function of the control path is modified. According to the amplitude optimum method a PID-controller could be used with the PT1-filter with feedback for the negative-sequence components. In contrast, the amplitude optimum method is applicable neither on control paths containing MAV-filters nor for the use of notch-filters. In this study the controller parameters are set by trial-and-error: the step responses of the positive-sequence and negative-sequence d-component are optimised separately. To set the controller parameters, only the rotor-side control part is considered in the simulations. The DC-link voltage is set to the nominal value and the grid-side inverter is disconnected from the stator. The results for the different filter possibilities – except the PT1-filter[2] – are given in Fig. 4.14.

[2]The PT1-filter without feedback is not analysed further as its dynamic behaviour is significantly worse than that of all other filter possibilities.

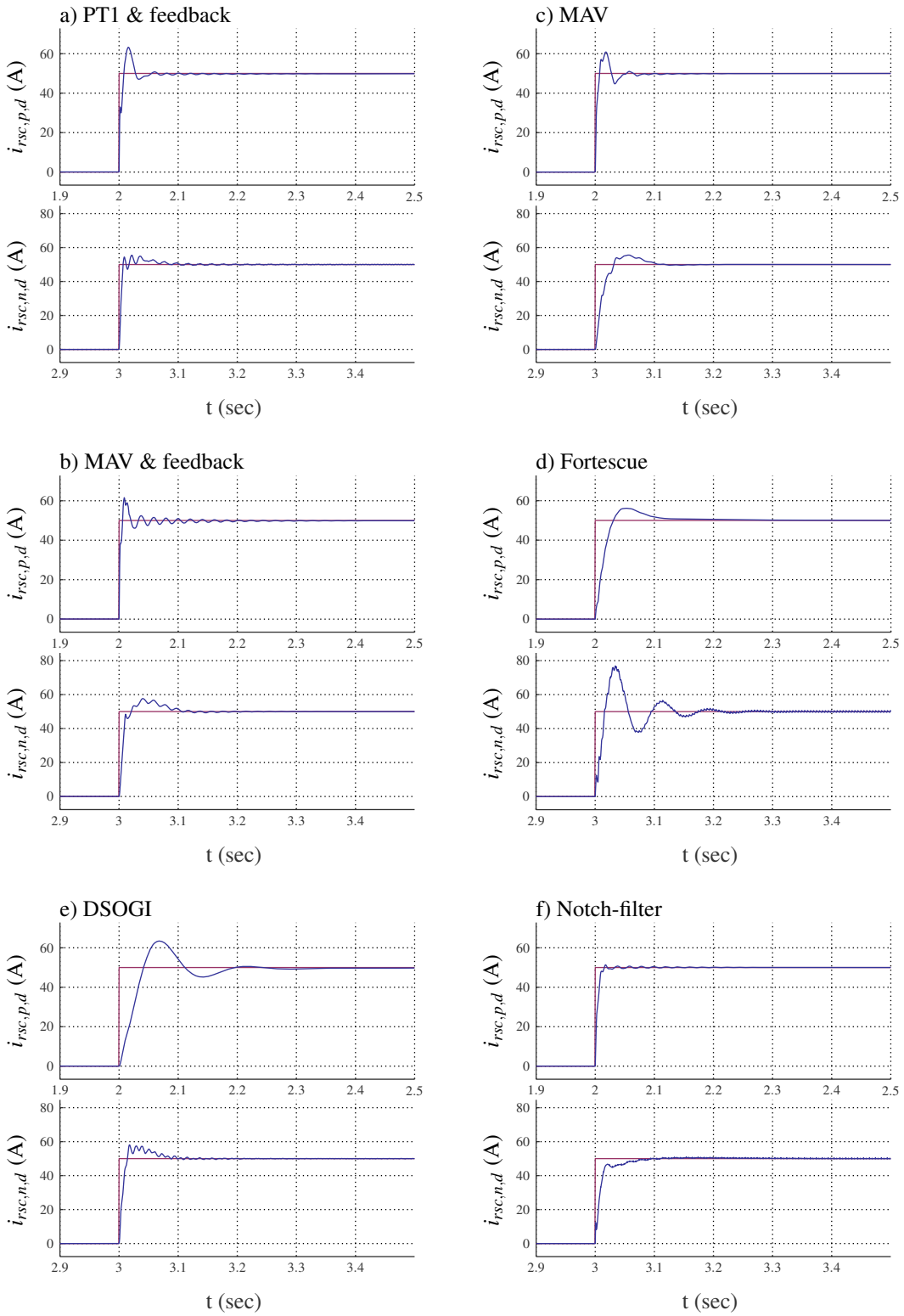

Figure 4.14: Results of PN control with different ways of component calculation – step responses of positive-sequence and negative-sequence rotor current d-components ($P_G = P_{nom}$, $n = 1.08 \cdot n_{s=0}$, DC-link voltage fixed, no grid-side inverter)

4.2.2 Limitation of current controllers

The outputs of the four current controllers are limited in two steps: firstly, the amplitude of the positive-sequence controller outputs is limited to the available converter output voltage ($= v_{DC}/\sqrt{3}$). To ensure the priority of the positive-sequence controllers, secondly, the amplitude of the negative-sequence controller outputs is limited to the remaining voltage reserve[3]:

$$\sqrt{v_{rsc,n,d,ref}^2 + v_{rsc,n,q,ref}^2} \leq v_{rsc,n,max} \tag{4.29}$$

$$v_{rsc,n,max} = v_{DC}/\sqrt{3} - \sqrt{v_{rsc,p,d,ref}^2 + v_{rsc,p,q,ref}^2} \tag{4.30}$$

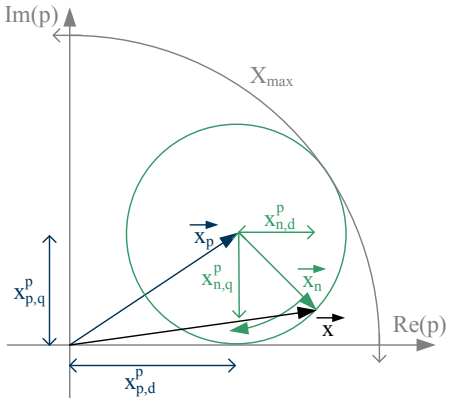

Figure 4.15: Limit calculation for n-current controllers (in positive-sequence coordinate system, x represents a current or voltage vector)

Fig. 4.15 illustrates this limit calculation.

4.2.3 Calculation of current reference values

The reference values for the positive-sequence current controllers are provided by the superior controllers. The reference values for the negative-sequence current controllers are calculated according to [39, p. 37 et seqq.] using the stator current components and the reference values for the positive-sequence current components. The objective of this calculation is to determine the negative-sequence rotor currents to minimise the torque oscillations during asymmetrical grid conditions. The calculation is given in the following equation:

$$\begin{pmatrix} i_{rsc,n,d,ref} \\ i_{rsc,n,q,ref} \end{pmatrix} = \frac{1}{i_{s,p,q}^2 + i_{s,p,d}^2} \cdot \begin{pmatrix} (i_{s,p,d} \cdot i_{s,n,d} - i_{s,p,q} \cdot i_{s,n,q}) & (i_{s,p,d} \cdot i_{s,n,q} + i_{s,p,q} \cdot i_{s,n,d}) \\ (i_{s,p,d} \cdot i_{s,n,q} + i_{s,p,q} \cdot i_{s,n,d}) & (i_{s,p,q} \cdot i_{s,n,q} - i_{s,p,d} \cdot i_{s,n,d}) \end{pmatrix} \cdot \begin{pmatrix} i_{rsc,p,d,ref} \\ i_{rsc,p,q,ref} \end{pmatrix} \tag{4.31}$$

The magnitude of the negative-sequence current reference values $\sqrt{i_{r,n,d,ref}^2 + i_{r,n,q,ref}^2}$ is limited to ensure the priority of the positive-sequence components. The limit is calculated from:

$$\sqrt{i_{rsc,n,d,ref}^2 + i_{rsc,n,q,ref}^2} \leq i_{rsc,n,max} = i_{rsc,max} - \sqrt{i_{rsc,p,d,ref}^2 + i_{rsc,p,q,ref}^2} \tag{4.32}$$

[3] The upper index of the coordinate system is omitted in Eqs. 4.29 – 4.30 and 4.31 – 4.32. Positive-sequence quantities are given in p-coordinate system, negative-sequence quantities are given in n-coordinate system.

with $i_{rsc,max}$ = maximum allowed rotor inverter current.

4.2.4 Power controllers

The outer cascade controllers for active and reactive machine power are not changed. The same structure and parameters as for the field-oriented control are used. These control parameters are given in Table D.2.

4.3 Grid-side positive-negative-sequence control

The objective of the grid-side inverter PN-control is to reduce the oscillations on the DC-link voltage during asymmetrical grid conditions. Analogous to the rotor-side PN-control, the grid-side inverter control is deduced from the field-oriented control scheme in the following way.

- From the three-phase grid-side inverter currents, the positive-sequence and negative-sequence components are calculated as described in Section 4.1.
- Two current controllers for the negative-sequence current components are added. These controllers work in a coordinate system contra-rotating to the coordinate system of the positive-sequence current controllers.
- The two positive-sequence current controllers are decoupled by $\omega_{grid} \cdot L_{gscT\sigma}$ as shown in Fig. 3.7.
- Analogously, the two negative-sequence current controllers are decoupled by $-\omega_{grid} \cdot L_{gscT\sigma}$.
- Different possibilities exist to calculate the reference values for the four current controllers. These are described in Section 4.3.3.
- The actuating variables of the four current controllers are transferred back to the stator-oriented coordinate system. The negative-sequence and the positive-sequence components are summed up in this coordinate system.
- The superior DC-link voltage controller is not changed, except for the use with the current filter method described in Section 4.1.7.

The structure of the grid-side PN-control scheme is depicted in Fig. 4.16. Again, each of the two blocks "$G_{C,gsc,i}(p) - \underline{i}_{gsc,pn}$-controller" contains two current controllers and the block "*Ref-calc*" represents the calculation of current reference values described in Section 4.3.3.

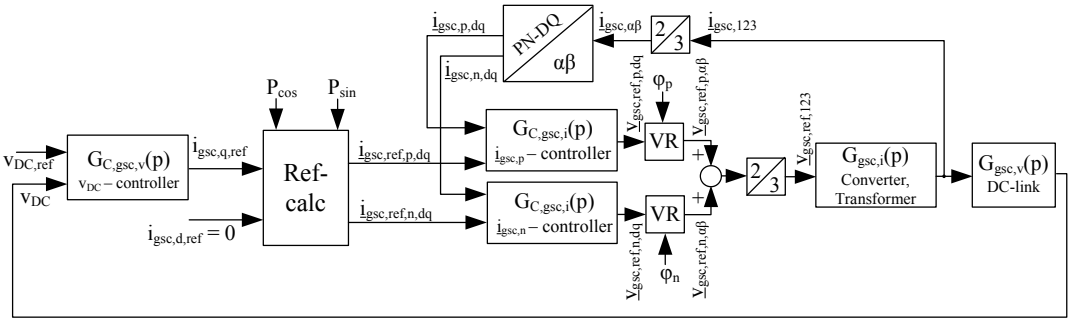

Figure 4.16: Grid-side PN-control

4.3.1 Current controller parameters

As in the case of the rotor-side current control, the grid-side current control can be deduced from the field-oriented control scheme described in Section 3.2.1. The transfer function of the filter method used is added to the transfer function of the current control path (Eqs. 3.53 – 3.56), resulting in:

$$G_{gsc,i,p,dq}(p) = \frac{1}{R_{gscT} + p \cdot L_{gscT\sigma}} \cdot \frac{1}{1 + p \cdot T_{gsc,p}} \cdot G_{filter,p}(p) \tag{4.33}$$

$$G_{gsc,i,n,dq}(p) = \frac{1}{R_{gscT} + p \cdot L_{gscT\sigma}} \cdot \frac{1}{1 + p \cdot T_{gsc,p}} \cdot G_{filter,n}(p) \tag{4.34}$$

The parameters of the current controllers are set by trial-and-error using the step responses of the current's d-components. Only the grid-side inverter is considered in the simulations for the optimisation, the stator and rotor of the machine are "disconnected" and the DC-link voltage is set to a fixed value. The results of the optimisation are given in Fig. 4.17 for the six filter methods described in Sections 4.1.3 – 4.1.8.

4.3.2 Limitation of current controllers

The outputs of the current controllers are limited with priority given to the positive-sequence in the same way as described above for the limitation of the rotor-side current controllers. The following equations are used:

$$\sqrt{v_{gsc,n,d,ref}^2 + v_{gsc,n,q,ref}^2} \leq v_{gsc,n,max} \tag{4.35}$$

$$v_{gsc,n,max} = v_{DC}/\sqrt{3} - \sqrt{v_{gsc,p,d,ref}^2 + v_{gsc,p,q,ref}^2} \tag{4.36}$$

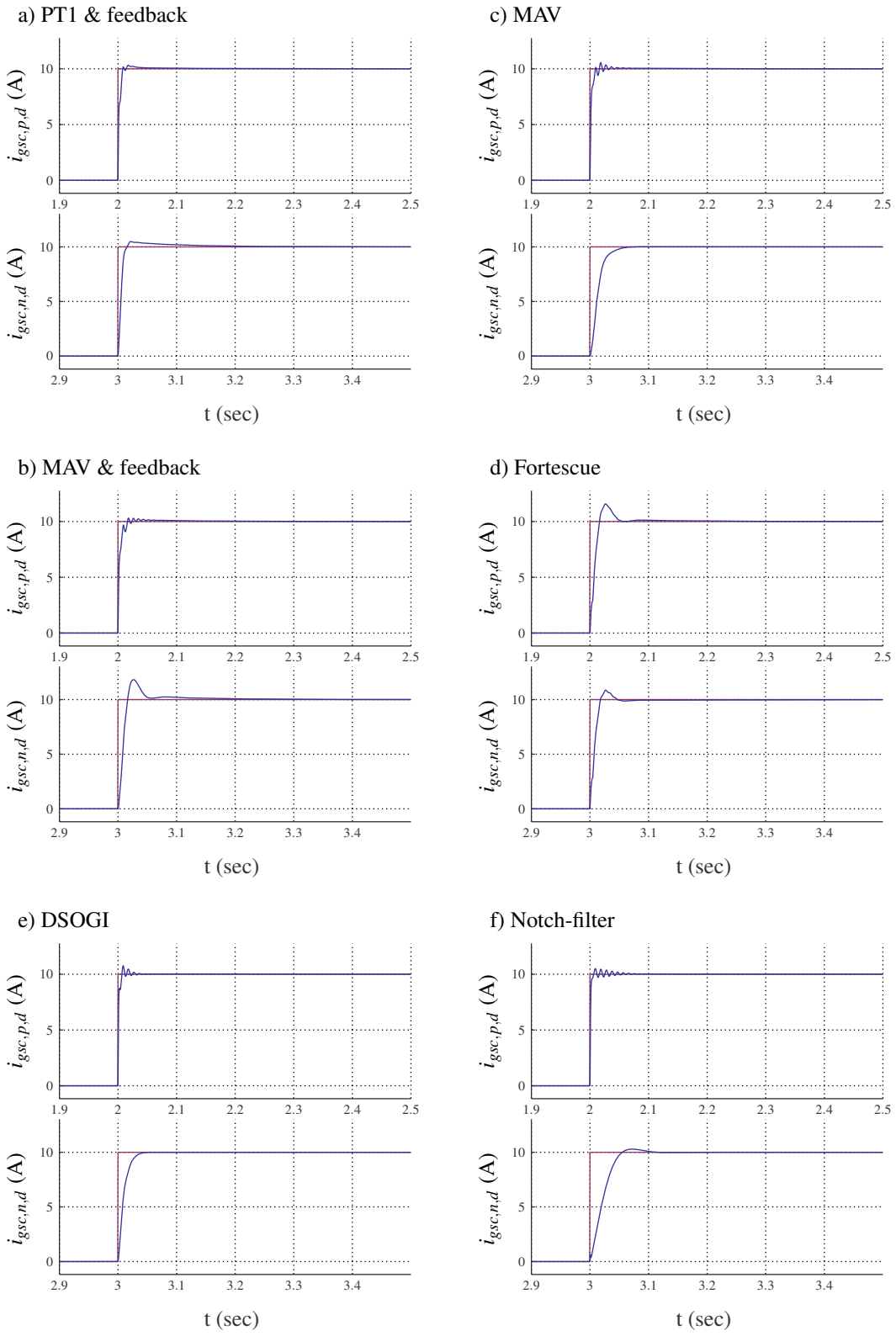

Figure 4.17: Results of PN control with different ways of component calculation – step responses of positive-sequence and negative-sequence grid-side inverter current d-components ($v_{DC} = v_{DC,nom}$, generator and rotor-side inverter disconnected)

4.3.3 Calculation of current reference values

As mentioned above, the objective of the grid-side PN-control is to reduce oscillations at double the grid frequency of the DC-link voltage during asymmetrical grid conditions. These oscillations are caused by the oscillating power fed to or provided by the rotor-side inverter and the grid-side inverter. If the DC-link voltage is to remain constant during asymmetries, rotor-side and grid-side inverter power have to be identical.

In general, the instantaneous values of active and reactive power of an asymmetrical three-phase system can be calculated from the positive-sequence and negative-sequence components of currents and voltages:

$$P(t) = P_{DC} + P_{cos} \cdot \cos\left(2 \cdot \omega_{grid} \cdot t\right) + P_{sin} \cdot \sin\left(2 \cdot \omega_{grid} \cdot t\right) \tag{4.37}$$

$$Q(t) = Q_{DC} + Q_{cos} \cdot \cos\left(2 \cdot \omega_{grid} \cdot t\right) + Q_{sin} \cdot \sin\left(2 \cdot \omega_{grid} \cdot t\right) \tag{4.38}$$

with

$$\begin{pmatrix} P_{dc} \\ P_{cos} \\ P_{sin} \\ Q_{dc} \\ Q_{cos} \\ Q_{sin} \end{pmatrix} = \frac{3}{2} \cdot \begin{pmatrix} v_{p,d} & v_{p,q} & v_{n,d} & v_{n,q} \\ v_{n,d} & v_{n,q} & v_{p,d} & v_{p,q} \\ v_{n,q} & -v_{n,d} & -v_{p,q} & v_{p,d} \\ v_{p,q} & -v_{p,d} & v_{n,q} & -v_{n,d} \\ v_{n,q} & -v_{n,d} & v_{p,q} & -v_{p,d} \\ -v_{n,d} & -v_{n,q} & v_{p,d} & v_{p,q} \end{pmatrix} \cdot \begin{pmatrix} i_{p,d} \\ i_{p,q} \\ i_{n,d} \\ i_{n,q} \end{pmatrix} \tag{4.39}$$

The following procedure is used in this study to achieve identical power values for the two inverters:

1. From rotor voltages and currents the oscillating rotor inverter power components $P_{rsc,sin}$, $P_{rsc,cos}$ are calculated according to Eq. 4.39. For this calculation the positive-sequence current and voltage components are filtered using MAV-elements.
2. The reference values of the grid-side inverter current components are calculated with the objective to satisfy the following conditions: $P_{gsc,sin} = P_{rsc,sin}$, $P_{gsc,cos} = P_{rsc,cos}$. Different possibilities exist for this calculation. These are given in this section. The simulation results of these methods are shown in Appendix E.3.2.

Four current components are controlled separately. This means that a maximum of four of the possible six power components of Eq. 4.39 can be controlled.

Calculation of all four current reference values Typically, the output of the DC-link voltage controller is used as reference value for the active current component of the grid-side inverter.

Instead of this, it is possible to calculate an equivalent power value from the controller output to use the following equations for the reference value calculation (w_{gscT} = winding ratio of grid-side transformer):

$$\begin{pmatrix} P_{gsc,dc,ref} \\ P_{gsc,cos,ref} \\ P_{gsc,sin,ref} \\ Q_{gsc,dc,ref} \end{pmatrix} = \begin{pmatrix} \frac{3}{2} \cdot v_{dc} \cdot i_{gsc,q,ref} \\ P_{rsc,cos} \\ P_{rsc,sin} \\ 0 \end{pmatrix} \tag{4.40}$$

$$= \frac{3}{2} \cdot w_{gscT} \cdot \begin{pmatrix} v_{s,p,d} & v_{s,p,q} & v_{s,n,d} & v_{s,n,q} \\ v_{s,n,d} & v_{s,n,q} & v_{s,p,d} & v_{s,p,q} \\ v_{s,n,q} & -v_{s,n,d} & -v_{s,p,q} & v_{s,p,d} \\ v_{s,p,q} & -v_{s,p,d} & v_{s,n,q} & -v_{s,n,d} \end{pmatrix} \cdot \begin{pmatrix} i_{gsc,p,d,ref} \\ i_{gsc,p,q,ref} \\ i_{gsc,n,d,ref} \\ i_{gsc,n,q,ref} \end{pmatrix} \tag{4.41}$$

Eq. 4.41 can be rearranged to calculate the four current reference values. The detailed result is given in [39, p. 42 et seqq.]. To calculate the reference values of the grid-side inverter current components, it is necessary to measure the stator voltages and calculate the positive-sequence and negative-sequence components of these voltages as described in Section 4.1.

One result of this calculation method is given in Appendix E in Fig. E.9.

Calculation of negative sequence current reference values and pd-component Alternatively to the previous calculation, it is possible to use the output of the DC-link voltage controller directly. This results in the following calculation:

$$i_{gsc,p,q,ref} = i_{gsc,q,ref} = \text{output of DC-link controller} \tag{4.42}$$

$$\begin{pmatrix} P_{gsc,cos,ref} \\ P_{gsc,sin,ref} \\ Q_{gsc,dc,ref} \end{pmatrix} = \begin{pmatrix} P_{rsc,cos} \\ P_{rsc,sin} \\ 0 \end{pmatrix} \tag{4.43}$$

$$= \frac{3}{2} \cdot w_{gscT} \cdot \begin{pmatrix} v_{s,n,d} & v_{s,n,q} & v_{s,p,d} & v_{s,p,q} \\ v_{s,n,q} & -v_{s,n,d} & -v_{s,p,q} & v_{s,p,d} \\ v_{s,p,q} & -v_{s,p,d} & v_{s,n,q} & -v_{s,n,d} \end{pmatrix} \cdot \begin{pmatrix} i_{gsc,p,d,ref} \\ i_{gsc,p,q,ref} \\ i_{gsc,n,d,ref} \\ i_{gsc,n,q,ref} \end{pmatrix} \tag{4.44}$$

By introducing Eq. 4.43 into Eq. 4.44 and rearranging the result, one obtains:

$$\frac{2}{3 \cdot w_{gscT}} \cdot \begin{pmatrix} P_{rsc,cos} \\ P_{rsc,sin} \\ 0 \end{pmatrix} - \begin{pmatrix} v_{s,n,q} \\ -v_{s,n,d} \\ -v_{s,p,d} \end{pmatrix} \cdot i_{gsc,p,q,ref} = \begin{pmatrix} v_{s,n,d} & v_{s,p,d} & v_{s,p,q} \\ v_{s,n,q} & -v_{s,p,q} & v_{s,p,d} \\ v_{s,p,q} & v_{s,n,q} & -v_{s,n,d} \end{pmatrix} \cdot \begin{pmatrix} i_{gsc,p,d,ref} \\ i_{gsc,n,d,ref} \\ i_{gsc,n,q,ref} \end{pmatrix} \quad (4.45)$$

Inverting the voltage matrix of Eq. 4.45 it is possible to calculate the remaining three current reference values. As an example, one result of this calculation is given in Fig. E.10.

Calculation of negative sequence current reference values and pq-component The reference value of the reactive current component is set to zero in the control scheme described in Section 3.2.1. This setting can be used for the calculation resulting in:

$$i_{gsc,p,d,ref} = 0 \quad (4.46)$$

$$\begin{pmatrix} P_{gsc,dc,ref} \\ P_{gsc,cos,ref} \\ P_{gsc,sin,ref} \end{pmatrix} = \begin{pmatrix} \frac{3}{2} \cdot v_{dc} \cdot i_{gsc,q,ref} \\ P_{rsc,cos} \\ P_{rsc,sin} \end{pmatrix} \quad (4.47)$$

$$= \frac{3}{2} \cdot w_{gscT} \cdot \begin{pmatrix} v_{s,p,q} & v_{s,n,d} & v_{s,n,q} \\ v_{s,n,q} & v_{s,p,d} & v_{s,p,q} \\ -v_{s,n,d} & -v_{s,p,q} & v_{s,p,d} \end{pmatrix} \cdot \begin{pmatrix} i_{gsc,p,q,ref} \\ i_{gsc,n,d,ref} \\ i_{gsc,n,q,ref} \end{pmatrix} \quad (4.48)$$

By inverting the voltage matrix of Eq. 4.48, it is possible to rearrange the equation to calculate the three remaining current reference values. Fig. E.11 shows one result of this calculation method.

Calculation of negative sequence current reference values Combining the last two calculation methods, $i_{gsc,p,d,ref}$ is set to zero and the output of the DC-link voltage controller is used directly as reference value of the positive-sequence active current component ($i_{gsc,p,q,ref}$). This results in the following equations:

$$i_{gsc,p,d,ref} = 0 \quad (4.49)$$

$$i_{gsc,p,q,ref} = i_{gsc,q,ref} = \text{output of DC-link controller} \quad (4.50)$$

and:

$$\begin{pmatrix} P_{gsc,cos,ref} \\ P_{gsc,sin,ref} \end{pmatrix} = \begin{pmatrix} P_{rsc,cos} \\ P_{rsc,sin} \end{pmatrix} \tag{4.51}$$

$$= \frac{3}{2} \cdot w_{gscT} \cdot \begin{pmatrix} v_{s,n,d} & v_{s,n,q} & v_{s,p,d} & v_{s,p,q} \\ v_{s,n,q} & -v_{s,n,d} & -v_{s,p,q} & v_{s,p,d} \end{pmatrix} \cdot \begin{pmatrix} i_{gsc,p,d,ref} \\ i_{gsc,p,q,ref} \\ i_{gsc,n,d,ref} \\ i_{gsc,n,q,ref} \end{pmatrix} \tag{4.52}$$

Eq. 4.52 can be rearranged to:

$$\begin{pmatrix} i_{gsc,n,d,ref} \\ i_{gsc,n,q,ref} \end{pmatrix} = \frac{1}{v_{s,p,d}^2 + v_{s,p,q}^2} \cdot \begin{pmatrix} v_{s,p,d} & -v_{s,p,q} \\ v_{s,p,q} & v_{s,p,d} \end{pmatrix} \cdot \left[\frac{2}{3 \cdot w_{gscT}} \cdot \begin{pmatrix} P_{rsc,cos} \\ P_{rsc,sin} \end{pmatrix} - \begin{pmatrix} v_{s,n,q} \\ -v_{s,n,d} \end{pmatrix} \cdot i_{gsc,q,ref} \right] \tag{4.53}$$

For this method fewest changes of the control structure described in Section 3.2.1 are necessary, because the control path of the positive-sequence current components is changed only by the component calculation and not by the calculation of the current reference values. A result of this method is shown in Fig. E.12.

The results of all four calculation methods show only slight differences during the transients. The last method was used for the simulations of the present study, because it involves the fewest changes of the positive-sequence components control path.

Reduction of active power oscillations The four methods used to calculate the grid-side inverter current reference values described above all are employed with the intention of reducing the DC-link voltage oscillation. Alternatively, it is possible to use the stator-power values instead of the rotor-power values with the intention to reduce the generator active power oscillations as is suggested in [18]. This corresponds to two conditions: $-P_{s,cos} = P_{gsc,cos}$ and $-P_{s,sin} = P_{gsc,sin}$. Based on Eq. 4.53, the following equations could be used to calculate the grid-side negative-sequence current reference values:

$$\begin{pmatrix} i_{gsc,n,d,ref} \\ i_{gsc,n,q,ref} \end{pmatrix} = \frac{-1}{v_{s,p,d}^2 + v_{s,p,q}^2} \cdot \begin{pmatrix} v_{s,p,d} & -v_{s,p,q} \\ v_{s,p,q} & v_{s,p,d} \end{pmatrix} \cdot \left[\frac{2}{3 \cdot w_{gscT}} \cdot \begin{pmatrix} P_{s,cos} \\ P_{s,sin} \end{pmatrix} + \begin{pmatrix} v_{s,n,q} \\ -v_{s,n,d} \end{pmatrix} \cdot i_{gsc,q,ref} \right] \tag{4.54}$$

The stator power values can be calculated from:

$$\begin{pmatrix} P_{s,cos} \\ P_{s,sin} \end{pmatrix} = \frac{3}{2} \cdot \begin{pmatrix} v_{s,n,d} & v_{s,n,q} & v_{s,p,d} & v_{s,p,q} \\ v_{s,n,q} & -v_{s,n,d} & -v_{s,p,q} & v_{s,p,d} \end{pmatrix} \cdot \begin{pmatrix} i_{s,p,d} \\ i_{s,p,q} \\ i_{s,n,d} \\ i_{s,n,q} \end{pmatrix} \tag{4.55}$$

Theoretically, both possibilities should give similar results: if torque and DC-link voltage do not contain oscillations and the machine speed is constant, the overall power will also be a constant (disregarding all losses). Therefore, this method to calculate the reference values was not analysed further in the present study.

Limitation of reference values Analogously to the rotor-side control, the reference values of the grid-side inverter currents are limited with priority given to the positive-sequence components. The magnitude of the negative-sequence current reference values $\sqrt{i_{gsc,n,d,ref}^2 + i_{gsc,n,q,ref}^2}$ is limited by:

$$\sqrt{i_{gsc,n,d,ref}^2 + i_{gsc,n,q,ref}^2} \leq i_{gsc,n,max} = i_{gsc,max} - \sqrt{i_{gsc,p,d,ref}^2 + i_{gsc,p,q,ref}^2} \tag{4.56}$$

with $i_{gsc,max}$ = maximum allowed grid-side inverter current.

4.3.4 DC-link voltage controller

Except for the use of the filter version "Fortescue-transformation", the parameters of the DC-link voltage controller are not changed[4]. For the use of the filter version "Fortescue-transformation" it is necessary to change the control parameters to achieve a stable control. The controller parameters are adapted by trial-and-error using the step response of the DC-link voltage. The results are given in Table D.3.

4.4 Simulation results of positive-negative-sequence control

To test the complete PN-control scheme, grid-side and rotor-side PN-control are combined. Some simulation results are given in this section[5]. Additional to the PN-control a brake chopper is added to the model. In real configurations this brake chopper is necessary to discharge the DC-link capacitor during voltage dips and limit the acceleration of the DC-link voltage. The

[4] Simulations with the complete PN-control scheme showed that these controller parameters are suboptimal for operation with higher slip values (super synchronous and sub synchronous). For an implementation of the control scheme especially the DC-link voltage controller parameters would need to be optimised.

[5] The inverter models are mean-value-models as described in Chapter 2. This may limit the validity of the simulation results especially during transients, where the inverters reach their voltage limits.

brake chopper resistance is connected in parallel to the DC-link capacitor and is controlled by an on/off-controller with hysteresis.

For most of the filter versions – namely PT1 & feedback, MAV & feedback, DSOGI and Fortescue-transformation – described in Section 4.1, the combination of rotor-side and grid-side PN-control results in an unstable system. This may be caused by the cross-couplings between positive-sequence and negative-sequence components introduced to the system by the component calculation. To achieve stable control, adaption of the outer cascade controller parameters would be required. Calculation of the current- and voltage components using MAV-elements or notch-filters for the negative-sequence component (Sections 4.1.4 and 4.1.6) will yield stable control results if rotor-side and grid-side PN-control are deployed. These two calculation methods do not introduce a cross-coupling between positive and negative-sequence components, the positive-sequence control path is not changed. The results of these two control configurations are given in Figs. 4.18 and 4.19 for fixed machine speed and the conditions given below.

- $n = 1.08 \cdot n_{s=0}$,
- $t = 1\,\mathrm{s} \ldots 2\,\mathrm{s}$ – 2-phase dip on the grid-side of the main transformer to 95% remaining voltage,
- $t = 3\,\mathrm{s}$ – step from $v_{DC,ref} = v_{DC,nom}$ to $v_{DC,ref} = 1.025 \cdot v_{DC,nom}$,
- $t = 4\,\mathrm{s}$ – step from $P_{G,ref} = P_{G,nom}$ to $P_{G,ref} = 0.75 \cdot P_{G,nom}$,
- $t = 5\,\mathrm{s}$ – step from $Q_{G,ref} = 0\,\mathrm{kVAr}$ to $Q_{G,ref} = 0.0625 \cdot [P_{G,nom}]\mathrm{kVAr}$.

All quantities are related to the nominal values[6] ($x_{rel} = x/x_{nom}$), the reference values of the grid-side inverter current components are calculated as described in Section 4.3.3 by Eqs. 4.49, 4.50 and 4.53 with the aim of reducing the DC-link voltage oscillations. Comparison with Fig. 3.9 shows that a reduction of the torque oscillations during asymmetrical grid conditions is possible with PN-control, while the reference reaction deteriorates at least when MAV-filters are used. However, the effect of the PN-control on torque and DC-link voltage is not very strong. It is limited by the constraints discussed in the following sections.

[6]The scale bases are given in Appendix E in Table E.1.

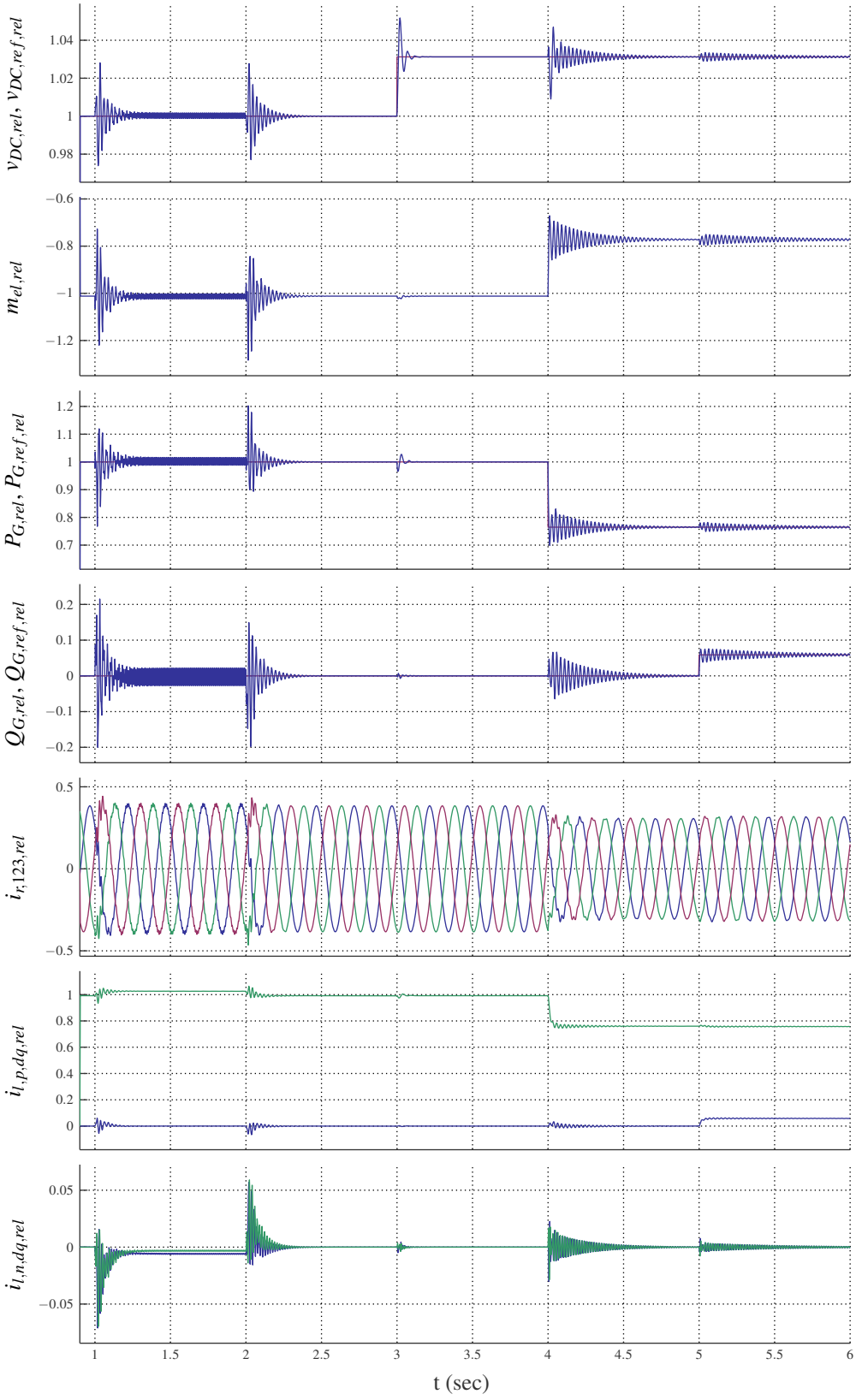

Figure 4.18: PN-control with MAV-filter, 2-phase dip to 95% remaining voltage and step responses of active and reactive power and DC-link voltage

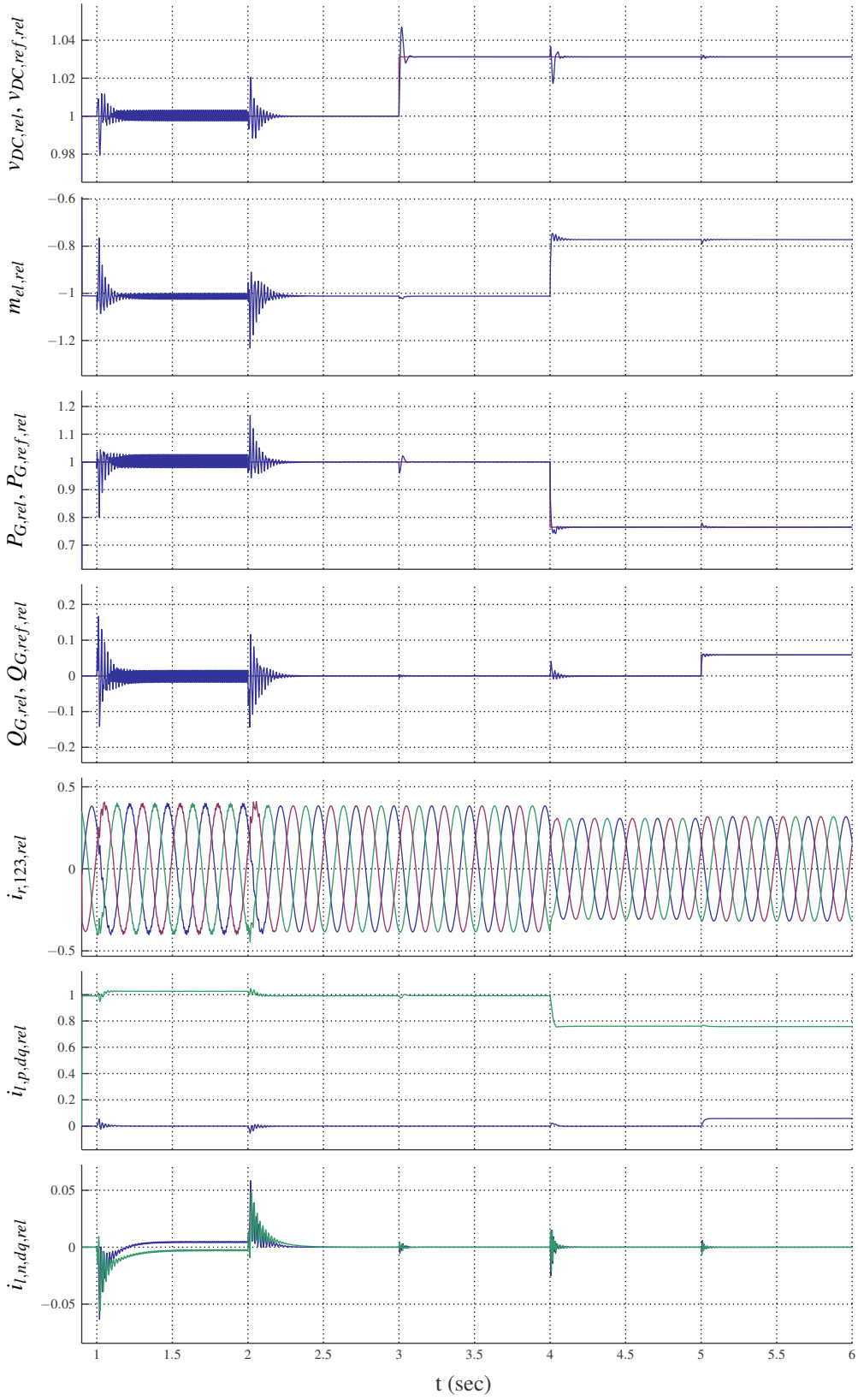

Figure 4.19: PN-control with notch-filter, 2-phase dip to 95% remaining voltage and step responses of active and reactive power and DC-link voltage

4.4.1 Maximum inverter voltages

The voltage of the DC-link capacitor limits the possible output voltages of the inverters to $\sqrt{3} \cdot v_{DC}$ and thus limits the controllability of the converters. This limitation is important especially for the rotor-side inverter as negative-sequence stator voltages are "transformed" to the rotor at approximately the double grid frequency. Additionally, the natural flux decay during transients increases the arising rotor voltages. Both effects are described in [24] and in [25]. The maximum arising rotor voltages are estimated in Appendix C.2 and are summarised in Table 4.4 with the following assumptions and simplifications.

- No rotor current is possible, the rotor terminals are neither connected nor short circuited.
- The voltage dip is occurring directly at the stator terminal.
- $d = 1 - \frac{v_{s,dip}}{v_{s,nom}} = 0 \ldots 1$ = relative dip-depth.
- $\frac{L_m}{L_m + L_{s\sigma}} \approx 1$
- For asymmetrical dips the maximum voltage depends on the time of the dip start (or rather on the phase of the stator voltage). The worst-case is given in the table.
- The voltage components given in the table correspond to the positive-sequence linked stator flux (subscript p), to the negative-sequence linked stator flux (subscript n) and to the natural flux component (subscript *nat*). The latter is a transient component decaying with the stator time constant $\tau = L_s/R_s$

Table 4.4: Maximum rotor voltages with asymmetrical stator voltages according to [24] and [25]

Dip type	Maximum rotor voltage components (related to nominal stator voltage) $v_{r,rel} = \frac{v_{r,dip,max}^{s,(s)}}{v_{s,nom,max}}$		
	$v_{r,p,rel}$	$v_{r,n,rel}$	$v_{r,nat,rel}$
3-phase	$(1-d) \cdot s \cdot e^{j \cdot \omega_{grid} \cdot t}$	0	$d \cdot (s-1) \cdot e^{-t/\tau}$
2-phase	$(1-2/3 \cdot d) \cdot s \cdot e^{j \cdot \omega_{grid} \cdot t}$	$1/3 \cdot d \cdot (2-s) \cdot e^{-j \cdot \omega_{grid} \cdot t}$	$d \cdot (s-1) \cdot e^{-t/\tau}$
1-phase	$(1-1/3 \cdot d) \cdot s \cdot e^{j \cdot \omega_{grid} \cdot t}$	$1/3 \cdot d \cdot (2-s) \cdot e^{-j \cdot \omega_{grid} \cdot t}$	$2/3 \cdot d \cdot (s-1) \cdot e^{-t/\tau}$
phase-phase	$(1-1/2 \cdot d) \cdot s \cdot e^{j \cdot \omega_{grid} \cdot t}$	$1/2 \cdot d \cdot (2-s) \cdot e^{-j \cdot \omega_{grid} \cdot t}$	$d \cdot (s-1) \cdot e^{-t/\tau}$

The worst-case is the phase-to-phase dip during sub-synchronous operation of the generator. In reality the resistances and inductances of the grid, the main transformer and the generator reduce the voltage on the terminal of the rotor-side inverter. Nevertheless, maintaining controllability of the rotor-side inverter during severe dips would require a DC-link voltage of several thousand volt ($\approx \sqrt{3} \cdot w_{GW} \cdot 2.6 \cdot \sqrt{2/3} \cdot V_{s,nom}$ with $s = -0.3$ and $d = 1$) and is thus impossible. The values given in Table 4.4 also imply that the maximum dip-depth the system can ride through does not only depend on the rated DC-link voltage but also on the operating point of the DFIG before and during the dip, because the induced rotor voltage components depend on the slip s.

In contrast, the voltage on the terminal of the grid-side inverter is reduced during grid faults. During the transients of dip start and recovery, some overvoltage is possible but will not be as high as on the rotor-side inverter.

To illustrate the effect of this constraint, simulation results for two different DC-link voltage values are given in Fig. 4.20 for the following configuration:

- $n = 1.08 \cdot n_{s=0}$,
- $Q_{G,ref} = 0\,\mathrm{kVAr}$,
- $t = 1\,\mathrm{s} \ldots 1.5\,\mathrm{s}$: 1-phase dip to 50% remaining voltage on the grid-side of the main transformer,
- component calculation with notch-filters.

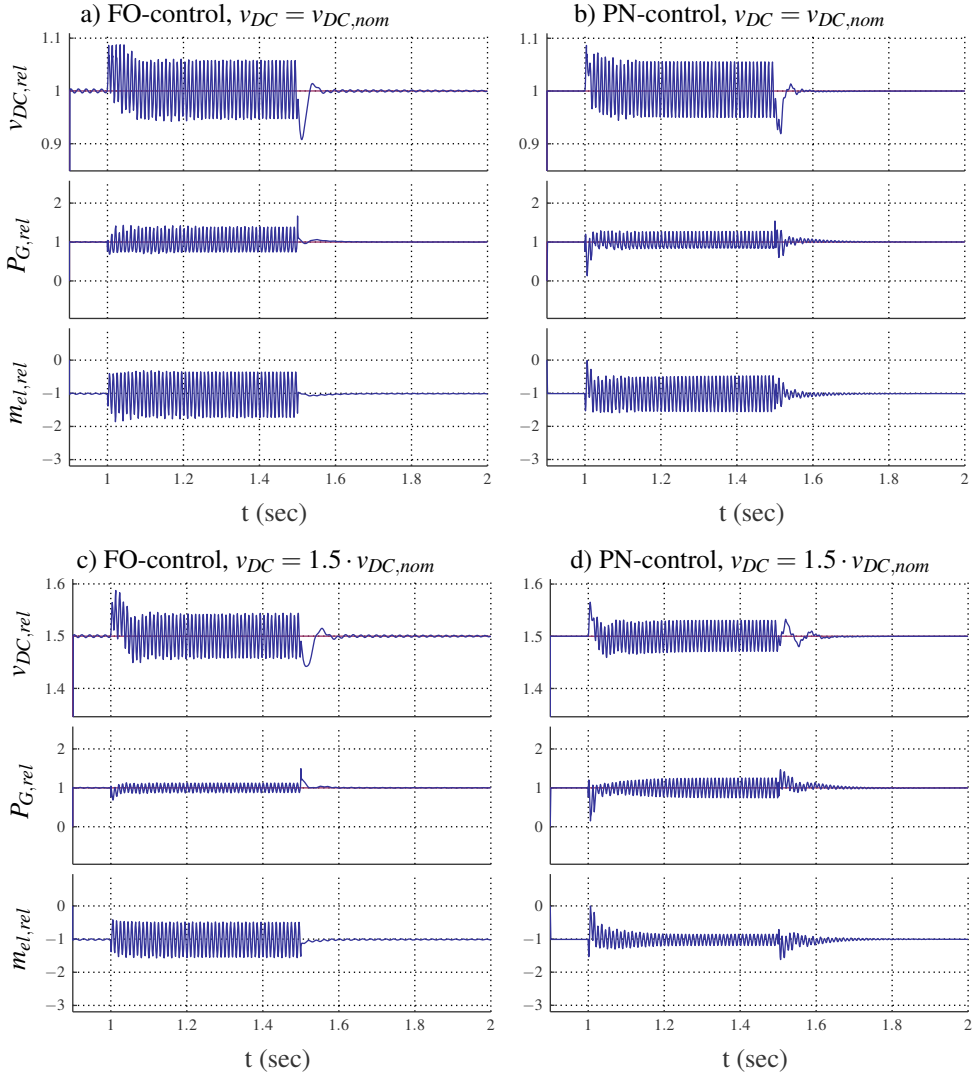

Figure 4.20: Field-oriented control and PN-control during asymmetrical voltage dip with different DC-link voltage values

4.4.2 Maximum allowed inverter current

The ampacity of the inverters limits the inverter currents allowed. This limitation strongly depends on the dimensioning of the inverters. As described by Eqs. 4.32 and 4.56 the reference values for the negative-sequence current controllers are limited to ensure the priority of the positive-sequence currents.

4.4.3 Component calculation and current reference calculations

Obviously, the behaviour during the first instants of a dip (and the voltage recovery) is not improved. The reason is that the calculation of the symmetrical components needs at least half a grid period to detect the changes.

Furthermore, the remaining DC-link voltage oscillation visible in Figs. 4.18 – 4.22 are caused by the voltage used to calculate the grid-side negative-sequence current references: to avoid additional measurements in a real setup, the stator voltage components are used in Eq. 4.53. These differ slightly from the grid-side inverter voltage because of the voltage drop over the grid-side transformer. Therefore, the calculated current reference values do not exactly fulfil the condition of Eq. 4.51. To prove the theoretical correctness of the proposed control scheme, a simulation was conducted using the grid-side inverter voltages to calculate the negative-sequence current references. The results are given in Fig. 4.21 for the following conditions: $t = 1\,\mathrm{s}\ldots2\,\mathrm{s}$: 2-phase dip to 95% remaining voltage on the grid-side of the main transformer and $v_{DC} = 1.5 \cdot v_{DC,nom}$.

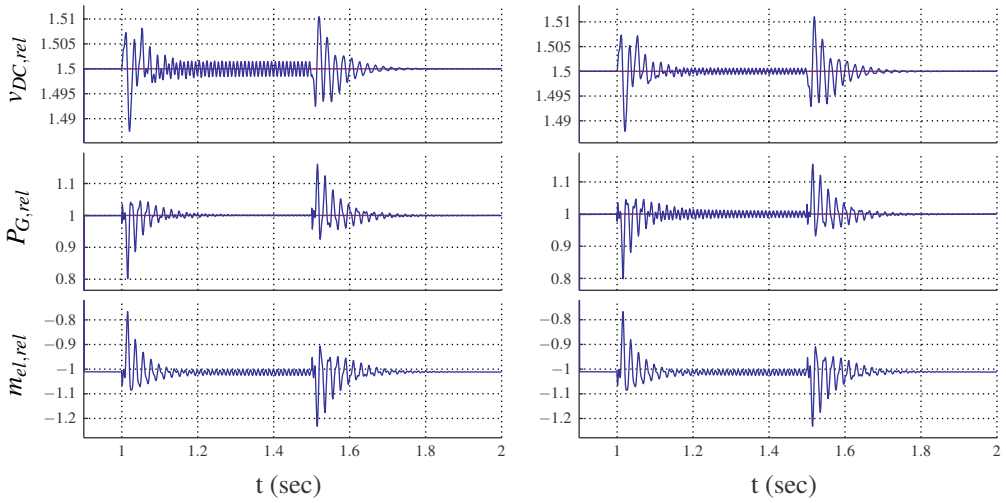

Figure 4.21: Influence of deployed voltage components for reference value calculation on PN-control results – left: $i_{gsc,ref}$-calculation using stator voltage components, right: $i_{gsc,ref}$-calculation with grid-side inverter voltages

These figures show that the remaining voltage oscillation can be reduced if the grid-side inverter voltage is used for the current reference calculation. Nevertheless, it is not reduced to zero, which may be attributable to the following reason: the oscillating DC-link voltage causes the DC-link voltage controller output to oscillate. This is due to the chosen controller dynamics and could be improved using less dynamic controller parameters.

4.4.4 Nonlinear system behaviour

If a sufficiently high DC-link voltage is chosen and the reference values for all current components are unlimited, the PN-control scheme should be able to reduce the oscillations of the electrical torque to zero. Contrary to expectations, the torque remains oscillating also during slight dips. This can be explained by the linear model used for the calculation of the rotor-side negative-sequence current component references (Eq. 4.31), which is based on the following equation (cf. [39, p. 38]):

$$m_{el} = \frac{3}{2} \cdot p_p \cdot \mathrm{Im}\left\{\left(L_s \cdot \underline{i}_s^{s*} + L_m \cdot \underline{i}_r^{s*}\right) \cdot \underline{i}_s^{s}\right\} = \frac{3}{2} \cdot p_p \cdot L_m \cdot \mathrm{Im}\left\{\underline{i}_r^{s*} \cdot \underline{i}_s^{s}\right\} \tag{4.57}$$

$$\begin{aligned} =& \frac{3}{2} \cdot p_p \cdot L_m \cdot \left[i_{s,p,q} \cdot i_{r,p,d} - i_{s,p,d} \cdot i_{r,p,q} + i_{s,n,q} \cdot i_{r,n,d} - i_{s,n,d} \cdot i_{r,n,q}\right. \\ &+ \left(\; i_{s,n,q} \cdot i_{r,p,d} - i_{s,n,d} \cdot i_{r,p,q} + i_{s,p,q} \cdot i_{r,n,d} - i_{s,p,d} \cdot i_{r,n,q}\right) \cdot \cos\left(2 \cdot \omega_{grid} \cdot t\right) \\ &\left. + \left(-i_{s,n,d} \cdot i_{r,p,d} - i_{s,n,q} \cdot i_{r,p,q} + i_{s,p,d} \cdot i_{r,n,d} + i_{s,p,q} \cdot i_{r,n,q}\right) \cdot \sin\left(2 \cdot \omega_{grid} \cdot t\right)\right] \end{aligned} \tag{4.58}$$

This equation does not include the saturation of the main inductance[7]. To prove the proper functioning of the PN-control, a simulation with constant mutual inductance was conducted. The comparison of the results with and without saturation of the generator's mutual inductance is given in Fig. 4.22 for the following specifications:

- $t = 1\,\mathrm{s} \ldots 2\,\mathrm{s}$: 2-phase dip to 95% remaining voltage on the grid-side of the main transformer.
- $v_{DC} = 1.5 \cdot v_{DC,nom}$.

[7] The saturation model used in the present study is described in Appendix B.2.3.

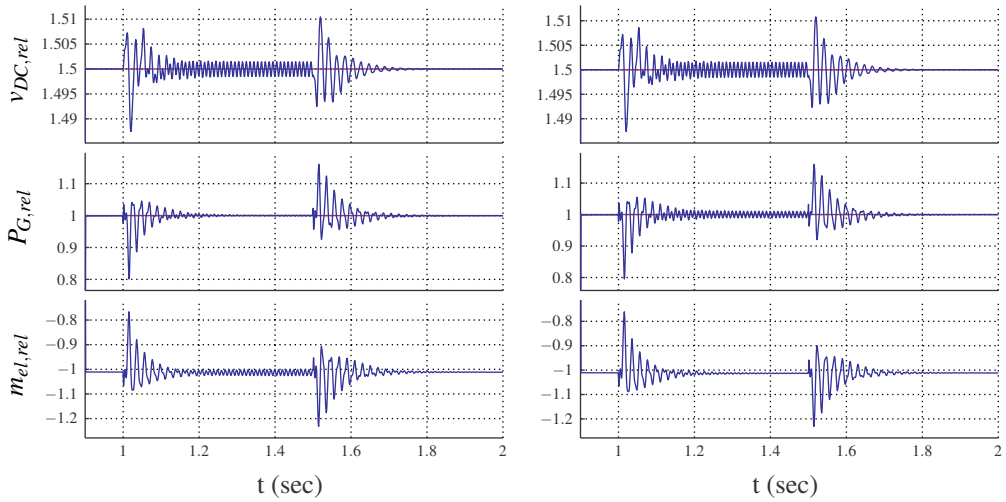

Figure 4.22: Influence of mutual inductance saturation on the electrical torque oscillations with PN-control – left: mutual inductance with saturation, right: constant mutual inductance

These figures show that the torque oscillations could be suppressed completely by the proposed control scheme if the generator was a linear system. The nonlinearity of the mutual inductance deteriorates the control results and limits the possible improvements.

5 Frequency-selective control of doubly-fed induction generators

The currents controlled in the DFIG control system are alternating quantities. The grid-side converter currents alternate at grid frequency while the rotor currents alternate at slip frequency. In the case of conventional field-oriented control these alternating quantities are transferred into rotating coordinate systems to get direct quantities, because the latter can be controlled by proportional-integral controllers without steady-state error[1]. It is also possible to use a different method of controlling the alternating currents directly (without steady-state error), namely specially adapted controllers, referred to as frequency-selective controllers (FSC) in the literature[2]. There are two different considerations which result in a control scheme which is able to control alternating quantities directly. These are described in the following section.

5.1 Principle of frequency-selective control in continuous time domain

Inner model principle (IMP) In [27, p. 342] the "inner model principle" is described[3]. This approach is also used in [12] and in [13] to design a controller for a single-phase active filter and for a three-phase utility-interface converter. Application of the IMP means that tracking of a reference value without remaining offset will be possible with a feedback controller if two conditions are fulfilled (cf. [13]):

- "The closed loop is asymptotically stable.
- The open-loop transfer function of the system includes a mathematical model which can generate the required reference input."

For example, the Laplace transformation or reference signal model of a step-like reference signal $\theta(t)$ with

$$\theta(t) = \begin{cases} 0, & t < 0 \\ 1, & t \geq 0 \end{cases} \tag{5.1}$$

[1] As described in [27, Section 7.3.3, p. 337], a control loop will enable asymptotic tracking of step-like reference values if the open loop (i.e. the controller or the plant) is of the type showing integral behaviour.

[2] In the literature such control algorithms are usually proposed for the control of harmonic currents, while in this study they are used for the control of the fundamental components.

[3] The "inner model principle" is not to be confused with the "internal model control" (IMC) described in [27, Section 12.2, p. 519 et seqq.]. The latter deploys a model of the complete control path as part of the controller.

is $1/p$. Hence, such reference values can be controlled without steady-state error if the controller or the control path contains an integrating element. Alternating reference and disturbance signals can be represented by the following models:

$$f(t) = \sin(\omega_0 t) \circ\!\!-\!\!\bullet F(p) = \frac{\omega_0}{p^2 + \omega_0^2} \tag{5.2}$$

$$f(t) = \cos(\omega_0 t) \circ\!\!-\!\!\bullet F(p) = \frac{p}{p^2 + \omega_0^2} \tag{5.3}$$

To control such signals without remaining offset, the denominator of the controller transfer function must contain $p^2 + \omega_0^2$ – the "inner model" of the signal. The controller can be written as:

$$G_{C,fsc} = \frac{N_c(p)}{\tilde{D}_c(p) \cdot \left(p^2 + \omega_0^2\right)} \tag{5.4}$$

In the design of the controller, $N_c(p)$ and $\tilde{D}_c(p)$ can be chosen freely. Using the control path transfer functions deduced in Section 3.1.2 (Eqs. 3.28 to 3.30) for the rotor-side current controller, the open loop transfer function becomes:

$$G_{0,fsc,rsc} = \frac{1}{\bar{R} + p \cdot L_\sigma} \cdot \frac{1}{1 + p \cdot T_{rsc,p}} \cdot \frac{N_{rsc,c}(p)}{\tilde{D}_{rsc,c}(p) \cdot \left(p^2 + \omega_0^2\right)} \tag{5.5}$$

The simplified transfer function of the grid-side current control loop – using Eqs. 3.53 and 3.54 – becomes:

$$G_{0,fsc,gsc} = \frac{1}{R_{gscT} + p \cdot L_{gscT\sigma}} \cdot \frac{1}{1 + p \cdot T_{gsc,p}} \cdot \frac{N_{gsc,c}(p)}{\tilde{D}_{gsc,c}(p) \cdot \left(p^2 + \omega_0^2\right)} \tag{5.6}$$

Because of the inner model, the open loop contains a pair of conjugate-complex poles without real component, which must be taken into account when designing the controller. As the extended control path with the inner model is not itself stable, the controller needs to stabilise the system. In [13] a combination of PI- and frequency-selective controller is suggested. This results in the following control transfer function, which is used in the following sections:

$$G_{C,fsc} = K_P + K_I \cdot \frac{1}{p} + K_S \cdot \frac{p}{p^2 + \omega_0^2} \tag{5.7}$$

Lowpass-bandpass-transformation (LP-BP-transformation) The second approach is described in [15, Chapter 4]. The resulting control scheme is named "frequency-selective control" (FSC). The frequency-selective controller is deduced directly from the proportional-integral controller using lowpass-bandpass-transformation of the controller transfer function, for which the complete mathematical deduction is given in [15, Chapter 4][4]. It is an exact transformation

[4] This mathematical deduction is also given in Appendix C.3.1.

only for integral elements. In the work cited, the lowpass-bandpass-transformation replaces p by $\left(p^2+\omega_0^2\right)/(2\cdot p)$. This substitution results in an approximately equivalent transfer function of FSC and PI-controller with park transformation. The transformation result for a PI-controller is given in Table 5.1.

Table 5.1: Controller transfer functions in continuous domain using LP-BP-transformation

DC-controller $G_{C,dc}(p)$	equivalent FSC in p-domain $G_{C,fsc}(p)$
$\frac{1}{p}$	$\frac{2\cdot p}{p^2+\omega_0^2}$
$K_c\cdot\left(1+\frac{1}{p\cdot T_c}\right)$	$2\cdot K_c\cdot\left(1+\frac{1}{T_c}\frac{p}{p^2+\omega_0^2}\right)$

Comparison of LP-BP-Transformation and IMP Depending on the definition of $N_c(p)$ and $\tilde{D}_c(p)$ both these approaches result in the same transfer function of the controller. A comparison is given in Table 5.2.

Table 5.2: Transfer functions of frequency-selective controllers

LP-BP-transformation	IMP
$2\cdot K_c\cdot\left(1+\frac{1}{T_c}\frac{p}{p^2+\omega_0^2}\right)=2\cdot K_c\cdot\frac{p^2\cdot T_c+p\cdot+T_c\cdot\omega_0^2}{T_c\cdot\left(p^2+\omega_0^2\right)}$	$\frac{N_c(p)}{\tilde{D}_c(p)\cdot\left(p^2+\omega_0^2\right)}$

5.2 Coordinate system and frequency adaptation

In the present study, rotor-side and grid-side inverter currents are controlled in a stator-oriented coordinate system using FSC. As in the field-oriented control scheme, each part of the control system contains the means of controlling two current components, named the α- and the β-component. This requires a transformation of the rotor-side currents to the stator-oriented coordinate system using vector rotation (Appendix A.5). Thus, all controlled currents alternate at grid frequency and the FSC deployed is designed for grid frequency. An adaptation of the control parameters (namely ω_0) to variations of the grid frequency is necessary and can be easily realised if a frequency-locked-loop is used for the calculation of the grid angle.

If the alternating quantities are controlled directly using FSC, the reference values provided by the outer-loop controllers must be transferred using inverse park transformation.

5.3 Stability analysis of frequency-selective controllers

The open loop transfer functions of the grid-side and the rotor-side current control loops (Eqs. 5.5 and 5.6) are of the same type: they both consist of two low-pass elements. An abstract transfer function of this type is used in the following series of equations to analyse the stability

of the system. The control transfer function has been set to Eq. 5.7. This transfer function combines a proportional, integral and frequency-selective component. The resulting open loop transfer function is:

$$G_{0,fsc}(p) = \frac{1}{R+p\cdot L}\cdot\frac{1}{1+p\cdot T_p}\cdot\left[K_P + K_I\cdot\frac{1}{p} + K_S\cdot\frac{p}{p^2+\omega_0^2}\right] \tag{5.8}$$

$$= \frac{K_P\cdot\left(p^2+\omega_0^2\right)\cdot p + K_I\cdot\left(p^2+\omega_0^2\right) + K_S\cdot p^2}{(R+p\cdot L)\cdot(1+p\cdot T_p)\cdot p\cdot\left(p^2+\omega_0^2\right)} \tag{5.9}$$

The control transfer function of the closed loop is:

$$G_{fsc} = \frac{G_{0,fsc}}{1+G_{0,fsc}} \tag{5.10}$$

The system will be stable if the real components of all poles are negative. The denominator of G_{fsc} can be transformed to a fifth-degree polynomial:

$$0 = 1 + G_{0,fsc} \tag{5.11}$$

$$= 1 + \frac{K_P\cdot\left(p^2+\omega_0^2\right)\cdot p + K_I\cdot\left(p^2+\omega_0^2\right) + K_S\cdot p^2}{(R+p\cdot L)\cdot(1+p\cdot T_p)\cdot p\cdot\left(p^2+\omega_0^2\right)} \tag{5.12}$$

$$= (R+p\cdot L)\cdot(1+p\cdot T_p)\cdot p\cdot\left(p^2+\omega_0^2\right) + K_P\cdot\left(p^2+\omega_0^2\right)\cdot p + K_I\cdot\left(p^2+\omega_0^2\right) + K_S\cdot p^2 \tag{5.13}$$

$$0 = a_5p^5 + a_4p^4 + a_3p^3 + a_2p^2 + a_1p + a_0 \tag{5.14}$$

$$a_5 = LT_p \tag{5.15}$$

$$a_4 = L + RT_p \tag{5.16}$$

$$a_3 = K_P + R + LT_p\omega_0^2 \tag{5.17}$$

$$a_2 = K_I + K_S + RT_p\omega_0^2 + L\omega_0^2 \tag{5.18}$$

$$a_1 = K_P\omega_0^2 + R\omega_0^2 \tag{5.19}$$

$$a_0 = K_I\omega_0^2 \tag{5.20}$$

This polynomial (Eqs. 5.14 – 5.20) is analysed using Hurwitz's stability criterion[5]. If all coefficients and all main section determinants of the matrix H given in Eq. 5.21 are positive, the

[5] A description of Hurwitz's stability criterion can be found in [27, p. 392 et seqq.] and in [29, p. 205]

system will be stable[6].

$$H = \begin{pmatrix} a_1 & a_3 & a_5 & 0 & 0 \\ a_0 & a_2 & a_4 & 0 & 0 \\ 0 & a_1 & a_3 & a_5 & 0 \\ 0 & a_0 & a_2 & a_4 & 0 \\ 0 & 0 & a_1 & a_3 & a_5 \end{pmatrix} \tag{5.21}$$

The conditions resulting from the required positive coefficients are:

$$a_0 > 0 \;\rightarrow\; K_I > 0 \tag{5.22}$$

$$a_1 > 0 \;\rightarrow K_P > -R \tag{5.23}$$

$$a_2 > 0 \;\rightarrow\; K_I > -K_S - \omega_0^2 \cdot (L + RT_p) \tag{5.24}$$

$$a_3 > 0 \;\rightarrow K_P > -R - LT_p \qquad \text{redundant to condition } a_1 > 0 \tag{5.25}$$

$$a_4 > 0 \;\rightarrow\; 0 < L + RT_p \qquad \text{fulfilled} \tag{5.26}$$

$$a_5 > 0 \;\rightarrow\; 0 < LT_p \qquad \text{fulfilled} \tag{5.27}$$

For the main section determinants to be positive, the following conditions must be fulfilled.

$$0 < D_1 = a_1 \tag{5.28}$$

$\rightarrow$ This condition is redundant to the condition of Eq. 5.23.

$$0 < D_2 = a_1 a_2 - a_0 a_3$$

$$\rightarrow\; K_I < \frac{1}{\omega_0^2 L T_p} \cdot \left(K_P K_S + K_P L \omega_0^2 + K_P R T_p \omega_0^2 + K_S R + L R \omega_0^2 + R^2 T \omega_0^2\right) = M_2 \tag{5.29}$$

$$0 < D_3 = a_1 \left(a_2 a_3 - a_1 a_4\right) - a_0 a_3^2 + a_0 a_1 a_5 \tag{5.30}$$

$\rightarrow$ This results in a condition which is redundant to $D_2 > 0$

$$0 < D_4 = \begin{vmatrix} a_1 & a_3 & a_5 & 0 \\ a_0 & a_2 & a_4 & 0 \\ 0 & a_1 & a_3 & a_5 \\ 0 & a_0 & a_2 & a_4 \end{vmatrix}$$

$$\rightarrow \begin{cases} K_S < 0 & \rightarrow & K_I > M_4 \\ K_S > 0 & \rightarrow & K_I < M_4 \end{cases}$$

with

$$M_4 = \frac{1}{L T_p \left(K_P + R - L T_p \omega_0^2\right)} \left(-K_P L^2 T_p \omega_0^2 - K_P K_S L T_p + K_P^2 L + 2 K_P R L + 2 K_P R^2 T_p - \ldots \right.$$
$$\left. \ldots R^2 L T_p \omega_0^2 - K_P R L T_p^2 \omega_0^2 + K_P^2 R T_p - R L^2 T_p \omega_0^2 + R^2 L + R^3 T_p - K_S R L T_p\right) \tag{5.31}$$

[6] "Main section determinants" describes all determinants that can be calculated using the first x lines and x columns of the matrix. In this case, there are five main section determinants.

$$0 < D_5 = \begin{vmatrix} a_1 & a_3 & a_5 & 0 & 0 \\ a_0 & a_2 & a_4 & 0 & 0 \\ 0 & a_1 & a_3 & a_5 & 0 \\ 0 & a_0 & a_2 & a_4 & 0 \\ 0 & 0 & a_1 & a_3 & a_5 \end{vmatrix} \tag{5.32}$$

$\rightarrow$ This results in a condition which is redundant to $D_4 > 0$

Eqs. 5.22 – 5.25, 5.29 and 5.31 define the possible range of controller gains. They can be depicted in a tridimensional diagram as shown in Fig. 5.1. The following are the parameters used for this figure:

$$L = 2\,\text{mH} \tag{5.33}$$

$$R = 30\,\text{m}\Omega \tag{5.34}$$

$$\omega_0 = 2 \cdot \pi \cdot 50\,\text{Hertz} \tag{5.35}$$

$$T_p = 0.1\,\text{ms} \tag{5.36}$$

The planes depicted delimit the array of controller gain triplets allowed.

5.4 Frequency-selective control – rotor-side controllers

Fig. 5.2 shows the structure of the rotor-side control using frequency-selective current controllers. In this structure, the block designated "$G_{C,rsc,i}(p) - \underline{i}_{rsc}$-controller" represents the structure depicted in Fig. 5.3.

5.4.1 Rotor-side current controllers

As mentioned above, the current controllers are realised in the stator-oriented coordinate system. There is thus a need for coordinate transformation of the rotor currents and back transformation of the actuating variables to the rotor-oriented coordinate system. The transformation angle is the rotor angle γ. The coordinate transformation involves coupling the two current component control loops (this is comparable to the coupling of d-component and q-component in the field-oriented control scheme described in Section 3.1.2). A decoupling algorithm will therefore be necessary. A feed-forward algorithm analogous to the one described in Section 3.1.2 would be possible but was omitted in the simulations on which this chapter is based. The resulting current control structure is depicted in Fig. 5.3. Each of the two blocks "$G_{C,rsc,i}(p) - i_{rsc,\alpha\beta}$-controller" contains a transfer function of the type given by Eq. 5.7.

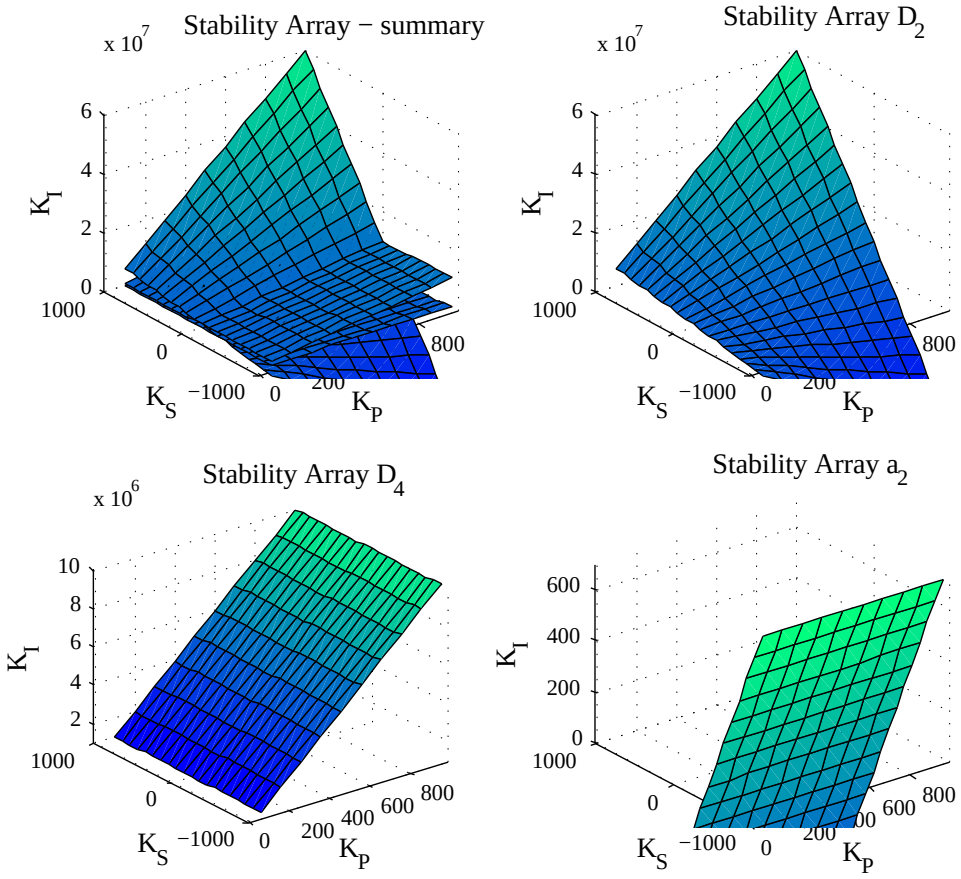

Figure 5.1: Stability array of controller gains for frequency-selective control of a standard control loop

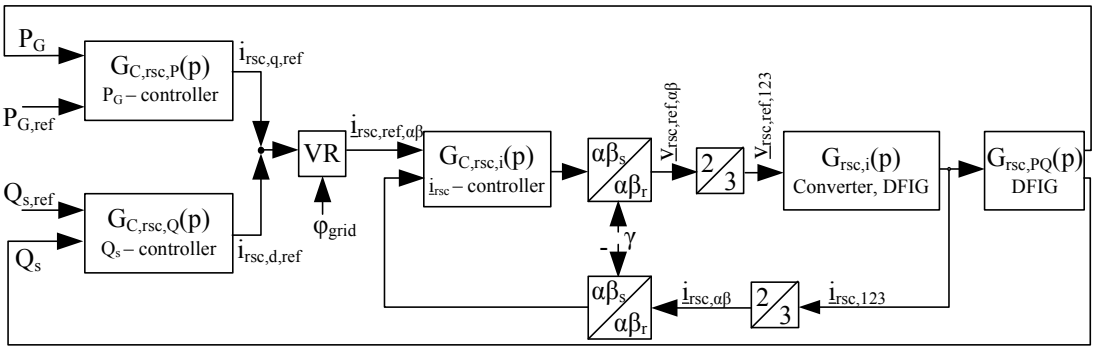

Figure 5.2: Rotor-side control scheme with frequency-selective current controllers

The parameters of the current controllers are set by trial-and-error as described in [12] using Matlab/Simulink®simulations, in which the parameters of field-oriented control are used as starting values. The stability of the current control loops with these parameters can be anal-

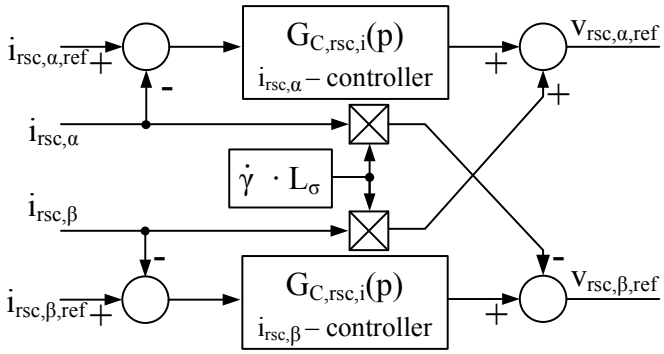

Figure 5.3: Rotor-side current controllers with decoupling

ysed using Eqs. 5.22 – 5.24, 5.29 and 5.31 deduced above. Both the parameters and the results of the stability analysis are given in Table 5.3.

Table 5.3: Stability of rotor-side current controllers

Parameter	Value		Stability condition	Fulfilled?
$\bar{R}$	$= 0.046\,\mathrm{V/A}$	Eq. 5.22	$K_{I,rsc} > 0$	✓
L_σ	$= 0.0013\,\mathrm{Vs/A}$	Eq. 5.23	$K_{P,rsc} > -\bar{R}$	✓
$T_{p,rsc}$	$= 0.0002\,\mathrm{s}$	Eq. 5.24	$K_{I,rsc} > -K_{S,rsc} - \omega_0^2 \cdot \left(L_\sigma + \bar{R}T_{p,rsc}\right)$	✓
$K_{P,rsc}$	$= 5\,\mathrm{V/A}$	Eq. 5.29	$K_{I,rsc} < M_{2,rsc} = 90300$	✓
$K_{S,rsc}$	$= 330\,\mathrm{Vs/A}$	Eq. 5.31	$K_{S,rsc} > 0 \rightarrow K_{I,rsc} < M_{4,rsc} = 25077$	✓
$K_{I,rsc}$	$= 100\,\mathrm{Vs/A}$			

A comparison of the step responses of rotor current d-component with field-oriented control and with frequency-selective control is given for the selected control parameters in Fig. E.13 in Appendix E. The dynamic behaviour of both control loops is comparable.

5.4.2 Power controllers

Because of the dynamic equivalence of field-oriented current control and frequency-selective current control, the superior power controllers are adopted from the field-oriented control scheme described in Section 3.1.3 without changes. The current reference values provided by the active and reactive power controllers must be transferred from the field-oriented coordinate system to the stator-oriented coordinate system using vector rotation.

5.5 Frequency-selective control – grid-side controllers

The structure of the grid-side control is shown in Fig. 5.4. In this case, the block designated "$G_{C,gsc,i}(p) - \underline{i}_{gsc}$-controller" represents the structure shown in Fig. 5.5.

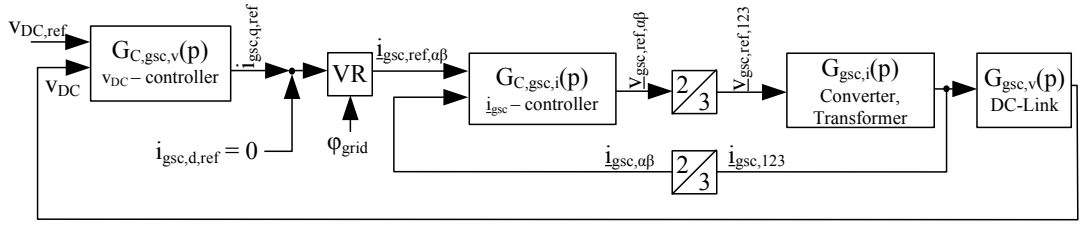

Figure 5.4: Grid-side control scheme with frequency-selective current controllers

5.5.1 Grid-side current controllers

The current controllers are realised in the static coordinate system so that no coordinate transformation of the controlled currents is necessary and the two current components to be controlled are not coupled. Consequently, a decoupling algorithm is not necessary. In the simulations on which this chapter is based, a feed-forward algorithm was used analogous to the one described in Section 3.2.1. Fig. 5.5 shows the resulting current control structure.

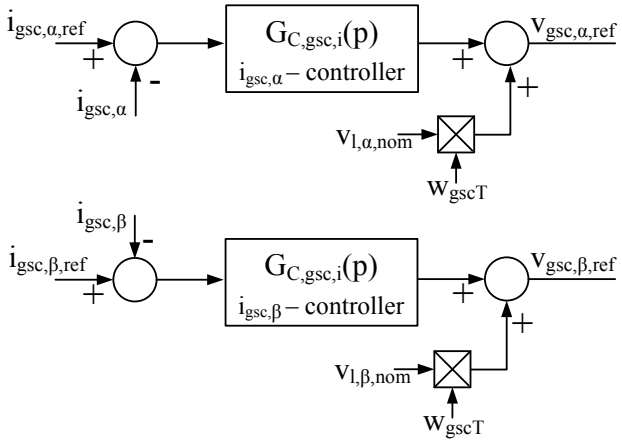

Figure 5.5: Grid-side current controllers

As with the rotor-side current controllers, the parameters of the frequency-selective grid-side current controllers are selected by trial-and-error using Matlab/Simulink®simulations. The selected control parameters and how they fulfil the stability conditions are given in Table 5.4.

Table 5.4: Stability of grid-side current controllers

Parameter	Value		Stability condition	Fulfilled?
R_{gscT}	$= 0.0296\,\mathrm{V/A}$	Eq. 5.22	$K_{I,gsc} > 0$	✓
$L_{gscT,\sigma}$	$= 0.0017\,\mathrm{Vs/A}$	Eq. 5.23	$K_{P,gsc} > -R_{gscT}$	✓
$T_{p,gsc}$	$= 0.0001\,\mathrm{s}$	Eq. 5.24	$K_{I,gsc} > -K_{S,gsc} - \omega_0^2 \cdot \left(L_{gscT,\sigma} + R_{gscT} T_{p,gsc}\right)$	✓
$K_{P,gsc}$	$= 8.5\,\mathrm{V/A}$	Eq. 5.29	$K_{I,gsc} < M_{2,gsc} = 517560$	✓
$K_{S,gsc}$	$= 850\,\mathrm{Vs/A}$	Eq. 5.31	$K_{S,gsc} > 0 \rightarrow K_{I,gsc} < M_{4,gsc} = 84593$	✓
$K_{I,gsc}$	$= 20\,\mathrm{Vs/A}$			

Fig. E.14 shows a comparison of the current step responses with field-oriented control and with frequency-selective control.

5.5.2 DC-link voltage controller

The superior controller for the DC-link voltage is adopted from the field-oriented control scheme. The same controller parameters (given in Table D.2) are used because the dynamic behaviour of the inner control loop is comparable to that of the inner control loop using field-oriented current controllers. A coordinate transformation of the current reference value (q-component) to the static coordinate system is necessary, in which the second reference value (d-component) is set to zero.

5.6 Discretisation of the current controller transfer functions

The implementation of frequency-selective controllers in a DSP requires a transformation of the continuous controller transfer function to a discrete transfer function. The sampling time of the discrete controller is preset by the hardware employed. The ratio between sampling time ($T_{p,rsc} = 0.0002\,\mathrm{s}$ and $T_{p,gsc} = 0.0001\,\mathrm{s}$) and periodic time $T_0 = 2\pi/\omega_0 = 0.02\,\mathrm{s}$ of the frequency-selective controller is 200 for the grid-side controller and 100 for the rotor-side controller and, therefore, sufficiently large to avoid aliasing and to permit quasi-continuous control[7].

Methods of transformation from p- to z-domain There are different possibilities for the generation of a discrete transfer function from the continuous controller transfer function.

- In [29, p. 578 et seqq.], an approximate transformation using numerical integration methods (forward and backward rectangular approximation of integral, trapezoidal approximation of integral) is given. Another approximation, the bilinear transformation with frequency adaptation, is deduced in [11, Section 4.2] and applied in [15, Section 4.3.2].
- In [29, p. 501 et seqq.], the z-transform and corresponding transformation tables are likewise given. A description of this approach is also given in [11, Section 4.4].
- Mapping of poles and zeros of the continuous transfer function to z-domain is described in [11, Section 4.3].

The various possibilities, summarised in Table 5.5, were tested by simulation using a simple PT1-element as control path and a controller containing a proportional, integral and frequency-selective component (Eq. 5.7). The simulation results are shown in Fig. 5.6.

[7] In [28, p. 527] the author states that good approximation results can be achieved for sample times up to $1/20$ of the critical frequency.

Table 5.5: Controller transfer functions in z-domain

Method	$p \rightarrow z$	$K_S \cdot \frac{p}{p^2+\omega_0^2}$ in z-domain
Forward difference approximation	$p \rightarrow \frac{z-1}{T_p}$	$K_S T_p \cdot \frac{z-1}{z^2-2z+1+\omega_0^2 T_p^2}$
Backward difference approximation	$p \rightarrow \frac{z-1}{T_p \cdot z}$	$K_S T_p \cdot \frac{z^2-z}{z^2 \cdot \left(1+\omega_0^2 T_p^2\right)-2z+1}$
Bilinear transformation[a]	$p \rightarrow \frac{2}{T_p} \cdot \frac{z-1}{z+1}$	$\frac{\frac{K_S T_p}{2} \cdot \left(z^2-1\right)}{z^2 \cdot \left(\left(\frac{\omega_0 T_p}{2}\right)^2+1\right)+2z \cdot \left(\left(\frac{\omega_0 T_p}{2}\right)^2-1\right)+\left(\left(\frac{\omega_0 T_p}{2}\right)^2+1\right)}$
Bilinear transformation with frequency adapttion	$\frac{p}{\omega_0} \rightarrow \frac{1}{\tan\frac{\omega_0 T_p}{2}} \cdot \frac{z-1}{z+1}$	$\frac{K_S \sin(\omega_0 T_p)}{2\omega_0} \cdot \frac{z^2-1}{z^2-2 \cdot z \cdot \cos(\omega_0 T_p)+1}$
Z-transform with 0-order hold element	$G_z(z) = \frac{z-1}{z} \cdot Z\left\{\frac{G_p(p)}{p}\right\}$	$\frac{K_S \sin(\omega_0 T_p)}{\omega_0} \cdot \frac{z-1}{z^2-2 \cdot z \cdot \cos(\omega_0 T_p)+1}$
Pole-zero-mapping	$p_{1,2} = -\delta \pm j\omega \rightarrow z_{1,2} = e^{T_p(-\delta \pm j\omega)}$	$K_S T_p \cdot \frac{z^2-1}{z^2-2 \cdot z \cdot \cos(\omega_0 T_p)+1}$

[a] Tustin transformation, trapezoidal approximation.

The best control result is achieved using pole-zero-mapping method. If this method is used, the transient oscillation will reduce even faster than with a continuous controller. The bilinear transformation methods and the z-transform with zero-order hold element result also in good control performance. The only two methods obviously unemployable are the two difference approximation methods, as they cause a permanent control deviation.

The pole-zero-mapping method was used to implement discrete current controllers in the Simulink®model. The current control transfer function is described by Eq. 5.37. The integral element of the controller was approximated using backward difference approximation; the additional unit delay of one sample period represents the computation time demand of a controller implemented on a DSP.

$$G_{C,i,fsc}(z) = z^{-1} \cdot \left(K_P + K_I T_p \cdot \frac{z}{z-1} + K_S T_p \cdot \frac{z^2-1}{z^2-2 \cdot z \cdot \cos(\omega_0 T_p)+1} \right) \tag{5.37}$$

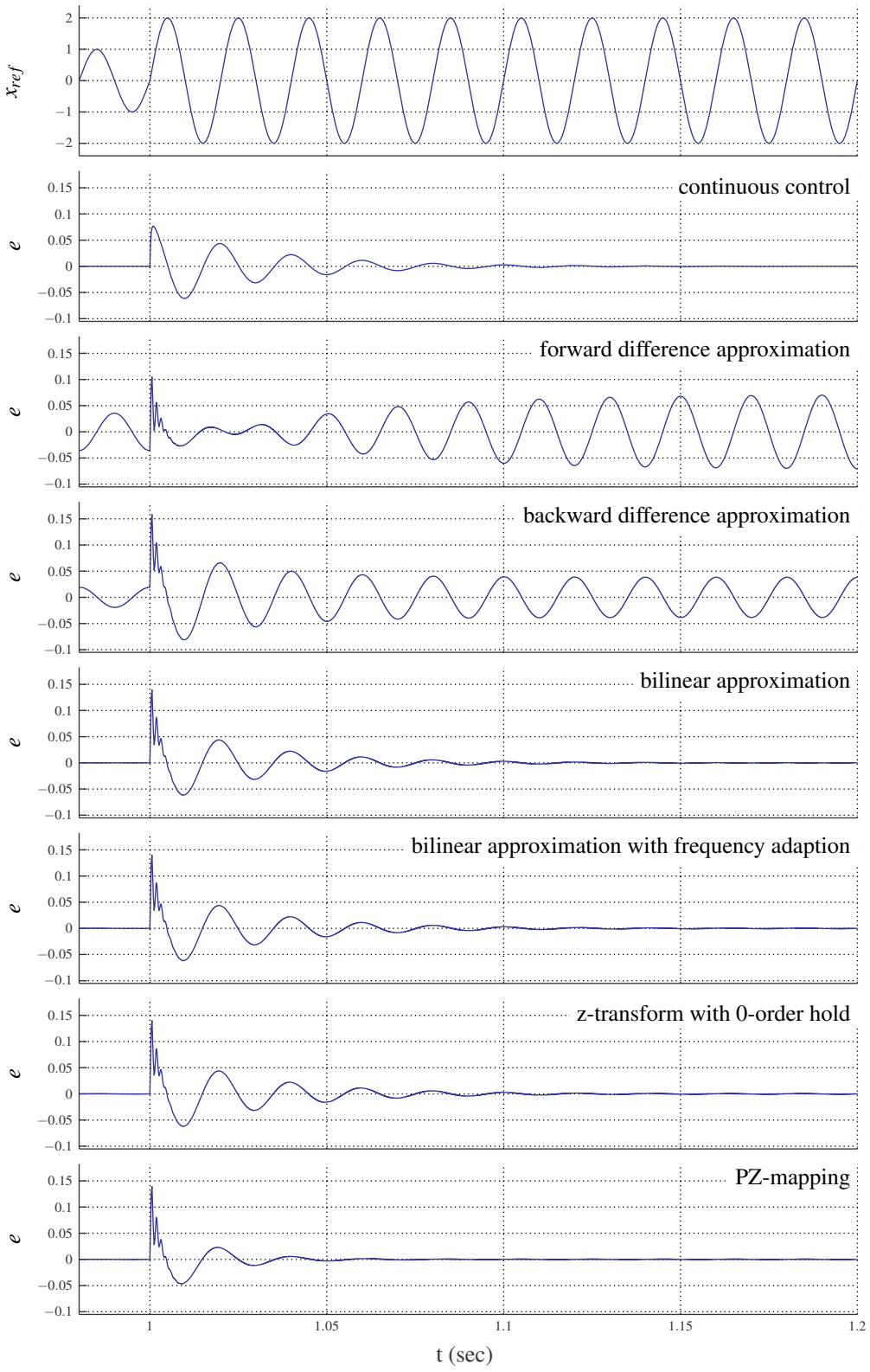

Figure 5.6: Results of different discretisation methods of frequency-selective controller: x_{ref} reference value; e: control deviations

Stability of the discrete control loop The stability of the control loop with discrete controller was analysed using a simplified transfer function of the control path: for the rotor-side control Eq. 3.23 was used and for the grid-side control Eq. 3.53. These equations are of the same type:

$$G_i(p) = \frac{1}{R + p \cdot L} \tag{5.38}$$

and are transferred to z-domain using z-transformation with zero-order hold element (Eqs. 5.39 – 5.41). The approach is described in [29, p. 530 et seqq.] and transformation tables can be found in [29, p. 512 et seqq.].

$$G_i(z) = \frac{z-1}{z} \cdot Z\left\{\frac{G_i(p)}{p}\right\} \tag{5.39}$$

$$= \frac{z-1}{z} \cdot Z\left\{\frac{1}{p \cdot (R + p \cdot L)}\right\} \tag{5.40}$$

$$= \frac{1}{R} \cdot \frac{1 - e^{-T_p \cdot \frac{R}{L}}}{z - e^{-T_p \cdot \frac{R}{L}}} \tag{5.41}$$

Using Eqs. 5.37 and 5.41, the open loop transfer function to be analysed is:

$$G_{0,fsc}(z) = \left(K_P + K_I T_p \cdot \frac{z}{z-1} + K_S T_p \cdot \frac{z^2 - 1}{z^2 - 2 \cdot z \cdot \cos(\omega_0 T_p) + 1}\right) \cdot \frac{1}{R} \cdot \frac{1}{z} \cdot \frac{1 - e^{-T_p \cdot \frac{R}{L}}}{z - e^{-T_p \cdot \frac{R}{L}}} \tag{5.42}$$

The system will be stable if all poles of $1 + G_0$ are located inside the unit circle, that is, if all magnitudes are < 1. This was checked using the Matlab®-function "roots". The poles and zeros of the rotor-side and grid-side closed current control loops are depicted in Figs. E.15 and E.16 respectively. All poles and zeros are located inside the unit circle, but some are very close to the stability limit.

5.7 Limitation of the current controllers

The implementation of the suggested control transfer functions in a DSP would involve a limitation of all hold elements because of data-type constraints and therefore would imply a limitation of all controller output values. Additionally, the maximum converter voltages are limited by the DC-link voltage. These two limitations are included in the model on which this chapter is based. The current control transfer functions are simulated using individual sample-and-hold elements, where each is limited by a saturation-element. In addition, the limitation scheme of the field-oriented current controllers is deployed: the outputs of the two current controllers are converted to amplitude and phase, the amplitude is limited and afterwards the set values are converted back to α- and β-components.

5.8 Frequency-selective control with PN-reference value calculation (FSC(PN))

In the static coordinate system in which this control strategy is implemented, the positive-sequence and the negative-sequence current components are both alternating quantities oscillating at grid frequency. Thus, it is possible to control positive-sequence and negative-sequence d- and q-components using only two frequency-selective controllers. To get well-defined negative-sequence current components, it is necessary to add reference values for these components in the static (stator-oriented) $\alpha\beta$-coordinate system. This can be done using the reference value calculation described in Chapter 4: the reference values for the negative-sequence rotor currents $i_{rsc,n,dq,ref}$ are calculated according to Eq. 4.31 and the reference values for the negative-sequence current components of the grid-side inverter $i_{gsc,n,dq,ref}$ are calculated according to Eq. 4.53. These negative-sequence reference values are defined in a rotating coordinate system and have to be transferred to the static coordinate system. In the static coordinate system, negative-sequence and positive-sequence reference values can be added. The modified control schemes for rotor-side and grid-side frequency-selective control are given in Figs. 5.7 and 5.8 respectively. The block designated "$G_{C,rsc,i}(p) - \underline{i}_{rsc}$-controller" in Fig. 5.7 contains two frequency-selective controllers and a decoupling structure as shown in Fig. 5.3. The block designated "$G_{C,gsc,i}(p) - \underline{i}_{gsc}$-controller" in Fig. 5.8 refers to two frequency-selective controllers as shown in Fig. 5.5. To calculate the negative-sequence reference values it is necessary to know $i_{s,pn,dq}$, $i_{rsc,pn,dq}$, $v_{s,pn,dq}$ and $v_{rsc,pn,dq}$. In the simulations on which this chapter is based, these values are calculated using the DSOGI-filter described in Section 4.1.8. The modified control scheme necessitates an adaptation of the controller parameters. Starting from the control parameters defined in Sections 5.4 and 5.5, some of the control parameters are slightly changed to reduce oscillations of the machine active and reactive power. The control parameters as well as the filter quality factors of the DSOGI-filters are listed in Table D.5.

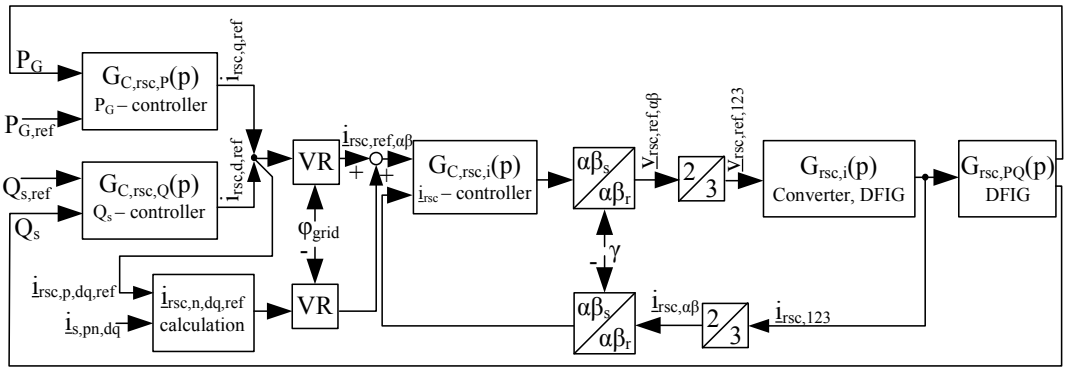

Figure 5.7: Rotor-side control scheme with frequency-selective current controllers and calculation of negative-sequence reference values

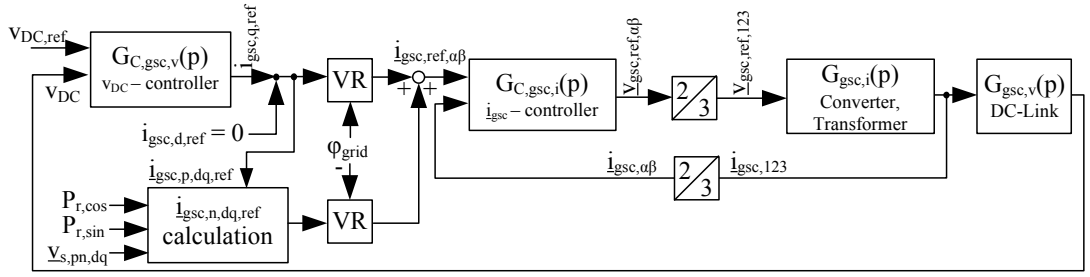

Figure 5.8: Grid-side control scheme with frequency-selective current controllers and calculation of negative-sequence reference values

5.9 Simulation results of frequency-selective control and frequency-selective control with negative-sequence reference specification

Simulation results of the frequency-selective control scheme are given in Fig. 5.9 for the following conditions:

- grid-side and rotor-side frequency-selective current control,
- use of related quantities,
- $n = 1.08 \cdot n_{s=0}$,
- $t = 1\,\mathrm{s} - 2\,\mathrm{s}$: 2-phase dip on the grid-side of the main transformer to 95% remaining voltage,
- $t = 3\,\mathrm{s}$ – step from $v_{DC,ref} = v_{DC,nom}$ to $v_{DC,ref} = 1.025 \cdot v_{DC,nom}$,
- $t = 4\,\mathrm{s}$ – step from $P_{G,ref} = P_{G,nom}$ to $P_{G,ref} = 0.75 \cdot P_{G,nom}$,
- $t = 5\,\mathrm{s}$ – step from $Q_{G,ref} = 0\,\mathrm{kVAr}$ to $Q_{G,ref} = 0.0625 \cdot [P_{G,nom}]\mathrm{kVAr}$.

Again, comparison with the field-oriented control results of Fig. 3.9 shows that the frequency-selective current controllers restrain the oscillations on the rotor currents as well as the asymmetry of the line currents. Also, the oscillation of the electrical torque of the generator is reduced. Nevertheless, the influence of the control on power and DC-link voltage is very limited, which is probably due to the fact that no reference values for the negative-sequence current components are taken into account. Thus, the frequency-selective current controllers try to force the negative-sequence current components to zero, and this is not the same thing as smooth power and DC-link voltage. The control scheme can be improved by setting reference values also for the negative-sequence current components as described in the previous section (FSC(PN)). Simulation results generated by this modified control scheme are given in Fig. 5.10. Here, the line currents contain higher negative-sequence components during asymmetrical dips, but active power, electrical torque and DC-link voltage oscillation are reduced significantly.

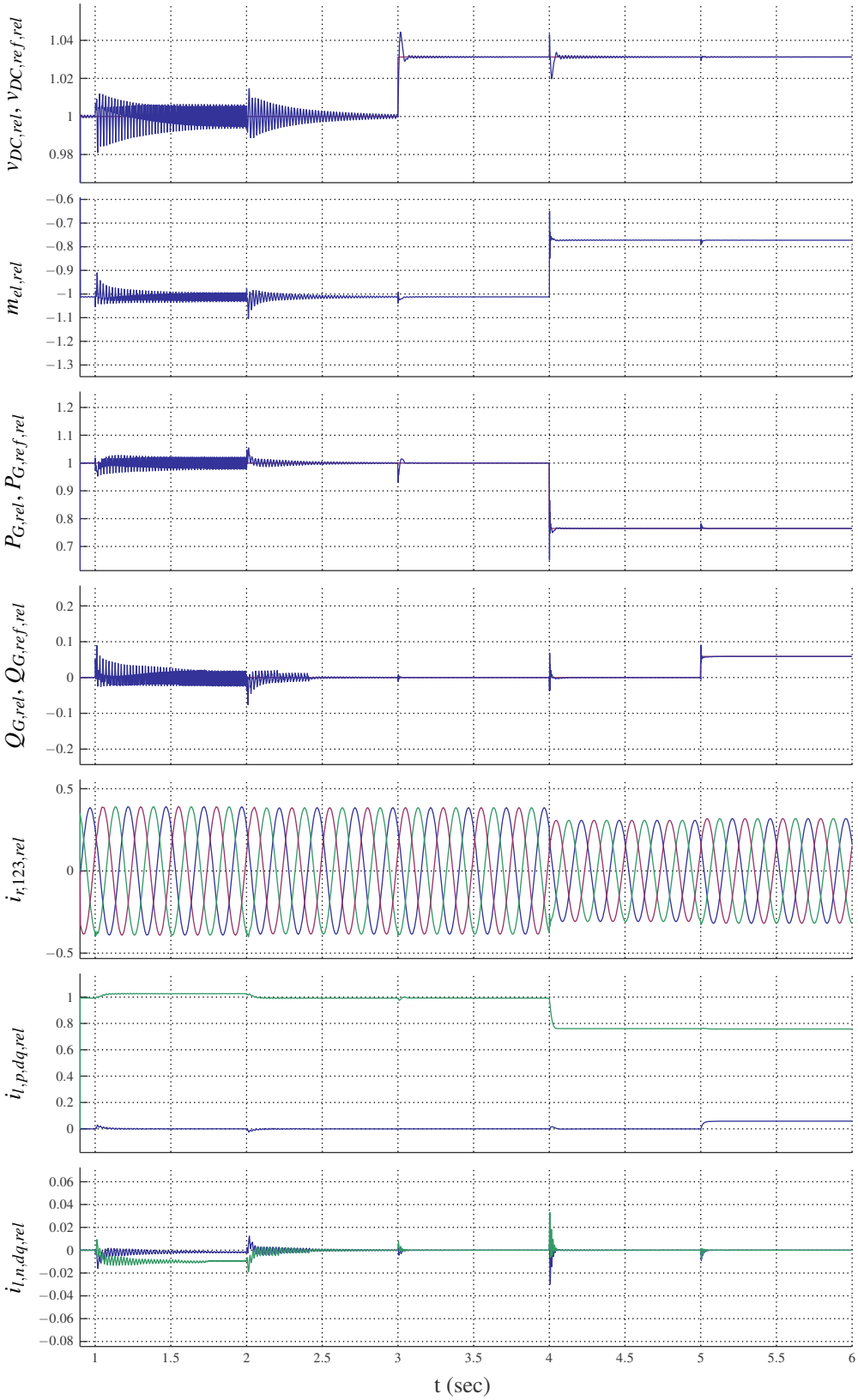

Figure 5.9: FSC results, 2-phase dip to 95% remaining voltage and step responses of power and DC-link voltage, discrete simulation of current controllers

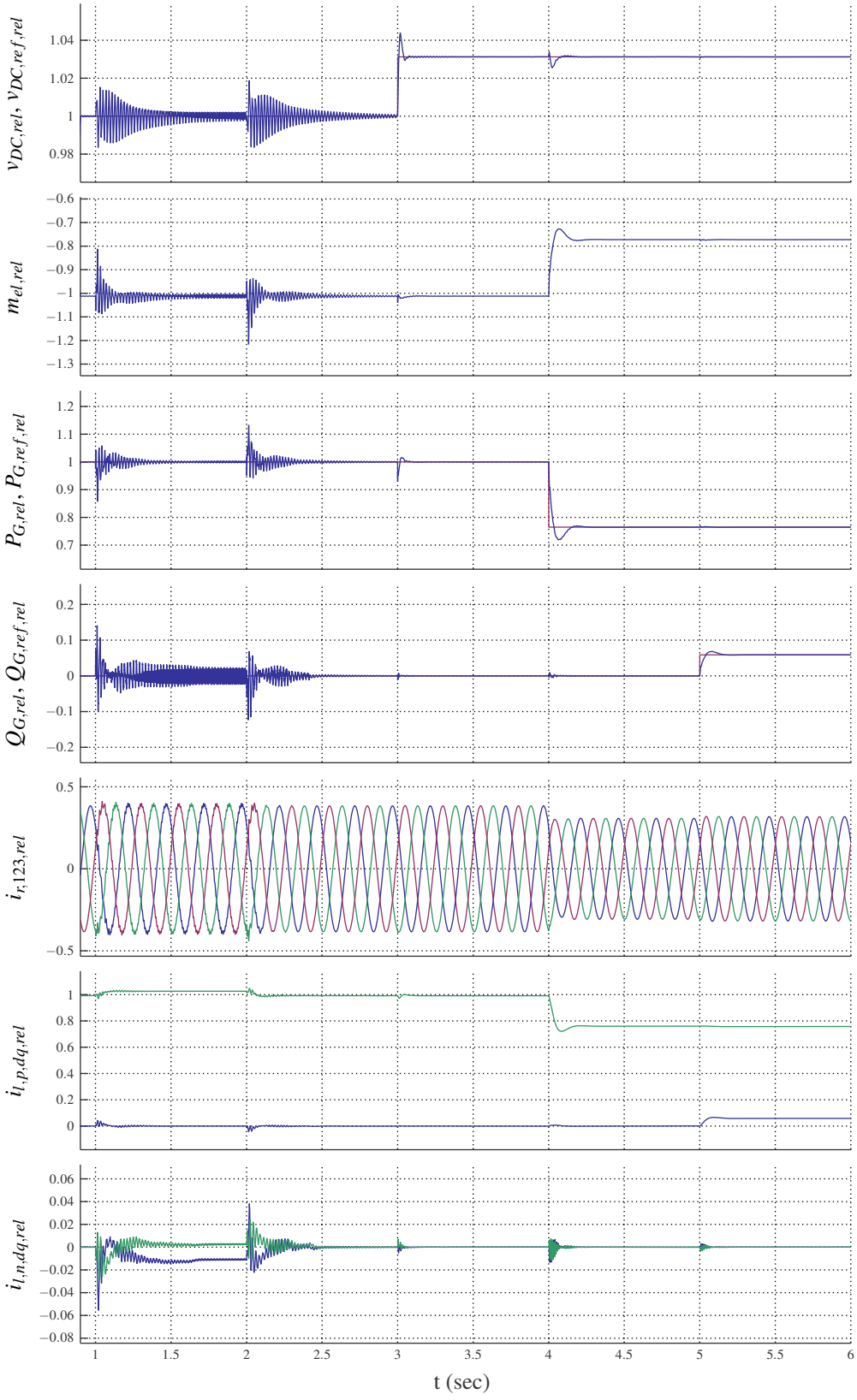

Figure 5.10: FSC(PN) results, 2-phase dip to 95% remaining voltage and step responses of power and DC-link voltage, discrete simulation of current controllers

6 Comparison of the different control possibilities

In the three previous chapters four control strategies for the inverter currents of a doubly-fed induction generator were presented. The nature of the control achieved by each of these strategies is compared in Section 6.1. Then, in Section 6.2, the different control possibilities are systematised.

6.1 Comparison of the four control schemes analysed

To compare the performance of the four types of control of the DFIG, i.e. field-oriented control, PN-control[1], frequency-selective control and FSC(PN)-control, several simulations were carried out. Each control scheme was tested by simulation of grid voltage situations with the following specifications:

- 2-phase voltage dip down to a remaining voltage of 95% of the nominal voltage, $n = 1.08 \cdot n_{s=0}$ (setting 1), $n = n_{s=0}$ (setting 2) and $n = 0.92 \cdot n_{s=0}$ (setting 3),
- 2-phase voltage dip down to a remaining voltage of 80% of the nominal voltage, $n = 1.08 \cdot n_{s=0}$ (setting 4) and $n = 0.92 \cdot n_{s=0}$ (setting 5),
- 2-phase voltage dip down to a remaining voltage of 50% of the nominal voltage, $n = 1.08 \cdot n_{s=0}$ (setting 6) and $n = 0.92 \cdot n_{s=0}$ (setting 7),
- 1-phase voltage dip down to a remaining voltage of 50% of the nominal voltage, $n = 1.08 \cdot n_{s=0}$ (setting 8) and $n = 0.92 \cdot n_{s=0}$ (setting 9),
- 2-phase voltage dip as shown in Fig. 6.1, $n = 1.08 \cdot n_{s=0}$ (setting 10) and $n = 0.92 \cdot n_{s=0}$ (setting 11).

To evaluate the behaviour of the system with different control schemes, close attention was given to the following variables:

- the height of the torque peak during dip start – more precisely, the difference between maximum and minimum torque, related to nominal torque ($\Delta m_{el,rel}$),
- the energy consumed by the brake chopper – related to the nominal energy of the generator generated during half a grid cycle ($E_{BC,rel}$),

[1] The PN-control scheme was tested using notch-filters and calculating the grid-side current reference values according to Eqs. 4.49 – 4.53.

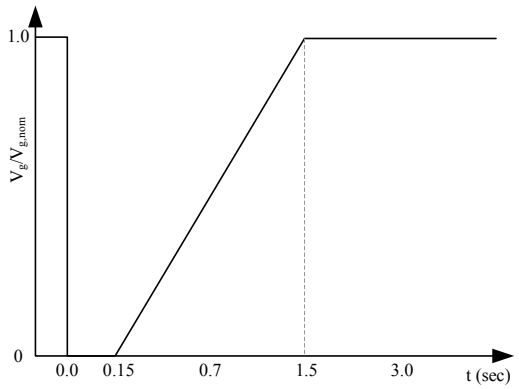

Figure 6.1: Dip voltage curve

and for long term voltage dips (settings 1 – 9) also:

- the steady-state oscillation (difference between maximum and minimum) of the electrical torque ($m_{el,\Delta,rel}$),
- the steady-state oscillation (difference between maximum and minimum) of active and reactive power – related to the nominal power ($P_{G,\Delta,rel}$, $Q_{G,\Delta,rel}$),
- the steady-state oscillation (difference between maximum and minimum) of the DC-link voltage – related to 10% of the nominal DC-link voltage ($v_{DC,\Delta,rel}$) and
- the amplitude of the negative-sequence line current components – related to the nominal line current ($I_{l,n,rel}$).

Here are examples of the results: for setting 1 and setting 7, in Figs. 6.2 and 6.3 respectively. The results of all other settings are given in Appendix E in Figs. E.17 – E.24. The figures

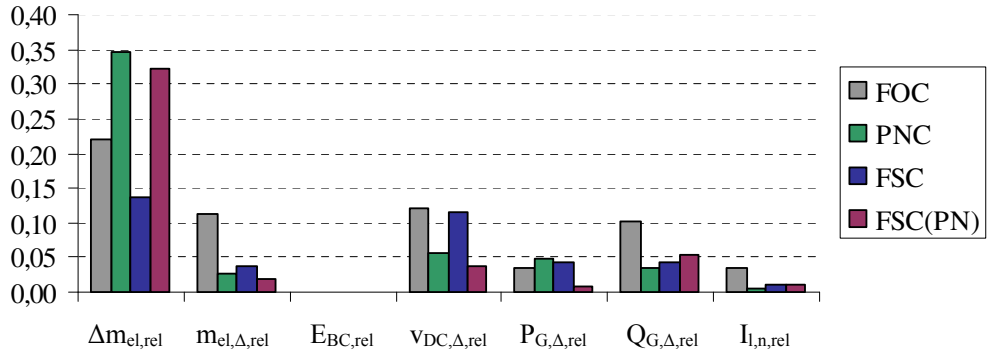

Figure 6.2: Comparison of simulation results with different control strategies, 2-phase voltage dip down to 95% remaining voltage, $n = 1.08 \cdot n_{s=0}$ (setting 1)

overall show that during slight asymmetrical voltage dips all three alternative control strategies

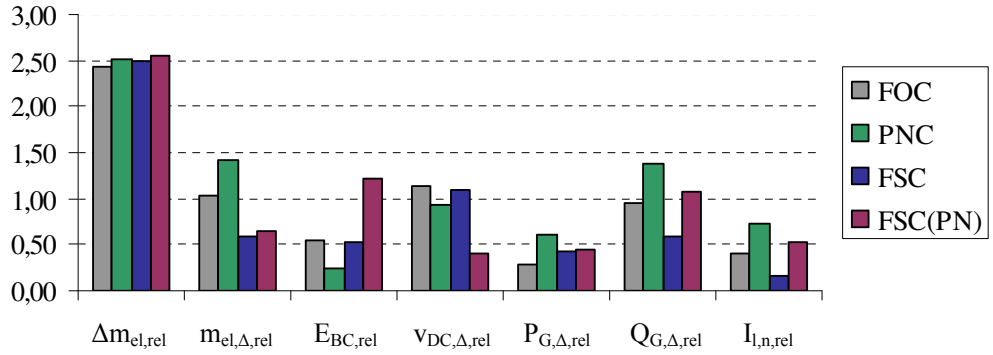

Figure 6.3: Comparison of simulation results with different control strategies, 2-phase voltage dip down to 50% remaining voltage, $n = 0.92 \cdot n_{s=0}$ (setting 7)

reduce the degree of oscillation of the electrical torque as well as of the DC-link voltage during "dip-steady-state". The initial torque peaks during dip start are not reduced, perhaps even increased, which may be caused by the different current control dynamics. The differences between the control strategy results decrease with increasing dip-depth (Figs. E.21 and 6.3), this is explainable by the limited controllability described in Section 4.4. The energy dissipation of the brake chopper is not reduced by the alternative control strategies, in some cases it is increased.

Remarkably, the simulation results show that the oscillation of the generator active power will increase in many cases, even if torque and DC-link voltage oscillations are reduced. As the machine speed is fixed, one would expect a positive correlation between torque and active power oscillation. As expected, an analysis of rotor- and stator power showed that the sum of both will contain less oscillation if the torque oscillation is reduced. But the oscillation of the stator power is increased (compensating the major oscillation of the rotor power). Because the voltages of the inverters are limited, this increase cannot be compensated completely by the grid-side inverter, resulting in an increase of overall power oscillation.

6.2 Systematisation of different control possibilities

In this section the possible control strategies are outlined using a three-phase converter as basic control path. The DC-link voltage is assumed to be constant. The control path can be described by one PT1-element representing the filter inductance and resistance and a second PT1-element approximating the delay of the converter:

$$G(p) = \frac{1}{R + p \cdot L} \cdot \frac{1}{1 + p \cdot T_p} \tag{6.1}$$

The currents to be controlled alternate at grid frequency.

6.2.1 Current control in different coordinate systems

In principle, the currents can be controlled in a static coordinate system (currents represented by alternating $\alpha\beta$-components) or in a rotating coordinate system (currents represented by direct dq-components). It is possible to control the positive-sequence components (d-component and q-component) or to control positive-sequence and negative-sequence components (pd-, pq-, nd-, nq-component) separately. This allows for different combinations, which are outlined in this section. No decoupling algorithms are considered here, these are described in Section 6.2.2.

Two PI-controllers in rotating coordinate system (PI-P)[2] Two PI-controllers are used to control d- and q-components in a coordinate system rotating with grid frequency: the current components being controlled are thus direct quantities. It is possible to implement a decoupling algorithm so that active (q-component) and reactive (d-component) currents can be controlled independently. The set values of the individual PI-controllers can be limited, as can the amplitude of the set values ($\sqrt{v_d^2 + v_q^2}$). The transfer function of the current controllers is:

$$G_C = K_{P,PI} + K_{I,PI} \cdot \frac{1}{p} \tag{6.2}$$

The structure of this control scheme is shown in Fig. 6.4.

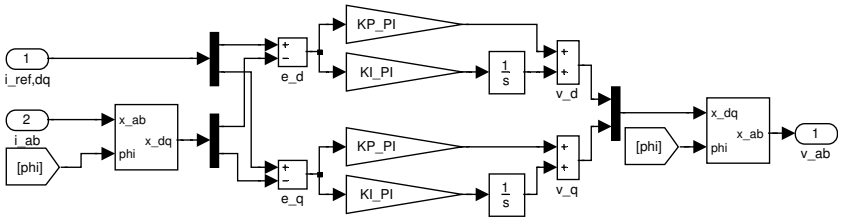

Figure 6.4: Conventional PI-controllers without decoupling

Four PI-controllers in two different rotating coordinate systems (PI-PN) In [15, p. 29] a control scheme for positive-sequence and negative-sequence components is described. The structure of this scheme is given in Fig. 6.5. It contains four proportional-integral current controllers, two of which act in a coordinate system rotating with grid frequency (positive-sequence current controllers for pd-component and pq-component) and the other two of which act in a coordinate system rotating with grid frequency in the opposite direction (negative-sequence current controllers for nd-component and nq-component). The control deviation is calculated in the static coordinate system ($\alpha\beta$-components) and then transferred to the two rotating coordinate

[2]The abbreviation PI-P refers to the control of the positive-sequence current components. The controllers will also respond to negative-sequence current components, but are not designed to control them in a purposeful way.

systems. The two set values ($\alpha\beta$-components) are built as sum of the positive-sequence and negative-sequence set values in the static coordinate system. The transfer function of one individual current component controller is identical to Eq. 6.2, though the control parameters can differ. With this control scheme the four controllers cause a coupling between positive-sequence and negative-sequence components because in the positive-sequence coordinate system the negative-sequence components appear as alternating quantities with double grid frequency (and the other way round).

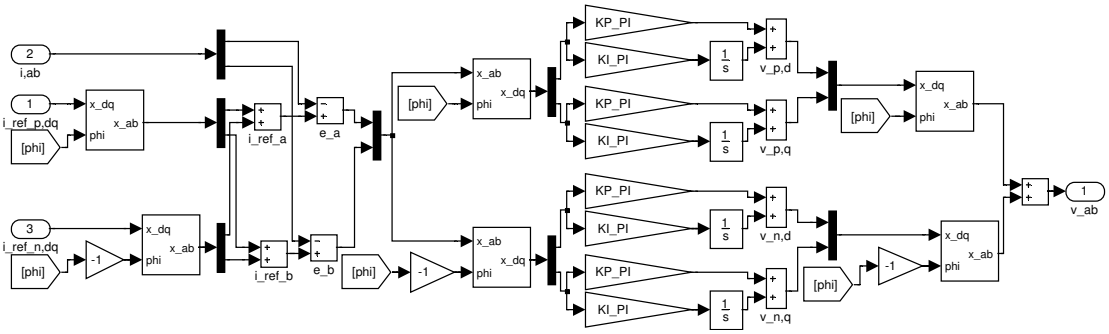

Figure 6.5: Two PI-controllers for positive-sequence components, two PI-controllers for negative-sequence components

Four PI-controllers in two different rotating coordinate systems with filtering of the current components (PNC) It is from PI-PN-control scheme (described immediately above) that the control scheme described in Chapter 4 is developed, with the introduction of a filter algorithm to calculate positive-sequence and negative-sequence current components. The aim is to achieve control without coupling between positive-sequence and negative-sequence components. The effectiveness of the decoupling is limited by the quality of the filter algorithm. Furthermore, the filter algorithm introduces a delay to the control path, so that the control parameters have to be adapted. The control deviations are calculated in the two rotating coordinate systems individually. Fig. 6.6 shows the structure of this control scheme.

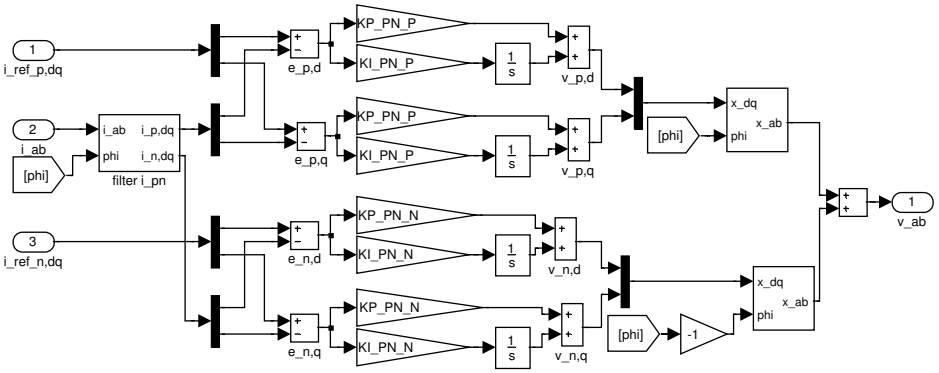

Figure 6.6: PN-control scheme with filtering of current components

Two PIS-controllers in a rotating coordinate system (PI-NFSC) Another possible way of controlling positive-sequence and negative-sequence current components is to add a frequency-selective component to the conventional PI-controllers. This structure is called PIS-controller (proportional-integral-sine) in [13] or PI-R-controller (proportional-integral-resonant) in [18]. Fig. 6.7 shows the control structure with specified reference values for the negative-sequence components. If these reference values are omitted, the controller will try to force the negative-sequence current components to zero. The transfer function of one individual current controller is:

$$G_C = K_{P,PINFSC} + K_{I,PINFSC} \cdot \frac{1}{p} + K_{S,PINFSC} \cdot \frac{p}{p^2 + (2 \cdot \omega_0)^2} \tag{6.3}$$

This type of control structure could also be deduced from a transformation of the n-sequence controllers of the PI-PN control scheme to the positive-sequence coordinate system. This transformation is given in Appendix C.3.2. It induces a coupling term between the two current controllers. If this term is omitted, one will obtain the transfer function given above in Eq. 6.3.

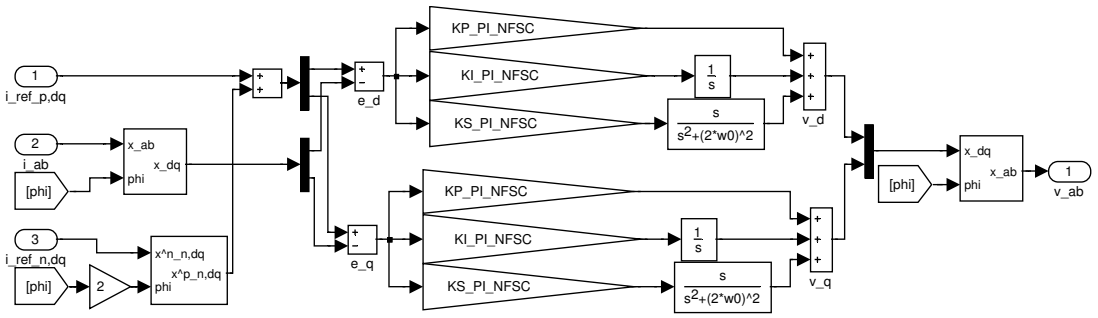

Figure 6.7: Conventional PI-control scheme, supplemented by frequency-selective component for negative-sequence current components

Two FS-controllers in a static coordinate system (FSC(PN)) The transformation of the PI-PN-control scheme to the static coordinate system is described in [15] and is given in Appendix C.3.1. It results in two frequency-selective controllers ($\alpha\beta$-components). This control strategy was described in detail in Section 5.8 as applied to the control of a DFIG and its structure is depicted in Fig. 6.8. The transfer function of one individual controller is:

$$G_C = K_{P,FSC} + K_{I,FSC} \cdot \frac{1}{p} + K_{S,FSC} \cdot \frac{p}{p^2 + \omega_0^2} \tag{6.4}$$

If the structure of Fig. 6.5 – without decoupling algorithm – is used for the transformation, the two control schemes PI-PN and FSC(PN) will be mathematically identical with the following

relations:

$$K_{P,FSC} = 2 \cdot K_{P,PI} \tag{6.5}$$

$$K_{I,FSC} = 0 \tag{6.6}$$

$$K_{S,FSC} = 2 \cdot K_{I,PI} \tag{6.7}$$

The α- and β-components are not coupled in this control strategy. The active current component and the reactive current component (d- and q-components) are, however, coupled.

Different possible ways of limiting the output of the frequency-selective controllers exist:

- limitation of the amplitude of the set values ($\sqrt{v_\alpha^2 + v_\beta^2}$),
- limitation of the individual integrating elements (one frequency-selective component contains two integrators),
- limitation of the control deviation, possibly only for the frequency-selective components.

For the simulations on which Chapter 5 is based, a combination of the first two limitation methods was used.

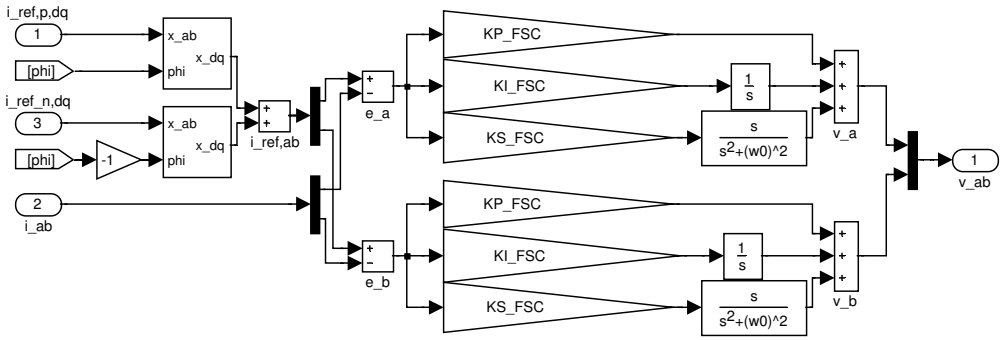

Figure 6.8: Frequency-selective controllers in static coordinate system

6.2.2 Decoupling algorithms

The control strategies described above can be complemented by means of decoupling algorithms to achieve independent control of positive-sequence d- and q-components and, accordingly, the active and reactive current. Decoupling algorithms for PI-controllers in a rotating coordinate system (PI-P) are:

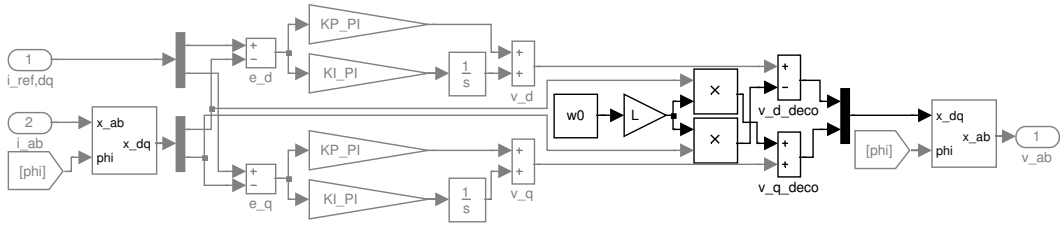

Figure 6.9: Decoupling structure using current values

Decoupling using the actual current values (*i*-decoupling) This decoupling algorithm is deduced in Section 3.2.1. The equivalent Simulink®structure is depicted in Fig. 6.9. One drawback of this algorithm is that the actual current values are measured and therefore contain measurement noise. The decoupling algorithm introduces this noise to the controller and thus to the set values of the controller.

Decoupling using the current reference values (i_{ref}-decoupling) To avoid this drawback, the reference values of the current components could be used. The corresponding Simulink®structure is shown in Fig. 6.10.

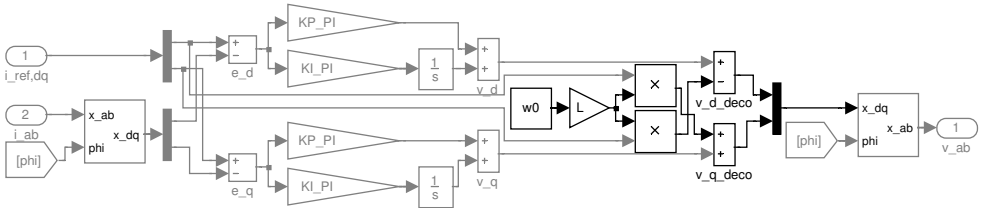

Figure 6.10: Decoupling structure using current reference values

Decoupling using the controller set values (*v*-decoupling) Another possibility is to use the set values of the controller. This algorithm is described in [34, p. 49] (amongst others) and is depicted in Fig. 6.11. The current i of the decoupling term $i \cdot \omega_0 \cdot L$ is replaced by

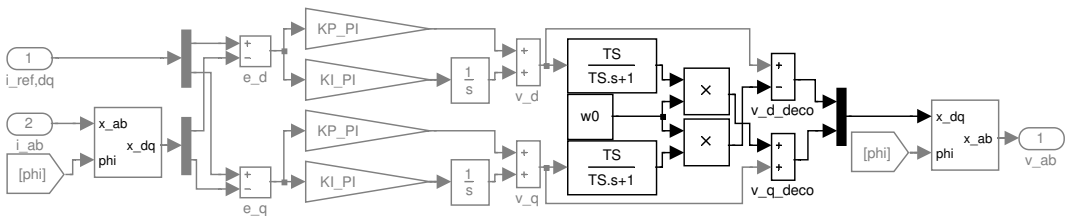

Figure 6.11: Decoupling structure using controller set values

$$
\begin{aligned}
i &= \frac{v}{R + L \cdot p} \\
&= \frac{v \cdot 1/R}{1 + T_\sigma \cdot p}
\end{aligned}
\tag{6.8}
$$

with $T_\sigma = L/R$. The decoupling term can thus be rewritten as

$$
i \cdot \omega_0 \cdot L = \frac{v \cdot \omega_0 \cdot T_\sigma}{1 + T_\sigma \cdot p} \tag{6.9}
$$

Results of the different decoupling algorithms are shown in Fig. 6.12. A step in the reference value of i_d was used as test signal. The control path contains two PT1-elements (one representing the inverter delay, one representing R and L). The step responses and the behaviour of the current q-components are depicted.

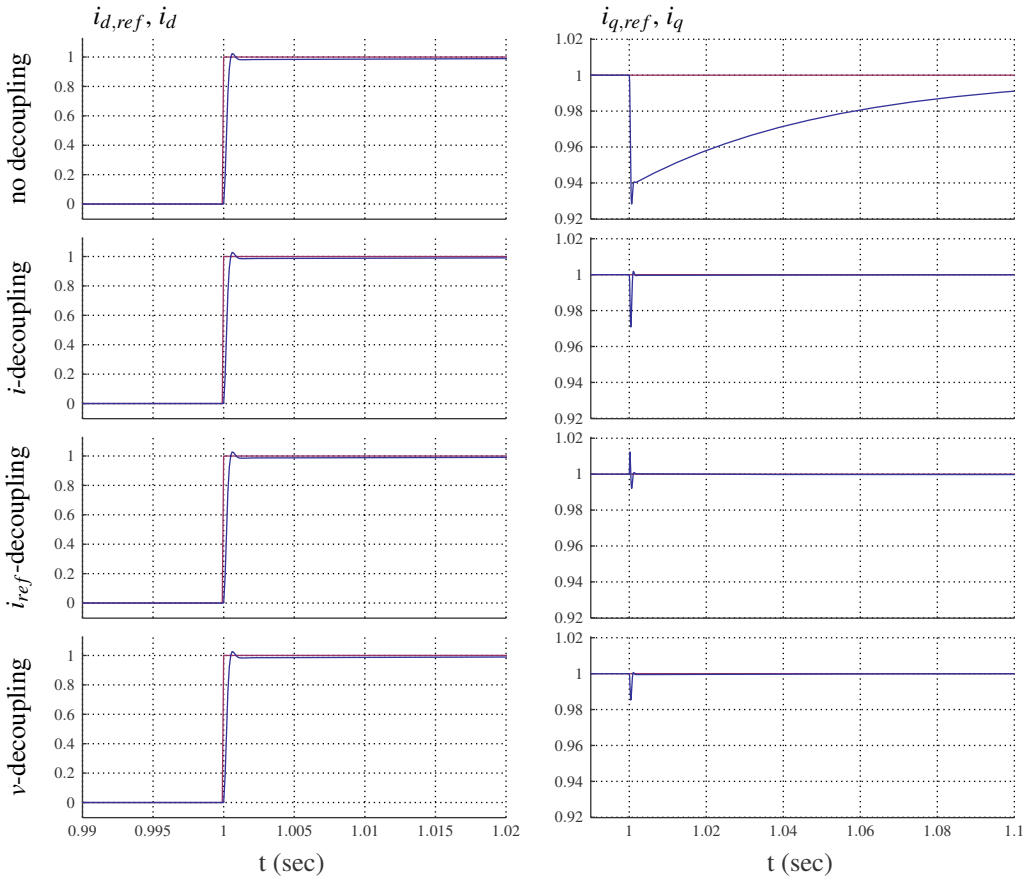

Figure 6.12: Simulation results of PI-control with different decoupling algorithms

All three algorithms cause a nearly complete decoupling[3] of the two current components. Because the first algorithm (i-decoupling) may be sensitive to measurement noise, i_{ref}- or v-decoupling will be preferable for implementation in a real setup. Moreover, the latter strategy can also be used together with the PI-NFSC control scheme. It results in a (nearly) complete

[3]The remaining small coupling visible in Figs. 6.12 and 6.14 is caused by the fact that the decoupling algorithms do not include the delay of the inverter.

decoupling of active and reactive positive-sequence currents. The simulation results of PI-NFSC with and without *v*-decoupling algorithm are given in Fig. 6.14.

A transformation of this decoupling algorithm to the static coordinate system (applicable for FSC) results in the structure shown in Fig. 6.13. Despite the decoupling structure, this scheme causes a coupling of positive-sequence d- and q-component because the transformation of the PI-NFS-controller to the static coordinate system does not yield exactly the FS-controller but adds a coupling component. The transformation result is given in Appendix C.3.4. The remaining coupling could be compensated by an additional decoupling term. Alternatively, it is possible to transfer the complete scheme, containing PI-NFSC and *v*-decoupling algorithm, to the static coordinate system.

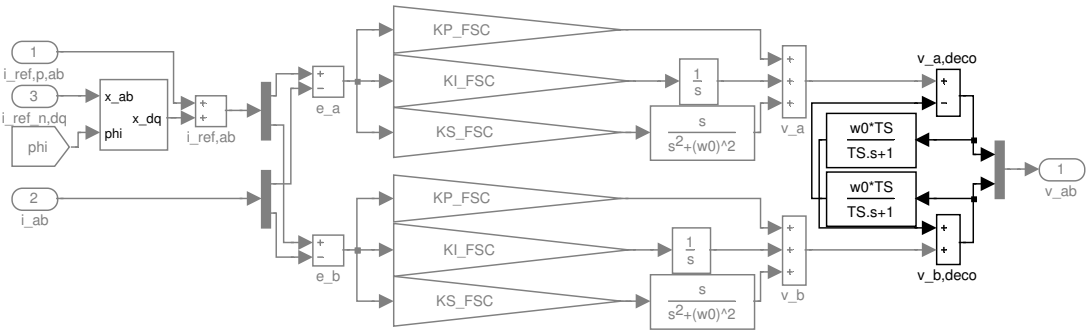

Figure 6.13: Equivalent *v*-decoupling structure for FSC

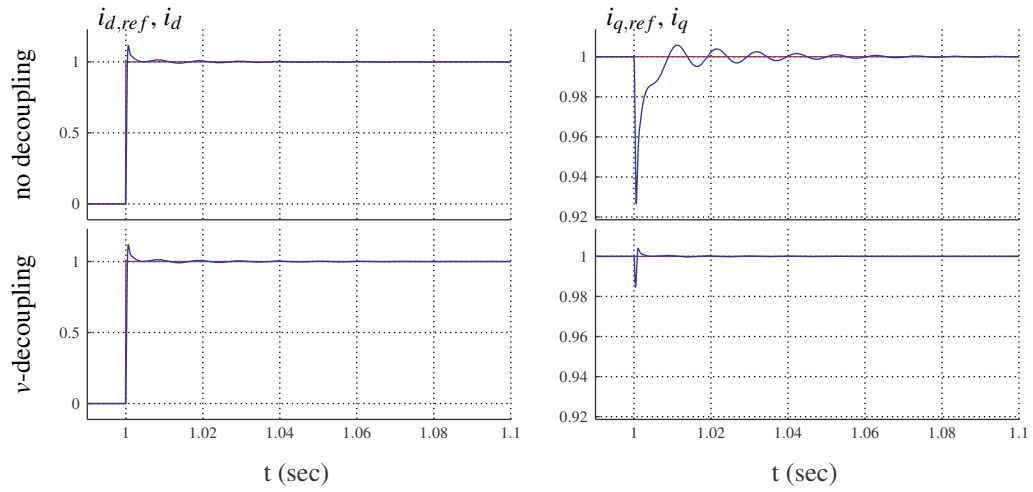

Figure 6.14: Simulation results of PI-NFSC with and without *v*-decoupling algorithm

Table 6.1 summarises the possible control strategies and the applicable decoupling algorithms.

Table 6.1: Basic control strategies

Control scheme	Control of p-components	Control of n-components	Decoupling of p-components possible?
PI-P	In p-CS	No	Nearly complete decoupling: with *i*- or *v*-algorithm, incomplete decoupling with i_{ref}-algorithm
PI-PN	In p-CS	In n-CS	Slight coupling remains, due to the negative-sequence current controllers
PNC	In p-CS	In n-CS	Slight coupling remains, due to the negative-sequence current controllers
PI-NFSC	In p-CS	In p-CS	Nearly complete decoupling: with *v*-algorithm
FSC(PN)	In $\alpha\beta$-CS	In $\alpha\beta$-CS	Slight coupling remains (with transferred *v*-algorithm), nearly complete decoupling is possible using transfer function C.124.

7 Summary and Outlook

In this study, four strategies for controlling the inverter currents of a doubly-fed induction generator (DFIG) system are described, each of which can be varied. There is also given a description of the main variations. An overview is given in Fig. 7.1. Simulation with Matlab/Simulink®was

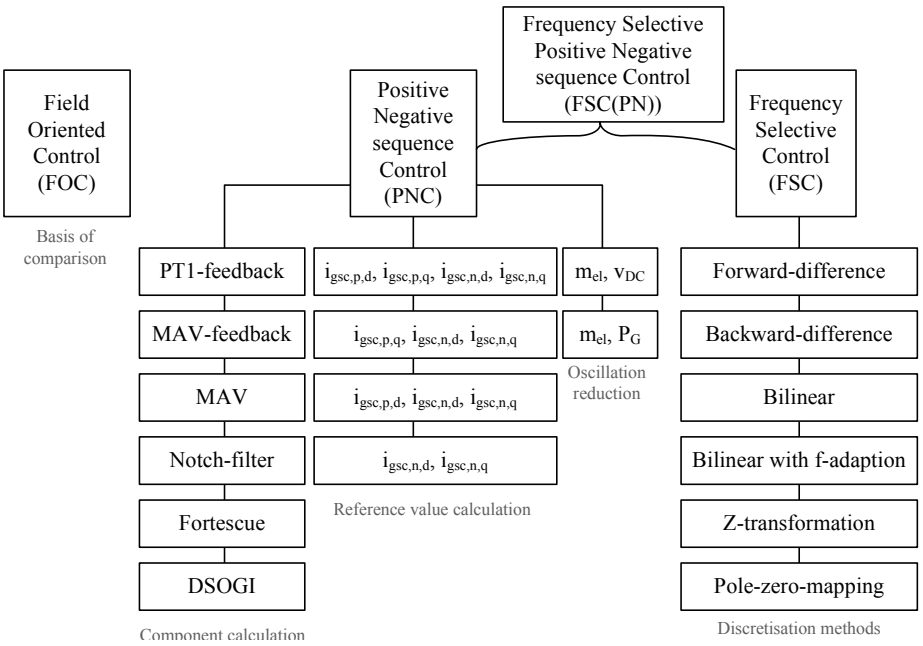

Figure 7.1: Overview: analysed control strategies

employed to test the strategies and evaluate their ability to reduce torque, DC-link voltage and active power oscillations during asymmetrical voltage dips. The type of control known as field-oriented control (FOC, Chapter 3) is the most common for DFIGs. This serves as basis of comparison within the study. Another strategy described in the literature is positive-negative-sequence control (PNC) and this is analysed in Chapter 4. Frequency-selective controllers (FSC, Chapter 5) constitute a strategy for controlling the doubly-fed induction generator, which has been developed in the present piece of work. In addition, the combination of frequency-selective current controllers with the specification of reference values for the negative-sequence current components (FSC(PN), Section 5.8), also new, is here analysed. Section 6.1 shows that the three control strategies (PNC, FSC, FSC(PN)) which are alternative to field-oriented control have the effect of improving DFIG system behaviour during slight asymmetries (voltage dips down to a remaining voltage of 80%). In all three, the oscillations of the electrical torque as

well as of the DC-link voltage are reduced during "dip-steady-state", whereas the torque peak during the initial transient increases in many cases. Although it is theoretically possible to eliminate torque oscillations completely, this was not achieved in the simulations on which this study is based, because of the nonlinearity of the DFIG's mutual inductance, which is described in Section 4.4.4. In general, the improvements from the use of any of the three alternative control schemes will be subject to the limits described in Section 4.4 for PN-control:

- DC-link voltage and resulting maximum inverter voltages (Section 4.4.1),
- maximum permissible inverter currents (Section 4.4.2),
- computation lag in components and delayed i_{ref}-calculation (PNC, FSC(PN)) (Section 4.4.3),
- the nonlinear behaviour of the system (saturation of mutual inductance of the DFIG, Section 4.4.4).

The main problem in the control of a DFIG system during grid voltage asymmetries is that (very high) rotor voltages (which are induced by the negative-sequence stator voltages and by the transient natural flux) cannot be compensated by the rotor-side inverter. Therefore, the effect of every effort to improve the system's behaviour during asymmetries by modifying the control strategy will be limited. Additional hardware modifications will be necessary if the system is to be able to ride through severe voltage dips. Such adaptations are outlined in Section 1.4.1. Because it is not possible to improve the behaviour of the system during worst-case dips using the proposed alternative control strategies, there should be no reduction in the size or energy dissipation ability of the hardware protecting the DFIG system such as crowbar or brake chopper. The following issues have not been addressed in this study and could be a matter for future research:

- application of the control strategies to a test bench,
- use of superior controllers for negative-sequence stator or line currents,
- application of superior line current controllers during voltage dips to better meet the requirements of grid codes[1].

Even though the proposed control strategies do not substantially improve the behaviour of DFIG systems, they can be applied beneficially to other systems as solar inverters, STATCOMs or full-scale inverters for wind power plants. In these systems, the inverter terminal voltages will drop during grid-voltage dips and therefore will not restrict the controllability of the grid-side inverter currents as much as in a DFIG system. Moreover, in photovoltaic systems or wind power plants using full-scale inverters, the inverter decouples the generator completely from the grid,

[1] Some grid codes specify that accurately defined reactive and/or active current must be fed to the grid during voltage dips in which the amplitude depends on dip-depth.

allowing for an independent control of active and reactive power fed to the grid. The application of different control strategies to such systems is outlined in Section 6.2. Other problems which could be further analysed in respect of the use of the control strategies are:

- application of the control strategies to a full-scale converter system (simulation and test bench) and
- analysis of the FRT-ability of full-scale converter systems which make use of these control strategies.

Bibliography

[1] Abo-Khalil, A.G.; Lee, D.-C.; Jang, J.-I.: *Control of Back-to-Back PWM Converters for DFIG Wind Turbine Systems under Unbalanced Grid Voltage*, In: IEEE International Symposium on Industrial Electronics, p. 2637–2642, 2007

[2] Bundesregierung der BRD: *Verordnung zu Systemdienstleistungen durch Windenergieanlagen (Systemdienstleistungsverordnung - SDLWindV)*, In: BGBl. I, p. 1734 and BGBl. I, p. 1634, 2009

[3] Chen, Z.; Guerrero, J.M.; Blaabjerg, F.: *A Review of the State of the Art of Power Electronics for Wind Turbines*, In: IEEE Transactions on Power Electronics, No. 8, p. 1859–1875, 2009

[4] DENA – Deutsche Energie Agentur GmbH (publisher): *Energiewirtschaftliche Planung für die Netzintegration von Windenergie in Deutschland an Land und Offshore bis zum Jahr 2020*, consortium: DEWI, E.ON Netz, EWI, RWE Transportnetz Strom, VE Transmission, Köln, 2005

[5] DIN – Deutsches Institut für Normung e.V. (publisher): *Elektrische Energietechnik – Modale Komponenten in Drehstromsystemen – Größen und Transformationen (IEC 62428:2008); Deutsche Fassung EN62428:2008*, 2009

[6] DIN – Deutsches Institut für Normung e.V. (publisher): *Zeitabhängige Größen – Teil 3: Komplexe Datstellung sinusförmig zeitabhängiger Größen*, 3rd edition, Berlin, 1994

[7] Dolinar, D.; Pihler, J.; Grčar, B.: *Dynamic Model of a Three-Phase Power Transformer*, In: IEEE Transactions on Power Delivery, No. 4, p. 1811–1819, 1993

[8] Ender, C.; DEWI GmbH (publisher): *Wind Energy Use in Germany – Status 30.06.2011*, In: DEWI Magazin, No. 39, p. 40–49, 2011

[9] E.ON Netz GmbH (publisher): *Netzanschlussregeln: Hoch- und Höchstspannung*, Bayreuth, 2006

[10] Förster, M.: *Untersuchung von verschiedenen Flussmodellen und PLL-Strukturen für die Feldorientierte Regelung einer Doppeltgespeisten Asynchronmaschine: Diplomarbeit*, Technische Universität Ilmenau, 2003

[11] Franklin, G.F.; Powell, J.D.; Workman, M.L.: *Digital Control of Dynamic Systems*, Reading, Massachusetts, Addison-Wesley Publishing Company, 1990

[12] Fukuda, S.; Ryota, I.: *Application of a Sinusoidal Internal Model to Current Control of Three-Phase Utility-Interface Converters*, In: IEEE Transactions on Industrial Electronics, No. 2, p. 420–426, 2005

[13] Fukuda, S.; Yoda, T.: *A Novel Current-Tracking Method for Active Filters Based on a Sinusoidal Internal Model*, In: IEEE Transactions on Industrial Applications, No. 3, p. 888–895, 2001

[14] GWEC – Global Wind Energy Council (publisher): *Annual Market Update 2010*, 2011

[15] Großmann, U.; Petzoldt, J.: *Frequenzselektive Regelung eines parallelen Hybridfilters zur Oberschwingungskompensation in Energieversorgungsnetzen: Dissertation*, Technische Universität Ilmenau, 2006

[16] Happoldt, H.; Oeding, D.: *Elektrische Kraftwerke und Netze*, 5th edition, Springer-Verlag, ISBN 3540083057, 1978

[17] Hau, E.: *Windkraftanlagen: Grundlagen, Technik, Einsatz, Wirtschaftlichkeit*, 4th edition, Springer-Verlag, ISBN 3540721509, 2008

[18] Hu, J.; He, Y.; Xu, L.; Williams, B.W.: *Improved Control of DFIG Systems During Network Unbalance Using PI-R Current Regulators*, In: IEEE Transactions on Industrial Electronics, No. 2, p. 439–451, 2009

[19] Iov, F.; Blaabjerg, F.: *Power Electronics and Control for Wind Power Systems*, In: Power Electronics and Machines in Wind Applications, p. 1–16, 2009

[20] Iov, F.; Hansen, A.D.; Sørensen, P.; Cutuluis, N.A.: *Mapping of grid faults and grid codes: Risø-R-1617(EN)*, Risø National Laboratory, Technical University of Denmark, Roskilde, 2007

[21] Kawkabani, B.; Simond, J.-J.: *Improved modeling of three-phase transformer analysis based on magnetic equivalent circuit diagrams and taking into account nonlinear B-H curve*, In: Electromotion, 2005

[22] Lima, F.K.A.; Luna, A.; Rodriguez, P.; Watanabe, E.H.; Blaabjerg, F.: *Rotor Voltage Dynamics in the Doubly Fed Induction Generator During Grid Faults*, In: IEEE Transactions on Power Electronics, p. 118–130, 2010

[23] Lima, F.K.A.; Rodriguez, P.; Watanabe, E.H.; Teodorescu, R.; Blaabjerg, F.: *Doubly-Fed Induction Generator Control Under Voltage Sags*, In: Energy 2030 Conference, p. 1–6, 2008

[24] López, J.; Gubía, E.; Sanchis, P.; Roboam, X.; Marroyo, L.: *Wind Turbines Based on Doubly-Fed Induction Generator under Asymmetrical Voltage Dips*, In: IEEE Transactions on Energy Conversion, No. 23, p. 321–330, 2008

[25] López, J.; Sanchis, P.; Roboam, X.; Marroyo, L.: *Dynamic Behaviour of the Doubly-Fed Induction Generator during Three-Phase Voltage Dips*, In: IEEE Transactions on Energy Conversion, No. 22, p. 709–717, 2007

[26] Luna, A.; Kleber, F.; Lima, A.; Rodriguez, P.; Watanabe, E.H.; Teodorescu, R.: *Comparison of Power Control Strategies for DFIG wind turbines*, In: 34th Annual Conference of the IEEE Industrial Electronics Society, 2008

[27] Lunze, J.: *Regelungstechnik 1: Systemtheoretische Grundlagen, Analyse und Entwurf einschleifiger Regelungen*, Vol. 1, 7th edition, Springer-Verlag, Berlin, Heidelberg, ISBN 9783540689096, 2008

[28] Lunze, J.: *Regelungstechnik 2: Mehrgrößensysteme, Digitale Regelung*, Vol. 2, 5th edition, Springer-Verlag, Berlin, Heidelberg, 2008

[29] Lutz, H.; Wendt, W.: *Taschenbuch der Regelungstechnik*, 6th edition, Verlag Harri Deutsch, Frankfurt am Main, ISBN 3817117493, 2005

[30] Mohseni, M.; Islam, S.M.; Masoum, M.A.S.: *Enhanced Hysteresis-Based Current Regulators in Vector Control of DFIG Wind Turbines*, In: IEEE Transactions on Power Electronics, No. 1, p. 223–234, 2011

[31] Monroy, A.; Alvarez-Icaza, L.; Espinosa-Pérez, G.: *Passivity-based control for variable speed constant frequency operation of a DFIG wind turbine*, In: International Journal of Control, No. 9, p. 1399–1407, 2008

[32] Mueller, G.: *Elektrische Maschinen: Grundlagen, Aufbau und Wirkungsweise*, 7th edition, Berlin, VEB Verlag Technik, 1989

[33] Navarro Gevers, D.; Gamesa Eólica (publisher): *Validation document for the PSCAD® simulation model*, Technical Report, 2006

[34] Navarro Gevers, D.: *Beitrag zur Regelung einer doppeltgespeisten Asynchronmaschine ohne Lagegeber für Windkraftanlagen: Dissertation*, Technische Universität Ilmenau, 2004

[35] Nilsson, T.; Perez, M.: *Introduction to Passivity-based Control of Euler-Lagrange Systems: Thesis*, Växjö, 2003

[36] Pena, R.; Clare, J.C.; Asher, G.M.: *Doubly fed induction generator using back-to-back PWM converters and its application to variable speed wind-energy generation*, In: IEE Proceedings on Electrical Power Application, No. 3, p. 231–241, 1996

[37] Peng, L.; Francois, B.; Li, Y.: *Improved Crowbar Control Strategy of DFIG Based Wind Turbines for Grid Fault Ride-Through*, In: Applied Power Electronics Conference and Exposition, p. 1932–1938, 2009

[38] Råde, L.; Westergren, B.: *Springers Mathematische Formeln*, 3rd edition, Springerverlag, Berlin, Heidelberg, 2000

[39] Richter, M.: *Control of doubly-fed induction generators under asymmetrical grid conditions: Diplomarbeit*, Technische Universität Ilmenau, 2006

[40] Rodríguez, P.; Luna, A.; Ciobotaru, M.; Teodorescu, R.; Blaabjerg, F.: *Advanced Grid Synchronization System for Power Converters under Unbalanced and Distorted Operating Conditions*, In: IEEE Annual Conference on Industrial Electronics, p. 5173–5178, 2006

[41] Rodriguez, P.; Luna, A.; Medeiros, G.; Tedorescu, R.; Blaabjerg, F.: *Control of STATCOM in Wind Power Plants based on Induction Generators during Asymmetrical Grid Faults*, In: International Power Electronics Conference, p. 2066–2073, 2010

[42] Schlabbach, J.: *Elektroenergieversorgung: Betriebsmittel und Auswirkungen der elektrischen Energieverteilung*, VDE-Verlag, Berlin Offenbach, ISBN 3800719991, 1995

[43] Song, H.-S.; Nam, K.: *Dual Current Control Scheme for PWM Converter Under Unbalanced Input Voltage Conditions*, In: IEEE Transactions on Industrial Electronics, No. 5, p. 953–959, 1999

[44] Tsili, M.; Papathanassiou, S.: *A review of grid code technical requirements for wind farms*, In: IET Renewable Power Generation, p. 308–332, 2009

[45] Wessels, Ch.; Fuchs, F.W.: *Fault Ride Through of DFIG Wind Turbines during symmetrical voltage dip with Crowbar or Stator Current Feedback Solution*, In: Energy Conversion Congress and Exposition, p. 2771–2777, 2010

Nomenclature

Indices If more than one subscript or superscript is necessary to identify a quantity, the single elements will be separated by ",". *Example:* $i_{gsc,p,d}$ refers to the positive sequence d-component of the grid-side inverter current. If several elements are labelled by one variable, the corresponding subscripts will *not* be separated. *Example:* $i_{gsc,p,dq}$ refers to the positive-sequence d-component *and* the positive-sequence q-component of the grid-side inverter current.

x	Real quantity
X	RMS-value
$\hat{x}$	Amplitude
$\underline{x}$	Complex quantity
$\vec{x}$	Vector or space vector
x_{123}	Three-phase real quantities
$\underline{x}_{123}$	Three-phase complex quantities (phasors)
$\underline{x}_p$	Positive sequence quantity of symmetrical components
$\underline{x}_n$	Negative sequence quantity of symmetrical components
$\underline{x}_0$	Zero sequence quantity of symmetrical components
x_{dq}	Complex components of direct quantity
$x_{\alpha\beta}$	Complex components of alternating quantity (in some figures *ab* is used instead of $\alpha\beta$)
x^r	Quantity in rotor-oriented coordinate system
x^s	Quantity in stator-oriented coordinate system
x^R	Quantity in a rotating coordinate system
x^S	Quantity in a stationary coordinate system
$x_r^{(s)}$	Rotor quantity related to the stator
$x_s^{(r)}$	Stator quantity related to the rotor
x_r	Rotor quantity/parameter/transfer function
x_s	Stator quantity/parameter/transfer function
x_{gsc}	Parameter/transfer function/variable of the grid-side control
x_{rsc}	Parameter/transfer function/variable of the rotor-side control
x_{MT}	Main transformer quantity

x_{gscT}	GSC-transformer quantity
x_H	Quantity of the high voltage side of a transformer
x_L	Quantity of the low voltage side of a transformer
$x_H^{(L)}$	Transformer quantity of the high voltage side, related to low voltage side
$x_L^{(H)}$	Transformer quantity of the low voltage side, related to high voltage side
x_g	Grid quantity/parameter (on the HV-side of the main transformer)
x_l	Line quantity (e.g. sum of stator and grid-side inverter current)
x_{ref}	Reference value
x_{nom}	Nominal value

Symbols and variables

C	Constant (e.g. used in Eq. C.35 in the context of an integration)
C_{DC}	DC-link capacitor
C_f	Filter capacitor connecting DFIG, main transformer and grid-side converter transformer
e	Control deviation
$E_{BC,rel}$	Energy consumption of the brake chopper, related value
f	Frequency
$G(p)$	Transfer function
$G_0(p)$	Open loop transfer function
G_C	Transfer function of a controller
i	Current
$I_{l,n,rel}$	Related negative-sequence line current amplitude
K	Controller gain
L_m	Mutual inductance of the generator, related to $\alpha\beta$-phase model (this is the value given in data sheets)
L_{m3}	Mutual inductance of the generator, related to 3-phase model
$L_{\mathbf{r}\sigma}$	Leakage inductance of the rotor windings without inductance of the rotor inductor
$L_{r\sigma}$	Leakage inductance of the rotor windings including inductance of the rotor inductor
L_r	Rotor inductance of a DFIG
L_{ri}	Inductance of the rotor inductor
$L_{s\sigma}$	Leakage inductance of the stator windings
L_s	Stator inductance of a DFIG
L_σ	Equivalent leakage inductance of a DFIG
m_{el}	Inner torque, also referred to as "electrical torque"
$\Delta m_{el,rel}$	Difference between maximum and minimum torque, related to nominal torque

$m_{el,\Delta,rel}$	Steady-state oscillation of the electrical torque
n	Mechanical velocity of the machine
$n_{s=0}$	Synchronous speed, velocity with slip $s = 0$
p	Laplace variable
	(in the literature and in some Figures of this work s is used instead of p)
P_{gsc}	Active power of grid-side converter (although P and Q are time-variable quantities,
	capital letters are used for active and reactive power)
P_{rsc}	Active power of rotor-side converter
P_G	Generated active power (stator and grid-side inverter power)
$P_{G,\Delta,rel}$	Steady-state oscillation of active power
p_p	Number of pole pairs
Q_f	Filter quality of a band rejection filter or band-pass
Q_G	Generated reactive power (stator and grid-side inverter reactive power,
	typically the grid-side inverter power is controlled to zero)
$Q_{G,\Delta,rel}$	Steady-state oscillation of reactive power
R_f	Ohmic resistance of filter capacitor
$R_\mathbf{r}$	Rotor resistance without resistance of the rotor inductor
R_r	Rotor resistance + resistance of the rotor inductor
R_{ri}	Resistance of the rotor inductor
R_s	Stator resistance
s	Slip
T_{MAV}	Time constant of moving average element
T_p	Pulsing period of an inverter
T_f	Time constant of low-pass filter
v	Voltage
v_{DC}	DC-link voltage
$v_{DC,\Delta,rel}$	Steady-state oscillation of DC-link voltage
w_{GW}	Winding ratio of a DFIG
w_G	Transmission ratio of a DFIG with Δ-connected stator windings
w_{TW}	Winding ratio of a transformer

Greek symbols and parameters

γ_m	Angle between stator and rotor
γ	Equivalent rotor angle (in stator-oriented coordinate system)
θ	Variable of an integral
σ	Subscript for leakage inductances

τ	Time constant of the first order differential equation C.23
ω	Angular frequency
ω_{grid}	Grid angular frequency (in stator-oriented coordinate system)
ω_{slip}	Angular slip frequency
Ψ	Linked flux

Abbreviations

AC	Alternating current
BCC	Brake chopper control
BW	Backward (difference)
CS	Coordinate system (synonymously, "reference frame" is used in the literature)
d	Relative dip-depth
DC	Direct current, in this study also used for other direct quantities
deco	Decoupling
DFIG	Doubly-fed induction generator
DSOGI	Dual second order generalised integrator
DSP	Digital signal processor
EMF	Electromagnetic force
FLL	Frequency locked loop
FOC	Field-oriented control
FRT	Fault ride through
FSC	Frequency-selective control (in subscripts small letters are used instead: fsc)
FSC(PN)	FSC with negative-sequence reference value calculation
FW	Forward (difference)
GSC	Grid-side converter or grid-side controller (in subscripts small letters are used instead: gsc)
HV	High voltage side (of a transformer)
IMP	Inner model principle
LP-BP	Lowpass-bandpass(-transformation)
LTI	Linear time-invariant
LV	Low voltage side (of a transformer)
LVRT	Low voltage ride through
MAV	Moving average element
nom	Nominal
PCI	Pulse controlled inverter

PLL	Phase locked loop
PNC	Positive-negative-sequence control
PNSC	Positive-negative-sequence calculation (for FLL)
PWM	Pulse width modulation
QSG	Quadrature signal generation
RSC	Rotor-side converter or controller
	(in subscripts small letters are used instead: rsc)
SOGI	Second order generalised integrator
STATCOM	Static synchronous compensator
SVM	Space vector modulation
VOC	Voltage oriented control
VR	Vector rotation
VSI, VSC	Voltage source inverter/converter
	(both terms are used synonymously in this study)

Basic mathematical correlations

$\underline{a}$	$= e^{j \cdot 2 \cdot \pi/3}$
L_{m3}	$= \frac{2}{3} \cdot L_m$
L_r	$= L_{r\sigma} + L_m$
L_s	$= L_{s\sigma} + L_m$
L_σ	$= L_r - \frac{L_m^2}{L_s}$
P_G	$= P_s + P_{gsc}$
Q_G	$= Q_s + Q_{gsc}$
T_{grid}	$= 2 \cdot \pi / \omega_{grid}$
γ	$= p_p \cdot \gamma_m$

A Mathematical basics and coordinate systems

The electrical system analysed in this study is a three-phase system. Different possibilities exist to describe the three-phase quantities. The descriptions used in the present study are based on [5] and [6] and are described in the following sections. For most of the transformations two different options exist: *power invariance* versus *reference vector invariance*. Furthermore, for space vector and complex phasor representation it is possible to chose between a *stationary coordinate system* (superscript *S*) – then the space vector or the complex phasors are rotating – and a *rotating coordinate system* (superscript *R*) – in which the space vector and the complex phasors are static.

A.1 Original quantities

The original quantities are the three line currents and the three line-earth or line-line voltages. These quantities are time dependent scalar variables. They are applicable for the description of transient and stationary states. In this study they are symbolised by:
$x_1(t), x_2(t), x_3(t)$
The three quantities can also be given as a three element column vector:

$$\vec{x}(t) = \begin{pmatrix} x_1(t) \\ x_2(t) \\ x_3(t) \end{pmatrix} \tag{A.1}$$

A.2 Complex phasors

The three-phase quantities can be described as three complex phasors during stationary state with only the fundamental frequency component according to [6]. These complex phasors are symbolised by:
$\underline{x}_1, \underline{x}_2, \underline{x}_3$
The calculation of phasor values is given in Eqs. A.2 – A.4. The instantaneous values can be calculated as the real component of the respective complex phasor. This can be represented by a projection of the respective phasor on the real axis as illustrated in Fig. A.1.

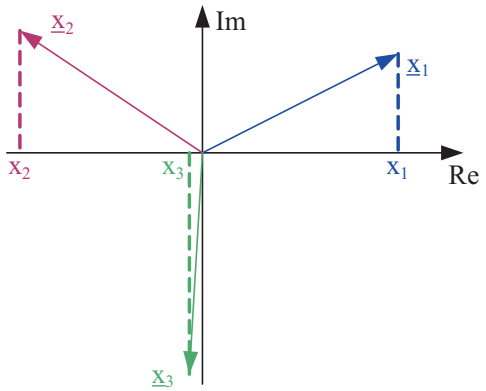

Figure A.1: Transformation from complex phasors to original quantities

$$\underline{x}_1 = \hat{x}_1 \cdot e^{j(\omega t+\varphi_1)} \tag{A.2}$$

$$\underline{x}_2 = \hat{x}_2 \cdot e^{j\left(\omega t-\frac{2\pi}{3}+\varphi_2\right)} \tag{A.3}$$

$$\underline{x}_3 = \hat{x}_3 \cdot e^{j\left(\omega t-\frac{4\pi}{3}+\varphi_3\right)} \tag{A.4}$$

$$x_1 = \mathrm{Re}\{\underline{x}_1\} = \hat{x}_1 \cos(\omega t + \varphi_1) \tag{A.5}$$

$$x_2 = \mathrm{Re}\{\underline{x}_2\} = \hat{x}_2 \cos\left(\omega t - \frac{2\pi}{3} + \varphi_2\right) \tag{A.6}$$

$$x_3 = \mathrm{Re}\{\underline{x}_3\} = \hat{x}_3 \cos\left(\omega t - \frac{4\pi}{3} + \varphi_3\right) \tag{A.7}$$

The phasors are rotating with $e^{j\cdot\omega\cdot t}$. Alternatively, static phasors can be used in a coordinate system rotating with $e^{j\cdot\omega\cdot t}$.

A.3 Fortescue transformation

In [5] different modal transformations are defined that transform the three original variables or the three complex phasors to three modal components. One of these transformations is the Fortescue transformation that yields the symmetrical components. This transformation is used to describe asymmetrical steady-state conditions. The reference vector invariant transformation equations are Eqs. A.8 and A.9:

$$\begin{pmatrix} \underline{x}_p \\ \underline{x}_n \\ \underline{x}_0 \end{pmatrix} = \frac{1}{3} \cdot \begin{pmatrix} 1 & \underline{a} & \underline{a}^2 \\ 1 & \underline{a}^2 & \underline{a} \\ 1 & 1 & 1 \end{pmatrix} \cdot \begin{pmatrix} \underline{x}_1 \\ \underline{x}_2 \\ \underline{x}_3 \end{pmatrix} \tag{A.8}$$

$$\begin{pmatrix} \underline{x}_1 \\ \underline{x}_2 \\ \underline{x}_3 \end{pmatrix} = \begin{pmatrix} 1 & 1 & 1 \\ \underline{a}^2 & \underline{a} & 1 \\ \underline{a} & \underline{a}^2 & 1 \end{pmatrix} \cdot \begin{pmatrix} \underline{x}_p \\ \underline{x}_n \\ \underline{x}_0 \end{pmatrix} \tag{A.9}$$

with $\underline{a} = e^{j\cdot 2\pi/3}$. The Fortescue transformation yields three complex phasors, each representing a symmetrical three-phase system. The symbols and characteristics of the three components are given in Table A.1.

A.4 Space vector

Another modal transformation is the transformation to space vector representation (cf. [5]). This transformation yields a vector, its conjugate and a real zero sequence component. In this study,

Table A.1: Symmetrical components

Symbol	Component	Phase sequence
$\underline{x}_p$	Positive-sequence component	1-2-3
$\underline{x}_n$	Negative-sequence component	3-2-1
$\underline{x}_0$	Zero sequence component	No phase shift between the three phases

only the space vector (not the conjugate and the zero sequence component) is used and it is symbolised by $\vec{x}$. It can be interpreted as a two element vector or as a complex quantity:

$$\vec{x} = \begin{pmatrix} x_\alpha \\ x_\beta \end{pmatrix} \tag{A.10}$$

$$\vec{x} \leftrightarrow \underline{x} = x_\alpha + j \cdot x_\beta \tag{A.11}$$

The transformation equations (reference vector invariant) are Eqs. A.12 and A.13:

$$\begin{pmatrix} \vec{x} \\ \vec{x}^* \\ x_0 \end{pmatrix} = \frac{2}{3} \cdot \begin{pmatrix} 1 & \underline{a} & \underline{a}^2 \\ 1 & \underline{a}^2 & \underline{a} \\ \frac{1}{2} & \frac{1}{2} & \frac{1}{2} \end{pmatrix} \cdot \begin{pmatrix} x_1 \\ x_2 \\ x_3 \end{pmatrix} = \begin{pmatrix} x_\alpha + j \cdot x_\beta \\ x_\alpha - j \cdot x_\beta \\ x_0 \end{pmatrix} \tag{A.12}$$

$$\begin{pmatrix} x_1 \\ x_2 \\ x_3 \end{pmatrix} = \frac{1}{2} \cdot \begin{pmatrix} 1 & 1 & 2 \\ \underline{a}^2 & \underline{a} & 2 \\ \underline{a} & \underline{a}^2 & 2 \end{pmatrix} \cdot \begin{pmatrix} \vec{x} \\ \vec{x}^* \\ x_0 \end{pmatrix} \tag{A.13}$$

If only the space vector is used, this equations will reduce to Eqs. A.14 and A.15 – A.17:

$$\vec{x} = \frac{2}{3} \cdot \left(x_1 + x_2 \cdot \underline{a} + x_3 \cdot \underline{a}^2 \right) \tag{A.14}$$

$$x_1 = \mathrm{Re}\left\{ \vec{x} \right\} \tag{A.15}$$

$$x_2 = \mathrm{Re}\left\{ \underline{a}^2 \cdot \vec{x} \right\} \tag{A.16}$$

$$x_3 = \mathrm{Re}\left\{ \underline{a} \cdot \vec{x} \right\} \tag{A.17}$$

The transformation from space vector to original variables can be represented by a projection of the space vector on three different axes as shown in Fig. A.2 b).

A.5 Rotating coordinate system

As mentioned above, space vector and complex phasors can be given in a stationary and in a rotating coordinate system. The transformation between two coordinate systems is possible by

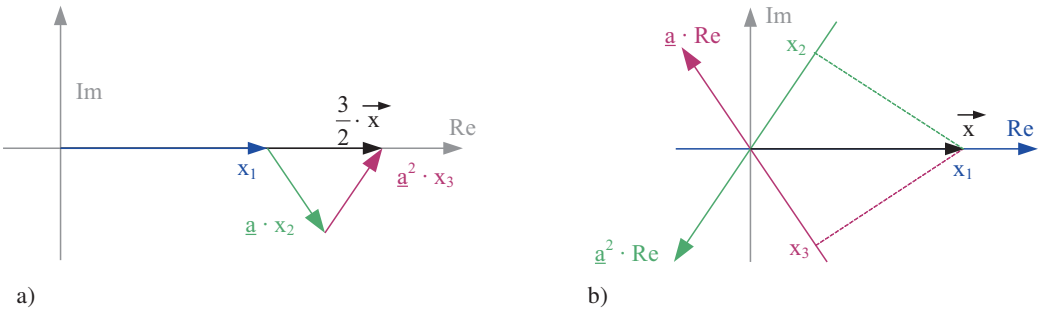

Figure A.2: Space vector transformation: a) transformation from original quantities to space vector and b) inverse transformation

Eqs. A.18 - A.21.

$$\vec{x}^R = \begin{pmatrix} \cos(\vartheta) & \sin(\vartheta) \\ -\sin(\vartheta) & \cos(\vartheta) \end{pmatrix} \cdot \vec{x}^S \tag{A.18}$$

$$\vec{x}^S = \begin{pmatrix} \cos(\vartheta) & -\sin(\vartheta) \\ \sin(\vartheta) & \cos(\vartheta) \end{pmatrix} \cdot \vec{x}^R \tag{A.19}$$

$$\underline{x}^R = e^{-j\vartheta} \cdot \underline{x}^S \tag{A.20}$$

$$\underline{x}^S = e^{j\vartheta} \cdot \underline{x}^R \tag{A.21}$$

with $\vartheta = \omega \cdot t$. The explanation of the different indices is given in Table A.2.

Table A.2: Representation in different coordinate systems

Symbol	
$\vec{x}^R$	Space vector in rotating coordinate system
$\vec{x}^S$	Space vector in stationary coordinate system
$\underline{x}^R$	Complex phasor in rotating coordinate system
$\underline{x}^S$	Complex phasor in stationary coordinate system

This transformation can be generalised to a transformation between two different arbitrarily chosen coordinate systems.

A.6 Clarke transformation

Clark transformation as defined in [5] yields the α- and β-components of Eqs. A.22 and A.23. The three-phase quantities are transformed to one real zero sequence component and two alter-

nating components in a stationary coordinate system.

$$\begin{pmatrix} x_\alpha \\ x_\beta \\ x_0 \end{pmatrix} = \frac{2}{3} \cdot \begin{pmatrix} 1 & -\frac{1}{2} & -\frac{1}{2} \\ 0 & \frac{\sqrt{3}}{2} & -\frac{\sqrt{3}}{2} \\ \frac{1}{2} & \frac{1}{2} & \frac{1}{2} \end{pmatrix} \cdot \begin{pmatrix} x_1 \\ x_2 \\ x_3 \end{pmatrix} = [C] \cdot \begin{pmatrix} x_1 \\ x_2 \\ x_3 \end{pmatrix} \tag{A.22}$$

$$\begin{pmatrix} x_1 \\ x_2 \\ x_3 \end{pmatrix} = \begin{pmatrix} 1 & 0 & 1 \\ -\frac{1}{2} & \frac{\sqrt{3}}{2} & 1 \\ -\frac{1}{2} & -\frac{\sqrt{3}}{2} & 1 \end{pmatrix} \cdot \begin{pmatrix} x_\alpha \\ x_\beta \\ x_0 \end{pmatrix} = [C]^{-1} \cdot \begin{pmatrix} x_\alpha \\ x_\beta \\ x_0 \end{pmatrix} \tag{A.23}$$

This transformation is similar to the space vector transformation. The following equation describes the correlation:

$$\vec{x}^S = x_\alpha + j \cdot x_\beta \tag{A.24}$$

A.7 Park transformation

The combination of Clarke transformation and a rotation of the result to a rotating coordinate system is called Park transformation. The integration of the two transformation steps to one equation yields the transformation matrices of Eqs. A.25 and A.26.

$$\begin{pmatrix} x_d \\ x_q \\ x_0 \end{pmatrix} = \frac{2}{3} \cdot \begin{pmatrix} \cos(\vartheta) & \cos\left(\vartheta - \frac{2\pi}{3}\right) & \cos\left(\vartheta + \frac{2\pi}{3}\right) \\ -\sin(\vartheta) & -\sin\left(\vartheta - \frac{2\pi}{3}\right) & -\sin\left(\vartheta + \frac{2\pi}{3}\right) \\ \frac{1}{2} & \frac{1}{2} & \frac{1}{2} \end{pmatrix} \cdot \begin{pmatrix} x_1 \\ x_2 \\ x_3 \end{pmatrix} = [P] \cdot \begin{pmatrix} x_1 \\ x_2 \\ x_3 \end{pmatrix} \tag{A.25}$$

$$\begin{pmatrix} x_1 \\ x_2 \\ x_3 \end{pmatrix} = \begin{pmatrix} \cos(\vartheta) & -\sin(\vartheta) & 1 \\ \cos\left(\vartheta - \frac{2\pi}{3}\right) & -\sin\left(\vartheta - \frac{2\pi}{3}\right) & 1 \\ \cos\left(\vartheta + \frac{2\pi}{3}\right) & -\sin\left(\vartheta + \frac{2\pi}{3}\right) & 1 \end{pmatrix} \cdot \begin{pmatrix} x_d \\ x_q \\ x_0 \end{pmatrix} = [P]^{-1} \cdot \begin{pmatrix} x_d \\ x_q \\ x_0 \end{pmatrix} \tag{A.26}$$

Like the Clarke transformation, the Park transformation is similar to the space vector transformation to a rotating coordinate system. The following equation describes the correlation:

$$\vec{x}^R = x_d + j \cdot x_q \tag{A.27}$$

B Mathematical model of the system

All models used in this study are built in Matlab/Simulink®. The model equations for transformer, generator, DC-link and FLL are given in the following sections.

B.1 YΔ-Transformation

The high voltage side of the main transformer and the stator windings of the generator are connected in Δ. Therefore, the models of DFIG and transformers use the winding quantities of the coils. The relationship between winding quantities and line quantities is depicted in Fig. B.1 for a Y-connected 3-phase system with arbitrary elements and in Fig. B.2 for a Δ-connected system. The transformation equations are given in Eqs. B.1 – B.4.

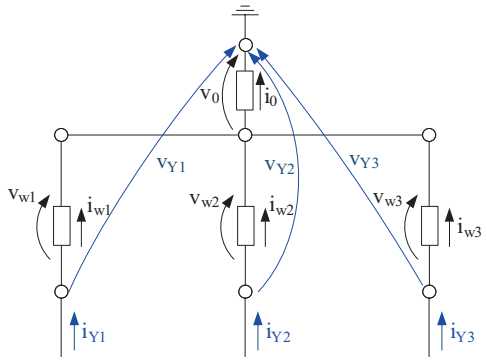

$$\begin{pmatrix} v_{w1} \\ v_{w2} \\ v_{w3} \end{pmatrix} = \begin{pmatrix} 1 & 0 & 0 \\ 0 & 1 & 0 \\ 1 & 0 & 1 \end{pmatrix} \cdot \begin{pmatrix} v_{Y1} \\ v_{Y2} \\ v_{Y3} \end{pmatrix} - v_0 \tag{B.1}$$

$$\begin{pmatrix} i_{Y1} \\ i_{Y2} \\ i_{Y3} \end{pmatrix} = \begin{pmatrix} 1 & 0 & 0 \\ 0 & 1 & 0 \\ 0 & 0 & 1 \end{pmatrix} \cdot \begin{pmatrix} i_{w1} \\ i_{w2} \\ i_{w3} \end{pmatrix} \tag{B.2}$$

Figure B.1: Winding quantities and Y-quantities

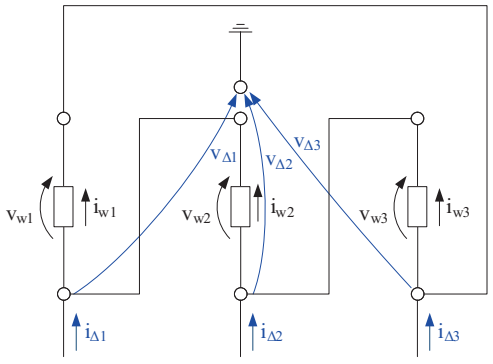

$$\begin{pmatrix} v_{w1} \\ v_{w2} \\ v_{w3} \end{pmatrix} = \begin{pmatrix} 1 & 0 & -1 \\ -1 & 1 & 0 \\ 0 & -1 & 1 \end{pmatrix} \cdot \begin{pmatrix} v_{\Delta 1} \\ u_{\Delta 2} \\ v_{\Delta 3} \end{pmatrix} \tag{B.3}$$

$$\begin{pmatrix} i_{\Delta 1} \\ i_{\Delta 2} \\ i_{\Delta 3} \end{pmatrix} = \begin{pmatrix} 1 & -1 & 0 \\ 0 & 1 & -1 \\ -1 & 0 & 1 \end{pmatrix} \cdot \begin{pmatrix} i_{w1} \\ i_{w2} \\ i_{w3} \end{pmatrix} \tag{B.4}$$

Figure B.2: Winding quantities and Δ-quantities

In $\alpha\beta$-coordinates and for space vectors, the transformation from winding to Δ-quantities corresponds to a vector rotation of 30° and a multiplication with $\sqrt{3}$:

$$\vec{\underline{v}}_w = \sqrt{3} \cdot e^{j30^\circ} \cdot \vec{\underline{v}}_\Delta \tag{B.5}$$

$$\vec{i}_\Delta = \sqrt{3} \cdot e^{-j30^\circ} \cdot \vec{i}_w \tag{B.6}$$

Eqs. B.5 and B.6 can be proved by:

$$\begin{aligned}
\begin{pmatrix} v_{w\alpha} \\ v_{w\beta} \\ v_{w0} \end{pmatrix} =& \frac{2}{3} \cdot \begin{pmatrix} 1 & -\frac{1}{2} & -\frac{1}{2} \\ 0 & \frac{\sqrt{3}}{2} & -\frac{\sqrt{3}}{2} \\ \frac{1}{2} & \frac{1}{2} & \frac{1}{2} \end{pmatrix} \cdot \begin{pmatrix} 1 & 0 & -1 \\ -1 & 1 & 0 \\ 0 & -1 & 1 \end{pmatrix} \cdot \begin{pmatrix} 1 & 0 & 1 \\ -\frac{1}{2} & \frac{\sqrt{3}}{2} & 1 \\ -\frac{1}{2} & -\frac{\sqrt{3}}{2} & 1 \end{pmatrix} \cdot \begin{pmatrix} v_{\Delta\alpha} \\ v_{\Delta\beta} \\ v_{\Delta 0} \end{pmatrix} \\
=& \sqrt{3} \cdot \begin{pmatrix} \frac{\sqrt{3}}{2} & \frac{1}{2} & 0 \\ -\frac{1}{2} & \frac{\sqrt{3}}{2} & 0 \\ 0 & 0 & 0 \end{pmatrix} \cdot \begin{pmatrix} v_{\Delta\alpha} \\ v_{\Delta\beta} \\ v_{\Delta 0} \end{pmatrix} \\
\hat{=} & \sqrt{3} \cdot \begin{pmatrix} \cos(30^\circ) & \sin(30^\circ) & 0 \\ -\sin(30^\circ) & \cos(30^\circ) & 0 \\ 0 & 0 & 0 \end{pmatrix} \cdot \begin{pmatrix} v_{\Delta\alpha} \\ v_{\Delta\beta} \\ v_{\Delta 0} \end{pmatrix}
\end{aligned} \tag{B.7}$$

and

$$\begin{aligned}
\begin{pmatrix} i_{\Delta\alpha} \\ i_{\Delta\beta} \\ i_{\Delta 0} \end{pmatrix} =& \frac{2}{3} \cdot \begin{pmatrix} 1 & -\frac{1}{2} & -\frac{1}{2} \\ 0 & \frac{\sqrt{3}}{2} & -\frac{\sqrt{3}}{2} \\ \frac{1}{2} & \frac{1}{2} & \frac{1}{2} \end{pmatrix} \cdot \begin{pmatrix} 1 & -1 & 0 \\ 0 & 1 & -1 \\ -1 & 0 & 1 \end{pmatrix} \cdot \begin{pmatrix} 1 & 0 & 1 \\ -\frac{1}{2} & \frac{\sqrt{3}}{2} & 1 \\ -\frac{1}{2} & -\frac{\sqrt{3}}{2} & 1 \end{pmatrix} \cdot \begin{pmatrix} i_{w\alpha} \\ i_{w\beta} \\ i_{w0} \end{pmatrix} \\
=& \sqrt{3} \cdot \begin{pmatrix} \frac{\sqrt{3}}{2} & -\frac{1}{2} & 0 \\ \frac{1}{2} & \frac{\sqrt{3}}{2} & 0 \\ 0 & 0 & 0 \end{pmatrix} \cdot \begin{pmatrix} i_{w\alpha} \\ i_{w\beta} \\ i_{w0} \end{pmatrix} \\
\hat{=} & \sqrt{3} \cdot \begin{pmatrix} \cos(-30^\circ) & \sin(-30^\circ) & 0 \\ -\sin(-30^\circ) & \cos(-30^\circ) & 0 \\ 0 & 0 & 0 \end{pmatrix} \cdot \begin{pmatrix} i_{w\alpha} \\ i_{w\beta} \\ i_{w0} \end{pmatrix}
\end{aligned} \tag{B.8}$$

Eqs. B.7 and B.8 show that no zero sequence component is possible in a Δ-connected system. A zero sequence "circular" current in the Δ will not be transmitted to the line currents. Respectively, a zero sequence component of the line voltages will not cause a zero sequence component of the phase-to-phase voltages.

B.2 Doubly-fed induction generator

Extensive deduction of equivalent circuits and equations to describe asynchronous generators can be found in [32, p. 349 et seqq.]. In the present study a model considering only the funda-

mental frequency is used. Grooves, iron and eddy current losses are disregarded. The leakage inductances and ohmic resistances are assumed to be constant. Based on the 3-phase equations of the DFIG four different models are developed:

- 3-phase model in natural coordinates without any saturation
- 3-phase model in natural coordinates with saturation of mutual inductance
- $\alpha\beta$-model in stator coordinates without any saturation
- $\alpha\beta$-model in stator coordinates with saturation of mutual inductance

The reduction from 3-phase model to $\alpha\beta$-model is possible without loss of information because the neutrals of stator and rotor are not grounded. In this study the speed of the machine is assumed to be fixed, so the model of the generator mechanical behaviour – the calculation of the machine speed from electrical and load torque – is omitted. That limits the applicability of the models to short times below 1 sec. The input and output quantities of the models are given in Table B.1.

Table B.1: DFIG model ports

Quantity	Symbol	Port type	Dimension
Stator voltages	$v_{s,123}$	Input	3
Rotor voltages	$v_{r,123}$	Input	3
Mechanical speed	n	Input	1
Stator currents	$i_{s,123}$	Output	3
Rotor currents	$i_{r,123}$	Output	3
Electrical torque	m_{el}	Output	1

B.2.1 Three-phase DFIG model without saturation

The 3-phase voltage equations of stator and rotor, each in Y-connection, are given in Eqs. B.9 and B.10.

$$\begin{pmatrix} v^s_{s1} \\ v^s_{s2} \\ v^s_{s3} \end{pmatrix} = R_s \cdot \begin{pmatrix} i^s_{s1} \\ i^s_{s2} \\ i^s_{s3} \end{pmatrix} + \frac{d}{dt} \begin{pmatrix} \Psi^s_{s1} \\ \Psi^s_{s2} \\ \Psi^s_{s3} \end{pmatrix} \tag{B.9}$$

$$\begin{pmatrix} v^r_{r1} \\ v^r_{r2} \\ v^r_{r3} \end{pmatrix} = R_r \cdot \begin{pmatrix} i^r_{r1} \\ i^r_{r2} \\ i^r_{r3} \end{pmatrix} + \frac{d}{dt} \begin{pmatrix} \Psi^r_{r1} \\ \Psi^r_{r2} \\ \Psi^r_{r3} \end{pmatrix} \tag{B.10}$$

Fig. B.3 depicts the generation of stator and rotor main and leakage linked fluxes that are calculated by Eqs. B.12 and B.13. If the machine has more than one pole pair, the equivalent rotor

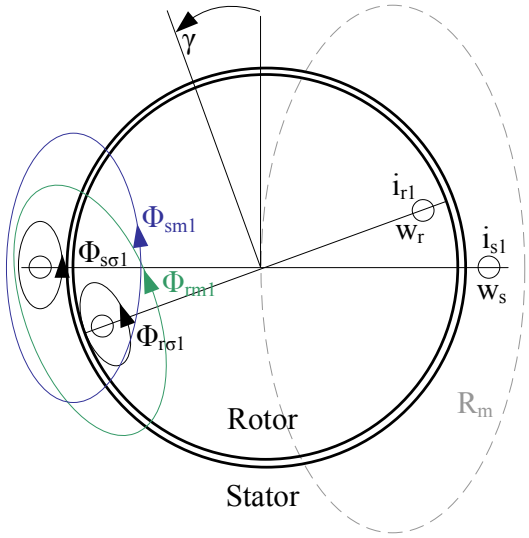

Figure B.3: Flux generation in a two-pole simplified DFIG

angle γ has to be calculated from the mechanical angle γ_m between stator and rotor with

$$\gamma = p_p \cdot \gamma_m \tag{B.11}$$

$$\begin{aligned}
\begin{pmatrix} \Psi^s_{s1} \\ \Psi^s_{s2} \\ \Psi^s_{s3} \end{pmatrix} &= \begin{pmatrix} L_{s\sigma}+L_{m3} & -\frac{L_{m3}}{2} & -\frac{L_{m3}}{2} \\ -\frac{L_{m3}}{2} & L_{s\sigma}+L_{m3} & -\frac{L_{m3}}{2} \\ -\frac{L_{m3}}{2} & -\frac{L_{m3}}{2} & L_{s\sigma}+L_{m3} \end{pmatrix} \cdot \begin{pmatrix} i^s_{s1} \\ i^s_{s2} \\ i^s_{s3} \end{pmatrix} \\
&\quad + w_{GW} \cdot L_{m3} \cdot \begin{pmatrix} \cos(\gamma) & \cos\left(\gamma+\frac{2\pi}{3}\right) & \cos\left(\gamma-\frac{2\pi}{3}\right) \\ \cos\left(\gamma-\frac{2\pi}{3}\right) & \cos(\gamma) & \cos\left(\gamma+\frac{2\pi}{3}\right) \\ \cos\left(\gamma+\frac{2\pi}{3}\right) & \cos\left(\gamma-\frac{2\pi}{3}\right) & \cos(\gamma) \end{pmatrix} \cdot \begin{pmatrix} i^r_{r1} \\ i^r_{r2} \\ i^r_{r3} \end{pmatrix} \\
&= [L_{ss}] \cdot \begin{pmatrix} i^s_{s1} \\ i^s_{s2} \\ i^s_{s3} \end{pmatrix} + [L_{sr}] \cdot \begin{pmatrix} i^r_{r1} \\ i^r_{r2} \\ i^r_{r3} \end{pmatrix}
\end{aligned} \tag{B.12}$$

$$\begin{aligned}
\begin{pmatrix} \Psi^r_{r1} \\ \Psi^r_{r2} \\ \Psi^r_{r3} \end{pmatrix} &= \begin{pmatrix} L_{r\sigma}+w^2_{GW} \cdot L_{m3} & -\frac{w^2_{GW} \cdot L_{m3}}{2} & -\frac{w^2_{GW} \cdot L_{m3}}{2} \\ -\frac{w^2_{GW} \cdot L_{m3}}{2} & L_{r\sigma}+w^2_{GW} \cdot L_{m3} & -\frac{w^2_{GW} \cdot L_{m3}}{2} \\ -\frac{w^2_{GW} \cdot L_{m3}}{2} & -\frac{w^2_{GW} \cdot L_{m3}}{2} & L_{r\sigma}+w^2_{GW} \cdot L_{m3} \end{pmatrix} \cdot \begin{pmatrix} i^r_{r1} \\ i^r_{r2} \\ i^r_{r3} \end{pmatrix} \\
&\quad + w_{GW} \cdot L_{m3} \cdot \begin{pmatrix} \cos(\gamma) & \cos\left(\gamma-\frac{2\pi}{3}\right) & \cos\left(\gamma+\frac{2\pi}{3}\right) \\ \cos\left(\gamma+\frac{2\pi}{3}\right) & \cos(\gamma) & \cos\left(\gamma-\frac{2\pi}{3}\right) \\ \cos\left(\gamma-\frac{2\pi}{3}\right) & \cos\left(\gamma+\frac{2\pi}{3}\right) & \cos(\gamma) \end{pmatrix} \cdot \begin{pmatrix} i^s_{s1} \\ i^s_{s2} \\ i^s_{s3} \end{pmatrix}
\end{aligned} \tag{B.13}$$

$$= [L_{rr}] \cdot \begin{pmatrix} i^r_{r1} \\ i^r_{r2} \\ i^r_{r3} \end{pmatrix} + [L_{rs}] \cdot \begin{pmatrix} i^s_{s1} \\ i^s_{s2} \\ i^s_{s3} \end{pmatrix}$$

With the parameters given in Eq. B.14.

$$w_{GW} = \frac{w_r}{w_s} \qquad L_{m3} = \frac{w_s^2}{R_m} \qquad L_{r\sigma} = \frac{w_r^2}{R_{mr\sigma}} \qquad L_{s\sigma} = \frac{w_s^2}{R_{ms\sigma}} \tag{B.14}$$

R_m is the magnetic resistance of the respective flux path, w_s the number of turns of the stator windings and w_r the number of turns of the rotor windings. The flux path of the main flux is drafted in Fig. B.3. The Eqs. B.9 – B.14 can be integrated in one equation:

$$\vec{v}(t) = [R] \cdot \vec{i}(t) + \frac{d}{dt} \cdot \Big([L(\gamma(t))] \cdot \vec{i}(t) \Big) \tag{B.15}$$

with $\vec{v}(t)$ and $\vec{i}(t) =$ column vectors with six elements and $[R]$ and $[L(\gamma(t))] = 6 \times 6$-matrices.

The inner – in this study named "electrical" – torque of the machine can be calculated from Eq. B.16. The deduction of this equation is given in [32, p. 347].

$$m_{el} = \frac{3}{2} \cdot p_p \cdot \mathrm{Im}\{\underline{\Psi}^{s*}_s \cdot \underline{i}^s_s\} \tag{B.16}$$

B.2.2 $\alpha\beta$-model of a DFIG without saturation

Eqs. B.9 – B.13 can be transferred to $\alpha\beta$-coordinates using the Clarke transformation defined in A.6. For example, the transformation of Eqs. B.9 and B.12 yields:

$$\begin{pmatrix} v^s_{s\alpha} \\ v^s_{s\beta} \\ v^s_{s0} \end{pmatrix} = [C] \cdot \left[R_s \cdot \left[C^{-1}\right] \cdot \begin{pmatrix} i^s_{s\alpha} \\ i^s_{s\beta} \\ i^s_{s0} \end{pmatrix} + \left[C^{-1}\right] \cdot \begin{pmatrix} \Psi^s_{s\alpha} \\ \Psi^s_{s\beta} \\ \Psi^s_{s0} \end{pmatrix} \right] \tag{B.17}$$

and

$$\begin{pmatrix} \Psi^s_{s\alpha} \\ \Psi^s_{s\beta} \\ \Psi^s_{s0} \end{pmatrix} = [C] \cdot \left[[L_{ss}] \cdot \left[C^{-1}\right] \cdot \begin{pmatrix} i^s_{s\alpha} \\ i^s_{s\beta} \\ i^s_{s0} \end{pmatrix} + [L_{sr}] \cdot \left[C^{-1}\right] \cdot \begin{pmatrix} i^r_{r\alpha} \\ i^r_{r\beta} \\ i^r_{r0} \end{pmatrix} \right] \tag{B.18}$$

The transformations of Eqs. B.10 and B.13 can be done in the same way. Eq. B.18 shows that the inductance matrices have to be transformed to get the $\alpha\beta$-model of the generator. The

transformation results for the four inductance matrices of Eqs. B.12 and B.13 are :

$$\left[L_{ss,\alpha\beta 0}\right] = [C] \cdot [L_{ss}] \cdot \left[C^{-1}\right] = \begin{pmatrix} L_{s\sigma} + \frac{3}{2} \cdot L_{m3} & 0 & 0 \\ 0 & L_{s\sigma} + \frac{3}{2} \cdot L_{m3} & 0 \\ 0 & 0 & L_{s\sigma} \end{pmatrix} \tag{B.19}$$

$$\left[L_{rr,\alpha\beta 0}\right] = [C] \cdot [L_{rr}] \cdot \left[C^{-1}\right] = \begin{pmatrix} L_{r\sigma} + \frac{3}{2} \cdot w_{GW}^2 \cdot L_{m3} & 0 & 0 \\ 0 & L_{r\sigma} + \frac{3}{2} \cdot w_{GW}^2 \cdot L_{m3} & 0 \\ 0 & 0 & L_{r\sigma} \end{pmatrix} \tag{B.20}$$

$$\left[L_{sr,\alpha\beta 0}\right] = [C] \cdot [L_{sr}] \cdot \left[C^{-1}\right] = \frac{3}{2} \cdot w_{GW} \cdot L_{m3} \cdot \begin{pmatrix} \cos(\gamma) & -\sin(\gamma) & 0 \\ \sin(\gamma) & \cos(\gamma) & 0 \\ 0 & 0 & 0 \end{pmatrix} \tag{B.21}$$

$$\left[L_{rs,\alpha\beta 0}\right] = [C] \cdot [L_{rs}] \cdot \left[C^{-1}\right] = \frac{3}{2} \cdot w_{GW} \cdot L_{m3} \cdot \begin{pmatrix} \cos(\gamma) & \sin(\gamma) & 0 \\ -\sin(\gamma) & \cos(\gamma) & 0 \\ 0 & 0 & 0 \end{pmatrix} \tag{B.22}$$

To get a simple and fast model the equations above are rearranged and simplified.

- Because of the Δ-connection of the stator and of the high voltage side of the main transformer, no zero sequence voltage or current is considered. Hence, the 3-phase model can be reduced to an $\alpha\beta$-model. For most simulations this model will be sufficient. One possible exception is the asymmetrical saturation of the leakage inductances. Because the zero sequence is omitted, the space vector representation is used instead of $\alpha\beta$-vectors in the following equations.
- The Δ-connection of the stator windings is considered by a phase shift of 30° and an adaption of the winding ratio $w_G = \sqrt{3} \cdot w_{GW}$
- The mutual inductance L_{m3} is substituted by the equivalent mutual inductance:

$$L_m = \frac{3}{2} \cdot L_{m3} \tag{B.23}$$

- The rotor currents and voltages are referred to the stator:

$$i_r^{r,(s)} = w_G \cdot i_r^r \tag{B.24}$$

$$v_r^{r,(s)} = \frac{1}{w_G} \cdot v_r^r \tag{B.25}$$

- The rotor leakage inductance and the rotor resistance are referred to the stator:

$$L_{r\sigma}^{(s)} = \frac{1}{w_G^2} \cdot L_{r\sigma} \tag{B.26}$$

$$R_r^{(s)} = \frac{1}{w_G^2} \cdot R_r \tag{B.27}$$

- Furthermore, rotor current and rotor magnetic flux are described in stator coordinate system:

$$\vec{i}_r^{\,s,(s)} = e^{j\gamma} \cdot \vec{i}_r^{\,r,(s)} \tag{B.28}$$

$$\vec{\Psi}_r^{s,(s)} = e^{j\gamma} \cdot \vec{\Psi}_r^{r,(s)} \tag{B.29}$$

With these specifications, Eqs. B.9 – B.13 can be written as:

$$\vec{v}_s^{\,s} = R_s \cdot \vec{i}_s^{\,s} + \frac{d}{dt}\vec{\Psi}_s^s \quad \Rightarrow \quad \vec{\Psi}_s^s = \int_0^t \left(\vec{v}_s^{\,s} - R_s \cdot \vec{i}_s^{\,s}\right) d\theta \tag{B.30}$$

$$\vec{v}_r^{\,r,(s)} = R_r^{(s)} \cdot \vec{i}_r^{\,r,(s)} + \frac{d}{dt}\vec{\Psi}_r^{r,(s)} \quad \Rightarrow \quad \vec{\Psi}_r^{r,(s)} = \int_0^t \left(\vec{v}_r^{\,r,(s)} - R_r^{(s)} \cdot \vec{i}_r^{\,r,(s)}\right) d\theta \tag{B.31}$$

$$\vec{v}_r^{\,s,(s)} = R_r^{(s)} \cdot \vec{i}_r^{\,s,(s)} + \frac{d}{dt}\vec{\Psi}_r^{s,(s)} - j \cdot \dot{\gamma} \cdot \vec{\Psi}_r^{s,(s)} \tag{B.32}$$

$$\vec{\Psi}_s^s = (L_m + L_{s\sigma}) \cdot \vec{i}_s^{\,s} + L_m \cdot \vec{i}_r^{\,s,(s)} \tag{B.33}$$

$$\vec{\Psi}_r^{s,(s)} = L_m \cdot \vec{i}_s^{\,s} + \left(L_m + L_{r\sigma}^{(s)}\right) \cdot \vec{i}_r^{\,s,(s)} \tag{B.34}$$

Eqs. B.33 and B.34 can be rearranged to get the stator and rotor currents:

$$\vec{i}_s^{\,s} = \frac{L_m + L_{r\sigma}^{(s)}}{\left(L_m + L_{r\sigma}^{(s)}\right) \cdot (L_m + L_{s\sigma}) - L_m^2} \cdot \vec{\Psi}_s^s - \frac{L_m}{\left(L_m + L_{r\sigma}^{(s)}\right) \cdot (L_m + L_{s\sigma}) - L_m^2} \cdot \vec{\Psi}_r^{s,(s)} \tag{B.35}$$

$$\vec{i}_r^{\,s,(s)} = -\frac{L_m}{\left(L_m + L_{r\sigma}^{(s)}\right) \cdot (L_m + L_{s\sigma}) - L_m^2} \cdot \vec{\Psi}_s^s + \frac{L_m + L_{s\sigma}}{\left(L_m + L_{r\sigma}^{(s)}\right) \cdot (L_m + L_{s\sigma}) - L_m^2} \cdot \vec{\Psi}_r^{s,(s)} \tag{B.36}$$

Eqs. B.30 – B.31 and B.35 – B.36 are realised in a Simulink®model. The equivalent circuit corresponding to these equations is given in Fig. B.4 (cf. [32, p. 361]).

B.2.3 Saturation of main inductance

The saturation of the mutual inductance of the generator can be integrated in the 3-phase as well as in the $\alpha\beta$-model using a look-up-table. The available data was the open circuit stator volt-

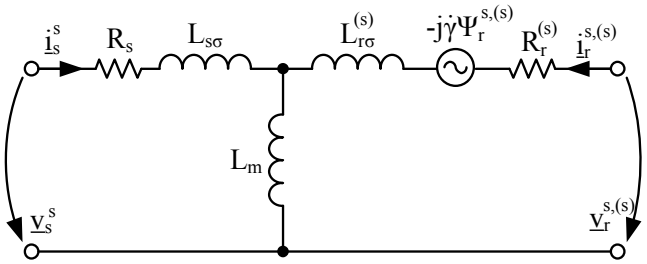

Figure B.4: DFIG equivalent circuit

age (phase-phase RMS-value) for different values of the rotor magnetising current (amplitude). From these pairs of values the respective mutual inductance can be calculated by:

$$\vec{i}_m^{(r)} = \vec{i}_r \qquad \text{if} \qquad \vec{i}_s = 0 \tag{B.37}$$

$$L_m = L_m\left(\hat{i}_m^{(r)}\right) = \frac{\sqrt{\frac{2}{3}} \cdot V_s}{\omega_{grid} \cdot w_G \cdot \hat{i}_m^{(r)}} \tag{B.38}$$

The magnetising current is defined by the following equation:

$$\vec{i}_m^{(r)} = \frac{\vec{\Psi}_m^{(r)}}{L_m} = \vec{i}_s^{(r)} + \vec{i}_r^{(r)} \tag{B.39}$$

$$\hat{i}_m^{(r)} = \text{abs}\left\{\vec{i}_s^{(r)} + \vec{i}_r^{(r)}\right\} \tag{B.40}$$

To avoid an arithmetic loop, the value of L_m is updated with a delay of one simulation step.

The $\alpha\beta$-model with saturation of the mutual inductance is validated by comparison with measurement as well as with simulation results from PSCAD®. The measurements were made with open stator terminals. For the simulations a stator voltage is applied to force the stator current below $0.02 \cdot \hat{i}_m^{(r)}$. The results are given in Fig. B.5. The stator voltage is related to the nominal stator voltage, the rotor magnetising current to the rotor current affiliated to the nominal stator voltage.

The saturation was integrated in both models, the three-phase and the $\alpha\beta$-model. The results of both models are identical. In the simulations on which this study is based, the $\alpha\beta$-model with saturation of the mutual inductance was used.

B.3 Three-phase transformer with three-limb core

In [32, p. 102 et seqq.] detailed descriptions and deductions of linear model equations for three-phase transformers can be found. More complex models incorporating hysteresis and eddy current effects are described in [7, 21]. In the present study a model considering only the

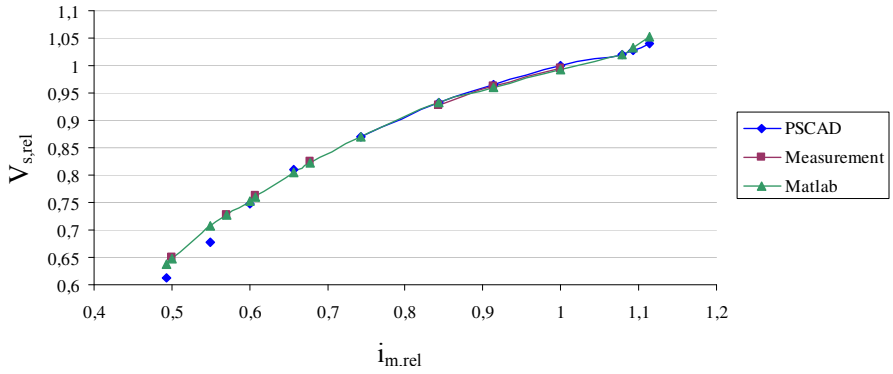

Figure B.5: Stator voltage of the DFIG for different rotor magnetising currents, related quantities

fundamental frequency was used. Hysteresis and eddy current losses were disregarded – because no data was available (core geometry and material characteristics) – or rather approximated by an ohmic resistance. The inductances and ohmic resistances are assumed to be constant. Four different transformer models were developed:

- 3-phase model without consideration of iron losses
- $\alpha\beta 0$-model without consideration of iron losses
- $\alpha\beta$-model with iron losses serial to main inductance
- $\alpha\beta$-model with iron losses parallel to main inductance

The input and output quantities of the models are given in Table B.2. The main transformer of

Table B.2: Transformer model ports

Quantity	Symbol	Port type	Dimension
HV voltages	$v_{H,123}$	Input	3
LV voltages	$v_{L,123}$	Input	3
HV currents	$i_{H,123}$	Output	3
LV currents	$i_{L,123}$	Output	3

the system is connected in ΔY. The transformation from winding to line quantities is realised by Eqs. B.5 and B.6. In the following deduction the winding quantities (subscript W) are used, the transformation is omitted.

B.3.1 Three-phase transformer model

The three-phase voltage equations are:

$$\begin{pmatrix} v_{H1W} \\ v_{H2W} \\ v_{H3W} \end{pmatrix} = R_H \cdot \begin{pmatrix} i_{H1W} \\ i_{H2W} \\ i_{H3W} \end{pmatrix} + \frac{d}{dt} \begin{pmatrix} \Psi_{H1} \\ \Psi_{H2} \\ \Psi_{H3} \end{pmatrix} = R_H \cdot \begin{pmatrix} i_{H1W} \\ i_{H2W} \\ i_{H3W} \end{pmatrix} + w_H \cdot \frac{d}{dt} \begin{pmatrix} \Phi_{H1} \\ \Phi_{H2} \\ \Phi_{H3} \end{pmatrix} \tag{B.41}$$

$$\begin{pmatrix} v_{L1W} \\ v_{L2W} \\ v_{L3W} \end{pmatrix} = R_L \cdot \begin{pmatrix} i_{L1W} \\ i_{L2W} \\ i_{L3W} \end{pmatrix} + \frac{d}{dt} \begin{pmatrix} \Psi_{L1} \\ \Psi_{L2} \\ \Psi_{L3} \end{pmatrix} = R_L \cdot \begin{pmatrix} i_{L1W} \\ i_{L2W} \\ i_{L3W} \end{pmatrix} + w_L \cdot \frac{d}{dt} \begin{pmatrix} \Phi_{L1} \\ \Phi_{L2} \\ \Phi_{L3} \end{pmatrix} \tag{B.42}$$

with

$$\begin{pmatrix} \Phi_{H1} \\ \Phi_{H2} \\ \Phi_{H3} \end{pmatrix} = \begin{pmatrix} \Phi_{H1\sigma} + \Phi_{H1m} + \Phi_{L1m} - \Phi_{21} - \Phi_{31} \\ \Phi_{H2\sigma} + \Phi_{H2m} + \Phi_{L2m} - \Phi_{12} - \Phi_{32} \\ \Phi_{H3\sigma} + \Phi_{H3m} + \Phi_{L3m} - \Phi_{13} - \Phi_{23} \end{pmatrix} \tag{B.43}$$

$$\begin{pmatrix} \Phi_{L1} \\ \Phi_{L2} \\ \Phi_{L3} \end{pmatrix} = \begin{pmatrix} \Phi_{L1\sigma} + \Phi_{L1m} + \Phi_{H1m} - \Phi_{21} - \Phi_{31} \\ \Phi_{L2\sigma} + \Phi_{L2m} + \Phi_{H2m} - \Phi_{12} - \Phi_{32} \\ \Phi_{L3\sigma} + \Phi_{L3m} + \Phi_{H3m} - \Phi_{13} - \Phi_{23} \end{pmatrix} \tag{B.44}$$

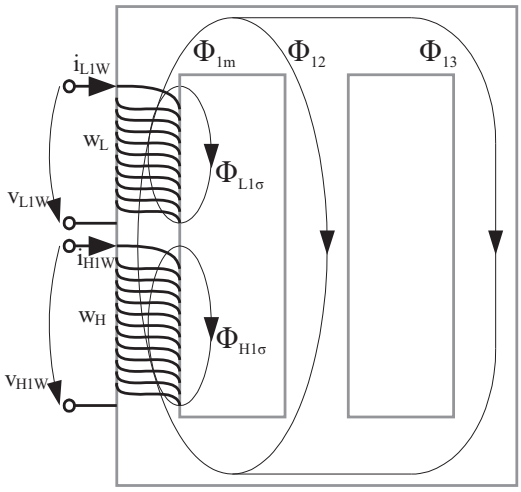

Figure B.6: Flux generation in a three-phase three-limb transformer

The generation of the flux is shown in Fig. B.6 for one phase. Assuming a symmetrical core with identical magnetic coupling between each pair of windings the flux values can be calculated

from the currents by the following equations:

$$\Phi_{H1\sigma} = \frac{w_H}{R_{mH\sigma}} \cdot i_{H1} \qquad \Phi_{H2\sigma} = \frac{w_H}{R_{mH\sigma}} \cdot i_{H2} \qquad \Phi_{H3\sigma} = \frac{w_H}{R_{mH\sigma}} \cdot i_{H3} \tag{B.45}$$

$$\Phi_{L1\sigma} = \frac{w_L}{R_{mL\sigma}} \cdot i_{L1} \qquad \Phi_{L2\sigma} = \frac{w_L}{R_{mL\sigma}} \cdot i_{L2} \qquad \Phi_{L3\sigma} = \frac{w_L}{R_{mL\sigma}} \cdot i_{L3} \tag{B.46}$$

$$\Phi_{H1m} = \frac{w_H}{R_{mm11}} \cdot i_{H1} \qquad \Phi_{H2m} = \frac{w_H}{R_{mm22}} \cdot i_{H2} \qquad \Phi_{H3m} = \frac{w_H}{R_{mm33}} \cdot i_{H3} \tag{B.47}$$

$$\Phi_{L1m} = \frac{w_L}{R_{mm11}} \cdot i_{L1} \qquad \Phi_{L2m} = \frac{w_L}{R_{mm22}} \cdot i_{L2} \qquad \Phi_{L3m} = \frac{w_L}{R_{mm33}} \cdot i_{L3} \tag{B.48}$$

$$\Phi_{12} = \frac{w_L \cdot i_{L1} + w_H \cdot i_{H1}}{R_{mm12}} \qquad \Phi_{21} = \frac{w_L \cdot i_{L2} + w_H \cdot i_{H2}}{R_{mm21}} \tag{B.49}$$

$$\Phi_{13} = \frac{w_L \cdot i_{L1} + w_H \cdot i_{H1}}{R_{mm13}} \qquad \Phi_{31} = \frac{w_L \cdot i_{L3} + w_H \cdot i_{H3}}{R_{mm31}} \tag{B.50}$$

$$\Phi_{23} = \frac{w_L \cdot i_{L2} + w_H \cdot i_{H2}}{R_{mm23}} \qquad \Phi_{32} = \frac{w_L \cdot i_{L3} + w_H \cdot i_{H3}}{R_{mm32}} \tag{B.51}$$

With the following magnetic resistances:

$$R_{mm} = R_{mm11} \qquad = R_{mm22} \qquad = R_{mm33} \tag{B.52}$$

$$2 \cdot R_{mm} = R_{mm12} \qquad = R_{mm21} \qquad = R_{mm13} \qquad = R_{mm31} \qquad = R_{mm23} \qquad = R_{mm32} \tag{B.53}$$

Based on Eqs. B.45 – B.53 the following inductances can be defined:

$$L_{H\sigma} = \frac{w_H^2}{R_{mH\sigma}} \qquad L_{L\sigma} = \frac{w_L^2}{R_{mL\sigma}} \tag{B.54}$$

$$L_{Hm3} = \frac{w_H^2}{R_{mm}} \qquad L_{Lm3} = \frac{w_L^2}{R_{mm}} \qquad M_{HLxx3} = \frac{w_H \cdot w_L}{R_{mm}} \tag{B.55}$$

$$M_{HHxy3} = \frac{w_H^2}{2 \cdot R_{mm}} \qquad M_{LLxy3} = \frac{w_L^2}{2 \cdot R_{mm}} \qquad M_{HLxy3} = \frac{w_H \cdot w_L}{2 \cdot R_{mm}} \tag{B.56}$$

With these definitions the Eqs. B.41 and B.42 can be written as:

$$\begin{pmatrix} v_{H1W} \\ v_{H2W} \\ v_{H3W} \end{pmatrix} = R_H \cdot \begin{pmatrix} i_{H1W} \\ i_{H2W} \\ i_{H3W} \end{pmatrix} + [L_{H3}] \cdot \frac{d}{dt} \begin{pmatrix} i_{H1W} \\ i_{H2W} \\ i_{H3W} \end{pmatrix} + [M_3] \cdot \frac{d}{dt} \begin{pmatrix} i_{L1W} \\ i_{L2W} \\ i_{L3W} \end{pmatrix} \tag{B.57}$$

$$\begin{pmatrix} v_{L1W} \\ v_{L2W} \\ v_{L3W} \end{pmatrix} = R_L \cdot \begin{pmatrix} i_{L1W} \\ i_{L2W} \\ i_{L3W} \end{pmatrix} + [M_3] \cdot \frac{d}{dt} \begin{pmatrix} i_{H1W} \\ i_{H2W} \\ i_{H3W} \end{pmatrix} + [L_{L3}] \cdot \frac{d}{dt} \begin{pmatrix} i_{L1W} \\ i_{L2W} \\ i_{L3W} \end{pmatrix} \tag{B.58}$$

The inductance matrices $[L_{H3}]$, $[L_{L3}]$ and $[M_3]$ are:

$$[L_{H3}] = \begin{pmatrix} L_{H\sigma} + L_{Hm3} & -M_{HHxy3} & -M_{HHxy3} \\ -M_{HHxy3} & L_{H\sigma} + L_{Hm3} & -M_{HHxy3} \\ -M_{HHxy3} & -M_{HHxy3} & L_{H\sigma} + L_{Hm3} \end{pmatrix} \tag{B.59}$$

$$[L_{L3}] = \begin{pmatrix} L_{L\sigma} + L_{Lm3} & -M_{LLxy3} & -M_{LLxy3} \\ -M_{LLxy3} & L_{L\sigma} + L_{Lm3} & -M_{LLxy3} \\ -M_{LLxy3} & -M_{LLxy3} & L_{L\sigma} + L_{Lm3} \end{pmatrix} \tag{B.60}$$

$$[M_3] = \begin{pmatrix} M_{HLxx3} & -M_{HLxy3} & -M_{HLxy3} \\ -M_{HLxy3} & M_{HLxx3} & -M_{HLxy3} \\ -M_{HLxy3} & -M_{HLxy3} & M_{HLxx3} \end{pmatrix} \tag{B.61}$$

Using the winding ratio $w_{TW} = w_L/w_H$ the voltage equation B.57 can be referred to the low voltage side of the transformer. Furthermore, the different mutual inductances of Eqs. B.55 and B.56 are replaced by fractions of L_{Lm3}.

$$i_{HW}^{(L)} = w_{TW} \cdot i_{HW} \tag{B.62}$$

$$u_{HW}^{(L)} = \frac{1}{w_{TW}} \cdot u_{HW} \tag{B.63}$$

$$R_H^{(L)} = \frac{1}{w_{TW}^2} \cdot R_H \tag{B.64}$$

$$\begin{pmatrix} v_{H1W}^{(L)} \\ v_{H2W}^{(L)} \\ v_{H3W}^{(L)} \end{pmatrix} = R_H^{(L)} \cdot \begin{pmatrix} i_{H1W}^{(L)} \\ i_{H2W}^{(L)} \\ i_{H3W}^{(L)} \end{pmatrix} + \left[L_{H3}^{(L)}\right] \cdot \frac{d}{dt} \begin{pmatrix} i_{H1W}^{(L)} \\ i_{H2W}^{(L)} \\ i_{H3W}^{(L)} \end{pmatrix} + \left[M_3^{(L)}\right] \cdot \frac{d}{dt} \begin{pmatrix} i_{L1W} \\ i_{L2W} \\ i_{L3W} \end{pmatrix} \tag{B.65}$$

$$\begin{pmatrix} v_{L1W} \\ v_{L2W} \\ v_{L3W} \end{pmatrix} = R_L \cdot \begin{pmatrix} i_{L1W} \\ i_{L2W} \\ i_{L3W} \end{pmatrix} + \left[M_3^{(L)}\right] \cdot \frac{d}{dt} \begin{pmatrix} i_{H1W}^{(L)} \\ i_{H2W}^{(L)} \\ i_{H3W}^{(L)} \end{pmatrix} + [L_{L3}] \cdot \frac{d}{dt} \begin{pmatrix} i_{L1W} \\ i_{L2W} \\ i_{L3W} \end{pmatrix} \tag{B.66}$$

With the inductance matrices:

$$\left[L_{H3}^{(L)}\right] = \begin{pmatrix} L_{H\sigma}^{(L)} + L_{Lm3} & -\frac{1}{2} \cdot L_{Lm3} & -\frac{1}{2} \cdot L_{Lm3} \\ -\frac{1}{2} \cdot L_{Lm3} & L_{H\sigma}^{(L)} + L_{Lm3} & -\frac{1}{2} \cdot L_{Lm3} \\ -\frac{1}{2} \cdot L_{Lm3} & -\frac{1}{2} \cdot L_{Lm3} & L_{H\sigma}^{(L)} + L_{Lm3} \end{pmatrix} \tag{B.67}$$

$$[L_{L3}] = \begin{pmatrix} L_{L\sigma} + L_{Lm3} & -\frac{1}{2} \cdot L_{Lm3} & -\frac{1}{2} \cdot L_{Lm3} \\ -\frac{1}{2} \cdot L_{Lm3} & L_{L\sigma} + L_{Lm3} & -\frac{1}{2} \cdot L_{Lm3} \\ -\frac{1}{2} \cdot L_{Lm3} & -\frac{1}{2} \cdot L_{Lm} & L_{L\sigma} + L_{Lm3} \end{pmatrix} \tag{B.68}$$

$$\left[M_3^{(L)}\right] = \begin{pmatrix} L_{Lm3} & -\frac{1}{2} \cdot L_{Lm} & -\frac{1}{2} \cdot L_{Lm3} \\ -\frac{1}{2} \cdot L_{Lm3} & L_{Lm3} & -\frac{1}{2} \cdot L_{Lm3} \\ -\frac{1}{2} \cdot L_{Lm3} & -\frac{1}{2} \cdot L_{Lm3} & L_{Lm3} \end{pmatrix} \tag{B.69}$$

B.3.2 $\alpha\beta 0$-transformer model

The transformer model of Eqs. B.65 and B.66 can be transferred to $\alpha\beta$-components using the transformation equations A.22 and A.23:

$$\begin{pmatrix} v^{(L)}_{H\alpha W} \\ v^{(L)}_{H\beta W} \\ v^{(L)}_{H0W} \end{pmatrix} = R^{(L)}_H \cdot \begin{pmatrix} i^{(L)}_{H\alpha W} \\ i^{(L)}_{H\beta W} \\ i^{(L)}_{H0W} \end{pmatrix} + \left[L^{(L)}_{H\alpha\beta 0}\right] \cdot \frac{d}{dt} \begin{pmatrix} i^{(L)}_{H\alpha W} \\ i^{(L)}_{H\beta W} \\ i^{(L)}_{H0W} \end{pmatrix} + \left[M^{(L)}_{\alpha\beta 0}\right] \cdot \frac{d}{dt} \begin{pmatrix} i_{L\alpha W} \\ i_{L\beta W} \\ i_{L0W} \end{pmatrix} \tag{B.70}$$

$$\begin{pmatrix} v_{L\alpha W} \\ v_{L\beta W} \\ v_{L0W} \end{pmatrix} = R_L \cdot \begin{pmatrix} i_{L\alpha W} \\ i_{L\beta W} \\ i_{L0W} \end{pmatrix} + \left[M^{(L)}_{\alpha\beta 0}\right] \cdot \frac{d}{dt} \begin{pmatrix} i^{(L)}_{H\alpha W} \\ i^{(L)}_{H\beta W} \\ i^{(L)}_{H0W} \end{pmatrix} + \left[L_{L\alpha\beta 0}\right] \cdot \frac{d}{dt} \begin{pmatrix} i_{L\alpha W} \\ i_{L\beta W} \\ i_{L0W} \end{pmatrix} \tag{B.71}$$

The inductance matrices of the $\alpha\beta 0$-model are:

$$\left[L^{(L)}_{H\alpha\beta 0}\right] = [C] \cdot \left[L^{(L)}_{H3}\right] \cdot \left[C^{-1}\right] = \begin{pmatrix} L^{(L)}_{H\sigma} + L_m & 0 & 0 \\ 0 & L^{(L)}_{H\sigma} + L_m & 0 \\ 0 & 0 & L^{(L)}_{H\sigma} \end{pmatrix} \tag{B.72}$$

$$\left[L_{L\alpha\beta 0}\right] = [C] \cdot [L_{L3}] \cdot \left[C^{-1}\right] = \begin{pmatrix} L_{L\sigma} + L_m & 0 & 0 \\ 0 & L_{L\sigma} + L_m & 0 \\ 0 & 0 & L_{L\sigma} \end{pmatrix} \tag{B.73}$$

$$\left[M^{(L)}_{\alpha\beta 0}\right] = [C] \cdot \left[M^{(L)}_3\right] \cdot \left[C^{-1}\right] = \begin{pmatrix} L_m & 0 & 0 \\ 0 & L_m & 0 \\ 0 & 0 & 0 \end{pmatrix} \tag{B.74}$$

with $L_m = \frac{3}{2} \cdot L_{Lm3}$.

Figs. B.7 and B.8 show the equivalent circuit diagrams of the transformer. If the high voltage windings are connected in Δ no zero sequence HV-current will be possible. In this case the equivalent circuit reduces to the one shown in Fig. B.9.

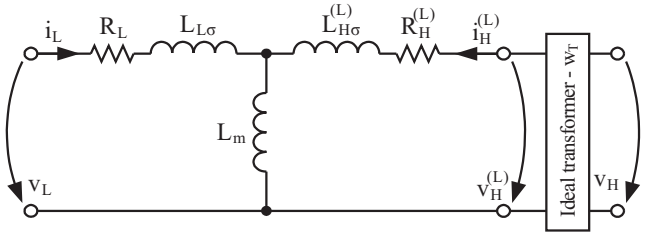

Figure B.7: Equivalent circuit of α- and β-component of a transformer

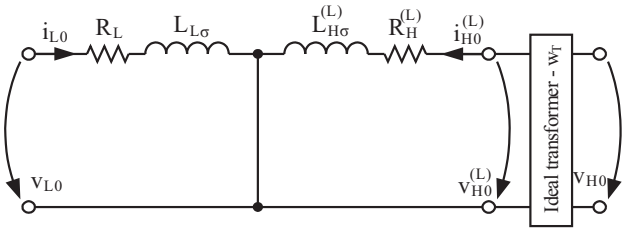

Figure B.8: Equivalent circuit of zero sequence component of a transformer

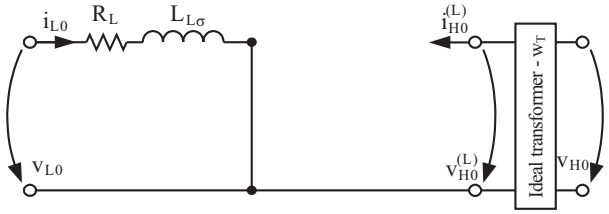

Figure B.9: Equivalent circuit of zero sequence component of a transformer with Δ-connected HV-windings

B.3.3 Transformer model with core losses

B.3.3.1 Transformer model with core losses serial to main inductance

The core losses caused by eddy currents and hysteresis of the core material can be integrated in the model approximately by an ohmic resistance serial to the main inductance. This approximation neglects the nonlinearity of the hysteresis and is only valid for one frequency and one saturation degree. The equivalent circuit for α- and β-component is given in Fig. B.10. The transformer Eqs. B.70 and B.71 have to be modified resulting in Eqs. B.75 – B.76 (space vector notation).

$$\vec{v}_{HW}^{(L)} = \left(R_H^{(L)} + R_{fe,s}\right) \cdot \vec{i}_{HW}^{(L)} + R_{fe,s} \cdot \vec{i}_{LW} + \left[L_{H\alpha\beta,s}^{(L)}\right] \cdot \frac{d}{dt}\vec{i}_{HW}^{(L)} + \left[M_{\alpha\beta,s}^{(L)}\right] \cdot \frac{d}{dt}\vec{i}_{LW} \tag{B.75}$$

$$\vec{v}_{LW} = R_{fe,s} \cdot \vec{i}_{HW}^{(L)} + (R_L + R_{fe,s}) \cdot \vec{i}_{LW} + \left[M_{\alpha\beta,s}^{(L)}\right] \cdot \frac{d}{dt}\vec{i}_{HW}^{(L)} + \left[L_{L\alpha\beta,s}\right] \cdot \frac{d}{dt}\vec{i}_{LW} \tag{B.76}$$

B.3.3.2 Transformer model with core losses parallel to main inductance

Alternatively to the serial resistance, the core losses can be approximated by a resistance parallel to the main inductance. The equivalent circuit for the α- and β-component is given in Fig. B.11.

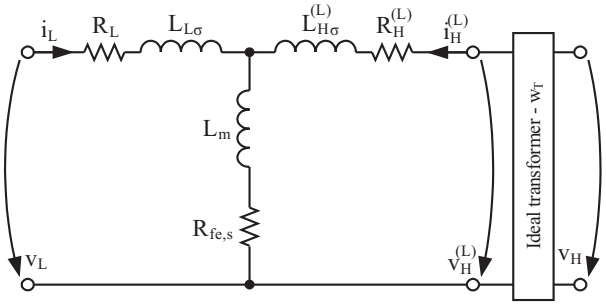

Figure B.10: Equivalent circuit of α- and β-component of a transformer with core loss resistance serial to main inductance

This model requires an additional independent state variable – the magnetising current i_m – and consequently an additional state equation:

$$\vec{v}_{HW}^{(L)} = R_H^{(L)} \cdot \vec{i}_{HW}^{(L)} + R_{fe,p} \cdot \left(\vec{i}_{HW}^{(L)} + \vec{i}_{LW} - \vec{i}_m \right) + L_{H\sigma}^{(L)} \cdot \frac{d}{dt} \vec{i}_{HW}^{(L)} \tag{B.77}$$

$$\vec{v}_{LW} = R_L \cdot \vec{i}_{LW} + R_{fe,p} \cdot \left(\vec{i}_{HW}^{(L)} + \vec{i}_{LW} - \vec{i}_m \right) + L_{L\sigma}^{(L)} \cdot \frac{d}{dt} \vec{i}_{LW} \tag{B.78}$$

$$\begin{pmatrix} 0 \\ 0 \end{pmatrix} = -R_{fe,p} \cdot \left(\vec{i}_{HW}^{(L)} + \vec{i}_{LW} - \vec{i}_m \right) + L_{m,p} \cdot \frac{d}{dt} \vec{i}_m \tag{B.79}$$

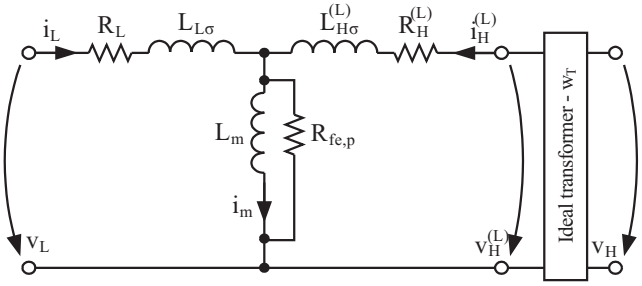

Figure B.11: Equivalent circuit of α- and β-component of a transformer with core loss resistance parallel to main inductance

B.3.3.3 Comparison of the two core loss models

If the two impedances are identical, the simulation results of the models will be the same. Therefore, the following equation has to be valid:

$$R_{fe,s} + j \cdot \omega \cdot L_{m,s} = \frac{1}{\frac{1}{R_{fe,p}} + \frac{1}{j \cdot \omega \cdot L_{m,p}}} \tag{B.80}$$

From Eq. B.80 the relations between the different elements of the equivalent circuits can be deduced:

$$R_{fe,s} = \frac{\omega^2 \cdot L_{m,p}^2 \cdot R_{fe,p}}{\omega^2 \cdot L_{m,p}^2 + R_{fe,p}^2} \quad \text{and} \quad L_{m,s} = \frac{L_{m,p} \cdot R_{fe,p}^2}{\omega^2 \cdot L_{m,p}^2 + R_{fe,p}^2} \tag{B.81}$$

$$R_{fe,p} = \frac{\omega^2 \cdot L_{m,s}^2}{R_{fe,s}} + R_{fe,s} \quad \text{and} \quad L_{m,p} = \frac{R_{fe,s}^2}{\omega^2 \cdot L_{m,s}} + L_{m,s} \tag{B.82}$$

Eqs. B.81 and B.82 imply that the models will only produce identical results for one specific frequency – the nominal frequency – of the input voltage. The simulation speed of the model with parallel resistance is significantly lower than the simulation speed of the model with serial resistance. This can be traced back to the fact that the leakage inductances and the parallel ohmic resistance build a low-pass element with a very small time constant. Hence, for the simulations on which this study is based, the model with serial resistance was used.

B.4 Inverter and DC-link

To simulate the back-to-back converter a simple model consisting of two three-phase voltage sources and a model for the DC-link capacitor was used. The structure of the model is shown in Fig. B.12 and input and output ports are summarised in Table B.3.

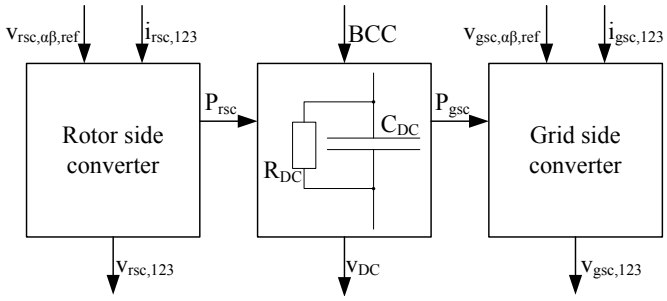

Figure B.12: Structure of converter and DC-link model

The three-phase terminal voltages are calculated from the controller outputs ($v_{\alpha\beta,ref}$) using inverse Clarke transformation. The resulting values are limited to $\pm v_{DC}/\sqrt{3}$ and are delayed by a PT1-element (time constant T_p of the inverter) representing the delay of the PWM-calculation.

The DC-link voltage is calculated from the instantaneous active power values of the two converter parts (Eq. B.83). R_{DC} can be switched from a loss resistance parallel to the DC-link capacitor to the brake chopper resistance (during line voltage dips).

$$v_{DC} = \sqrt{\frac{2}{C_{DC}} \cdot \int_0^t \left(P_{rsc} - P_{gsc} - \frac{v_{DC}^2}{R_{DC}} \right) d\theta} \tag{B.83}$$

The power values are calculated from Eqs. B.84 and B.85.

$$P_{gsc} = v_{gsc,1} \cdot i_{gsc,1} + v_{gsc,2} \cdot i_{gsc,2} + v_{gsc,3} \cdot i_{gsc,3} \tag{B.84}$$

$$P_{rsc} = v_{rsc,1} \cdot i_{rsc,1} + v_{rsc,2} \cdot i_{rsc,2} + v_{rsc,3} \cdot i_{rsc,3} \tag{B.85}$$

Table B.3: Converters and DC-link model ports

Quantity	Symbol	Port type	Dimension
Grid-side converter voltage reference values	$v_{gsc,\alpha\beta,ref}$	Input	2
Grid-side converter currents	$i_{gsc,123}$	Input	3
Rotor-side converter voltage reference values	$v_{rsc,\alpha\beta,ref}$	Input	2
Rotor-side converter currents	$i_{rsc,123}$	Input	3
Brake chopper control	BCC	Input	1
Grid-side converter voltage	$v_{gsc,123}$	Output	3
Rotor-side converter voltage	$v_{rsc,123}$	Output	3
DC-link voltage	v_{DC}	Output	1

B.5 Connection of inductive branches

B.5.1 Connection of DFIG, main transformer and GSC-transformer

Main transformer, grid-side converter transformer and DFIG are connected. All three need the terminal voltages as inputs and provide the line currents as model outputs. To connect the three elements in the model and calculate the line voltages, a capacitive branch is necessary. In reality a filter capacitor exists, which can be used to solve the inductive node of the model.

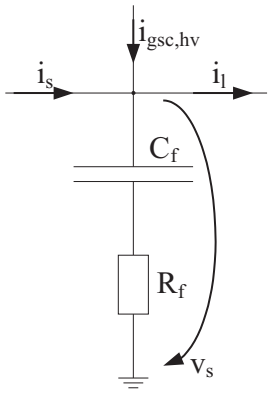

$$v_s = R_f \cdot \left(i_s - i_l + i_{gsc,hv}\right) + \frac{1}{C_f} \cdot \int_0^t \left(i_s - i_l + i_{gsc,hv}\right) d\theta \tag{B.86}$$

Figure B.13: Filter capacitor

B.5.2 Integration of rotor-side converter inductance (rotor inductor) in the DFIG model

The rotor-side converter contains a filter (inductor) of inductance and resistance between the converter switches and the rotor. To connect this inductor with the DFIG terminal (in the model), another capacitive branch would be necessary to solve the inductive node. To simplify the model, the inductor was integrated in the DFIG model, instead. The inductance and resistance of the inductor was added to rotor leakage inductance and rotor resistance respectively.

$$L_{r\sigma} = L_{\mathbf{r}\sigma} + L_{ri} \tag{B.87}$$

$$R_r = R_{\mathbf{r}} + R_{ri} \tag{B.88}$$

This causes a slight simulation error of the rotor voltage, as the point of measurement is not the same in the model and in reality.

B.6 Grid voltage angle detection

To synchronise the control of the DFIG with the grid voltage angle, usually a PLL is deployed. To maintain good behaviour and positive-sequence angle detection also during voltage dips an improved strategy was used in this study. It is deduced and described in detail in [40] and is called DSOGI-FLL (Dual Second Order Generalised Integrator with Frequency Locked Loop). The overall structure is shown in Fig. B.14. This strategy is applied in the static coordinate system using $\alpha\beta$-components and is composed of three main elements which are described in detail in this section.

SOGI-QSG Two second order generalised integrators (SOGI) combine the filtering of α- and β-direct components and the generation of the respective quadrature components (QSG

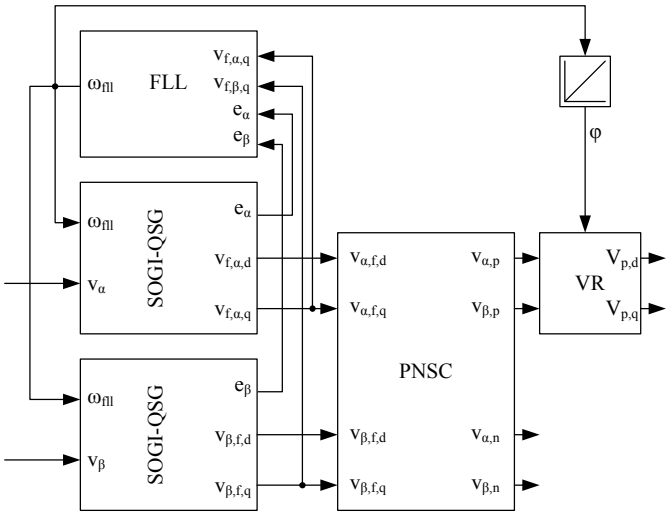

Figure B.14: Complete positive-sequence angle detection system (cf. [40])

– Quadrature Signal Generation, lagging behind the direct component by 90°). The structure of a single SOGI-QSG is given in Fig. 4.9 and the applied equations are Eqs. B.89 and B.90[1]:

$$\frac{v_{f\alpha,d}}{v_\alpha} = \frac{v_{f\beta,d}}{v_\beta} = \frac{Q_f \cdot \omega_{fll} \cdot p}{p^2 + Q_f \cdot \omega_{fll} \cdot p + \omega_{fll}^2} \tag{B.89}$$

$$\frac{v_{f\alpha,q}}{v_\alpha} = \frac{v_{f\beta,q}}{v_\beta} = \frac{Q_f \cdot \omega_{fll}^2}{p^2 + Q_f \cdot \omega_{fll} \cdot p + \omega_{fll}^2} \tag{B.90}$$

In [40] it was suggested to set $Q_f = \sqrt{2}$, therefore, this value was used for the simulations on which this study is based.

FLL A frequency locked loop (FLL) using an integral controller is employed to adapt the frequency of the SOGI-QSGs to the current grid frequency. The nominal grid frequency is added as a feed-forward control component. The controller is described by the following equation, where e_α and e_β are the differences between the original and the filtered direct components:

$$\omega_{fll} = \omega_{grid,nom} - \int_0^t K_{fll} \cdot \left(e_\alpha \cdot v_{f,\alpha,q} + e_\beta \cdot v_{f,\beta,q}\right) d\theta \tag{B.91}$$

$$e_\alpha = v_\alpha - v_{f,\alpha,d} \tag{B.92}$$

$$e_\beta = v_\beta - v_{f,\beta,d} \tag{B.93}$$

[1] Note that here, the subscripts d and q do not denote the quantity in dq-coordinate system but label the direct and quadrature component in the static $\alpha\beta$-coordinate system.

To define the gain of the integral controller of the FLL, the following considerations are made: simplified, the dynamics of the FLL can be rated by the following relation:

$$\frac{\Delta\omega_{fll}}{\Delta t} = K_{fll} \cdot e_{\%} \cdot v_{nom}^2 \tag{B.94}$$

where $e_{\%}$ represents the percentaged error of the DSOGIs and v_{nom} is the nominal value of the voltages used for the FLL (here: the stator voltages). $\Delta\omega_{fll}$ is the frequency variation that is to be recognised and adapted to by the FLL within the time Δt. $\Delta\omega_{fll}$ is set to 10% of the nominal frequency and Δt is set to one grid period, 20 ms. $e_{\%}$ depends on the frequency variation and was estimated by simulations with a frequency variation of 10%. With the resulting $e_{\%} = 0.025$ K_{fll} was set to 0.132.

PNSC Finally, the positive-sequence and negative-sequence $\alpha\beta$-components are calculated from the $\alpha\beta$-direct and -quadrature components by the PNSC (Positive Negative Sequence Calculation) using Eqs. B.95 and B.96:

$$\begin{pmatrix} v_{p,\alpha} \\ v_{p,\beta} \end{pmatrix} = \frac{1}{2} \cdot \begin{pmatrix} 1 & 0 & 0 & -1 \\ 0 & 1 & 1 & 0 \end{pmatrix} \cdot \begin{pmatrix} v_{f,\alpha,d} \\ v_{f,\alpha,q} \\ v_{f,\beta,d} \\ v_{f,\beta,q} \end{pmatrix} \tag{B.95}$$

$$\begin{pmatrix} v_{n,\alpha} \\ v_{n,\beta} \end{pmatrix} = \frac{1}{2} \cdot \begin{pmatrix} 1 & 0 & 0 & 1 \\ 0 & -1 & 1 & 0 \end{pmatrix} \cdot \begin{pmatrix} v_{f,\alpha,d} \\ v_{f,\alpha,q} \\ v_{f,\beta,d} \\ v_{f,\beta,q} \end{pmatrix} \tag{B.96}$$

As indicated by the vector rotation (VR) and the integrator in Fig. B.14, the dq-components in a rotating coordinate system can be calculated from the positive-sequence and negative-sequence $\alpha\beta$-components. The parameters used for the DSOGI-FLL are summarised in Table D.6. The functional efficiency of the FLL is illustrated by Fig. B.15.

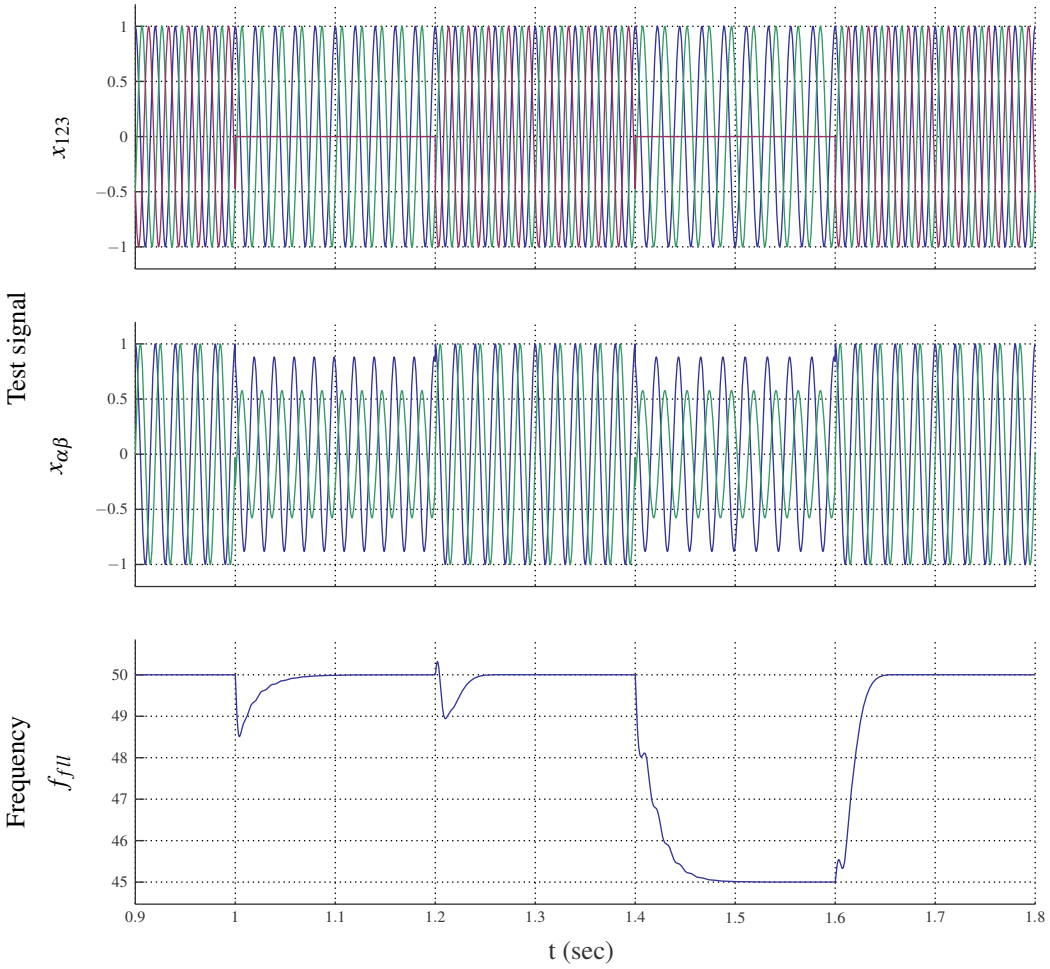

Figure B.15: FLL output frequency during one phase voltage dip to zero ($t = 1 \ldots 1.2\,\mathrm{s}$) and one phase voltage dip to zero in combination with frequency reduction to 90% of the nominal frequency ($t = 1.4 \ldots 1.6\,\mathrm{s}$)

C Auxiliary calculations

C.1 Reference value calculation in different coordinate systems

Different possibilities exist to determine the negative-sequence voltage angle for the PN-control scheme. During steady state, the angle difference will be a constant. Consequently, the reference values of the rotor-side and grid-side negative-sequence current components can be calculated in different coordinate systems. The following deduction shows that the results are equivalent, so that it is unimportant which reference angle and coordinate system is chosen. As an example, the rotor-side current reference value calculation of Eq. 4.31 is transferred from one arbitrarily chosen coordinate system (upper index $^{(1)}$) to another arbitrarily chosen coordinate system (upper index $^{(2)}$). The difference between the two n-coordinate systems is defined by $\Delta\varphi$:

$$\underline{x}_n^{(1)} = \underline{x}_n^{(2)} \cdot e^{-j\Delta\varphi} \tag{C.1}$$

$$\begin{pmatrix} x_{n,d}^{(1)} \\ x_{n,q}^{(1)} \end{pmatrix} = \begin{pmatrix} \cos(\Delta\varphi) & \sin(\Delta\varphi) \\ -\sin(\Delta\varphi) & \cos(\Delta\varphi) \end{pmatrix} \cdot \begin{pmatrix} x_{n,d}^{(2)} \\ x_{n,q}^{(2)} \end{pmatrix} \tag{C.2}$$

Eq. 4.31 in coordinate system 1 is

$$\begin{pmatrix} i_{r,n,d,ref}^{(1)} \\ i_{r,n,q,ref}^{(1)} \end{pmatrix} = \frac{1}{i_{s,p,q}^2 + i_{s,p,d}^2} \cdot \begin{pmatrix} \begin{pmatrix} i_{s,p,d} \cdot i_{s,n,d}^{(1)} - i_{s,p,q} \cdot i_{s,n,q}^{(1)} \\ i_{s,p,d} \cdot i_{s,n,q}^{(1)} + i_{s,p,q} \cdot i_{s,n,d}^{(1)} \end{pmatrix} & \begin{pmatrix} i_{s,p,d} \cdot i_{s,n,q}^{(1)} + i_{s,p,q} \cdot i_{s,n,d}^{(1)} \\ i_{s,p,q} \cdot i_{s,n,q}^{(1)} - i_{s,p,d} \cdot i_{s,n,d}^{(1)} \end{pmatrix} \end{pmatrix} \cdot \begin{pmatrix} i_{r,p,d,ref} \\ i_{r,p,q,ref} \end{pmatrix} \tag{C.3}$$

All negative-sequence components are replaced by negative-sequence components in coordinate system 2:

$$\begin{pmatrix} \cos(\Delta\varphi) & \sin(\Delta\varphi) \\ -\sin(\Delta\varphi) & \cos(\Delta\varphi) \end{pmatrix} \cdot \begin{pmatrix} i_{r,n,d,ref}^{(2)} \\ i_{r,n,q,ref}^{(2)} \end{pmatrix} = \frac{1}{i_{s,p,q}^2 + i_{s,p,d}^2} \cdot \begin{pmatrix} x_{11}^{(1)} & x_{12}^{(1)} \\ x_{21}^{(1)} & x_{22}^{(1)} \end{pmatrix} \cdot \begin{pmatrix} i_{r,p,d,ref} \\ i_{r,p,q,ref} \end{pmatrix} \tag{C.4}$$

with

$$x_{11}^{(1)} = \quad i_{s,p,d} \cdot \left(i_{s,n,d}^{(2)} \cos(\Delta\varphi) + i_{s,n,q}^{(2)} \sin(\Delta\varphi) \right) - i_{s,p,q} \cdot \left(i_{s,n,q}^{(2)} \cos(\Delta\varphi) - i_{s,n,d}^{(2)} \sin(\Delta\varphi) \right) \quad \text{(C.5)}$$

$$x_{12}^{(1)} = \quad i_{s,p,d} \cdot \left(i_{s,n,q}^{(2)} \cos(\Delta\varphi) - i_{s,n,d}^{(2)} \sin(\Delta\varphi) \right) + i_{s,p,q} \cdot \left(i_{s,n,d}^{(2)} \cos(\Delta\varphi) + i_{s,n,q}^{(2)} \sin(\Delta\varphi) \right) \quad \text{(C.6)}$$

$$x_{21}^{(1)} = \quad i_{s,p,d} \cdot \left(i_{s,n,q}^{(2)} \cos(\Delta\varphi) - i_{s,n,d}^{(2)} \sin(\Delta\varphi) \right) + i_{s,p,q} \cdot \left(i_{s,n,d}^{(2)} \cos(\Delta\varphi) + i_{s,n,q}^{(2)} \sin(\Delta\varphi) \right) \quad \text{(C.7)}$$

$$x_{22}^{(1)} = -i_{s,p,d} \cdot \left(i_{s,n,d}^{(2)} \cos(\Delta\varphi) + i_{s,n,q}^{(2)} \sin(\Delta\varphi) \right) + i_{s,p,q} \cdot \left(i_{s,n,q}^{(2)} \cos(\Delta\varphi) - i_{s,n,d}^{(2)} \sin(\Delta\varphi) \right) \quad \text{(C.8)}$$

Eq. C.4 can be rearranged by a multiplication with the inverse rotation matrix of Eq. C.2:

$$\begin{pmatrix} i_{r,n,d,ref}^{(2)} \\ i_{r,n,q,ref}^{(2)} \end{pmatrix} = \frac{1}{i_{s,p,q}^2 + i_{s,p,d}^2} \cdot \begin{pmatrix} x_{11}^{(2)} & x_{12}^{(2)} \\ x_{21}^{(2)} & x_{22}^{(2)} \end{pmatrix} \cdot \begin{pmatrix} i_{r,p,d,ref} \\ i_{r,p,q,ref} \end{pmatrix} \quad \text{(C.9)}$$

with

$$x_{11}^{(2)} = x_{11}^{(1)} \cos(\Delta\varphi) - x_{21}^{(1)} \sin(\Delta\varphi) = \quad i_{s,p,d} \cdot i_{s,n,d}^{(2)} - i_{s,p,q} \cdot i_{s,n,q}^{(2)} \quad \text{(C.10)}$$

$$x_{12}^{(2)} = x_{12}^{(1)} \cos(\Delta\varphi) - x_{22}^{(1)} \sin(\Delta\varphi) = \quad i_{s,p,d} \cdot i_{s,n,q}^{(2)} + i_{s,p,q} \cdot i_{s,n,d}^{(2)} \quad \text{(C.11)}$$

$$x_{21}^{(2)} = x_{11}^{(1)} \sin(\Delta\varphi) + x_{21}^{(1)} \cos(\Delta\varphi) = \quad i_{s,p,d} \cdot i_{s,n,q}^{(2)} + i_{s,p,q} \cdot i_{s,n,d}^{(2)} \quad \text{(C.12)}$$

$$x_{22}^{(2)} = x_{12}^{(1)} \sin(\Delta\varphi) + x_{22}^{(1)} \cos(\Delta\varphi) = -i_{s,p,d} \cdot i_{s,n,d}^{(2)} + i_{s,p,q} \cdot i_{s,n,q}^{(2)} \quad \text{(C.13)}$$

Eq. C.9 is identical to Eq. C.3. Of course, the distribution of the negative-sequence rotor and stator current components to nd- and nq-components will differ but the algorithm for the calculation of negative-sequence reference values is independent of the chosen coordinate system. Also, in the static $\alpha\beta$-coordinate system, the currents will not differ (during steady state).

C.2 Calculation of maximum rotor voltages during stator voltage dips

To estimate the rotor-side inverter voltage range necessary to guaranty the controllability of the DFIG during different types and dip-depths of stator voltage dips, in [24] and in [25] the following approach is proposed[1]: based on the machine equations given in Appendix B.2.2, the rotor voltage is calculated depending only on the stator voltages. It is assumed that the rotor terminals are not connected to the inverter nor are they short circuited. Therefore, no rotor

[1] Note: for the following estimation the saturation of the DFIGs mutual inductance is disregarded. This saturation may reduce the evolving rotor voltages in reality, hence, the calculated maximum rotor voltages build a worst-case scenario.

currents are possible. With this assumption Eqs. B.30 and B.32 – B.34 can be converted to:

$$\vec{i}_r \quad \stackrel{!}{=} 0 \tag{C.14}$$

$$\vec{v}_s^s \quad = R_s \cdot \vec{i}_s^s + \frac{d}{dt}\vec{\Psi}_s^s \qquad \Rightarrow \quad \vec{\Psi}_s^s = \int_0^t \left(\vec{v}_s^s - R_s \cdot \vec{i}_s^s\right) d\theta \tag{C.15}$$

$$\vec{v}_r^{s,(s)} = \left(\frac{d}{dt} - j \cdot \dot{\gamma}\right) \vec{\Psi}_r^{s,(s)} \tag{C.16}$$

$$\vec{\Psi}_s^s \quad = (L_m + L_{s\sigma}) \cdot \vec{i}_s^s \tag{C.17}$$

$$\vec{\Psi}_r^{s,(s)} = L_m \cdot \vec{i}_s^s \tag{C.18}$$

Using Eqs. C.17 and C.18 the linked rotor flux can be calculated from the linked stator flux:

$$\vec{\Psi}_r^{s,(s)} = \frac{L_m}{L_m + L_{s\sigma}} \cdot \vec{\Psi}_s^s \tag{C.19}$$

Inserting Eq. C.19 into Eq. C.16, the rotor voltage is obtained:

$$\vec{v}_r^{s,(s)} = \frac{L_m}{L_m + L_{s\sigma}} \cdot \left(\frac{d}{dt} - j \cdot \dot{\gamma}\right) \vec{\Psi}_s^s \tag{C.20}$$

$$\vec{v}_r^{s,(s)} = \frac{L_m}{L_m + L_{s\sigma}} \cdot \left(\frac{d}{dt} - j \cdot \omega_{grid} \cdot (1 - s)\right) \vec{\Psi}_s^s \tag{C.21}$$

To get the linked stator flux as a variable of the stator voltages, Eq. C.17 is inserted into Eq. C.15:

$$\vec{v}_s^s = \frac{R_s}{L_m + L_{s\sigma}} \cdot \vec{\Psi}_s^s + \frac{d}{dt}\vec{\Psi}_s^s \tag{C.22}$$

$$\vec{v}_s^s(t) = \frac{1}{\tau} \cdot \vec{\Psi}_s^s(t) + \frac{d}{dt}\vec{\Psi}_s^s(t) \quad \text{with} \quad \tau = \frac{L_m + L_{s\sigma}}{R_s} \tag{C.23}$$

The differential equation C.23 of the linked stator flux $\vec{\Psi}_s^s$ has to be solved to allow for a calculation of the rotor voltages using Eq. C.21. The general solution of this linear first order differential equation consists of a solution for the related homogeneous differential equation (subscript h) and a particular integral of the non homogeneous differential equation (subscript p), the latter depending on the time dependent behaviour of $\vec{v}_s^s$[2]:

$$\vec{\Psi}_s^s(t) = \vec{\Psi}_{s,h}^s + \vec{\Psi}_{s,p}^s \tag{C.24}$$

$$\vec{\Psi}_{s,h}^s(t) = \vec{\Psi}_s^s(t = t_0) \cdot e^{-(t-t_0)/\tau} \tag{C.25}$$

$$\vec{\Psi}_{s,p}^s(t) = e^{-t/\tau} \cdot \int_{t_0}^t \left(e^{\theta/\tau} \cdot \vec{v}_s^s(\theta)\right) d\theta \tag{C.26}$$

[2]For the particular integral given in Eq. C.26 see [38, p. 199]

In the following, Eqs. C.21 and C.23 – C.26 are used to calculate the maximum possible rotor voltage for each type of stator voltage dip, assuming that the fault occurs directly at the stator terminals. If the rotor is connected to the inverter or to a crowbar, the rotor terminal voltages will be less than these calculated voltages because of the voltage drop caused by the rotor resistance and the rotor leakage inductance. Furthermore, the voltage drop caused by the main transformer and grid impedances between the wind turbine and the failure location reduce the dip-depth on the stator terminals in real configurations and thus limit the loads on the DFIG system.

C.2.1 Symmetrical voltage dip (3P-dip)

Before and during a symmetrical dip the stator voltage is (t_0 = time of dip start):

$$\vec{v}_s^s(t) = \begin{cases} \hat{\vec{v}}_{s,nom}^s \cdot e^{j\cdot\omega_{grid}\cdot t} & \text{for} \quad t \le t_0 \\ (1-d)\cdot\hat{\vec{v}}_{s,nom}^s \cdot e^{j\cdot\omega_{grid}\cdot t} & \text{for} \quad t > t_0 \end{cases} \tag{C.27}$$

where d is the relative dip-depth: $d = 1 - v_{s,dip}/v_{s,nom} = 0\ldots1$. Neglecting the voltage drop caused by the (small) stator resistance, the linked stator flux before dip start can be calculated from:

$$\vec{\Psi}_s^s(t) = \int_0^t \vec{v}_s^s(\theta)\,d\theta \tag{C.28}$$

$$= \int_0^t \left(\hat{\vec{v}}_{s,nom}^s \cdot e^{j\cdot\omega_{grid}\cdot\theta}\right) d\theta \tag{C.29}$$

$$= \frac{\hat{\vec{v}}_{s,nom}^s}{j\cdot\omega_{grid}} \cdot e^{j\cdot\omega_{grid}\cdot t} - \frac{\hat{\vec{v}}_{s,nom}^s(t=0)}{j\cdot\omega_{grid}} \tag{C.30}$$

$$\vec{\Psi}_s^s(t=t_0) = \frac{\hat{\vec{v}}_{s,nom}^s}{j\cdot\omega_{grid}} \cdot e^{j\cdot\omega_{grid}\cdot t_0} \tag{C.31}$$

Where the second summand of Eq. C.30 is assumed to be zero. Introducing Eq. C.31 into Eq. C.25, the solution of the homogeneous differential equation becomes:

$$\vec{\Psi}_{s,h}^s(t) = \frac{\hat{\vec{v}}_{s,nom}^s}{j\cdot\omega_{grid}} \cdot e^{j\cdot\omega_{grid}\cdot t_0} \cdot e^{-(t-t_0)/\tau} \tag{C.32}$$

The particular integral of the non homogeneous equation can be obtained by introducing the second line of Eq. C.27 into Eq. C.26:

$$\vec{\Psi}_{s,p}^s(t) = e^{-t/\tau} \cdot \int_{t_0}^t \left(e^{\theta/\tau}\cdot(1-d)\cdot\hat{\vec{v}}_{s,nom}^s \cdot e^{j\cdot\omega_{grid}\cdot\theta}\right) d\theta \tag{C.33}$$

$$= (1-d)\cdot\hat{\vec{v}}^{s}_{s,nom}\cdot e^{-t/\tau}\cdot\int_{t_0}^{t} e^{\theta\cdot\left(1/\tau+j\cdot\omega_{grid}\right)}d\theta \tag{C.34}$$

$$= (1-d)\cdot\hat{\vec{v}}^{s}_{s,nom}\cdot e^{-t/\tau}\cdot\left(\frac{1}{1/\tau+j\cdot\omega_{grid}}\cdot e^{\theta\cdot\left(1/\tau+j\cdot\omega_{grid}\right)}\right)_{t_0}^{t} \tag{C.35}$$

$$= \frac{(1-d)\cdot\hat{\vec{v}}^{s}_{s,nom}}{1/\tau+j\cdot\omega_{grid}}\cdot\left(e^{j\cdot\omega_{grid}\cdot t}-e^{j\cdot\omega_{grid}\cdot t_0}\cdot e^{t_0/\tau}\cdot e^{-t/\tau}\right) \tag{C.36}$$

Because $1/\tau \ll \omega_{grid}$ Eq. C.36 can be simplified to:

$$\vec{\Psi}^{s}_{s,p}(t) = \frac{(1-d)\cdot\hat{\vec{v}}^{s}_{s,nom}}{j\cdot\omega_{grid}}\cdot\left(e^{j\cdot\omega_{grid}\cdot t}-e^{j\cdot\omega_{grid}\cdot t_0}\cdot e^{t_0/\tau}\cdot e^{-t/\tau}\right) \tag{C.37}$$

For symmetrical dips the instant of dip start does not affect the maximum rotor voltage, therefore, t_0 is set to zero. With this assumption the particular integral of the non homogeneous differential equation becomes:

$$\vec{\Psi}^{s}_{s,p}(t) = \frac{\hat{\vec{v}}^{s}_{s,nom}}{j\cdot\omega_{grid}}\cdot(1-d)\cdot e^{j\cdot\omega_{grid}\cdot t}+\frac{\hat{\vec{v}}^{s}_{s,nom}}{j\cdot\omega_{grid}}\cdot(d-1)\cdot e^{-t/\tau} \tag{C.38}$$

By applying the condition $t_0 = 0\,\mathrm{s}$ and introducing Eqs. C.32 and C.38 into Eq. C.24 the complete linked stator flux vector is obtained:

$$\vec{\Psi}^{s}_{s}(t) = \frac{\hat{\vec{v}}^{s}_{s,nom}}{j\cdot\omega_{grid}}\cdot\left[(1-d)\cdot e^{j\cdot\omega_{grid}\cdot t}+(d-1)\cdot e^{-t/\tau}+e^{-t/\tau}\right] \tag{C.39}$$

$$= \frac{\hat{\vec{v}}^{s}_{s,nom}}{j\cdot\omega_{grid}}\cdot\left[(1-d)\cdot e^{j\cdot\omega_{grid}\cdot t}+d\cdot e^{-t/\tau}\right] \tag{C.40}$$

The first summand of Eq. C.40 is called "forced flux" (subscript f) in the following, because it is directly dependent on the actual stator voltage. The second summand is named "natural flux" (subscript *nat*) as it is caused by the physical condition that the flux cannot be discontinuous.[3] For the sake of clarity, these components will be used separately in the following:

$$\vec{\Psi}^{s}_{s} = \vec{\Psi}^{s}_{s,f}+\vec{\Psi}^{s}_{s,nat} \tag{C.41}$$

$$\vec{\Psi}^{s}_{s,f} = \frac{\hat{\vec{v}}^{s}_{s,nom}}{j\cdot\omega_{grid}}\cdot(1-d)\cdot e^{j\cdot\omega_{grid}\cdot t} \tag{C.42}$$

$$\vec{\Psi}^{s}_{s,nat} = \frac{\hat{\vec{v}}^{s}_{s,nom}}{j\cdot\omega_{grid}}\cdot d\cdot e^{-t/\tau} \tag{C.43}$$

[3] In the following subsections this consideration will be used to calculate the linked stator flux without solving the differential equation for each configuration: the forced flux can be determined easily by inserting the actual stator voltage vector during the dip into Eq. C.30, while the natural flux can be obtained by calculating the difference between the forced flux at $t = t_0$ and the forced flux during the dip.

By introducing the linked flux components of Eqs. C.42 and C.43 into Eq. C.21 the respective rotor voltage components during a three-phase dip are calculated:

$$\vec{v}_{r,f}^{s,(s)} = \frac{L_m}{L_m + L_{s\sigma}} \cdot \hat{\vec{v}}_{s,nom}^{s} \cdot s \cdot (1-d) \cdot e^{j \cdot \omega_{grid} \cdot t} \tag{C.44}$$

$$\vec{v}_{r,nat}^{s,(s)} = \frac{L_m}{L_m + L_{s\sigma}} \cdot \hat{\vec{v}}_{s,nom}^{s} \cdot d \cdot \left[\frac{-1}{j \cdot \omega_{grid} \cdot \tau} - (1-s) \right] \cdot e^{-t/\tau} \tag{C.45}$$

By neglecting the term $1/\left(j\omega_{grid}\tau\right)$ in Eq. C.45 the maximum rotor voltage components become:

$$\vec{v}_{r,f}^{s,(s)} = \frac{L_m}{L_m + L_{s\sigma}} \cdot \hat{\vec{v}}_{s,nom}^{s} \cdot s \cdot (1-d) \cdot e^{j \cdot \omega_{grid} \cdot t} \tag{C.46}$$

$$\vec{v}_{r,nat}^{s,(s)} = \frac{L_m}{L_m + L_{s\sigma}} \cdot \hat{\vec{v}}_{s,nom}^{s} \cdot d \cdot (s-1) \cdot e^{-t/\tau} \tag{C.47}$$

In Table 4.4 the voltage component $\vec{v}_{r,f}^{s,(s)}$ is named $\vec{v}_{r,p}^{s,(s)}$ to allow for a consistent terminology (cf. the following sections), because it corresponds to the positive-sequence stator voltage.

C.2.2 Two-phase voltage dip to earth (2P-dip)

During a two-phase voltage dip the stator voltage will contain a positive-sequence component and a negative-sequence component. These two components can be calculated using the static phasor representation described in Appendix A.2 and the Fortescue transformation described in Appendix A.3[4]. The voltage dip is applied to phases two and three:

$$\begin{pmatrix} \underline{v}_{s,p} \\ \underline{v}_{s,n} \end{pmatrix} = \frac{1}{3} \cdot \begin{pmatrix} 1 & \underline{a} & \underline{a}^2 \\ 1 & \underline{a}^2 & \underline{a} \end{pmatrix} \cdot \hat{\vec{v}}_{s,nom} \cdot \begin{pmatrix} e^{j \cdot 0} \\ (1-d) \cdot e^{-j \cdot 2 \cdot \pi/3} \\ (1-d) \cdot e^{j \cdot 2 \cdot \pi/3} \end{pmatrix} \tag{C.48}$$

$$= \hat{\vec{v}}_{s,nom} \cdot \begin{pmatrix} (1 - 2/3 \cdot d) \\ d/3 \end{pmatrix} \tag{C.49}$$

$v_{s,p}$ corresponds to a space vector component rotating with grid frequency, while $v_{s,n}$ corresponds to a space vector component contra-rotating with negative grid frequency. The stator voltage vector can be represented by:

$$\vec{v}_s = \underline{v}_{s,p} \cdot e^{j \cdot \omega_{grid} \cdot t} + \underline{v}_{s,n} \cdot e^{-j \cdot \omega_{grid} \cdot t} \tag{C.50}$$

$$= \hat{\vec{v}}_{s,nom} \cdot \left[\left(1 - \frac{2 \cdot d}{3} \right) \cdot e^{j \cdot \omega_{grid} \cdot t} + \frac{d}{3} \cdot e^{-j \cdot \omega_{grid} \cdot t} \right] \tag{C.51}$$

[4]The main transformer connecting the DFIG to the grid is connected in $Y\Delta$, the low voltage neutral point is grounded, hence, no zero sequence voltage component is possible. Therefore, the zero sequence component is not considered in the following deductions.

Analogously to the considerations for the symmetrical dip, the stator voltage vector before and during a two-phase dip becomes:

$$\vec{v}_s^s(t) = \begin{cases} \hat{\vec{v}}_{s,nom}^s \cdot e^{j\cdot\omega_{grid}\cdot t} & \text{for} \quad t \le t_0 \\ \hat{\vec{v}}_{s,nom}^s \cdot \left[\left(1-\frac{2\cdot d}{3}\right)\cdot e^{j\cdot\omega_{grid}\cdot t} + \frac{d}{3}\cdot e^{-j\cdot\omega_{grid}\cdot t}\right] & \text{for} \quad t > t_0 \end{cases} \tag{C.52}$$

By using Eq. C.28 the forced stator flux before and during the dip is obtained:

$$\vec{\Psi}_{s,f}^s(t) = \frac{\hat{\vec{v}}_{s,nom}^s}{j\cdot\omega_{grid}} \cdot \begin{cases} e^{j\cdot\omega_{grid}\cdot t} & \text{for} \quad t \le t_0 \\ \left(1-\frac{2\cdot d}{3}\right)\cdot e^{j\cdot\omega_{grid}\cdot t} - \frac{d}{3}\cdot e^{-j\cdot\omega_{grid}\cdot t} & \text{for} \quad t > t_0 \end{cases} \tag{C.53}$$

The natural flux component can be calculated from the difference between the two linked flux values at $t = t_0$:

$$\vec{\Psi}_{s,nat}^s(t=t_0) = \frac{\hat{\vec{v}}_{s,nom}^s}{j\cdot\omega_{grid}} \cdot \left(e^{j\cdot\omega_{grid}\cdot t_0} - \left[\left(1-\frac{2\cdot d}{3}\right)\cdot e^{j\cdot\omega_{grid}\cdot t_0} - \frac{d}{3}\cdot e^{-j\cdot\omega_{grid}\cdot t_0}\right]\right) \tag{C.54}$$

$$= \frac{\hat{\vec{v}}_{s,nom}^s}{j\cdot\omega_{grid}} \cdot \left(\frac{2\cdot d}{3}\cdot e^{j\cdot\omega_{grid}\cdot t_0} + \frac{d}{3}\cdot e^{-j\cdot\omega_{grid}\cdot t_0}\right) \tag{C.55}$$

The amplitude of the natural flux component varies with the time instant of dip start. If the dip starts at $t_0 = 0$ the amplitude of the natural flux will become maximal and the natural flux obtained using this amplitude is:

$$\hat{\vec{\Psi}}_{s,nat,max}^s = d \cdot \frac{\hat{\vec{v}}_{s,nom}^s}{j\cdot\omega_{grid}} \cdot e^{-t/\tau} \tag{C.56}$$

During the dip the forced stator flux contains a positive-sequence and a negative-sequence component caused by positive-sequence and negative-sequence stator voltage components (second line of Eq. C.53). Again, these components are used separately in the following:

$$\vec{\Psi}_{s,f}^s = \vec{\Psi}_{s,p}^s + \vec{\Psi}_{s,n}^s \tag{C.57}$$

$$\vec{\Psi}_{s,p}^s = \frac{\hat{\vec{v}}_{s,nom}^s}{j\cdot\omega_{grid}} \cdot \left(1-\frac{2\cdot d}{3}\right)\cdot e^{j\cdot\omega_{grid}\cdot t} \tag{C.58}$$

$$\vec{\Psi}_{s,n}^s = -\frac{\hat{\vec{v}}_{s,nom}^s}{j\cdot\omega_{grid}} \cdot \frac{d}{3}\cdot e^{-j\cdot\omega_{grid}\cdot t} \tag{C.59}$$

The three linked stator flux components of Eqs. C.56, C.58 and C.59 are inserted into Eq. C.21 to obtain the respective rotor voltage components:

$$\vec{v}_{r,nat,max}^{s,(s)} = \frac{L_m}{L_m + L_{s\sigma}} \cdot \hat{\vec{v}}_{s,nom}^s \cdot d \cdot \left[\frac{-1}{j\cdot\omega_{grid}\cdot\tau} - (1-s)\right] \cdot e^{-t/\tau}$$

$$\approx \frac{L_m}{L_m + L_{s\sigma}} \cdot \hat{\vec{v}}_{s,nom}^s \cdot d \cdot (s-1) \cdot e^{-t/\tau} \tag{C.60}$$

$$\vec{v}_{r,p}^{s,(s)} = \frac{L_m}{L_m + L_{s\sigma}} \cdot \hat{\vec{v}}_{s,nom}^{s} \cdot s \cdot \left(1 - \frac{2 \cdot d}{3}\right) \cdot e^{j \cdot \omega_{grid} \cdot t} \tag{C.61}$$

$$\vec{v}_{r,n}^{s,(s)} = \frac{L_m}{L_m + L_{s\sigma}} \cdot \hat{\vec{v}}_{s,nom}^{s} \cdot \frac{d}{3} \cdot (2 - s) \cdot e^{-j \cdot \omega_{grid} \cdot t} \tag{C.62}$$

C.2.3 One-phase voltage dip to earth (1P-dip)

Analogously to the previous section, the rotor voltage during a one-phase dip can be calculated using the symmetrical component theory. The dip is applied to phase one:

$$\begin{pmatrix} \underline{v}_{s,p} \\ \underline{v}_{s,n} \end{pmatrix} = \frac{1}{3} \cdot \begin{pmatrix} 1 & \underline{a} & \underline{a}^2 \\ 1 & \underline{a}^2 & \underline{a} \end{pmatrix} \cdot \hat{\vec{v}}_{s,nom} \cdot \begin{pmatrix} (1-d) \cdot e^{j \cdot 0} \\ e^{-j \cdot 2 \cdot \pi/3} \\ e^{j \cdot 2 \cdot \pi/3} \end{pmatrix} \tag{C.63}$$

$$= \hat{\vec{v}}_{s,nom} \cdot \begin{pmatrix} (1 - 1/3 \cdot d) \\ -d/3 \end{pmatrix} \tag{C.64}$$

Thus, the stator voltage before and during a one-phase dip is:

$$\vec{v}_s^{s}(t) = \hat{\vec{v}}_{s,nom}^{s} \cdot \begin{cases} e^{j \cdot \omega_{grid} \cdot t} & \text{for} \quad t \le t_0 \\ \left(1 - \frac{d}{3}\right) \cdot e^{j \cdot \omega_{grid} \cdot t} - \frac{d}{3} \cdot e^{-j \cdot \omega_{grid} \cdot t} & \text{for} \quad t > t_0 \end{cases} \tag{C.65}$$

Again, Eq. C.28 is used to calculate the forced flux components before and during a dip:

$$\vec{\Psi}_{s,f}^{s}(t) = \frac{\hat{\vec{v}}_{s,nom}^{s}}{j \cdot \omega_{grid}} \cdot \begin{cases} e^{j \cdot \omega_{grid} \cdot t} & \text{for} \quad t \le t_0 \\ \left(1 - \frac{d}{3}\right) \cdot e^{j \cdot \omega_{grid} \cdot t} + \frac{d}{3} \cdot e^{-j \cdot \omega_{grid} \cdot t} & \text{for} \quad t > t_0 \end{cases} \tag{C.66}$$

The amplitude of the natural flux component can be calculated from the difference of the forced flux values for $t = t_0$:

$$\vec{\Psi}_{s,nat}^{s}(t = t_0) = \frac{\hat{\vec{v}}_{s,nom}^{s}}{j \cdot \omega_{grid}} \cdot \left[e^{j \cdot \omega_{grid} \cdot t_0} - \left(1 - \frac{d}{3}\right) \cdot e^{j \cdot \omega_{grid} \cdot t_0} - \frac{d}{3} \cdot e^{-j \cdot \omega_{grid} \cdot t_0} \right] \tag{C.67}$$

$$= \frac{\hat{\vec{v}}_{s,nom}^{s}}{j \cdot \omega_{grid}} \cdot \frac{d}{3} \cdot \left(e^{j \cdot \omega_{grid} \cdot t_0} - e^{-j \cdot \omega_{grid} \cdot t_0} \right) \tag{C.68}$$

If the dip starts at $t_0 = 0$, the natural flux component will be zero and no transient will arise. The maximum natural flux will arise if the dip starts at $t_0 = T_{grid}/4$, then its amplitude is:

$$\vec{\Psi}_{s,nat,max}^{s}(t = t_0) = \frac{\hat{\vec{v}}_{s,nom}^{s}}{j \cdot \omega_{grid}} \cdot \frac{2 \cdot d}{3} \tag{C.69}$$

With Eqs. C.66 (second line) and C.69 the three linked stator flux components during a one-phase dip are

$$\vec{\Psi}^{s}_{s,p} = \frac{\hat{\vec{v}}^{s}_{s,nom}}{j \cdot \omega_{grid}} \cdot \left(1 - \frac{d}{3}\right) \cdot e^{j \cdot \omega_{grid} \cdot t} \tag{C.70}$$

$$\vec{\Psi}^{s}_{s,n} = \frac{\hat{\vec{v}}^{s}_{s,nom}}{j \cdot \omega_{grid}} \cdot \frac{d}{3} \cdot e^{-j \cdot \omega_{grid} \cdot t} \tag{C.71}$$

$$\vec{\Psi}^{s}_{s,nat,max} = \frac{\hat{\vec{v}}^{s}_{s,nom}}{j \cdot \omega_{grid}} \cdot \frac{2 \cdot d}{3} \cdot e^{-t/\tau} \tag{C.72}$$

and the respective rotor voltage components become:

$$\vec{v}^{s,(s)}_{r,p} = \frac{L_m}{L_m + L_{s\sigma}} \cdot \hat{\vec{v}}^{s}_{s,nom} \cdot s \cdot \left(1 - \frac{d}{3}\right) \cdot e^{j \cdot \omega_{grid} \cdot t} \tag{C.73}$$

$$\vec{v}^{s,(s)}_{r,n} = \frac{L_m}{L_m + L_{s\sigma}} \cdot \hat{\vec{v}}^{s}_{s,nom} \cdot \frac{d}{3} \cdot (2 - s) \cdot e^{-j \cdot \omega_{grid} \cdot t} \tag{C.74}$$

$$\begin{aligned} \vec{v}^{s,(s)}_{r,nat,max} &= \frac{L_m}{L_m + L_{s\sigma}} \cdot \hat{\vec{v}}^{s}_{s,nom} \cdot \frac{2 \cdot d}{3} \cdot \left[\frac{-1}{j \cdot \omega_{grid} \cdot \tau} - (1 - s)\right] \cdot e^{-t/\tau} \\ &\approx \frac{L_m}{L_m + L_{s\sigma}} \cdot \hat{\vec{v}}^{s}_{s,nom} \cdot \frac{2 \cdot d}{3} \cdot (s - 1) \cdot e^{-t/\tau} \end{aligned} \tag{C.75}$$

C.2.4 Phase-to-phase voltage dip (PP-dip)

Following the definition proposed in [24] the voltages during a phase-to-phase fault between phases two and three are defined by:

$$\begin{pmatrix} \underline{v}_{s,1} \\ \underline{v}_{s,2} \\ \underline{v}_{s,3} \end{pmatrix} = \hat{\vec{v}}_{s,nom} \cdot e^{j \cdot \omega_{grid} \cdot t} \cdot \begin{pmatrix} e^{j \cdot 0} \\ e^{j \cdot 4 \cdot \pi/3} + j \cdot d \cdot \sqrt{3}/2 \\ e^{j \cdot 2 \cdot \pi/3} - j \cdot d \cdot \sqrt{3}/2 \end{pmatrix} \tag{C.76}$$

Again, using symmetrical component theory, positive-sequence and negative-sequence stator voltage components are calculated:

$$\begin{pmatrix} \underline{v}_{s,p} \\ \underline{v}_{s,n} \end{pmatrix} = \frac{1}{3} \cdot \begin{pmatrix} 1 & \underline{a} & \underline{a}^2 \\ 1 & \underline{a}^2 & \underline{a} \end{pmatrix} \cdot \hat{\vec{v}}_{s,nom} \cdot \begin{pmatrix} e^{j \cdot 0} \\ e^{j \cdot 4 \cdot \pi/3} + j \cdot d \cdot \sqrt{3}/2 \\ e^{j \cdot 2 \cdot \pi/3} - j \cdot d \cdot \sqrt{3}/2 \end{pmatrix} \tag{C.77}$$

$$= \hat{\vec{v}}_{s,nom} \cdot \begin{pmatrix} (1 - 1/2 \cdot d) \\ d/2 \end{pmatrix} \tag{C.78}$$

The stator voltage vector before and during a phase-to-phase dip is:

$$\vec{v}_s^s(t) = \hat{\vec{v}}_{s,nom}^s \cdot \begin{cases} e^{j\cdot\omega_{grid}\cdot t} & \text{for} \quad t \le t_0 \\ \left(1-\frac{d}{2}\right)\cdot e^{j\cdot\omega_{grid}\cdot t} + \frac{d}{2}\cdot e^{-j\cdot\omega_{grid}\cdot t} & \text{for} \quad t > t_0 \end{cases} \tag{C.79}$$

and the corresponding forced stator flux becomes:

$$\vec{\Psi}_{s,f}^s(t) = \frac{\hat{\vec{v}}_{s,nom}^s}{j\cdot\omega_{grid}} \cdot \begin{cases} e^{j\cdot\omega_{grid}\cdot t} & \text{for} \quad t \le t_0 \\ \left(1-\frac{d}{2}\right)\cdot e^{j\cdot\omega_{grid}\cdot t} - \frac{d}{2}\cdot e^{-j\cdot\omega_{grid}\cdot t} & \text{for} \quad t > t_0 \end{cases} \tag{C.80}$$

Analogously to the previous section, the amplitude of the natural flux component is calculated from the difference of the instantaneous flux before and during the dip at $t = t_0$:

$$\vec{\Psi}_{s,nat}^s(t=t_0) = \frac{\hat{\vec{v}}_{s,nom}^s}{j\cdot\omega_{grid}} \cdot \left[e^{j\cdot\omega_{grid}\cdot t_0} - \left(1-\frac{d}{2}\right)\cdot e^{j\cdot\omega_{grid}\cdot t_0} - \frac{d}{2}\cdot e^{-j\cdot\omega_{grid}\cdot t_0}\right] \tag{C.81}$$

$$= \frac{\hat{\vec{v}}_{s,nom}^s}{j\cdot\omega_{grid}} \cdot \frac{d}{2} \cdot \left(e^{j\cdot\omega_{grid}\cdot t_0} - e^{-j\cdot\omega_{grid}\cdot t_0}\right) \tag{C.82}$$

Similar to the one-phase dip, the amplitude of the natural flux component will be maximal if the dip starts at $t_0 = T_{grid}/4$. The maximal possible amplitude is:

$$\vec{\Psi}_{s,nat,max}^s(t=t_0) = \frac{\hat{\vec{v}}_{s,nom}^s}{j\cdot\omega_{grid}} \cdot d \tag{C.83}$$

The three linked stator flux components are thus:

$$\vec{\Psi}_{s,p}^s = \frac{\hat{\vec{v}}_{s,nom}^s}{j\cdot\omega_{grid}} \cdot \left(1-\frac{d}{2}\right)\cdot e^{j\cdot\omega_{grid}\cdot t} \tag{C.84}$$

$$\vec{\Psi}_{s,n}^s = \frac{\hat{\vec{v}}_{s,nom}^s}{j\cdot\omega_{grid}} \cdot \frac{d}{2}\cdot e^{-j\cdot\omega_{grid}\cdot t} \tag{C.85}$$

$$\vec{\Psi}_{s,nat,max}^s = \frac{\hat{\vec{v}}_{s,nom}^s}{j\cdot\omega_{grid}} \cdot d \cdot e^{-t/\tau} \tag{C.86}$$

And the corresponding rotor voltage components are:

$$\vec{v}_{r,p}^{s,(s)} = \frac{L_m}{L_m + L_{s\sigma}} \cdot \hat{\vec{v}}_{s,nom}^s \cdot s \cdot \left(1-\frac{d}{2}\right)\cdot e^{j\cdot\omega_{grid}\cdot t} \tag{C.87}$$

$$\vec{v}_{r,n}^{s,(s)} = \frac{L_m}{L_m + L_{s\sigma}} \cdot \hat{\vec{v}}_{s,nom}^s \cdot \frac{d}{2} \cdot (2-s)\cdot e^{-j\cdot\omega_{grid}\cdot t} \tag{C.88}$$

$$\vec{v}_{r,nat,max}^{s,(s)} = \frac{L_m}{L_m + L_{s\sigma}} \cdot \hat{\vec{v}}_{s,nom}^s \cdot d \cdot \left[\frac{-1}{j\cdot\omega_{grid}\cdot\tau} - (1-s)\right]\cdot e^{-t/\tau}$$

$$\approx \frac{L_m}{L_m + L_{s\sigma}} \cdot \hat{\vec{v}}_{s,nom}^s \cdot d \cdot (s-1)\cdot e^{-t/\tau} \tag{C.89}$$

The rotor voltage components estimated in the four previous sections are summarised in Table 4.4. As mentioned before, these values are worst-case values. During a real dip the voltage will be lower thanks to voltage drops over grid and transformer impedances and the stator resistance and leakage inductance of the generator.

C.3 Coordinate transformation of controller transfer functions

In the following, the transformation of an abstract transfer function as given in Eq. C.90 from one rotating coordinate system (R-CS, superscript R) to a static coordinate system (S-CS, superscript S) is demonstrated. The rotational speed of the R-CS relative to the S-CS is ω.

$$\underline{G}^R(p) = \frac{\underline{y}^R(p)}{\underline{x}^R(p)} = \frac{b_n p^n + b_{n-1} p^{n-1} + \cdots + b_1 p + b_0}{a_m p^m + a_{m-1} p^{m-1} + \cdots + a_1 p + a_0} \tag{C.90}$$

A transfer function in Laplace domain like the one given in Eq. C.90 corresponds to a differential equation as given in Eq. C.91.

$$\begin{aligned} a_m \underline{y}^{R(m)}(t) + a_{m-1} \underline{y}^{R(m-1)}(t) + \cdots + a_1 \underline{\dot{y}}^R(t) + a_0 \underline{y}^R(t) \\ = b_n \underline{x}^{R(n)}(t) + b_{n-1} \underline{x}^{R(n-1)}(t) + \cdots + b_1 \underline{\dot{x}}^R(t) + b_0 \underline{x}^R(t) \end{aligned} \tag{C.91}$$

For the transformation of a complex quantity from one CS to another CS, Eqs. C.92 – C.94 apply (cf. Eqs. A.20 and A.21).

$$\underline{x}^R = e^{-j\omega t} \cdot \underline{x}^S \tag{C.92}$$

$$\underline{\dot{x}}^R = e^{-j\omega t} \cdot \underline{\dot{x}}^S - j\omega \cdot e^{-j\omega t} \cdot \underline{x}^S = e^{-j\omega t} \cdot \left(\underline{\dot{x}}^S - j\omega \cdot \underline{x}^S \right) \tag{C.93}$$

$$\underline{\ddot{x}}^R = e^{-j\omega t} \cdot \underline{\ddot{x}}^S - 2j\omega \cdot e^{-j\omega t} \cdot \underline{\dot{x}}^S - \omega^2 \cdot e^{-j\omega t} \cdot \underline{x}^S = e^{-j\omega t} \cdot \left(\underline{\ddot{x}}^S - 2j\omega \cdot \underline{\dot{x}}^S - \omega^2 \cdot \underline{x}^S \right) \tag{C.94}$$

To transform the differential equation (Eq. C.91) from one CS to another CS $\underline{x}$, $\underline{y}$ and all derivatives of $\underline{x}$ and $\underline{y}$ have to be replaced according to Eqs. C.92 – C.94. Obviously, the term $e^{-j\omega t} \neq 0$ will appear in every summand of the new equation and can therefore be omitted. The Laplace transformation of the new differential equation results in

$$\begin{aligned} \Big(a_m (p - j\omega)^m + a_{m-1} (p - j\omega)^{m-1} + \cdots + a_1 (p - j\omega) + a_0 \Big) \cdot \underline{y}^S \\ = \Big(b_n (p - j\omega)^n + b_{n-1} (p - j\omega)^{n-1} + \cdots + b_1 (p - j\omega) + b_0 \Big) \cdot \underline{x}^S \end{aligned} \tag{C.95}$$

The transfer function in the new coordinate system is therefore:

$$\underline{G}^S(p) = \frac{\underline{y}^S(p)}{\underline{x}^S(p)} = \frac{b_n (p - j\omega)^n + b_{n-1} (p - j\omega)^{n-1} + \cdots + b_1 (p - j\omega) + b_0}{a_m (p - j\omega)^m + a_{m-1} (p - j\omega)^{m-1} + \cdots + a_1 (p - j\omega) + a_0} \tag{C.96}$$

Eq. C.96 shows that the transformation of a transfer function from one coordinate system to another coordinate system corresponds to a replacement of p by $p - j\omega$:

$$\underline{G}^S(p) = \underline{G}^R(p - j\omega) \tag{C.97}$$

This simple transformation rule is used in the following sections.

C.3.1 Transformation of PI-controllers from p-CS and n-CS to the static coordinate system

To transfer the PI-PN control scheme to static $\alpha\beta$-CS, the positive-sequence current controllers have to be rotated from p-CS to $\alpha\beta$-CS (relative rotation frequency $= \omega_0$) and the negative-sequence current controllers have to be rotated from n-CS to $\alpha\beta$-CS (relative rotation frequency $= -\omega_0$). The sum of both transformed current controllers builds the FS current controllers:

$$\underline{G}^p(p) = K_{P,PI} + K_{I,PI} \cdot \frac{1}{p} \tag{C.98}$$

$$\underline{G}^n(p) = K_{P,PI} + K_{I,PI} \cdot \frac{1}{p} \tag{C.99}$$

$$\underline{G}^S(p) = \underline{G}^p(p - j\omega_0) + \underline{G}^n(p + j\omega_0) \tag{C.100}$$

$$= 2K_{P,PI} + K_{I,PI} \cdot \left(\frac{1}{p - j\omega_0} + \frac{1}{p + j\omega_0} \right) \tag{C.101}$$

$$= 2K_{P,PI} + 2K_{I,PI} \cdot \frac{p}{p^2 + \omega_o^2} \tag{C.102}$$

C.3.2 Transformation of PI-PN control scheme to the p-CS

To transform the PI-PN control scheme to p-CS, only the negative-sequence current controllers have to be rotated from n-CS to p-CS (relative rotation frequency $= -2\omega_0$). Again, the sum of both controllers builds the control transfer function in p-CS:

$$\underline{G}^p(p) = K_{P,PI} + K_{I,PI} \cdot \frac{1}{p} \tag{C.103}$$

$$\underline{G}^n(p) = K_{P,PI} + K_{I,PI} \cdot \frac{1}{p} \tag{C.104}$$

$$\underline{G}^p_{p+n}(p) = \underline{G}^p(p) + \underline{G}^n(p + 2j\omega_0) \tag{C.105}$$

$$= 2K_{P,PI} + K_{I,PI} \cdot \left(\frac{1}{p} + \frac{1}{p + 2j\omega_0} \right) \tag{C.106}$$

$$= 2K_{P,PI} + K_{I,PI} \cdot \frac{1}{p} + K_{I,PI} \cdot \frac{p}{p^2 + 4\omega_0^2} - K_{I,PI} \cdot \frac{j2\omega_0}{p^2 + 4\omega_0^2} \tag{C.107}$$

The last term represents a coupling between d- and q-component. The first three terms comply with the PI-NFSC transfer function given in Eq. 6.3.

C.3.3 Transformation of v-decoupling algorithm to the static coordinate system

The v-decoupling algorithm is used in the p-CS. It can be transferred to the static coordinate system, where the relative rotation frequency is ω_0:

$$\underline{G}^{p}_{v\text{-deco}}(p) = \frac{\underline{v}_{dq,deco}}{\underline{v}_{dq}} = 1 + \frac{j\omega_0 T_\sigma}{T_\sigma p + 1} \tag{C.108}$$

$$\underline{G}^{S}_{v\text{-deco}}(p) = \frac{\underline{v}_{\alpha\beta,deco}}{\underline{v}_{\alpha\beta}} = \underline{G}^{p}_{v\text{-deco}}(p - j\omega_0) \tag{C.109}$$

$$= 1 + \frac{j\omega_0 T_\sigma}{T_\sigma \cdot (p - j\omega_0) + 1} \tag{C.110}$$

$$= \frac{pT_\sigma + 1}{pT_\sigma + 1 - j\omega_0 T_\sigma} \tag{C.111}$$

$$= \frac{1}{1 - \frac{j\omega_0 T_\sigma}{pT_\sigma + 1}} \tag{C.112}$$

The decomposition of Eq. C.112 into α- and β-components results in:

$$v_{\alpha,deco} = v_\alpha - \frac{\omega_0 T_\sigma}{pT_\sigma + 1} \cdot v_{\beta,deco} \tag{C.113}$$

$$v_{\beta,deco} = v_\beta + \frac{\omega_0 T_\sigma}{pT_\sigma + 1} \cdot v_{\alpha,deco} \tag{C.114}$$

These equations correspond to the structure shown in Fig. 6.13.

C.3.4 Transformation of PI-NFSC control scheme to the static coordinate system

The transformation of the PI-NFS control scheme to the static coordinate system is done by a rotation with the relative frequency ω_0.

$$\underline{G}^{p}(p) = K_{P,PINFSC} + K_{I,PINFSC} \cdot \frac{1}{p} + K_{S,PINFSC} \cdot \frac{p}{p^2 + 4\omega_0^2} \tag{C.115}$$

$$\underline{G}^{S}(p) = \underline{G}^{p}(p - j\omega_0) \tag{C.116}$$

$$= K_{P,PINFSC} + K_{I,PINFSC} \cdot \frac{1}{p - j\omega_0} + K_{S,PINFSC} \cdot \frac{p - j\omega_0}{(p - j\omega_0)^2 + 4\omega_0^2} \tag{C.117}$$

$$= K_{P,PINFSC} + K_{I,PINFSC} \cdot \frac{p + j\omega_0}{p^2 + \omega_0^2} + K_{S,PINFSC} \cdot \frac{p - j\omega_0}{p^2 - j2\omega_0 p + 3\omega_0^2} \tag{C.118}$$

The first two terms represent the frequency-selective controller given in Eq. 6.4, where the second term contains an additional coupling component. The third term is analysed more precisely

using partial fraction decomposition:

$$\frac{p-j\omega_0}{p^2-j2\omega_0 p+3\omega_0^2} = \frac{(p-j\omega_0)\cdot\left(p^2+3\omega_0^2+j2\omega_0 p\right)}{p^4+10p^2\omega_0^2+9\omega_0^4} \tag{C.119}$$

$$= \frac{p^3+5\omega_0^2 p+j\omega_0 p^2-3j\omega_0^3}{\left(p^2+\omega_0^2\right)\cdot\left(p^2+9\omega_0^2\right)} \tag{C.120}$$

$$= \frac{\left(p^3+5\omega_0^2 p\right)}{\left(p^2+\omega_0^2\right)\cdot\left(p^2+9\omega_0^2\right)} + j\cdot\frac{\omega_0 p^2-3\omega_0^3}{\left(p^2+\omega_0^2\right)\cdot\left(p^2+9\omega_0^2\right)} \tag{C.121}$$

$$= \frac{A}{p^2+\omega_0^2} + \frac{B}{p^2+9\omega_0^2} \tag{C.122}$$

With $A = (p-j\omega_0)/2$ and $B = (p+3j\omega_0)/2$ the expression of Eq. C.121 can be transformed to:

$$\frac{1}{2}\cdot\frac{p-j\omega_0}{p^2+\omega_0^2} + \frac{1}{2}\cdot\frac{p+3j\omega_0}{p^2+9\omega_0^2} \tag{C.123}$$

Therewith, the complete control transfer function in static coordinate system (without v-decoupling algorithm) is:

$$\underline{G}^S(p) = K_{P,PINFSC} + K_{I,PINFSC}\cdot\frac{p+j\omega_0}{p^2+\omega_0^2} + \frac{K_{S,PINFSC}}{2}\cdot\left(\frac{p-j\omega_0}{p^2+\omega_0^2} + \frac{p+3j\omega_0}{p^2+9\omega_0^2}\right) \tag{C.124}$$

The last equation (Eq. C.124) shows that the PI-NFS controller, transferred to the static coordinate system, contains a frequency-selective component for the third harmonic including a coupling term. As the two control schemes are mathematically identical, this is valid also for the original PI-NFSC in p-CS, although it is not obvious there.

D Simulation parameters and data sheets

Table D.1: System parameters

Part	Quantity	Symbol	Value
Grid	System fundamental frequency, grid frequency	f_{grid}	50 Hz
DFIG	Nominal power	$P_{G,nom}$	850 kW
RSC	Sample rate	$f_{rsc,p}$	5 kHz
DC-link	Nominal voltage, related to nominal stator voltage	$v_{DC,nom}/v_{s,nom}$	1.16
GSC	Sample rate	$f_{gsc,p}$	10 kHz
GSC-Transformer	Voltage ratio	w_{gscT}	0.696
Main Transformer	Voltage ratio	w_{MT}	0.0345

Table D.2: Field-oriented control: controller parameters

Control part	Controller	Symbol	Value[a]
RSC	Rotor current control	K_{IR}	$3.3\,\mathrm{V/A}$
		T_{IR}	29 ms
	Power control	$K_{P,Q}$	$4.16 \times 10^{-4}\,\mathrm{V^{-1}}$
		$T_{P,Q}$	30 ms
		$T_{f,P,Q}$	30 ms
GSC	Grid-side inverter current control	K_{IG}	$8.5\,\mathrm{V/A}$
		T_{IG}	57 ms
	DC-link voltage control	K_{VDC}	$2.45\,\mathrm{V/A}$
		T_{VDC}	12.8 ms
		$T_{f,v_{DC}}$	3 ms

[a] These control parameters were determined as described in Chapter 3 and are not identical to the parameters used for the validation of the model.

Table D.3: PN-control: DC-link voltage controller parameters

Filter method	Symbol	Value
PT1 & feedback, MAV & feedback, MAV, DSOGI, notch filter	K_{VDC}	$2.45\,\mathrm{V/A}$
	T_{VDC}	12.8 ms
Fortescue Transformation	K_{VDC}	$1\,\mathrm{V/A}$
	T_{VDC}	50 ms

Table D.4: PN-control: controller parameters

Component calculation	$G_{C,i,rsc}$	Value	$G_{C,i,gsc}$	Value
PT1-feedback	K_{IRP}	2 V/A	K_{IGP}	1.5 V/A
	T_{IRP}	500 ms	T_{IGP}	100 ms
	K_{IRN}	5 V/A	K_{IGN}	2 V/A
	T_{IRN}	20 ms	T_{IGN}	100 ms
MAV-feedback	K_{IRP}	2 V/A	K_{IGP}	1 V/A
	T_{IRP}	500 ms	T_{IGP}	100 ms
	K_{IRN}	3 V/A	K_{IGN}	1 V/A
	T_{IRN}	20 ms	T_{IGN}	100 ms
MAV	K_{IRP}	1 V/A	K_{IGP}	1 V/A
	T_{IRP}	100 ms	T_{IGP}	100 ms
	K_{IRN}	1.5 V/A	K_{IGN}	0.5 V/A
	T_{IRN}	10 ms	T_{IGN}	7 ms
Fortescue Transformation	K_{IRP}	0.4 V/A	K_{IGP}	0.5 V/A
	T_{IRP}	100 ms	T_{IGP}	100 ms
	K_{IRN}	1 V/A	K_{IGN}	0.5 V/A
	T_{IRN}	5 ms	T_{IGN}	250 ms
DSOGI	K_{IRP}	0.2 V/A	K_{IGP}	2 V/A
	T_{IRP}	200 ms	T_{IGP}	100 ms
	K_{IRN}	2 V/A	K_{IGN}	1 V/A
	T_{IRN}	20 ms	T_{IGN}	5 ms
Notch filter	K_{IRP}	1 V/A	K_{IGP}	2 V/A
	T_{IRP}	200 ms	T_{IGP}	50 ms
	K_{IRN}	5 V/A	K_{IGN}	1 V/A
	T_{IRN}	50 ms	T_{IGN}	50 ms

Table D.5: FSC(PN): modifications for PN-reference value integration

Control part	Symbol	Value
Power control	$K_{P,Q}$	8.32×10^{-5}/V
Rotor current control	K_{IR}	1 V/A
	T_{IR}	29 ms
$i_{s,n}$-filter	$Q_{DSOGI,IS}$	1.41
$i_{r,n}$-filter	$Q_{DSOGI,IR}$	0.1
$v_{r,n}$-filter	$Q_{DSOGI,VR}$	0.1

Table D.6: FLL-parameters

Parameter	Symbol	Value
DSOGI-Filter band width	Q_f	1.41
Integral controller gain	K_{fll}	0.132 $s^{-2}V^{-2}$

E Simulation and measurement results

E.1 Scale bases

Most of the simulation results are given related to the nominal values. In detail, the scale bases are:

Table E.1: Scale bases of simulation results

Quantities	P_G, Q_G	v_{DC}	i_{gsc}, i_{rsc}, i_l	m_{el}	n_{nom}
Scale base	$P_{G,nom}$	$v_{DC,nom}$	$\sqrt{\frac{2}{3}}\frac{P_{G,nom}}{V_{s,nom}}$	$\frac{P_{G,nom}\cdot 60}{n_{nom}\cdot 2\pi}$	$1.08 \cdot n_{s=0}$

E.2 Model validation

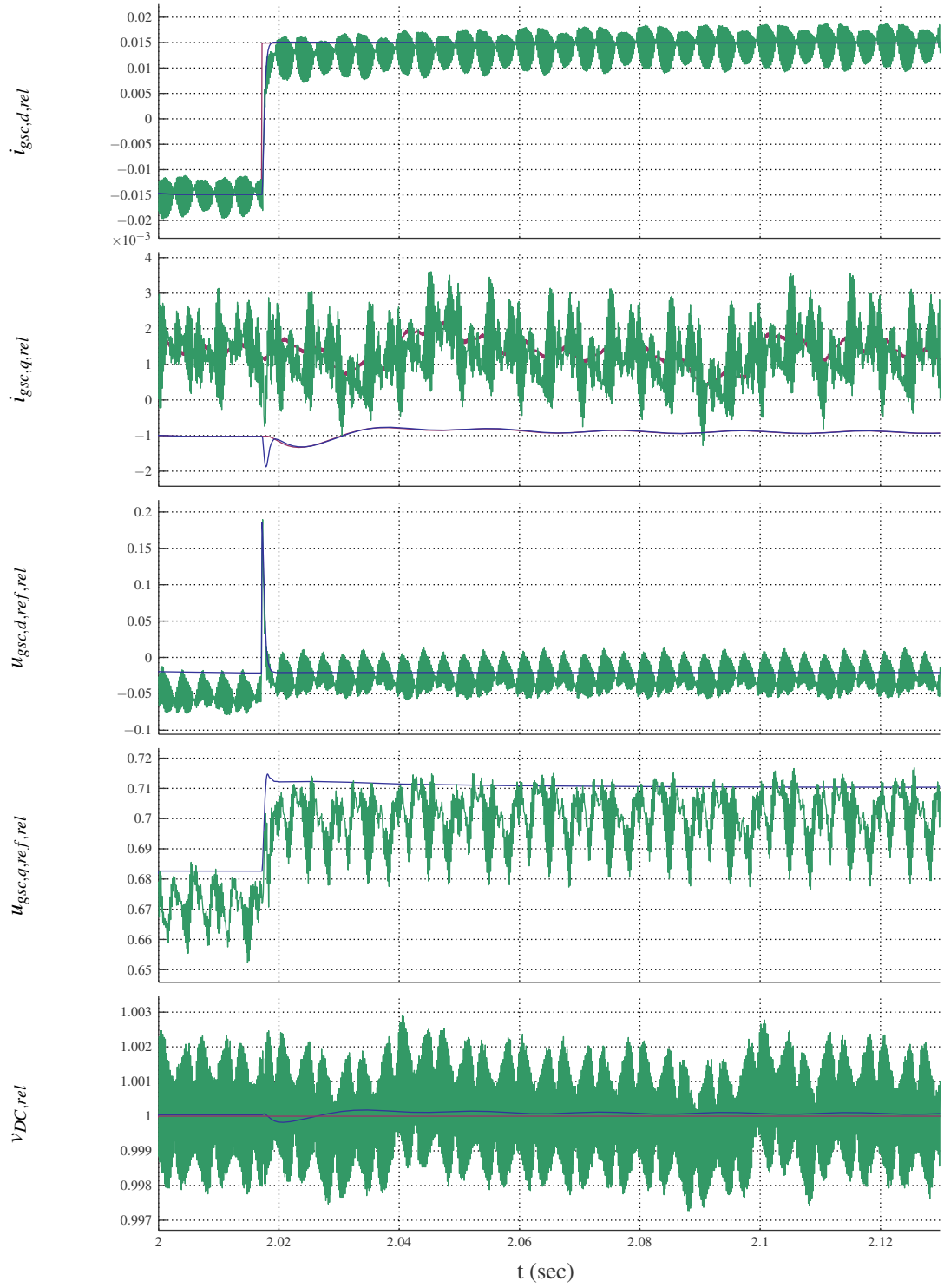

Figure E.1: Step response of $i_{gsc,d}$ with field-oriented control, simulation and measurement results: reference values, measurement results, simulation results, $P_G = 0$, $Q_G = 0$, $n = n_{nom}$

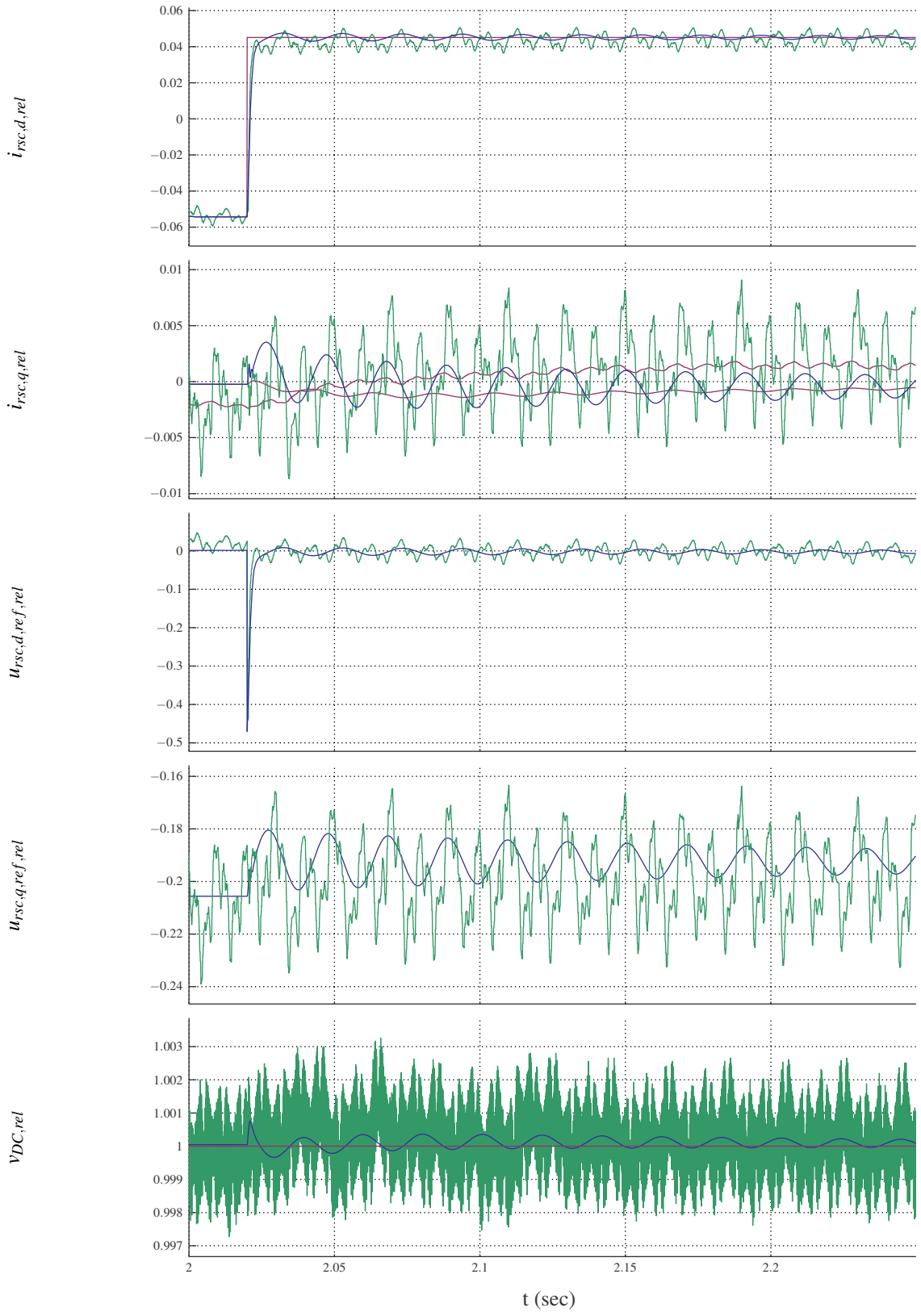

Figure E.2: Step response of $i_{rsc,d}$ with field-oriented control, simulation and measurement results: reference values, measurement results, simulation results, $P_G = 0$, $Q_G = 0$, $n = n_{nom}$

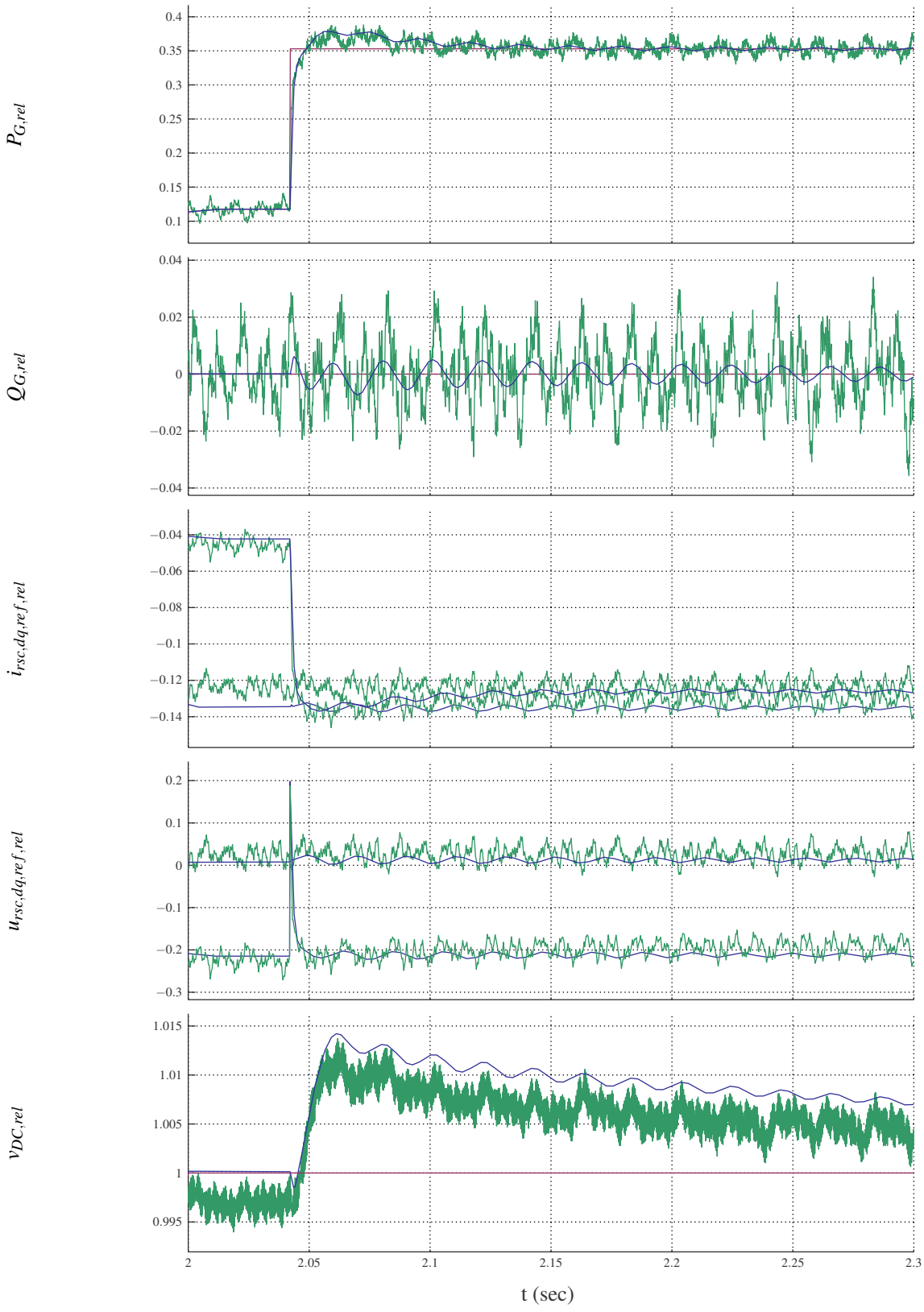

Figure E.3: Step response of P_G with field-oriented control, simulation and measurement results: reference values, measurement results, simulation results, $Q_G = 0$, $n = 1.08 \cdot n_{s=0}$

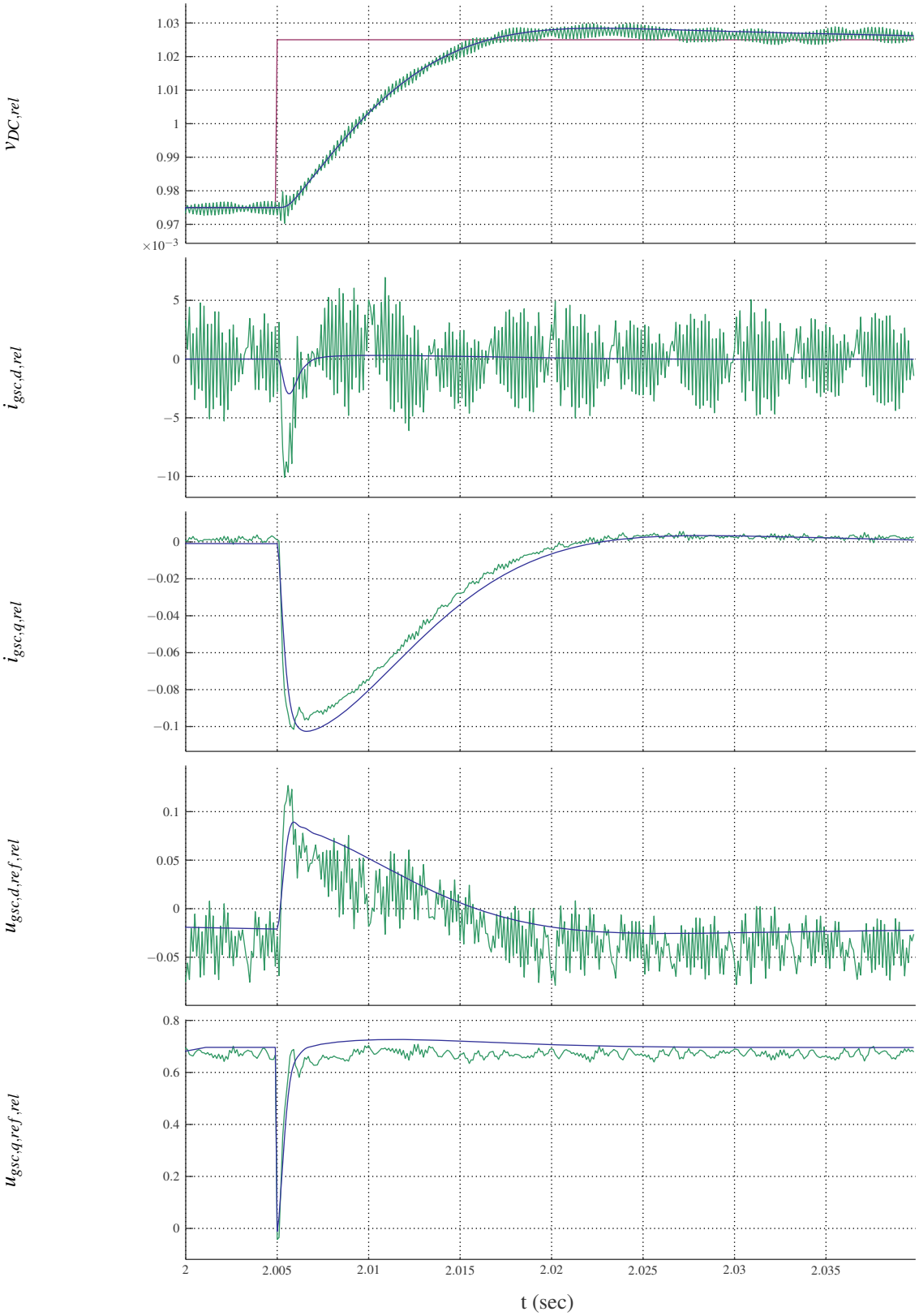

Figure E.4: Step response of v_{DC} with field-oriented control, simulation and measurement results: reference values, measurement results, simulation results, $P_G = 0$, $Q_G = 0$, $n = n_{nom}$

E.3 PN-control scheme

E.3.1 Identification of symmetrical components

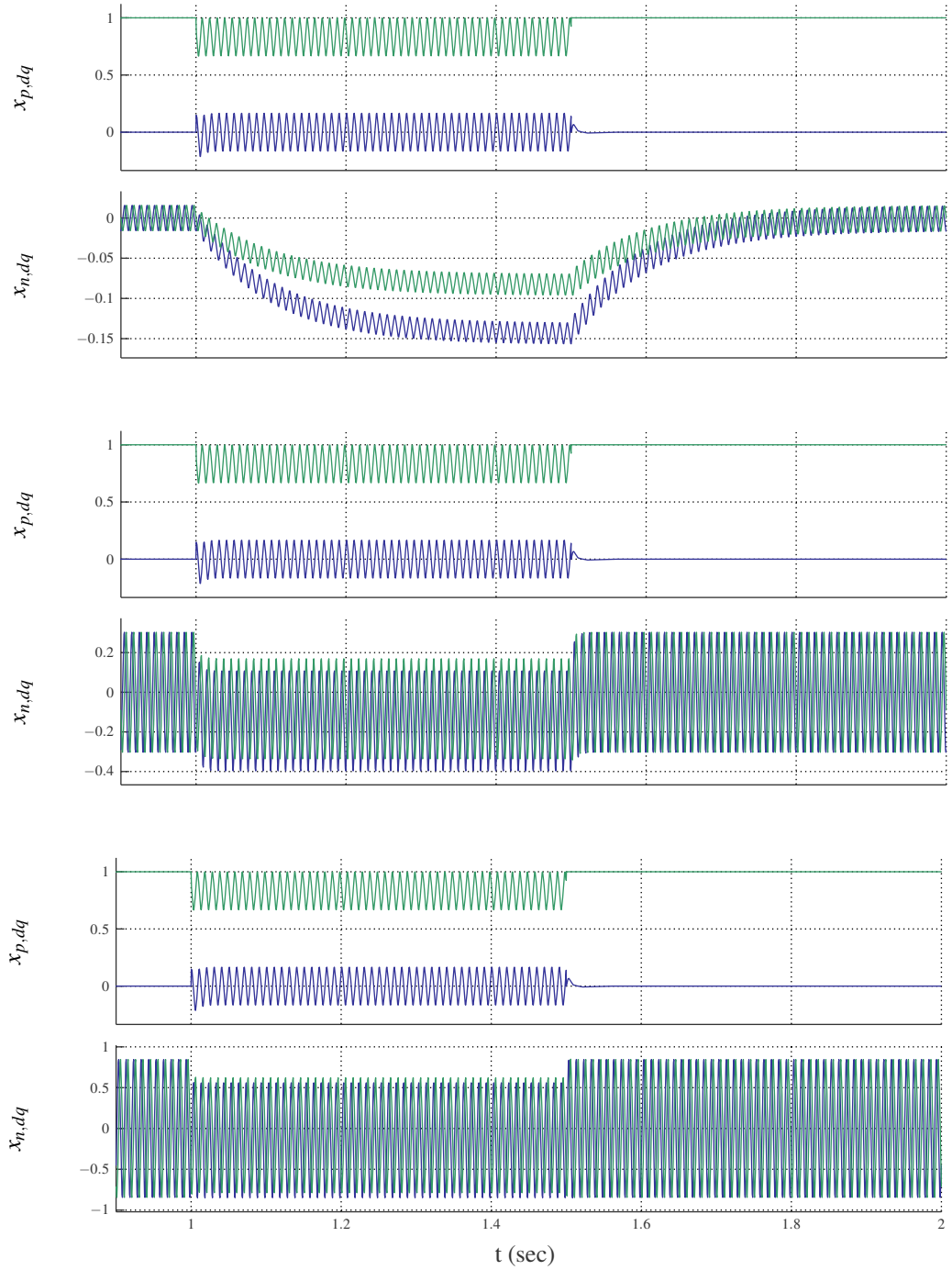

Figure E.5: Positive-sequence and negative-sequence components of asymmetrical line voltages, low-pass filter without signal feedback with three different time constants (top down): $T_f =$ 100 ms, 5 ms and 1 ms

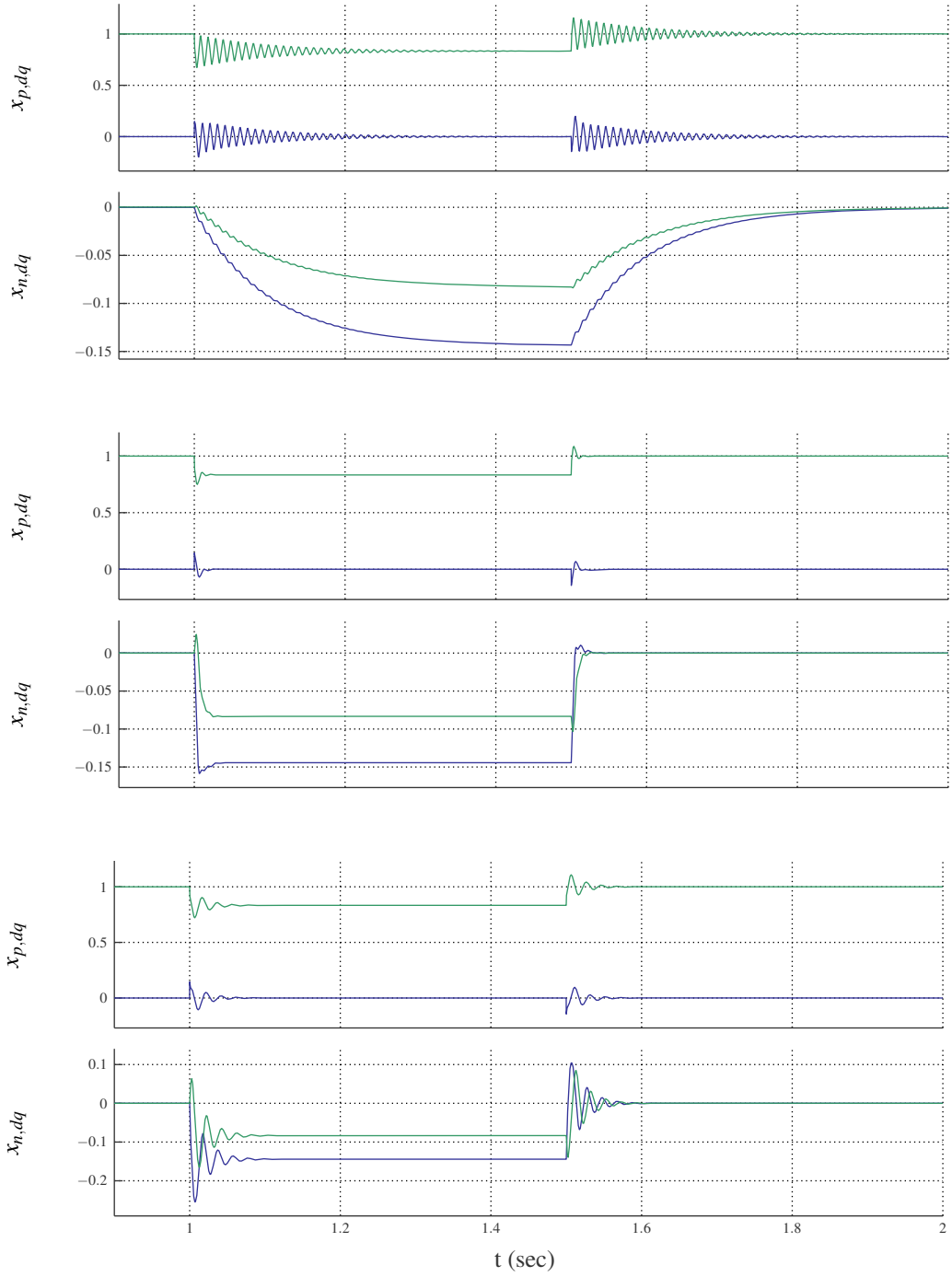

Figure E.6: Positive-sequence and negative-sequence components of asymmetrical line voltages, low-pass filter with signal feedback with three different time constants (top down): $T_f = 100\,\text{ms}$, 5 ms and 1 ms

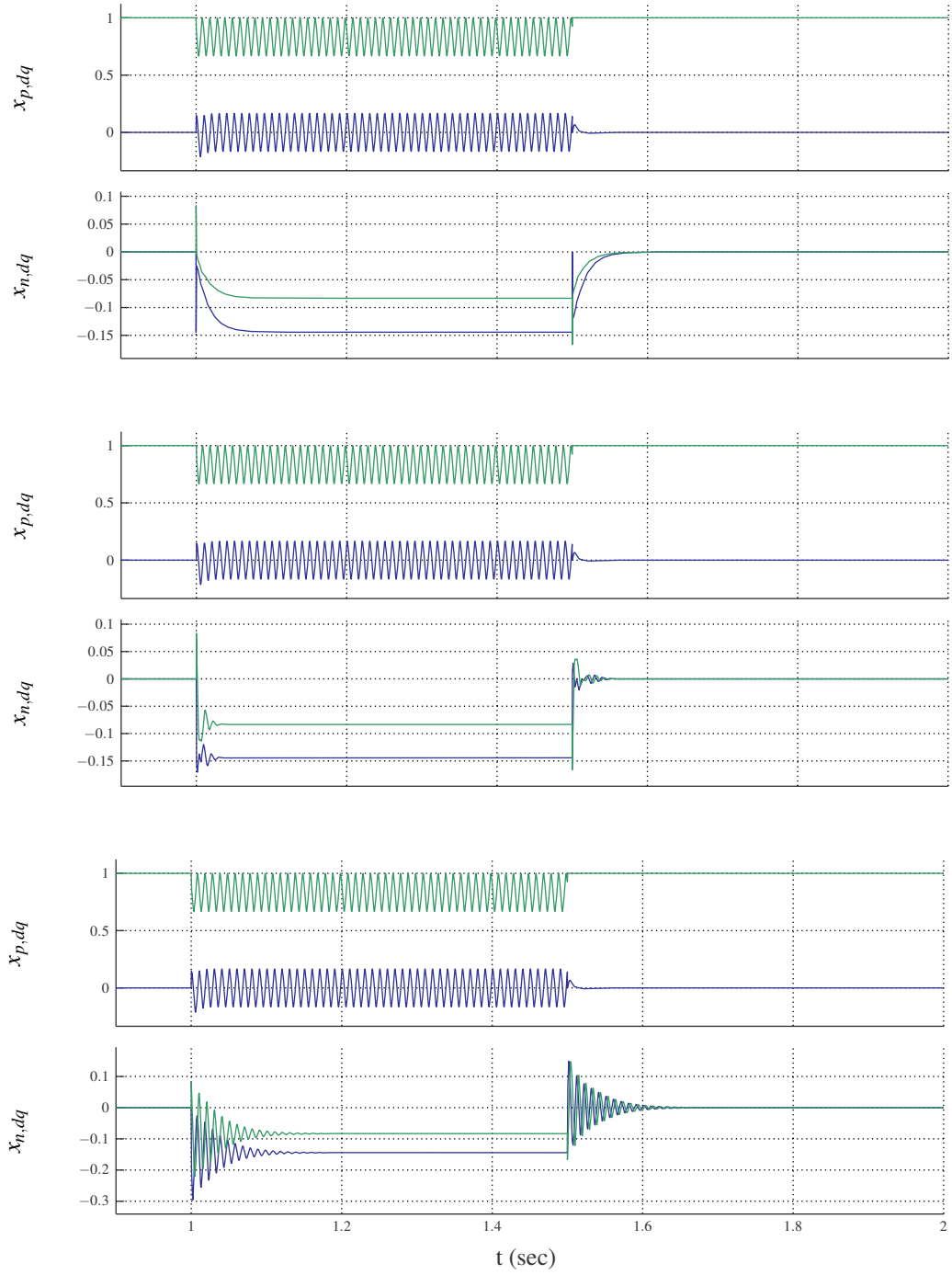

Figure E.7: Positive-sequence and negative-sequence components of asymmetrical line voltages, notch filter with three different bandwidth values (top down): $Q_f = 10$, 1 and 0.1

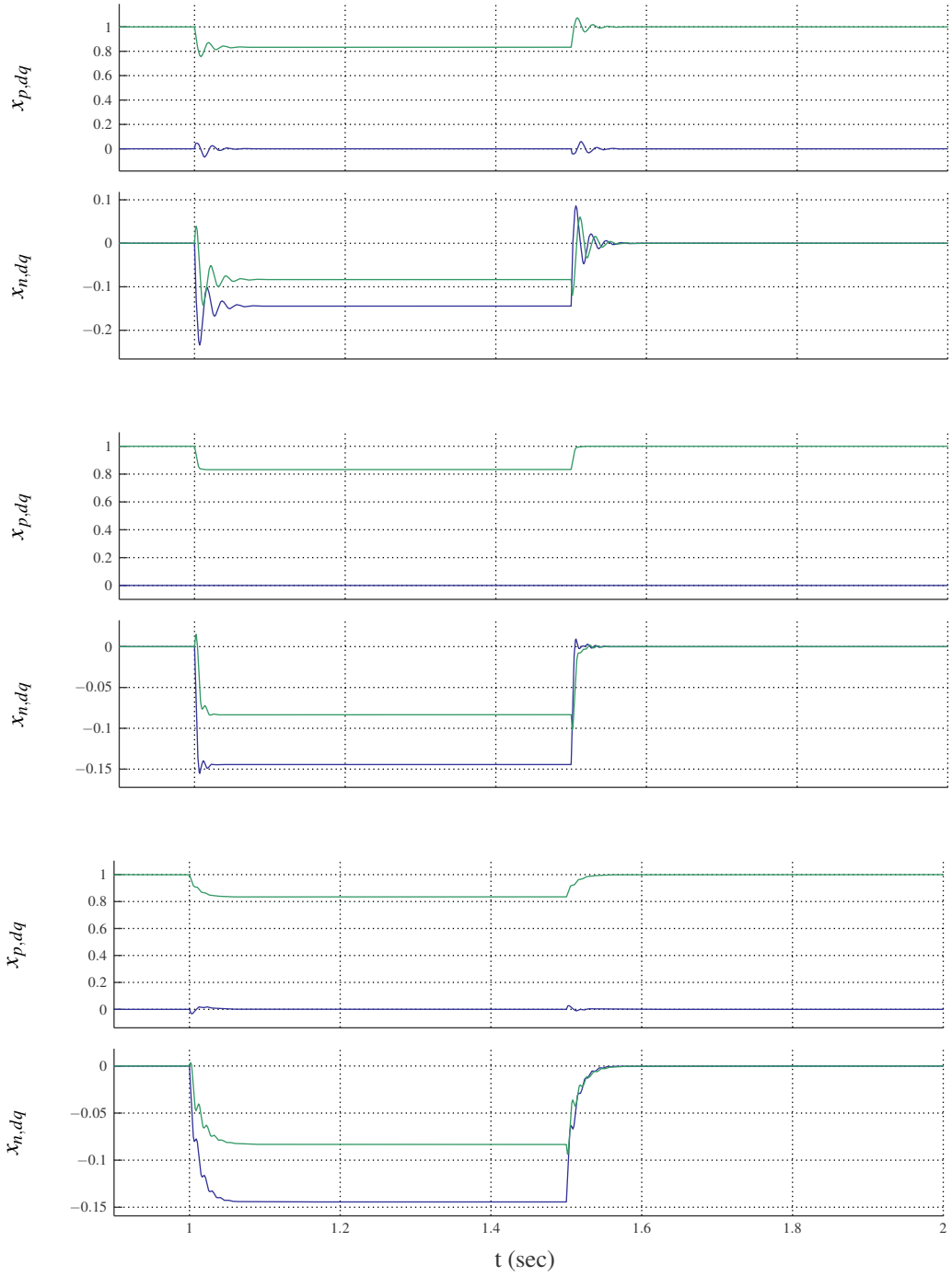

Figure E.8: Positive-sequence and negative-sequence components of asymmetrical line voltages, DSOGI-filter with three different bandwidth values (top down): $Q_f = 5$, 1.41 and 0.5

E.3.2 Calculation of reference values for grid-side current controllers with PN-control

The simulation results below are achieved using the following conditions and configuration:

- grid-side and rotor-side PN-control,
- $n = 1.08 \cdot n_{s=0}$,
- $Q_{G,ref} = 0\,\mathrm{kVAr}$,
- $P_{G,ref} = P_{G,nom}$,
- $v_{DC,ref} = v_{DC,nom}$,
- $t = 1\,\mathrm{s} \ldots 1.5\,\mathrm{s}$: 1-phase dip to 50% remaining voltage on the grid-side of the main transformer,
- MAV-filters for component calculation,

- line colours v_{DC}: v_{DC}, $v_{DC,ref}$,
- line colours $i_{gsc,ref}$: $i_{gsc,p,d,ref}$, $i_{gsc,p,q,ref}$, $i_{gsc,n,d,ref}$, $i_{gsc,n,q,ref}$.

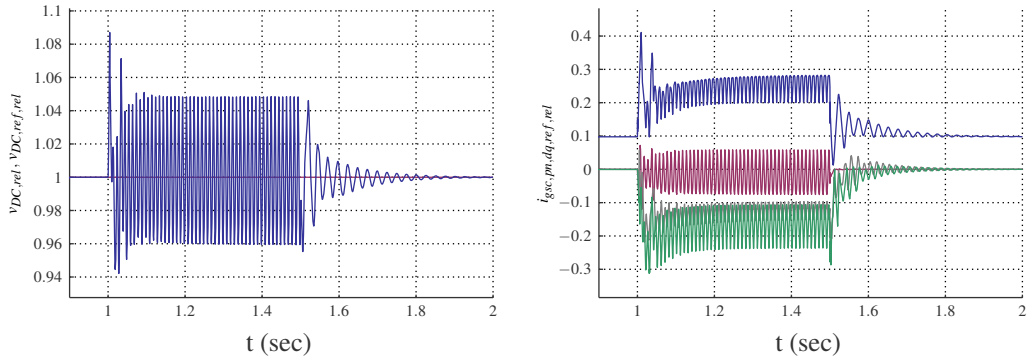

Figure E.9: Calculation of negative-sequence and positive-sequence component reference values

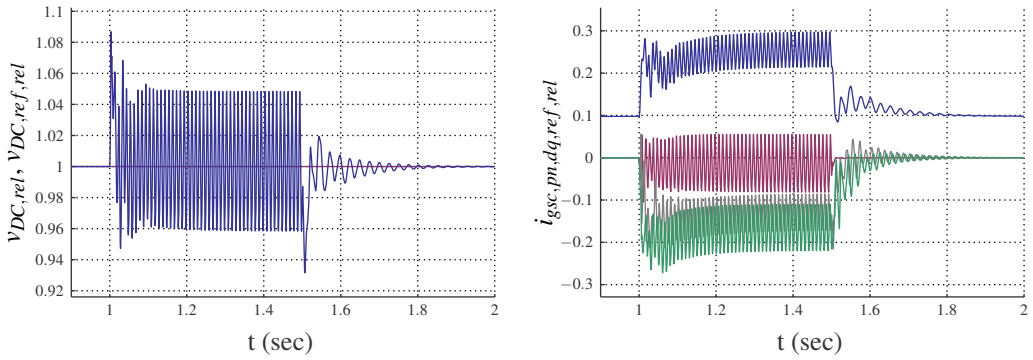

Figure E.10: Calculation of negative-sequence component reference values and $i_{gsc,p,d,ref}$, $i_{gsc,p,q,ref}$ = output of DC-link voltage controller

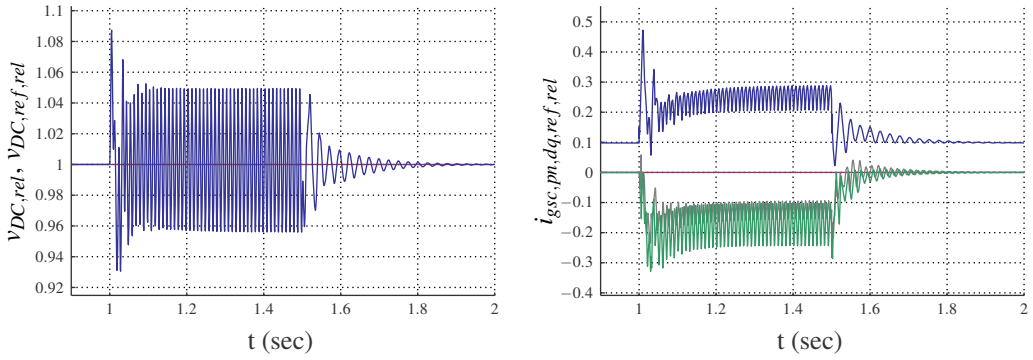

Figure E.11: Calculation of negative-sequence component reference values and $i_{gsc,p,q,ref}$, $i_{gsc,p,d,ref} = 0$

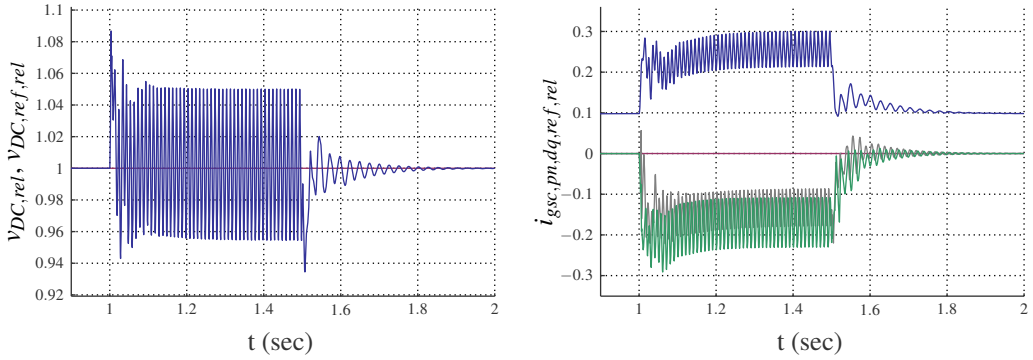

Figure E.12: Calculation of negative-sequence component reference values, $i_{gsc,p,d,ref} = 0$, $i_{gsc,p,q,ref}$ = output of DC-link voltage controller

E.4 Frequency-selective control

E.4.1 Step responses of curent d-components with field-oriented control and frequency-selective control

The following two simulation results are achieved using these conditions and configuration:

- grid-side and rotor-side frequency-selective current control,
- use of related quantities,
- $n = 1.08 \cdot n_{s=0}$,
- $t = 4\,\mathrm{s}$ – step of reference value of rotor-side current d-component,
- $v_{DC,ref} = v_{DC,nom}$,
- $P_{G,ref} = 0\,\mathrm{kW}$,
- no control of Q_G.

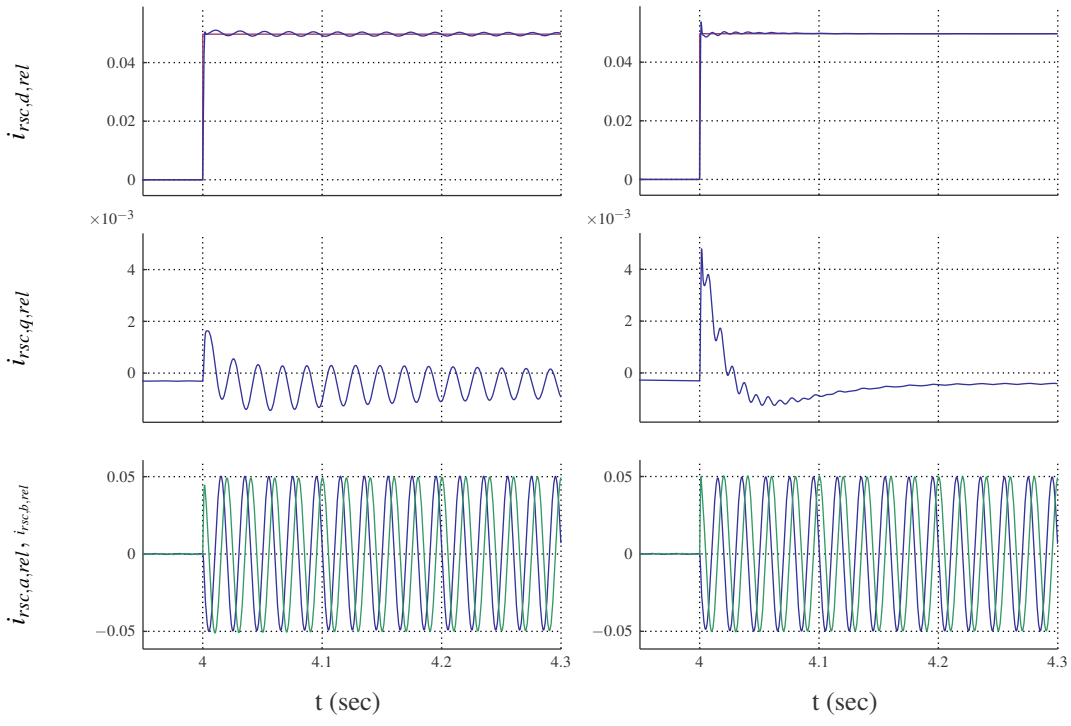

Figure E.13: Step response of rotor-side current d-component, left figure: FOC, right figure: FSC

The following two simulation results are achieved using these conditions and configuration:

- Grid-side and rotor-side frequency-selective current control,
- use of related quantities,
- $n = 1.08 \cdot n_{s=0}$,
- $t = 4\,\mathrm{s}$ – step of reference value of grid-side current d-component,
- $v_{DC,ref} = v_{DC,nom}$,
- $P_{G,ref} = 0\,\mathrm{kW}$,
- $Q_{G,ref} = 0\,\mathrm{kVAr}$.

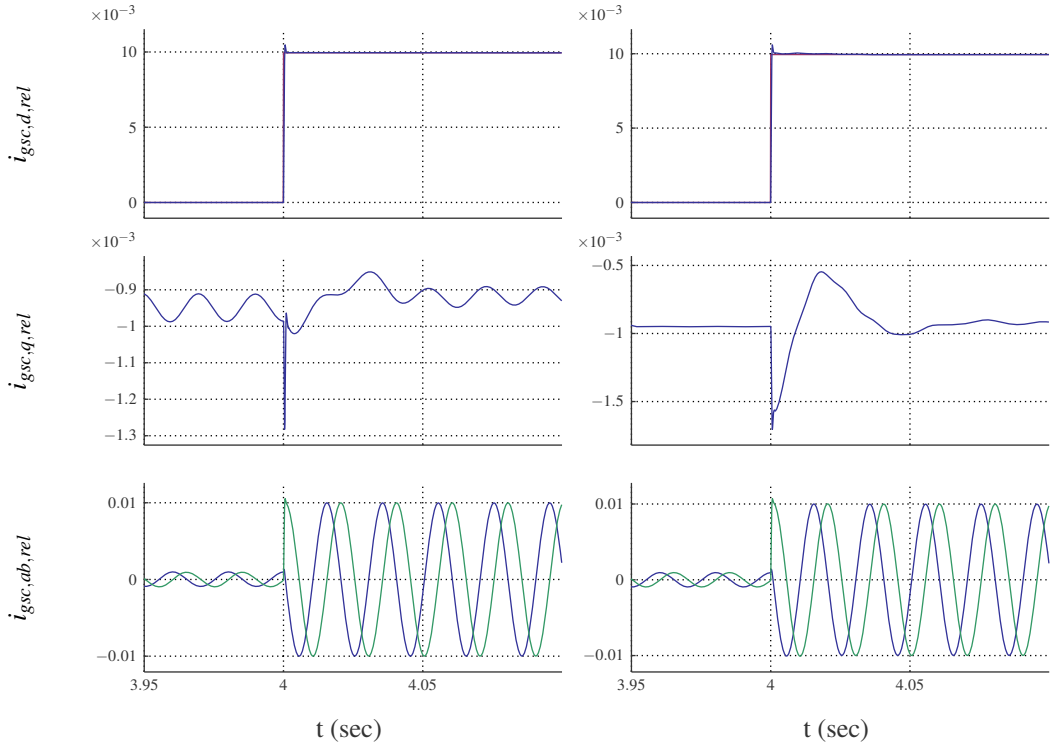

Figure E.14: Step response of grid-side current d-component, left figure: FOC, right figure: FSC

E.4.2 Stability analysis of discrete current controllers

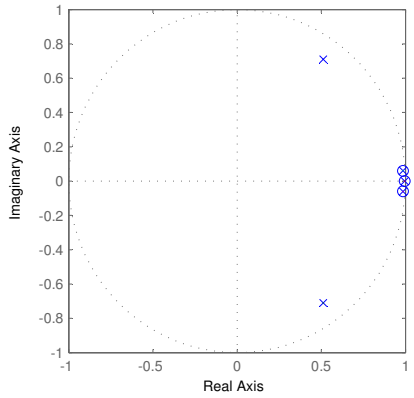

Figure E.15: Poles (x) and zeros (o) of closed rotor-side current control loop

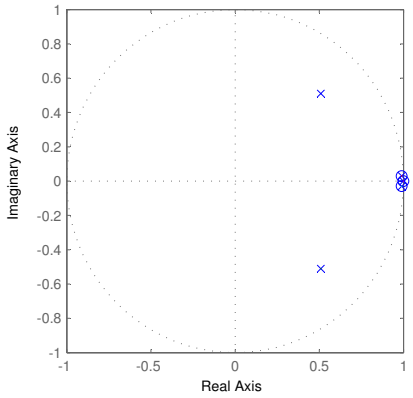

Figure E.16: Poles (x) and zeros (o) of closed grid-side current control loop

E.5 Comparison of simulation results with different control strategies

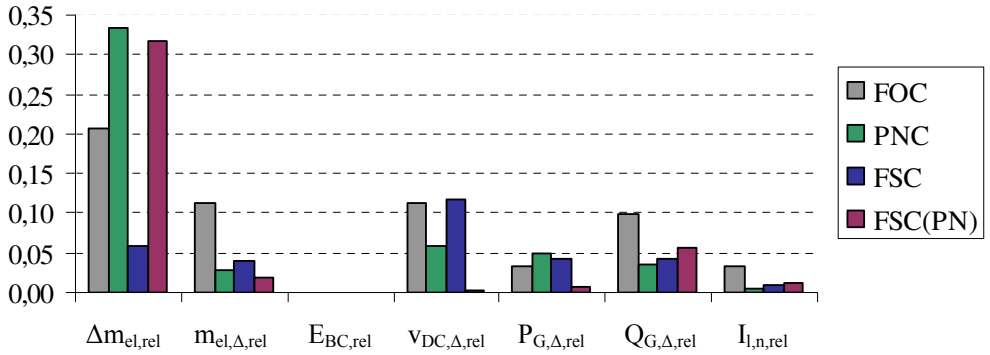

Figure E.17: Comparison of simulation results with different control strategies, 2-phase voltage dip down to 95% remaining voltage, $n = n_{s=0}$ (setting 2)

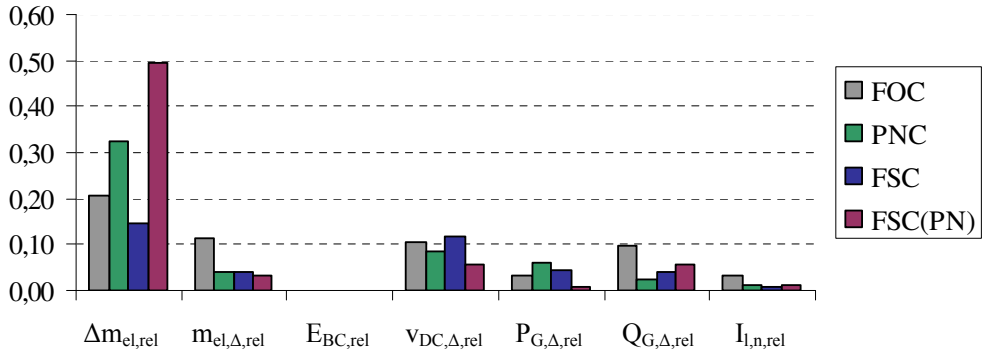

Figure E.18: Comparison of simulation results with different control strategies, 2-phase voltage dip down to 95% remaining voltage, $n = 0.92 \cdot n_{s=0}$ (setting 3)

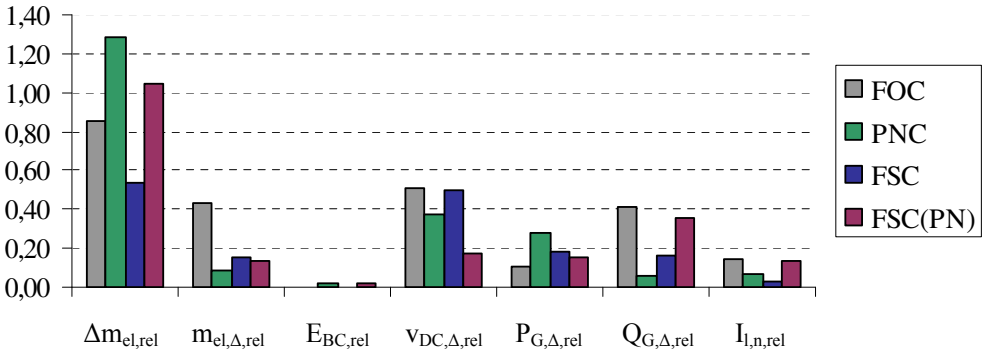

Figure E.19: Comparison of simulation results with different control strategies, 2-phase voltage dip down to 80% remaining voltage, $n = 1.08 \cdot n_{s=0}$ (setting 4)

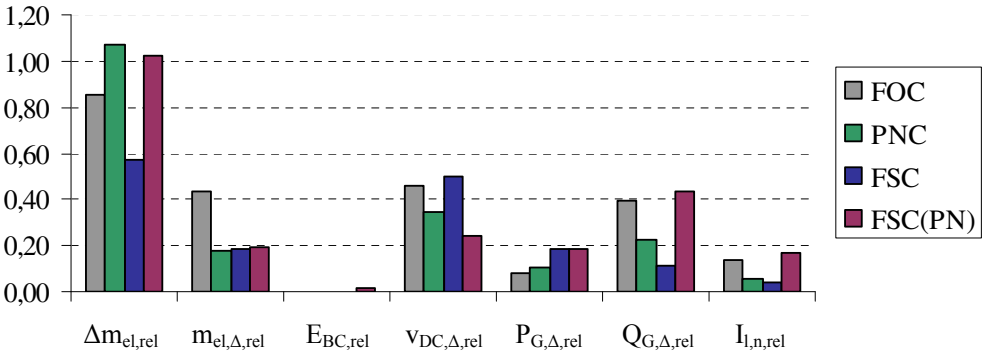

Figure E.20: Comparison of simulation results with different control strategies, 2-phase voltage dip down to 80% remaining voltage, $n = 0.92 \cdot n_{s=0}$ (setting 5)

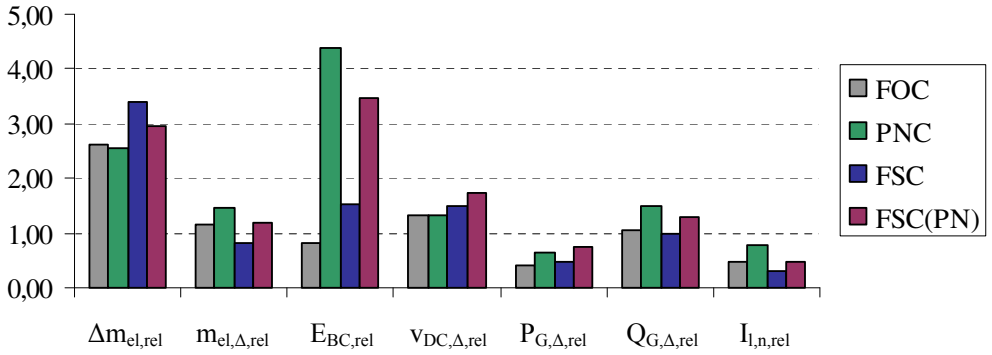

Figure E.21: Comparison of simulation results with different control strategies, 2-phase voltage dip down to 50% remaining voltage, $n = 1.08 \cdot n_{s=0}$ (setting 6)

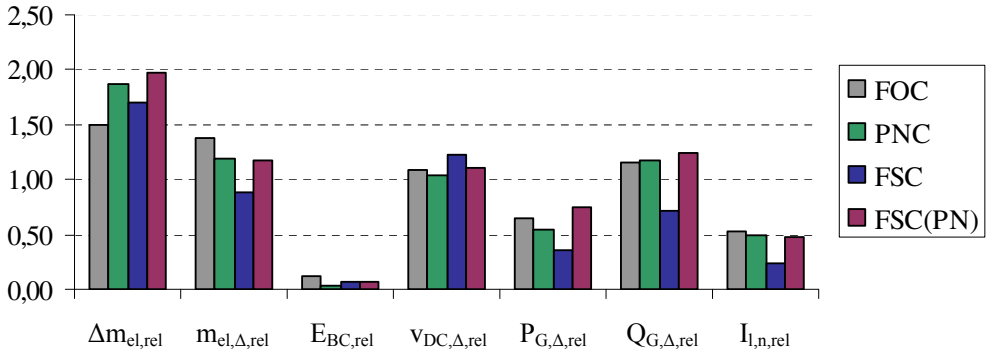

Figure E.22: Comparison of simulation results with different control strategies, 1-phase voltage dip down to 50% remaining voltage, $n = 1.08 \cdot n_{s=0}$ (setting 8)

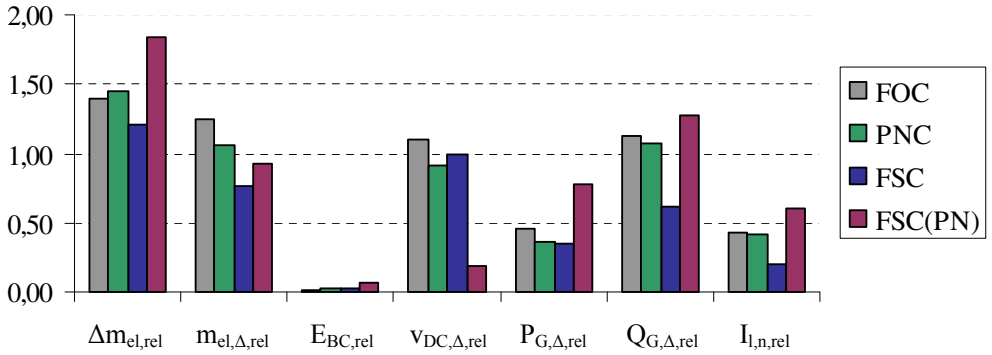

Figure E.23: Comparison of simulation results with different control strategies, 1-phase voltage dip down to 50% remaining voltage, $n = 0.92 \cdot n_{s=0}$ (setting 9)

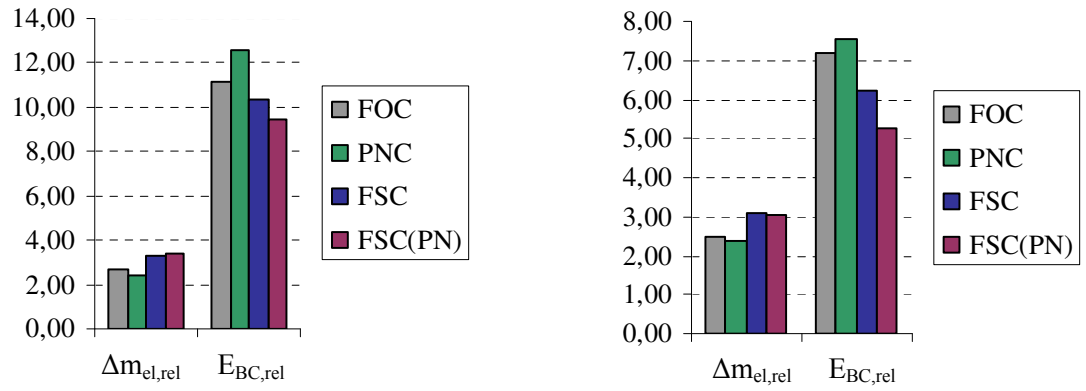

Figure E.24: Comparison of simulation results with different control strategies, 2-phase voltage dip according to Fig. 6.1, left: $n = 1.08 \cdot n_{s=0}$ (setting 10), right: $n = 0.92 \cdot n_{s=0}$ (setting 11)